

Official Cover and Approval pages include the Dean's signature, to be completed at the final exam or after required corrections are complete. No faculty/committee signatures are needed for these pages which become the first two pages of the thesis/dissertation (one consolidated document to be uploaded to Libra).

Regulation of Arteriogenesis by Mechanosensitive MicroRNAs and DNA Methylation: A Potential Epigenetic Approach for Treating Peripheral Arterial Disease

A Dissertation

Presented to

the faculty of the School of Engineering and Applied Science

University of Virginia

in partial fulfillment
of the requirements for the degree

Doctor of Philosophy

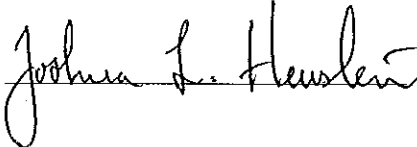
by

Joshua L. Heuslein

December 2016

APPROVAL SHEET

This Dissertation
is submitted in partial fulfillment of the requirements
for the degree of
Doctor of Philosophy

Author Signature: 

This Dissertation has been read and approved by the examining committee:

Advisor: Richard J. Price, Ph.D.

Committee Member: Brian P. Helmke, Ph.D.

Committee Member: Brian H. Annex, M.D.

Committee Member: Gary K. Owens, Ph.D.

Committee Member: Shayn M. Peirce, Ph.D.


Committee Member: _____

Accepted for the School of Engineering and Applied Science:



Craig H. Benson, School of Engineering and Applied Science

December 2016



Regulation of Arteriogenesis by Mechanosensitive MicroRNAs and DNA Methylation: A Potential Epigenetic Approach for Treating Peripheral Arterial Disease

A Dissertation

presented to the faculty of the School of Engineering and Applied Science
in partial fulfillment of the requirements for the degree of

Doctor of Philosophy

by

Joshua L. Heuslein

December 2016



Regulation of Arteriogenesis by Mechanosensitive MicroRNAs and DNA Methylation: A Potential Epigenetic Approach for Treating Peripheral Arterial Disease

A Dissertation

presented to the faculty of the School of Engineering and Applied Science
in partial fulfillment of the requirements for the degree of

Doctor of Philosophy

by

Joshua L. Heuslein

December 2016

Table of Contents

Table of Figures	viii
Table of Tables.....	xi
Acknowledgements	xii
1 Preface	1
1.1 Abstract	1
1.2 Preview of this thesis	2
2 Peripheral arterial disease (PAD) and arteriogenesis.....	2
2.1 Abbreviations.....	2
2.2 Clinical background and motivation.....	3
2.2.1 Peripheral arterial disease – definition and epidemiology	3
2.2.2 Clinical manifestations of PAD	4
2.2.3 Pathophysiology.....	5
2.2.4 Treatment options	5
2.3 Arteriogenesis.....	6
2.3.1 Initiation	6
2.3.2 Growth	7
2.3.3 Maturation.....	8
2.3.4 Shear stress set-point	8
3 Epigenetics in peripheral arterial disease (PAD)	11
3.1 Abbreviations.....	11
3.2 Epigenetics: an introduction	11
3.2.1 DNA methylation	12
3.2.2 Histone modifications	12
3.2.3 Non-coding RNA	13
3.3 A role for epigenetics in PAD	14
3.3.1 Histone modification and DNA methylation patterns and are likely to be altered in PAD patients	14
3.3.2 microRNAs in PAD.....	15
3.4 Epigenetic regulation in response to hindlimb ischemia	16
3.4.1 Histone post-translational modifications and DNA methylation.....	16
3.4.2 Non-coding RNAs	17

4	Mechanisms of amplified arteriogenesis in collateral artery segments exposed to reversed flow direction	21
4.1	Abstract	21
4.2	Abbreviations	22
4.3	Introduction.....	22
4.4	Materials and Methods.....	23
4.4.1	Mice.....	23
4.4.2	Femoral arterial ligation model.....	24
4.4.3	Muscular branch ligation model.....	24
4.4.4	Laser Doppler perfusion imaging.....	25
4.4.5	Tissue harvesting for cross sectional and collateral structure analysis by vascular casting.....	25
4.4.6	Cross sectional analysis of collateral artery structure.....	26
4.4.7	Cross sectional analysis for regional capillary density and muscle fiber atrophy.....	27
4.4.8	Immunofluorescence labeling of pericollateral Mac3 ⁺ cells.....	27
4.4.9	Tissue harvesting for in-vivo collateral artery endothelial planar cell polarization.....	28
4.4.10	Regional analysis of hypoxia.....	29
4.4.11	Human umbilical vein endothelial cell culture.....	30
4.4.12	In-vitro exposure of endothelial cells to simulated ligation shear stress.....	31
4.4.13	HUVEC RNA isolation, qRT-PCR, and microarray gene expression profiling.....	31
4.4.14	Immunofluorescence labeling for HUVEC planar cell polarity.....	33
4.4.15	Data analysis of endothelial cell planar polarity.....	33
4.4.16	HUVEC western blot and NF- κ B activity assays.....	34
4.4.17	siRNA transfection in HUVECs	34
4.4.18	Monocyte adhesion functional assay.....	35
4.5	Results.....	36
4.5.1	Planar polarization confirms endothelial cell responsiveness to predicted flow directions	36
4.5.2	Arteriogenesis is enhanced in collateral artery segments exposed to reversed flow after FAL.....	38
4.5.3	FAL does not elicit regional differences in hypoxia in gracilis adductor muscles.....	40
4.5.4	Amplified arteriogenesis in flow-reversed segments occurs independent of position.....	40

4.5.5	HUVECs exhibit directional responsiveness to simulated femoral artery ligation.	41
4.5.6	Reversed flow broadly enhances the arteriogenic transcriptional profile.....	43
4.5.7	NFkB as a predicted upstream regulator of gene expression patterns in flow-reversed conditions.....	45
4.5.8	Amplified arteriogenesis in flow-reversed collaterals depends on ICAM-1.....	47
4.6	Discussion	50
4.6.1	Reversed flow as an independent stimulus leading to amplified arteriogenesis.	50
4.6.2	Endothelial cell sensing of shear stress magnitude and reversed direction. ..	52
4.6.3	Endothelial cell repolarization and signaling for amplified arteriogenesis.....	53
4.6.4	Complex role of eNOS signaling in arteriogenesis.	54
4.6.5	Implications for understanding shear stress set-point.....	54
4.7	Acknowledgements.....	55
4.8	Sources of Funding.....	55
4.9	Supplemental Figures	56
4.10	Supplemental Tables	62
5	DNMT1-dependent DNA hypermethylation constrains arteriogenesis by augmenting shear stress set-point	85
5.1	Abstract	85
5.2	Abbreviations.....	86
5.3	Introduction.....	86
5.4	Materials and Methods.....	88
5.4.1	Mice.....	88
5.4.2	Femoral arterial ligation model.	88
5.4.3	5AZA treatment.....	89
5.4.4	Quantification of global DNA methylation by high resolution melting (HRM)..	89
5.4.5	Tissue harvesting for whole mount vascular casting and cross sectional analysis.....	90
5.4.6	Immunofluorescence labeling of 5-methylcytidine.	91
5.4.7	Cross sectional analysis of collateral artery structure.....	92
5.4.8	Human umbilical vein endothelial cell culture.	92
5.4.9	<i>In vitro</i> exposure of endothelial cells to biomimetic shear stress waveforms.	93
5.4.10	HUVEC RNA isolation and qRT-PCR.....	93
5.4.11	Reduced representation bisulfite sequencing (RRBS) and mRNA sequencing.	94

5.4.12	RRBS Analysis.....	94
5.4.13	Transillumination laser speckle imaging and shear stress analysis.	95
5.4.14	siRNA transfection in HUVECs.	96
5.4.15	Western blot analysis.	97
5.4.16	Monocyte adhesion functional assay.....	98
5.4.17	Statistical Analyses.	99
5.5	Results.....	99
5.5.1	Collateral artery segments exhibiting limited arteriogenic capacity exhibit hypermethylated DNA 12-weeks after FAL.	99
5.5.2	ECs exposed to a non-reversed increase in shear stress magnitude exhibit augmented DNMT1 expression.....	100
5.5.3	Altered genome-wide DNA methylation patterns in ECs exposed to a arteriogenic shear stress waveforms in-vitro	101
5.5.4	DNMT1 regulates the adhesion of monocytes to endothelial cells exposed to a non-reversed increase in shear stress magnitude in-vitro.	104
5.5.5	The arteriogenic capacity of non-reversed collateral artery segments is restored by DNMT1 inhibition.....	105
5.5.6	Shear stress set-point is re-established in non-reversed collateral artery segments by DNMT1 inhibition	107
5.6	Discussion	108
5.6.1	Mapping the EC mechanosensitive DNA methylation to differential arteriogenic capacity	109
5.6.2	The role of DNMT1 in flow-mediated endothelial inflammation is dependent on hemodynamic context	110
5.6.3	Molecular regulation of collateral artery shear stress set-point.....	111
5.6.4	Clinical perspective	112
5.7	Acknowledgements.....	113
5.8	Sources of Funding.....	113
5.9	Supplemental Figures	114
5.10	Supplemental Tables	120
6	Mechanosensitive microRNA-199a regulates perfusion recovery and collateral arteriogenesis in Balb/c mice following femoral arterial ligation	151
6.1	Abstract	151
6.2	Abbreviations.....	152
6.3	Introduction.....	152
6.4	Materials and Methods.....	154

6.4.1	Human umbilical vein endothelial cell culture.	154
6.4.2	<i>In vitro</i> exposure of endothelial cells to biomimetic shear stress waveforms.	154
6.4.3	HUVEC microarray gene expression profiling.	155
6.4.4	Transfection of miRNA antagomirs and mimics in HUVECs.	155
6.4.5	HUVEC RNA isolation and qRT-PCR.	155
6.4.6	Monocyte adhesion functional assay.	156
6.4.7	Mice.	157
6.4.8	Femoral arterial ligation model.	157
6.4.9	<i>In vivo</i> miR-199a antagomir treatment.	158
6.4.10	<i>In vivo</i> miR-199a mimic treatment.	158
6.4.11	Laser Doppler perfusion imaging.	158
6.4.12	Tissue harvesting for miRNA and target expression.	159
6.4.13	RNA isolation from tissues and qRT-PCR.	159
6.4.14	Tissue harvesting for whole mount vascular casting and cross sectional analysis.	160
6.4.15	Cross sectional analysis of collateral artery structure.	161
6.4.16	Immunofluorescence labeling of pericollateral Mac3 ⁺ cells.	161
6.4.17	Cross sectional analysis for gastrocnemius muscle morphology.	162
6.4.18	Cross sectional analysis for gastrocnemius capillary density.	163
6.4.19	Statistical analyses.	163
6.5	Results.	164
6.5.1	Endothelial cell miRNA expression is regulated by shear stress waveforms biomimetic of collateral artery segments exhibiting differential arteriogenic responses.	164
6.5.2	MicroRNA-199a negatively regulates pro-arteriogenic endothelial gene expression and monocyte adhesion to flow-exposed ECs in-vitro.	165
6.5.3	Overexpression of miR-199a limits foot reperfusion following FAL while miR-199a inhibition elicits complete perfusion recovery in Balb/c mice.	168
6.5.4	Overexpression of miR-199a inhibits arteriogenesis in Balb/c mice.	170
6.5.5	Inhibition of miR-199a amplifies arteriogenesis in Balb/c mice following FAL.	171
6.5.6	Pericollateral macrophage recruitment is modulated by miR-199a.	172
6.5.7	MicroRNA-199a inhibition improves gastrocnemius muscle composition in FAL-operated Balb/c mice.	173
6.6	Discussion.	174

6.6.1	Identification of microRNA-199a as a novel mechanosensitive regulator of pro-arteriogenic gene expression	175
6.6.2	Previous studies implicating a role of miRNA-regulated arteriogenesis	177
6.6.3	MicroRNA-199a as a regulator of arteriogenesis leading to enhanced perfusion recovery	178
6.6.4	Clinical perspective	179
6.7	Acknowledgements.....	179
6.8	Sources of Funding.....	180
6.9	Supplemental Figures	181
6.10	Supplemental Tables	187
7	Discussion and future directions	191
7.1	Summary	191
7.2	Thoughts and future studies: DNMT1, DNA methylation, and regulation to the shear stress set-point	192
7.3	Thoughts and future directions: miR-199a and mechanosensitive miRNA as regulators of arteriogenesis and as therapeutic targets	193
7.4	Thoughts and future studies: arteriogenesis, angiogenesis, and beyond	194
7.4.1	Promise for pro-arteriogenic and pro-angiogenic combination therapy	194
7.4.2	Need to consider muscle composition and metabolism	195
7.5	Thoughts and future directions: applications to other disease models.....	197
8	References.....	198

Table of Figures

Figure 2.1. Overview of arteriogenesis and regulation by shear stress set-point.....	9
Figure 4.1. Collateral artery endothelial cells repolarize in response to reversed shear stress after FAL.	37
Figure 4.2. Gracilis collateral artery regions exposed to reversed flow exhibit enhanced arteriogenesis after FAL.	39
Figure 4.3. Genome-wide analysis indicates that reversed flow broadly enhances the arteriogenic transcriptional profile.....	42
Figure 4.4. Reversed flow enhances monocyte adhesion in-vitro in an ICAM-1 dependent manner.	46
Figure 4.5. ICAM-1 is necessary for enhanced macrophage recruitment and amplified arteriogenesis in collateral segments exposed to a reversed flow.....	48
Figure 5.1. Gracilis collateral arteries exposed to a non-reversed increase in shear stress magnitude exhibit limited arteriogenic capacity and hypermethylated DNA.	100
Figure 5.2. ECs exposed to a non-reversed increase in shear stress magnitude exhibit augmented DNMT1 expression and altered genome-wide DNA methylation patterns in-vitro.	102
Figure 5.3. DNMT1 regulates the adhesion of monocytes to endothelial cells exposed to a non-reversed increase in shear stress magnitude in-vitro.....	105
Figure 5.4. The arteriogenic capacity of non-reversed collateral artery segments is restored by DNMT1 inhibition.....	106
Figure 5.5. Shear stress set-point in non-reversed collateral artery segments is restored by DNMT1 inhibition.....	108
Figure 5.6. Summary of DNMT1-dependent regulation of arteriogenic capacity and shear stress set-point in gracilis adductor collateral arteries following FAL.....	112
Figure 6.1. Endothelial cell miRNA expression is differentially regulated by shear stress waveforms biomimetic of collateral artery segments exhibiting varied arteriogenic responses.	165
Figure 6.2. MicroRNA-199a negatively regulates the expression of CD44, CCND1, and IKK β in endothelial cells exposed to biomimetic shear stress waveforms in-vitro.	166

Figure 6.3. Monocyte adhesion to HUVECs exposed to shear stress waveforms biomimetic of arteriogenic collaterals is modulated by miR-199a.	167
Figure 6.4. Overexpression of miR-199a limits foot reperfusion following FAL while miR- 199a inhibition leads to complete perfusion recovery in Balb/c mice.	169
Figure 6.5. Overexpression of miR-199a inhibits arteriogenesis in Balb/c mice.	170
Figure 6.6. Inhibition of miR-199a amplifies arteriogenesis in Balb/c mice following FAL.	172
Figure 6.7. Pericollateral macrophage recruitment is modulated by miR-199a.	173
Figure 6.8. MicroRNA-199a inhibition improves gastrocnemius muscle composition in FAL-operated Balb/c mice.	174

Supplemental Figures

Supplemental Figure 4.1. Laser Doppler perfusion recovery curve.	56
Supplemental Figure 4.2. Regional characterization of hypoxia, muscle fiber size, and capillary density in mouse gracilis muscle.	57
Supplemental Figure 4.3. Arteriogenesis in gracilis collateral artery segments exposed to a reversed flow after muscular branch ligation.	58
Supplemental Figure 4.4. HUVECs repolarize in response to directional change in shear stress induced by simulated FAL.	59
Supplemental Figure 4.5. Gene ontology clustering architecture of microarray expression in non-reversed and reversed flow waveforms.	60
Supplemental Figure 4.6. Amplified arteriogenesis in flow reversed segments does not require eNOS.	61
Supplemental Figure 5.1. Similar degree of methylation coverage in HUVECs exposed to biomimetic shear stress waveforms.	114
Supplemental Figure 5.2. DNA methylation across different gene regions.	115
Supplemental Figure 5.3. DNA methylation negatively correlates to mRNA expression in gene promoter regions.	116
Supplemental Figure 5.4. Genome-wide mRNA expression patterns in HUVECs exposed to arteriogenesis biomimetic shear stress waveforms.	117
Supplemental Figure 5.5. Top 50 most significantly overrepresented gene ontology (GO) biological processes.	118

Supplemental Figure 5.6. DNMT1 inhibition also restores the arteriogenic capacity of non-reversed collateral artery segments in Balb/c mice	119
Supplemental Figure 6.1. Regional analysis of Balb/c mice treated with miR-199a mimic after FAL.....	181
Supplemental Figure 6.2. Regional analysis of Balb/c mice treated with anti-miR-199a after FAL.....	182
Supplemental Figure 6.3. Regional pericollateral macrophage recruitment is modulated by miR-199a.	183
Supplemental Figure 6.4. Gastrocnemius muscle composition is not further impaired with miR-199a overexpression following FAL	184
Supplemental Figure 6.5. Sigmoidal response of CD44, IKK β , CCND1 mRNA expression and THP-1 monocyte adhesion to alterations in miR-199a expression in endothelial cells exposed to biomimetic shear stress waveforms in-vitro. .	185
Supplemental Figure 6.6. MicroRNA-199a inhibition does not affect capillary density in the gastrocnemius muscle of FAL-operated Balb/c mice.....	186

Table of Tables

Table 2.1. Comparison of microarray genes to RT-PCR analyses for selected genes known to mediate arteriogenesis	44
Table 2.2. NFkB is a predicted upstream regulator of gene expression patterns seen with flow reversed increased shear stress	45

Supplemental Tables

Supplemental Table 2.1. Gene ontology analysis for over-representation of molecular function	62
Supplemental Table 2.2. Predicted upstream regulators of gene expression patterns seen with reversed and non-reversed waveforms	63
Supplemental Table 2.3. Ingenuity Pathways Analysis significant canonical pathways	64
Supplemental Table 2.4. All differentially regulated genes between reversed versus control conditions with FDR<0.10	66
Supplemental Table 2.5. All differentially regulated genes between non-reversed versus control conditions with FDR<0.10	83
Supplemental Table 5.1. Summary of total number of reads, mapping ratio, and CpG coverage in RRBS datasets.....	120
Supplemental Table 5.2. Summary of total number of reads, mapped reads, and mapping ratio for mRNA-seq datasets.....	120
Supplemental Table 5.3. All DMRs corresponding to the promoter regions of genes with a methylation ratio difference $\geq 0.10 $ and FDR<0.1 between non-reversed and reversed conditions	122
Supplemental Table 5.4. All significantly hypermethylated promoter regions corresponding to genes that are down-regulated in non-reversed conditions compared to reversed conditions	138
Supplemental Table 5.5. All significantly hypomethylated promoter regions corresponding to genes that are up-regulated in non-reversed conditions compared to reversed conditions	146
Supplemental Table 5.6. Top 50 significantly overrepresented biological process GO terms for genes with expression patterns corresponding to differential promoter methylation under arteriogenic shear stress waveforms	149
Supplemental Table 6.1. Differential microRNA gene expression in ECs exposed to arteriogenesis-biomimetic shear stress waveforms.	187

Acknowledgements

Through my graduate studies, I have received a tremendous amount of support from many students, faculty, and staff. Thank you for letting me come to your labs and offices to ask questions, for providing your expertise, and for your dedication to a collaborative environment.

Thank you to my dissertation committee – Brian Helmke, Shayn Peirce-Cottler, Gary Owens, and Brian Annex. Our discussions, though they have challenged me at times, have ultimately shaped much of this work and have helped me improve as a scientist and as a thinker.

I am also thankful for the mentorship of my advisor, Rich Price. He has continually provided guidance and support that have helped me develop both scientifically and professionally. He has encouraged me to think independently and has allowed me the freedom to pursue my own ideas. Thank you for your patience and for the chance to succeed, as well as the chance to fail.

Thank you to all the past and present members of the Price lab. I would especially like to thank Josh Meisner, for his mentorship, friendship, and essential contributions to this work, as well as Ji Song, for all her technical expertise. I am also thankful to Devin Weinberg, Lauren Boerboom, and Christen Hamilton of the Blackman Lab for their guidance during my first two years of graduate school.

Thank you to all the undergraduate students that have trusted me as an advisor. Their questions have helped me grow as a mentor, teacher, and communicator, and their hard work has been essential to this work.

I am deeply grateful to my family for their unconditional love and support, not just during graduate school, but throughout my life. You have always encouraged me to pursue my interests, curiosities, and for me to always do the best I can.

Finally, I am incredibly grateful to my fiancée, Anna. Thank you for your incredible patience, encouragement, advice, friendship, love, and support. You keep me laughing and constantly remind me that the most important things are not in lab.

1 Preface

1.1 Abstract

Peripheral arterial disease (PAD) is the leading cause of lower limb amputation and is estimated to affect over 202 million people worldwide. PAD arises when atherosclerotic plaques block arteries in the lower limbs, thereby limiting blood flow to the distal tissue. The luminal expansion of pre-existing collateral arteries bypassing the occlusion(s) (i.e. arteriogenesis) remains a promising therapeutic option. However, large clinical trials have had limited success to date, highlighting the critical need to better understand the basic mechanisms regulating arteriogenesis.

In this thesis, we report that collateral artery segments in the mouse hindlimb exhibit either “moderate” or “amplified” arteriogenesis, depending on the initiating hemodynamics to which they are exposed (i.e. non-reversed or reversed flow waveforms, respectively) following femoral arterial ligation (FAL). We first determined this reversed flow-mediated amplification of collateral artery growth to be dependent on ICAM-1 mediated macrophage recruitment. Moreover, we were able to apply flow waveforms biomimetic of those quantified in-vivo, to endothelial cells (ECs) in-vitro, and perform genome-wide analyses to comprehensively map EC mechanosensitive signaling to sustained, differential arteriogenesis responses.

We next sought to uncover molecular regulators of arteriogenic capacity and collateral artery maturation. We determined that ECs exposed to a non-reversed flow waveform exhibit increased DNMT1 expression and DNA hypermethylation. Moreover, we determined that DNMT1-dependent EC DNA hypermethylation regulates arteriogenic capacity via adjustments to shear stress set-point in-vivo, identifying a novel role for DNA methylation in arteriogenesis.

Finally, we interrogated our genome-wide analysis of EC mechanosensitive signaling mapped to differential arteriogenesis responses to identify potentially novel microRNA regulators of arteriogenesis. Using this unique approach, we discovered microRNA-199a to be a potent

mechanosensitive regulator of perfusion recovery and arteriogenesis after arterial occlusion. To this end, miR-199a inhibition elicited complete foot perfusion recovery, markedly augmented collateral arteriogenesis, and improved gastrocnemius muscle tissue composition following FAL.

Overall, these studies demonstrate the critical roles of EC mechano-signaling, flow mediated inflammation, and epigenetic mechanisms in regulating endogenous shear stress-mediated arteriogenesis. These results may also have important bearing on the development of therapeutic arteriogenesis strategies in patients with peripheral arterial disease.

1.2 Preview of this thesis

In Chapter 2, this thesis will begin with an introduction to the definition, epidemiology, and pathophysiology of peripheral arterial disease, the primary clinical motivation for this work. Chapter 2 will also include an introduction to the individual stages of arteriogenesis and the concept of shear stress set-point. Chapter 3 will review epigenetic mechanisms, their relevancy to PAD, and recent work investigating epigenetic regulation of the response to hindlimb ischemia, the pre-dominant animal model used to study PAD. Chapters 4-6 will report our recent studies investigating the mechanisms of amplified arteriogenesis in collateral artery segments exposed to reversed flow direction, the regulation of arteriogenic capacity and shear stress set-point via DNMT1-dependent DNA hypermethylation, and the role for mechanosensitive microRNA-199a as a novel regulator of perfusion recovery and arteriogenesis, respectively. Finally, Chapter 7 will provide discussion for the significance and future directions of this work.

2 Peripheral arterial disease (PAD) and arteriogenesis

2.1 Abbreviations

PAD	peripheral artery disease
CAD	coronary artery disease
ABI	ankle brachial index

IC	intermittent claudication
CLI	critical limb ischemia
EC	endothelial cell
SMC	smooth muscle cell

2.2 Clinical background and motivation

2.2.1 Peripheral arterial disease – definition and epidemiology

Peripheral arterial disease (PAD) is a chronic disease that is caused by blockage(s) of the arteries, typically in the lower limbs, due to atherosclerosis¹. PAD is the leading cause of lower limb amputations and is estimated to have a total cost exceeding \$21 billion annually in the United States alone². It is estimated that >200 million people worldwide, in high-, middle, and low-income countries, have PAD, indicating that it is truly a global problem³.

PAD has a total prevalence that is nearly equal to that of coronary artery disease (CAD)⁴. Moreover, PAD prevalence increases with age, where total PAD prevalence is ~6-12% of people 50-60 years old and increases to 20-25% in people over 70 years^{1,5-9}. In addition to age, smoking is also a strong risk factor for PAD¹⁰. Smokers have been shown to develop symptoms of PAD almost 10 years earlier than non-smokers and are twice as likely to develop complications necessitating lower limb amputation¹¹. Smoking also appears to be more strongly associated with PAD than CAD and increases the likelihood of graft failure 3-fold¹¹. Diabetes mellitus has also been shown to be a strong risk factor for PAD; 26-33% of individuals with PAD also have concomitant diabetes^{6,12,13}. Patients with both diabetes and PAD have a 5-fold higher rate of lower limb amputation and 3-fold higher mortality than non-diabetic PAD patients over a 4.5 year follow-up period¹⁴. Other risk factors for PAD include hypertension, dyslipidemia, race, chronic kidney disease, c-reactive protein levels, and vitamin D deficiency. To date, searches for genetic susceptibility variants, such as GWAS, have had limited success for PAD¹⁵.

2.2.2 Clinical manifestations of PAD

PAD is clinically defined as an ankle-brachial index (ABI), the ratio of the highest systolic blood pressure in the dorsalis pedis or posterior tibial artery to the highest systolic blood pressure in the left or right brachial artery, of ≤ 0.90 ^{5,7}. Whereas a normal ABI is 1.0-1.4, an ABI ≤ 0.90 is indicative of hemodynamically significant occlusive disease between the heart and the ankle¹. An ABI ≤ 0.90 is associated with between a 3- to 4-fold increase in 10-year cardiovascular mortality¹⁶. While ABI diagnoses PAD, it does not predict or correlate with disease severity⁴.

There are two distinct symptomatic clinical manifestations of PAD – intermittent claudication (IC) and critical limb ischemia (CLI). Intermittent claudication is defined as calf or buttock pain with walking that is relieved with rest⁴. Approximately 10-35% of PAD patients present with classic claudication symptoms and 20-40% present with atypical leg pain¹¹. Patients with intermittent claudication have annual risk of amputation or death of 1-2%¹. Critical limb ischemia, in contrast, is defined as reduced blood flow to the lower limb resulting in pain, even at rest, with or without associated ulcers or gangrene⁴. These different clinical manifestations appear to be quite distinct as only 1-2% of IC patients actually progress to CLI per year and many CLI patients do not report previous IC⁷. In total, only 1-2% of PAD patients present with critical limb ischemia, though their prognosis is much more severe⁴. CLI patients have an annual mortality of 20-25% and a 25-40% 6-month risk of major amputation^{1,17}.

Interestingly, 20-50% of individuals with PAD report as “asymptomatic” in that they don’t typically experience leg symptoms, with walking or at rest, despite an ABI ≤ 0.90 ¹⁸. Despite the lack of self-reported symptoms, “asymptomatic” PAD patients have been shown to have poorer functional performance (6-minute walk test), poorer quality of life, and more adverse calf muscle characteristics (higher calf muscle fat percentage, smaller calf muscle area) than sedentary, normal individuals¹⁸. Moreover, “asymptomatic” patients still have an increased mortality¹⁹. Indeed, patients with PAD but with no clinical evidence of CAD have the same relative risk of

death from cardiac or cerebrovascular cause as those patients whose main diagnosis is CAD¹⁷. These studies demonstrate that there is no truly “asymptomatic” manifestation of PAD.

2.2.3 Pathophysiology

Peripheral arterial disease is a pathophysiological “manifestation of systemic atherosclerosis”¹⁷, whereby the underlying mechanisms for the functional limitations of PAD are hemodynamic in origin²⁰. Atherosclerosis is a progressive disease of the large arteries characterized by the accumulation of lipids and fibrous elements in the sub-endothelial space (intima), in arterial regions experiencing disturbed blood flow^{21,22}. Advanced lesions can grow sufficiently large, with the continued intimal accumulation of cholesterol-laden macrophages (i.e. foam cells), to block blood flow²². As a consequence of these atherosclerotic blockages, reduced blood flow to the lower extremities leads to an insufficient oxygen supply (i.e. ischemia) for meeting the metabolic demands of these distal tissues. The majority of patients with symptomatic PAD have a complete occlusion in the iliac or femoral arterial system between the aorta and the foot¹. In addition, PAD patients exhibit endothelial dysfunction^{23,24} and microvascular impairments (i.e. reduced capillarity²⁵ and increased arteriolar rarefaction²⁶) that further lead to distal tissue ischemia.

2.2.4 Treatment options

Surgical and catheter based revascularization methods are currently the preferred treatment for patients presenting with claudication⁴. In correctly chosen patients, these revascularization methods have been shown to have preserved life and limb of >75% of patients at 1 year following revascularization²⁷. However, many PAD patients are not amenable to surgical revascularization options and many that do undergo surgery receive little to no long term benefit⁴. This has led to new therapeutic strategies that have sought to use biochemical, molecular, and cellular-based approaches to induce endogenous revascularization (i.e. angiogenesis and/or arteriogenesis) to restore lower limb perfusion. The stimulation of angiogenesis, or the growth of new capillaries from pre-existing vessels, is important as capillary density is reduced in PAD patients^{4,25,28}.

However, it is also imperative to restore the driving pressure to the distal tissue via luminal expansion (i.e. arteriogenesis) of collateral arteries bypassing the occlusion(s)^{26,29,30}. Yet, large-scale therapeutic arteriogenesis clinical trials have been largely unsuccessful to date due to insufficient and/or impermanent collateral artery growth^{31–35}. These failures have highlighted our incomplete understanding of the basic mechanisms of arteriogenesis and underscore the critical need for the continued study of the endogenous regulation of this complex, highly orchestrated process in order to achieve eventual therapeutic success.

2.3 Arteriogenesis

It has been known since the 1780s that there is a pre-existing network of collateral arteries capable of compensating for a major arterial occlusion³⁶. Arteriogenesis, or the luminal growth of endogenous collateral arteries that provide alternate paths for blood flow around arterial occlusions, can prevent ischemic injury in downstream tissue. This collateral growth has been shown to occur in the human arterial systems of the lower limbs, heart, and brain^{36–38}. Altogether, arteriogenesis is a multi-faceted, highly coordinated signaling cascade involving recruitment, migration, and proliferation of multiple cell types, as well as the re-organization of the extracellular matrix. The progression of this complex process of arteriogenesis (or collateral growth) can be broken down into three stages: initiation, growth, and maturation³⁹.

2.3.1 Initiation

As early as 1893, Thoma observed a correlation between vessel diameter and blood flow⁴⁰. Biomechanical forces exerted by blood flow on the endothelium are now known to be critical in the regulation of cell phenotype and blood vessel remodeling^{37,41–48}. Indeed, a key initiating stimulus for arteriogenesis is an increase in shear stress^{37,49}.

Upon occlusion of a major artery, the downstream vascular network experiences a drop in pressure. This steep pressure gradient is further sustained by the higher resistance of the collateral network due to the increased vascular path length and small initial diameters of these

arteries. The resulting pressure gradient drives blood flow along any pre-existing collateral arteries that bridge the occlusion(s), resulting in an increased shear stress exerted on the endothelium³⁹. Endothelial cells (ECs) can sense and transduce changes in the wall shear stress into biophysical, biochemical, and gene signaling responses (i.e. mechanotransduction)⁴³, via mechanosensory complexes (e.g. CD31 / VE-Cadherin / VEGFR2)⁵⁰, that can initiate the growth response⁵¹.

2.3.2 Growth

Altered shear stress activates the ECs lining collateral arteries, inducing an inflammatory response that begins the collateral growth phase of arteriogenesis⁴⁹. Both in-vivo and in-vitro studies have shown increased shear stress promotes the expression of a wide array of inflammatory cytokines, chemokines, and adhesion molecules^{52–54}. Shear-stress mediated up-regulation of adhesion molecules, particularly ICAM-1⁵⁵, are of particular importance as they are known to be critical for collateral growth, primarily through their role in the recruitment of leukocytes⁵⁶. Additionally, the upregulation of a variety of chemokines (e.g. CCL2, GM-CSF, CXCL1) helps to induce the recruitment of bone-marrow derived cell populations that propagate the growth process^{57–59}. While multiple leukocyte populations play a role initiating collateral artery growth (see review by Meisner and Price³⁹), monocytes are the most-widely studied. The recruitment of monocytes and subsequent pericollateral accumulation of macrophages has been shown to be necessary for collateral artery growth^{56,60–68}. Recruited monocytes and macrophages act a “point-sources” of necessary paracrine growth factors (e.g. $\text{INF}\beta$ ⁶⁹, $\text{TNF}\alpha$ ⁷⁰, $\text{TGF}\beta$ ⁷¹, FGF ⁷²), which promote the proliferative activity of ECs, smooth muscle cells (SMCs), and adventitial fibroblasts^{73–75}. Additional growth factors are simultaneously released from a coordinated breakdown of basement membrane components (e.g. desmin and laminins) and of the internal elastic lamina by matrix metalloproteases (e.g. MMP-2 and MMP-9)³⁹. Furthermore, this

inflammatory signaling induces the differentiation of collateral artery smooth muscle cells from a contractile to a synthetic phenotype⁵².

2.3.3 Maturation

As vascular cells proliferate and collateral vessels grow, there is a corresponding expansion of the media and the formation of a neointima⁵². Over time, as lumenal diameter increases, the signaling environment shifts from pro-inflammatory to anti-inflammatory⁵³. The number of perivascular macrophages begins to decrease, paralleling a reduction in vascular cell proliferation^{52,62}. SMCs return to a contractile phenotype⁵² and there is a reestablishment of a mature basement membrane^{76,77}. Ultimately, the largest, most developed collateral vessels tend to mature and stabilize, but at the expense of the smaller, less developed collateral vessels which undergo eventual regression^{52,78,79}. Outward lumenal growth is hypothesized to continue until normalization to the original shear stress level (i.e. the shear stress “set-point”) has been achieved^{39,41,80,81}.

2.3.4 Shear stress set-point

Arteries adapt to chronic changes in blood flow by undergoing adjustments of their internal diameters^{41,46,47,49,82–84}. The concept of an arterial homeostatic wall shear stress magnitude (i.e. shear stress set-point) at which vessels maintain a steady-state lumenal diameter⁸⁵ arises from Murray’s principle of minimum work⁸⁶. In 1926, Murray⁸⁶ proposed that the vascular system is optimally configured such that there is a compromise between the frictional cost to drive blood through vessels and the metabolic cost of maintaining blood volume, given by:

$$H_t = \frac{8\eta l Q^2}{\pi r^4} + k\pi r^2 l$$

2.1

where H_t is the total power requirement, Q is volumetric flow rate, η is blood viscosity, r is vessel radius, l is vessel segment length, and k is a constant. By minimizing the total power requirement,

this compromise occurs at an optimal diameter (d_{opt})⁸⁷. Therefore, for an optimized vasculature, there ought to be a shear stress (τ) set-point for any given blood vessel segment such that:

$$\tau(d_{opt}) = \frac{32\eta Q}{\pi d_{opt}^3}$$

2.2

According to this theory, deviations of shear stress from the set-point initiate a negative feedback process that acts to return shear stress to the original set-point by chronically adapting the arterial diameter⁸⁴ (Figure 2.1).

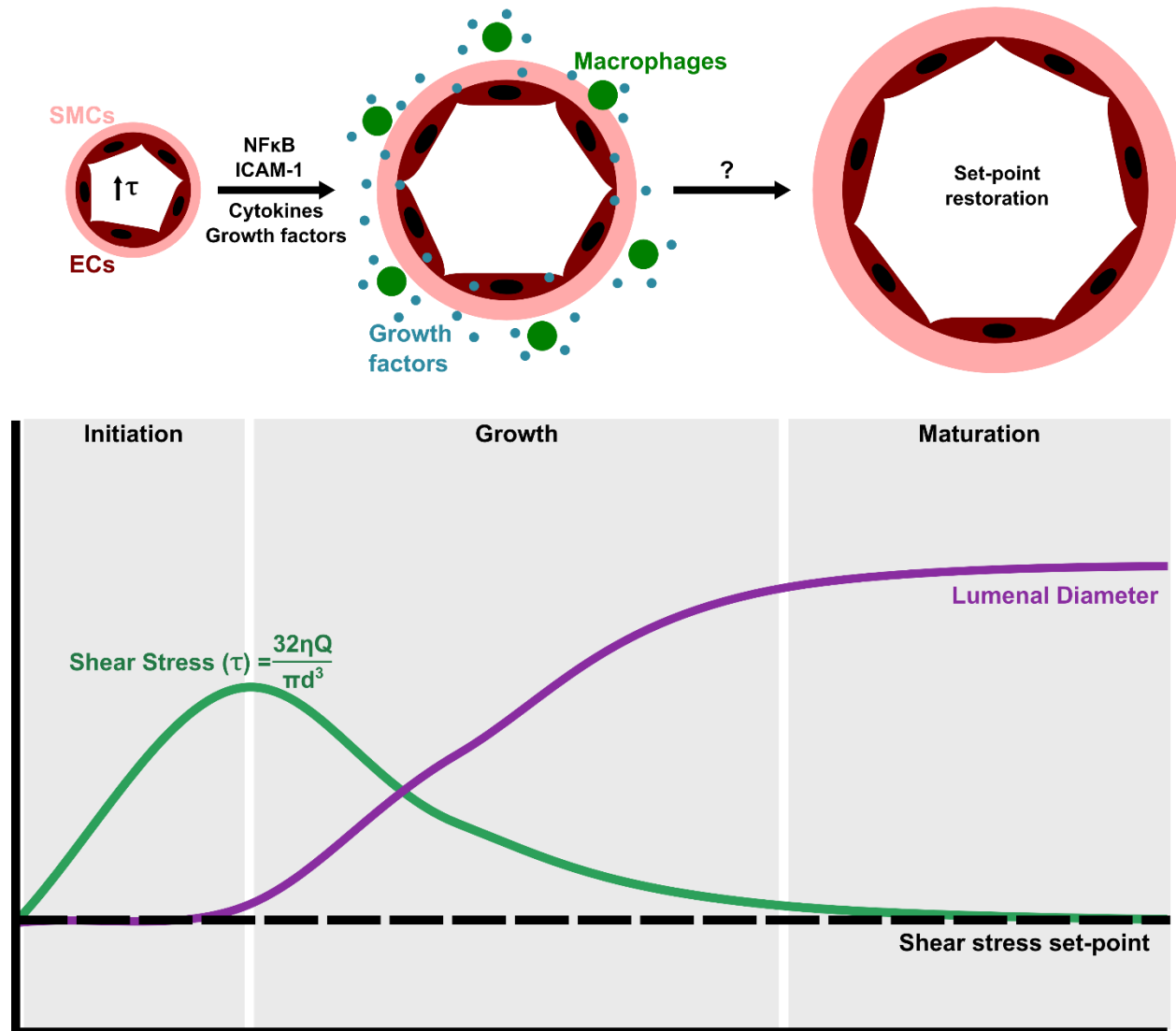


Figure 2.1. Overview of arteriogenesis and regulation by shear stress set-point.

Though its magnitude can vary in different vascular beds^{88,89}, numerous studies have either experimentally or theoretically supported the concept of a shear stress set-point^{41,47,48,83,85,90–93}. However, there are several studies reporting an altered set-point in arteries following adaptation. To this end, following remodeling of the common carotid artery in a canine arterio-venous shunt model, the wall shear rate returned to within 15% of baseline after 6-8 months, except for those arteries exposed to the greatest relative flow increases ($>4\times$ control)⁴⁷. In another study in which the carotid artery blood flow of mature rabbits was acutely increased by 60%, the lack of compensatory diameter enlargement caused shear stress to remain elevated two months later⁸³. Weanling rabbits, however, exhibited significant diameter enlargement, enabling for shear stress to normalize to the set-point⁸³. This age-dependent remodeling was also observed in rats in which ligation of the left internal and external carotid arteries increased right carotid flow by 46%. After 4-weeks, the right carotid outer diameter increased and shear stress returned to initial values in juvenile but not adult rats⁹⁴.

Though critical in determining ultimate arteriogenic capacity, the molecular mechanism(s) involved in establishing and maintaining the shear stress set-point remain unknown. A previous study recently demonstrated that VEGFR3 expression regulates differences in shear stress sensitivity (i.e. cell orientation) between ECs and lymphatic ECs and that the loss of VEGFR3 reduces the diameter of the descending aorta in mice⁹⁵. However, whether VEGFR3 regulates shear set-point in-vivo remains unclear, as in-vivo hemodynamics were not explicitly determined in this study⁹⁵. The overall paucity of data on the mechanism(s) regulating vessel maturation and shear stress set-point highlights both a critical need to enhance our basic understanding of this fundamental vascular growth response and an opportunity to discover new therapeutic targets for treating arterial occlusive diseases. As such, epigenetics are currently an area of intense research focus that could be a way to regulate long-term gene expression in response to local hemodynamic factors.

3 Epigenetics in peripheral arterial disease (PAD)

Epigenetic regulation of cardiovascular disease^{96,97}, vascular gene expression⁹⁸, and biomechanical signaling^{99–101} have been previously reviewed elsewhere. Here, we will focus on the epigenetic mechanisms and regulation specifically relevant to peripheral arterial disease.

3.1 Abbreviations

PAD	peripheral artery disease
CAD	coronary artery disease
EC	endothelial cell
SMC	smooth muscle cell
DNMT	DNA methyltransferase
HAT	histone acetyltransferase
HDAC	histone deacetyltransferase
lncRNA	long noncoding RNA
miRNA	microRNA
FAL	femoral arterial ligation

3.2 Epigenetics: an introduction

Epigenetics is “a bridge between genotype and phenotype” – it is the modification to gene expression and phenotype in a sequence-independent manner¹⁰². Epigenetic mechanisms, such as DNA methylation, histone modifications, and non-coding RNAs, can regulate gene expression by altering DNA accessibility and chromatin structure¹⁰². The significance of epigenetics in vascular biology, as regulators of molecular signaling and as potential therapeutic targets to treat disease, is now well-recognized^{98,99,103}.

3.2.1 DNA methylation

DNA methylation is the addition of a methyl group to a cytosine base pair at the 5' carbon-position, (i.e. 5-methylcytosine), occurring most often at CpG dinucleotide site¹⁰³. Methylation occurs through the activity of DNA methyltransferases (DNMTs), including DNMT1, DNMT3a, and DNMT3b^{98,104,105}. DNMT1 is thought to pre-dominate post-development, preferentially methylating hemi-methylated DNA, whereas DNMT3a and DNMT3b preferentially target fully unmethylated DNA during embryogenesis and gametogenesis¹⁰⁴. DNMT1, however, is also capable of de novo methylation¹⁰⁴. Demethylation can occur passively or actively, the latter thought to be mediated by the ten-eleven translocation enzyme family (TET1, TET2, TET3) and by oxidation of 5-methylcytosine to 5-hydroxymethylcytosine^{106,107}. Approximately 40-60% of human genes are associated with dense regions of CpG sites with higher than expected CG content called CpG islands^{98,108,109}. In healthy cells, CpG islands are typically hypomethylated thereby allowing for an open chromatin structure and transcriptional activity¹⁰⁸. However, DNA methylation of gene promoter regions is associated with repression of gene expression¹¹⁰⁻¹¹². Inhibition of gene expression is thought to be achieved by physically impeding transcription factor binding to the gene promoter and/or to methyl-CpG-binding domain proteins¹⁰⁰.

3.2.2 Histone modifications

Chromatin, is a “beaded chain” DNA-protein complex consisting of a string of nucleosomes (i.e. DNA nucleotides wrapped around an octamer of histone proteins) connected by linker DNA¹¹³. The higher order packing of chromatin can be dynamically regulated by post-translational modifications to histone proteins¹¹³. Typically, more open chromatin enables for transcription factor binding whereas more condensed chromatin represses gene expression⁹⁸. There are numerous (>100) post-translational histone modifications, though the most well characterized types are acetylation and lysine methylation^{103,114}. Histone acetylation is governed by histone acetyltransferase (HAT) and deacetyltransferase (HDAC) activity^{103,105}. Histone acetylation tends

to correlate with chromatin accessibility and transcriptional activity¹¹⁴. Histone lysine methyltransferases and demethyltransferases regulate histone lysine methylation¹⁰⁵. Importantly, histone lysine residues can be mono-, di-, or trimethylated and both the specific lysine residue and number of methyl groups on that residue determine the specific effect on transcription¹⁰³.

3.2.3 Non-coding RNA

In addition to DNA methylation and post-translational histone modifications, non-coding RNA can regulate gene expression. Non-coding RNA can be broadly classified as long noncoding RNAs (lncRNAs) and small noncoding RNAs (e.g. microRNAs). Long noncoding RNAs are arbitrarily defined as >200-nucleotide long, non-coding transcripts that may be 5'-capped, spliced, or polyadenylated, and are typically not well-conserved^{103,115}. Long noncoding RNAs are typically generated by the same transcriptional machinery as mRNAs¹¹⁶. Regulation of gene expression can be mediated by lncRNAs via RNA-, protein-, and DNA-binding interactions¹¹⁶, with several lncRNAs having been shown to regulate chromatin remodeling, splicing, and by acting as microRNA sponges¹¹⁵. In contrast to lncRNAs, small noncoding RNAs are well-conserved, <200-nucleotides long, and are endogenously processed by endonucleases¹¹⁵. There are a number of different classes of small noncoding RNAs, including microRNAs (miRNAs), PIWI-interacting RNAs (piRNAs), short interfering RNAs (siRNAs), tRNA-derived RNA fragments (tRFs), and small nucleolar RNAs (snoRNAs). Of these, miRNAs have been the most extensively studied to date. MicroRNAs are ~22 nucleotide non-coding RNAs that are endogenous regulators of gene expression¹¹⁷. Mature miRNA incorporates into the RNA-induced silencing complex (RISC) and then binds to a target mRNA, usually in the 3' untranslated region (UTR) of the mRNA¹¹⁸. MicroRNA binding acts to suppress target gene expression by inhibiting mRNA translation to protein or by promoting mRNA degradation¹¹⁹, depending on miRNA-target complementarity¹²⁰.

3.3 A role for epigenetics in PAD

PAD pathophysiology is likely governed by both genetic and epigenetic mechanisms. Though there has been limited success to date in identifying specific genetic variants (e.g. GWAS), it is clear that genetics are associated with PAD. To this point, people with a family history of PAD have a 2-fold greater risk of developing PAD than those without¹²¹. Moreover, the odds ratio of having PAD between monozygotic twins is 17.7 and 5.7 for dizygotic twins, with genetic effects accounting for 58% of the phenotypic variance¹²². However, a potential role for epigenetics in PAD is supported by the strong association of “environmental” risk factors (e.g. age, smoking, and diabetes) with PAD and the fact that the remaining 42% of phenotypic variance is due to environmental factors.

3.3.1 Histone modification and DNA methylation patterns and are likely to be altered in PAD patients

To date, however, there has been a paucity of reports investigating epigenomic changes in PAD. Though it has not yet been explicitly determined, PAD patients are likely to exhibit altered histone modifications and DNA methylation patterns. In support of this concept, altered chromatin structure (i.e. histone modifications) has been observed in patients with common risk factors of PAD such as aging¹²³, smoking¹²⁴, and diabetes¹²⁵. Additionally, global and gene-specific DNA methylation patterns are also altered with aging¹²³, smoking^{124,126–128}, and diabetes¹²⁹, promoting the likelihood of altered DNA methylation patterns in PAD patients. Furthermore, in CAD patients, there is a significant positive correlation of global DNA hypermethylation with elevated plasma levels of homocysteine¹³⁰, a non-protein forming amino acid that can alter DNA methylation patterns¹³¹. Interestingly, elevated homocysteine levels are also present in PAD patients¹³² and are negatively correlated with functional outcomes for critical limb ischemia (CLI)^{133,134}. Moreover, hyperhomocysteinemia (elevated homocysteine) has also been shown to alter the expression of key vascular genes (e.g. eNOS, VEGF, HIF1 α)^{135–137} and to suppresses perfusion recovery^{137–139},

angiogenesis^{137–139}, and collateralization¹³⁹ following arterial occlusion. Together, these results are consistent with the hypothesis that elevated homocysteine in PAD impairs revascularization and functional outcomes via altered DNA methylation.

3.3.2 microRNAs in PAD

MicroRNAs have been the most studied epigenetic modification in PAD, mostly as circulating biomarkers. To this end, miRNA transcriptome profiling identified 53-differentially expressed miRNAs in the peripheral blood of white, male, PAD patients presenting with intermittent claudication from non-symptomatic controls¹⁴⁰. This study further determined 12-miRNAs, including let-7e, miR-15b, -16, -20b, -25, -26b, -27b, -28-5p, -126, -195, -335, and -363, as diagnostic biomarkers of PAD¹⁴⁰. Several additional studies have also reported differential expression of miRNAs in PAD patients with concomitant diabetes. In diabetic patients, lower circulating miR-126 expression correlated with decreased ABI (ABI<0.9)¹⁴¹. Elevated serum expression of miR-15a, -15b, -16, -18a, -23a, -24, -27b, -103, -107, and -503 was seen in diabetic patients with CLI, while miR-222 and miR-497 were reduced compared to non-symptomatic controls¹⁴². Additionally, miR-15a and miR-16 expression predicted amputation occurrence in these diabetic patients with CLI¹⁴². Another study also identified elevated expression of miR-503 in calf muscle biopsies of diabetic patients with CLI¹⁴³.

Future studies are needed to more comprehensively determine potential biomarkers and functional targets in larger cohorts of PAD patient subpopulations. It is also important to note that while circulating miRNA expression is useful for diagnosis, disease monitoring, and outcome predictions, it does not necessitate a functional role for these miRNAs in disease pathophysiology. Differential miRNA expression in human muscle biopsies and in pre-clinical models may provide the best clues toward identifying specific miRNAs as potential therapeutic targets. Additionally, there is the potential that lncRNAs may play a role in PAD as the 9p21 locus, which is associated with several vascular disease phenotypes, has polymorphisms within the ANRIL lncRNA, a

directly silencer of the atheroprotective gene, CDKN2B¹⁵. However, a definitive association between PAD and lncRNAs has not yet been determined.

3.4 Epigenetic regulation in response to hindlimb ischemia

3.4.1 Histone post-translational modifications and DNA methylation

Studies exploring the role of the epigenetic mechanisms of histone post-translational modifications and DNA methylation in experimental models of PAD are limited. To date, histone acetylation is the only histone modification to be studied in this context. Transcriptional coactivator p300-CBP-associated factor (PCAF) is a HAT that promotes histone (H3 and H4) acetylation and the transcriptional activation of multiple pro-inflammatory genes¹⁴⁴. Both genetic and pharmacological inhibition of PCAF impaired blood flow recovery and arteriogenesis following hindlimb ischemia via suppression of inflammatory signaling and leukocyte recruitment¹⁴⁴. Additionally, though HDAC inhibition is a promising treatment for several ischemic diseases, it has been shown to have variable effects on the response to hindlimb ischemia¹⁴⁵. To this end, in a femoral arterial excision model, male C57BL/6 mice treated with a class I specific HDAC inhibitor (MS275) exhibited significant muscle atrophy and increased fibrosis. In contrast, treatment with the class IIa specific HDAC inhibitor (MC1568) increased the number of regenerating muscle fibers, though it delayed their terminal differentiation. Moreover, the class IIa inhibitor also modestly increased the arteriolar density in ischemic tissues, though neither class I or class IIa HDAC inhibitor affected capillary density or reperfusion¹⁴⁵. In another study¹⁴⁶, HDAC9 specific inhibition was shown to reduce EC tube formation, sprouting, and retinal vessel outgrowth. Defects in angiogenesis were rescued by both HDAC9 overexpression and by inhibition of miR-17-20a. Additionally, perfusion recovery was reduced ~50% in HDAC9 knockout mice compared to littermate controls, following induction of hindlimb ischemia. Interestingly, there appeared to be sex-differences in HDAC9^{-/-} mice, as female HDAC9^{-/-} mice trended toward improved perfusion recovery¹⁴⁶.

Only two previous studies to date have investigated the regulation of the ischemic response by DNA methylation. Both of these studies focused on a conserved family of methyl-CpG-binding proteins (MBD1, MBD2, MBD3, MBD4, and MeCP2) which are responsible for reading alterations to the DNA methylome and for enacting subsequent changes in transcriptional activity¹⁴⁷. EC-specific MeCP2-null mice were protected against a TGF- β induced impairment in angiogenesis¹⁴⁸. In-vitro, knockdown of MBD2 significantly enhanced angiogenesis and provided protection against peroxide-induced apoptosis¹⁴⁹. In vivo, Mbd2^{-/-} mice were protected against hindlimb ischemia demonstrating a significant improvement in perfusion recovery, along with increased capillary and arteriole densities following femoral arterial ligation (FAL) compared to littermate controls¹⁴⁹. MBD2 binds to hypermethylated CpG regions in the gene promoters of eNOS and VEGFR2, therefore loss of MBD2 increases eNOS and VEGFR2 expression¹⁴⁹. These studies demonstrate that DNA methylation is likely a crucial, though under-studied, mechanism regulating vascular growth following arterial occlusion.

3.4.2 Non-coding RNAs

Non-coding RNAs have been much more widely studied in experimental models of PAD than any other epigenetic mechanism. The vast majority of these studies have focused on microRNAs, which have been primarily identified by one of three methods: miRNA expression levels in isolated cells, miRNAs with functions known to be important for the response to hindlimb ischemia, and by examining altered miRNA in response to hindlimb ischemia in-vivo.

Several studies have identified relevant miRNAs by examining miRNA expression levels in isolated cells, namely ECs. To this end, the miR-17~92a cluster was found to be highly expressed in HUVECs and to negatively regulate angiogenesis in-vitro¹⁵⁰. Furthermore, systemic delivery of miR-92a antagomirs enhanced perfusion recovery in C57BL/6 mice following hindlimb ischemia¹⁵⁰. In another study, endothelial-specific deletion of the miR-17~92 cluster was also seen to increase foot perfusion 14 days following FAL, as well as arteriole density in FAL-operated

limbs¹⁵¹. Within this miR-17~92 cluster, antagonism of miR-19a/b in aged mice improved the perfusion recovery after ischemia by targeting key aspects of the WNT signaling pathway¹⁵¹. MicroRNA-223 was also found to be highly expressed in freshly isolated human, murine, and porcine ECs and to abrogate EC migration and sprouting in-vitro, via regulation of β 1 integrin¹⁵². Compared to littermate controls, miR-223^{-/-} mice exhibited enhanced perfusion recovery (nearly 2-fold), increased α -SMC⁺ staining in adductor muscles, and increased capillary density in gastrocnemius muscles following hindlimb ischemia¹⁵².

Other studies have sought to determine if miRNAs with known functions important for vascular growth also regulate the response to hindlimb ischemia. To this end, miR-15a had been previously shown to be overexpressed in oxygen-glucose deprived cerebral ECs and to regulate Bcl-2¹⁵³. Following hindlimb ischemia, EC-specific miR-15a overexpressing transgenic mice exhibited reduced capillary density in ischemic limbs and reduced perfusion recovery compared to littermate controls by suppression of FGF2 and VEGF¹⁵⁴. Another study identified candidate miRNAs bioinformatically through reverse target prediction of 197 genes known to be involved in neovascularization¹⁵⁵. This analysis identified 14q32 as an enriched cluster of miRNAs with targets involved in neovascularization¹⁵⁵. Systemic inhibition of 4 different 14q32 cluster miRNAs (miR-320, -487b, -494, and -495) increased perfusion (~25-40%), arteriolar diameter, and capillary densities following hindlimb ischemia¹⁵⁵. Another highly abundant, EC-specific miRNA that has been shown to have a role in vascular development is miR-126¹⁵⁶⁻¹⁵⁸. Following FAL in C57BL/6 mice, miR-126a [-3p] antagomirs impaired angiogenesis, both in-vivo and in-vitro, but had no effect on overall reperfusion in-vivo¹⁵⁶. However, overexpression of miR-126-3p through use of a non-invasive ultrasound-targeted microbubble destruction method, increased perfusion recovery and microvessel density in a rat hindlimb ischemia model¹⁵⁹. The miR-126~25 cluster, which includes 3 mature miRNAs (miR-106b, miR-93, and miR-25) and is a paralogue of the miR-17~92 and miR-106a~363 clusters, had been previously shown to be highly expressed in HUVECs and to promote tumor angiogenesis¹⁶⁰. This cluster also appears to be necessary for

normal reperfusion following FAL, as blood flow recovery was impaired in miR-126~25 knockout mice compared to controls, but was rescued by miR-126~25 overexpression¹⁶⁰.

Finally, several studies have quantified altered miRNA expression in the ischemic tissue following arterial occlusion in-vivo to identify potential regulators of reperfusion. To this end, miR-100 was found to be down-regulated in the adductor muscle of C57BL/6 mice 3 days post-FAL¹⁶¹. Subsequent inhibition of miR-100 enhanced perfusion recovery and capillary density through regulation of mTOR signaling¹⁶¹. Similarly, miR-155 was also down-regulated during hindlimb ischemia in C57BL/6 mice¹⁶². Inhibition of miR-155 increased EC proliferation and angiogenic tube formation in-vitro and promoted angiogenesis in the ischemic tissue of FAL-treated mice in-vivo¹⁶². Despite promoting angiogenesis, miR-155 deficient mice exhibited attenuated blood flow recovery and leukocyte recruitment, thereby indirectly implying miR-155 impairs arteriogenesis, though collateral diameters were not explicitly reported¹⁶². Another study identified miR-132/212 to be significantly up-regulated in the adductor muscles 4 and 7 days after femoral arterial occlusion¹⁶³. Perfusion recovery after arterial occlusion was slower in miR-132/212 knockout mice compared to wild-type mice¹⁶³. Hazarika et al. incorporated a variation on this approach by comparing differential genome-wide miRNA expression between C57BL/6 and Balb/c¹⁶⁴, two mouse strains known to exhibit widely different baseline vascular network structures and reperfusion capacities^{165–168}. From this approach, they identified miR-93 and determined that it enhanced perfusion recovery and capillary density by modulation of multiple genes involved in the regulation of cell proliferation and apoptosis¹⁶⁴.

Recently, other non-coding RNAs have been shown to play a role in the response to hindlimb ischemia. tRNA^{Val} and tRNA^{Gly}-derived fragments were shown to be up-regulated following hindlimb ischemia in mice and to inhibit EC proliferation, migration, and tube formation in-vitro¹⁶⁹. Several lncRNAs, including H19, MIR210HG, MEG9, MALAT1, and MIR22HG, were found to be up-regulated both in hypoxic ECs and in the gastrocnemius muscle of mice following femoral artery dissection¹⁷⁰. Moreover, H19 knockdown impaired capillary tube formation in-

vitro¹⁷⁰. In another study¹⁷¹, MALAT1 inhibition enhanced EC migration but impaired proliferation, leading to discontinuous sprouts in the presence of VEGF in-vitro. Pharmacological inhibition of MALAT1 reduced blood flow recovery and capillary density following hindlimb ischemia in-vivo¹⁷¹. These studies represent only very recent discoveries of functional roles for these non-coding RNAs. The regulation of vascular growth by lncRNAs and other non-coding RNAs will likely be an area of intense research focus in the near future.

4 Mechanisms of amplified arteriogenesis in collateral artery segments exposed to reversed flow direction

Heuslein JL, Meisner JK, Li X, Song J, Vincentelli H, Leiphart RJ, Ames EG, Blackman BR, Price RJ. Mechanisms of amplified arteriogenesis in collateral artery segments exposed to reversed flow direction. *Arterioscler Thromb Vasc Biol.* 2015;35:2354–2365.

4.1 Abstract

Objective: Collateral arteriogenesis, the growth of existing arterial vessels to a larger diameter, is a fundamental adaptive response that is often critical for the perfusion and survival of tissues downstream of chronic arterial occlusion(s). Shear stress regulates arteriogenesis; however, the arteriogenic significance of reversed flow direction, occurring in numerous collateral artery segments after femoral artery ligation (FAL), is unknown. Our objective was to determine if reversed flow direction in collateral artery segments differentially regulates endothelial cell signaling and arteriogenesis.

Approach and Results: Collateral segments experiencing reversed flow after FAL in C57BL/6 mice exhibit increased pericollateral macrophage recruitment, amplified arteriogenesis (30% diameter and 2.8-fold conductance increases), and remarkably permanent (12 weeks post-FAL) remodeling. Genome-wide transcriptional analyses on HUVECs exposed to reversed flow conditions mimicking those occurring in-vivo, yielded 10-fold more significantly regulated transcripts, as well as enhanced activation of upstream regulators (NFκB, VEGF, FGF2, TGFβ) and arteriogenic canonical pathways (PKA, PDE, MAPK). Augmented expression of key pro-arteriogenic molecules (KLF2, ICAM-1, eNOS) was also verified by qRT-PCR, leading us to test whether ICAM-1 and/or eNOS regulate amplified arteriogenesis in flow-reversed collateral segments in-vivo. Interestingly, enhanced pericollateral macrophage recruitment and amplified arteriogenesis was attenuated in flow-reversed collateral segments after FAL in ICAM-1^{-/-} mice; however, eNOS^{-/-} mice showed no such differences.

Conclusions: Reversed flow leads to a broad amplification of pro-arteriogenic endothelial signaling and a sustained ICAM-1-dependent augmentation of arteriogenesis. Further investigation of the endothelial mechanotransduction pathways activated by reversed flow may lead to more effective and durable therapeutic options for arterial occlusive diseases.

4.2 Abbreviations

LSF	laser speckle flowmetry
FAL	femoral arterial ligation
MBL	muscular branch ligation
EC	endothelial cell
HUVEC	human umbilical vein endothelial cells
NvC	non-reversed vs. control
RvC	reversed vs. control
PCP	planar cell polarization
MTOC	microtubule organizing center
GA	Golgi apparatus

4.3 Introduction

The importance of adequate remodeling of pre-existing arterial interconnections to form endogenous collateral bypasses – i.e. arteriogenesis – is highlighted by the extensive link between adequate collateral development and improved outcomes in patients with arterial occlusive disease^{36,172}. However, few clinical trials designed to therapeutically stimulate collateral development have proven successful^{34,35,173,174}. This is likely related to the fact that these interventions do not necessarily recapitulate the complex sequence of processes that must be coordinated to achieve functional collateral development^{37,39,172}. These clinical results have led to a re-examination of the basic mechanisms underlying collateral remodeling in the hope of identifying central signaling pathways for better therapeutic development.

As early as 1893, Thoma observed a correlation between vessel diameter and blood flow⁴⁰. We now know the biomechanical forces exerted by blood flow on the endothelium are critical in regulating cell phenotype and blood vessel remodeling^{37,41–45}. Indeed, a key initiating stimulus for arteriogenesis is a change in shear stress³⁷. Upon occlusion of a major artery, downstream pressure is reduced, causing an increase in pressure gradient, blood flow, and shear stress along pre-existing collateral arteries that bypass the occlusion. Both the magnitude¹⁵ and duration¹⁶ of increased shear stress determine maximal collateral outgrowth. Collateral artery growth is hypothesized to eventually resolve as the increased outward remodeling reduces shear stress magnitude to a homeostatic “set-point”⁸⁶.

Nonetheless, the topological arrangement of collateral arteries in skeletal muscle also dictates that shear stress will vary on a segment-to-segment basis along any given collateral pathway after the occlusion of a major artery. Recently, we applied transillumination based laser speckle flowmetry (LSF) to quantify, for the first time, the in-vivo “segment-to-segment” spatial distribution of collateral artery hemodynamics before and after femoral artery ligation in the mouse ischemic hindlimb, the most widely used model of peripheral arteriogenesis. While shear stress magnitude increased ~2-fold along the length of the collateral vessels in the gracilis adductor muscle, some pre-existing collateral artery segments also experienced reversed flow direction after femoral artery ligation¹⁷⁶. In the present study, we tested the hypothesis that a change in flow direction has a profound influence on both arteriogenesis and mechanotransductive endothelial cell signaling.

4.4 Materials and Methods

4.4.1 Mice.

All animal protocols were approved by the Institutional Animal Care and Use Committee at the University of Virginia and conformed to all regulations for animal use outlined in the American Heart Association Guidelines for the Use of Animals in Research. C57BL/6 mice were purchased

from Charles River Laboratory (Wilmington, MA). For ICAM-1^{-/-} and eNOS^{-/-} studies, wild-type C57BL/6 control mice, ICAM-1^{-/-} (B6.129S4-Icam1^{tm1Jcgr}), and eNOS^{-/-} (B6.129P2-Nos3^{tm1Unc/J}), were purchased from Jackson Laboratory (Bar Harbor, ME). All animals were housed in the animal facilities at the University of Virginia.

4.4.2 Femoral arterial ligation model.

To produce uniform hemodynamic changes in the collateral arteries in a superficial adductor muscle, we used a previously detailed femoral artery ligation scheme¹⁶⁷. This particular ligation pattern has been previously shown to produce consistent arteriogenesis in the collateral arteries of the gracilis adductor muscles^{177–180} with minimal heterogeneity in the baseline collateral structure and with the predicted changes in flow direction from baseline. Male mice, 9-13 weeks of age, were anesthetized (i.p 120 mg/kg ketamine, 12 mg/kg xylazine, and 0.08 mg/kg atropine), depilated, and prepped for aseptic surgery. On the left leg, an incision was made directly above and along the femoral artery, which was gently dissected from the femoral vein and nerve between the bifurcation of the superior epigastric artery and popliteal artery. Two 6.0 silk sutures were placed immediately distal to the epigastric artery, which served as the origin of the muscular branch artery in all mice, and the artery segment between the two ligatures was then severed with micro dissecting scissors. The surgical site was then closed with 5.0 prolene sutures. A sham surgery, wherein the femoral artery was exposed but not ligated, was performed on the right hindlimb (i.e. on the other leg). Animals received one injection of buprenorphine for analgesia at the time of surgery and a second dose 8-12 hours later.

4.4.3 Muscular branch ligation model.

Male mice were anesthetized (i.p 120 mg/kg ketamine, 12 mg/kg xylazine, and 0.08 mg/kg atropine), depilated, and prepped for aseptic surgery. On the left leg, an incision was made directly above and along the femoral artery. The muscular branch artery which was gently dissected from the paired vein and ligated with one 6.0 silk suture just distal to the epigastric artery. The surgical

site was then closed with 5.0 prolene sutures. A sham surgery, wherein the muscular branch artery was exposed but not ligated, was performed on the right hindlimb (i.e. on the other leg). Animals received one injection of buprenorphine for analgesia at the time of surgery and a second dose 8-12 hours later.

4.4.4 Laser Doppler perfusion imaging.

For monitoring blood flow recovery and post-surgical ischemia, mice were anesthetized (i.p 120 mg/kg ketamine, 12 mg/kg xylazine, and 0.08 mg/kg atropine) then placed prone on a surgical heating pad for 5 minutes to minimize temperature variation. The soles of the feet were scanned (Lisca PIM laser Doppler imager), and mean voltage of foot perfusion was used to calculate relative perfusion ratio (ligated/unligated).

4.4.5 Tissue harvesting for cross sectional and collateral structure analysis by vascular casting.

For analysis of lumenal diameters in the gracilis collateral arteries and to enable sectioning at specific regions, vascular casting was performed using an opaque polymer that allows for accurate lumenal diameter measurements¹⁷⁹. After femoral artery ligation, mice were anesthetized (i.p 120 mg/kg ketamine, 12 mg/kg xylazine, and 0.08 mg/kg atropine), euthanized via an overdose of pentobarbital, and then the abdominal aorta was cannulated. The lower body was then perfused with 7mL of 2% heparinized saline with 2mmol/L adenosine (16404, Fisher Scientific, Pittsburg, PA) and 0.1mmol/L papaverine (P3510, Sigma Aldrich, St Louis, MO) to clear and vasodilate the downstream vasculature at a constant rate of 1mL/min (PHD2000, Harvard Apparatus). Once perfused, we waited 5 minutes to enable vasodilation. Tissues were then perfused with 3mL of 4% paraformaldehyde solution (19943, Affymetrix, Cleveland, OH) at 1mL/min and allowed to fix for 10 minutes. The lower body was then perfused with 0.8mL of Microfil® casting agent (FlowTech, Inc, Carver, Massachusetts) at a constant pressure of 100mmHg. Viscosity of Microfil® was adjusted to minimize transport across capillaries. After

curing for 1.5 hours at room temperature, gracilis muscles were dissected free and then cleared in 50% glycerol in phosphate buffered saline (PBS) overnight. Cleared tissues were mounted between two coverslips using 500 μm thick spacers (645501, Grace Bio-Labs Inc) to keep constant thickness between muscles. Muscles were imaged using transmitted light at 4x magnification on a Nikon TE200 inverted microscope with a CCD camera (Quantifier, Optronics Inc). Individual fields of view were montaged together (Photoshop CS2, Adobe Systems Inc).

For analysis of lumenal diameter from intact gracilis collateral whole mounts (i.e. vascular casting), collateral entrance regions were defined according to the following method. A cropped portion (560 μm x 560 μm) of the montaged image (previously randomized and de-identified) was taken of the collateral artery at the first visible branch point of a terminal arteriole from the primary collateral as it extended from either the saphenous or muscular branch artery. This was done for each primary collateral running through the anterior and posterior heads of the gracilis muscle, yielding 4 total image regions per tissue whole mount. After each cropped image region was taken, all images were randomized and de-identified. The mean diameter was then taken from three separate diameter measurements along the length of cropped portion of the collateral artery.

After imaging, muscles were rehydrated, cut, and then paraffin embedded for cross sectional analysis at the muscular branch and saphenous artery entrance regions to the collateral arteries. Resulting cross sections were re-hydrated and immunolabeled for the macrophage marker Mac-3 (day 3 post-FAL), H&E stained for collateral artery structure analysis (day 7 and day 84 post-FAL), or fluorescently labeled with isolectin-B4 for capillary density analysis (day 7 post-FAL).

4.4.6 Cross sectional analysis of collateral artery structure.

Sections (5 μm thickness) of paraffin embedded muscle from the muscular and saphenous regions were labeled for H&E. Individual fields of view encompassing the collateral vessels were imaged with a 20x oil objective on a Nikon TE200 inverted microscope with a CCD camera (Quantifier,

Optronics Inc). All images were randomized and de-identified prior to analysis. Lumenal diameter, wall area, and wall thickness were determined using Fiji ¹⁸¹.

4.4.7 Cross sectional analysis for regional capillary density and muscle fiber atrophy.

Sections (5µm thickness) of paraffin embedded muscle from the muscular and saphenous regions were rehydrated and labeled with *Griffonia simplicifolia* isolectin-B₄ conjugated to Alexa 647 (GSL-I-B₄ 10 µg/ml, I32450 Life Technologies Inc) and 10nmol/L SYTOX green nuclear stain (S7020, Life Technologies Inc). The entire cross-section for each region (encompassing both the anterior and posterior heads of the gracilis muscle) was imaged at 20x magnification on a Nikon TE2000 C1 confocal microscope and individual fields of view were stitched together (Photoshop CS2, Adobe Systems Inc). All GSL-I-B₄ positive vessels <7µm in diameter and all muscle fibers (identified by autofluorescence) were counted in each section using Fiji ¹⁸¹. Total muscle area was determined by semi-automated threshold analysis for calculation of average muscle fiber area.

4.4.8 Immunofluorescence labeling of pericollateral Mac3⁺ cells.

Sections (5µm thickness) of paraffin embedded muscle from the muscular and saphenous regions were rehydrated and subjected to heat mediated antigen retrieval for 10 minutes in a citrate based antigen retrieval buffer (Vector Laboratories, Burlingame, CA; H-3300). Slides were then quenched of endogenous peroxidase activity with a 30 minute incubation in 3% H₂O₂, blocked, and labeled with rat-anti-Mac3 (1:100, M3/4 clone, 550292; BD Biosciences, San Jose, CA) overnight at 4°C. Slides were washed and incubated with a biotinylated sheep-anti-rat secondary antibody (Abcam, Cambridge, MA, ab6851, 1:500) for 1 hour at room temperature. Slides were washed and incubated with an avidin-biotin complex (Vectastain ABC solution, Vector Laboratories) for 30 minutes at room temperature. Slides were washed and incubated with a Tyramide Signal Amplification (TSA) reagent (Perkin Elmer, Waltham, MA; 1:50) for 10 minutes at room temperature. Slides were washed and incubated with streptavidin-488 (Life Technologies

Inc, 1:500), Cy3-anti-SMA (1A4 clone, Sigma, 1:1000) and DRAQ5 (Thermo Scientific Inc, 1:1000). Slides were then mounted with Prolong Gold (Life Technologies Inc) to minimize photobleaching, allowed to cure overnight, and imaged using a Nikon TE2000 C1 laser scanning confocal microscope with a 20x oil objective. Cropped fields of view (512x512 pixels) encompassing the collaterals in each region were randomized and de-identified. The pericollateral region was outlined (25 microns around the vessel) and pericollateral Mac3⁺ nuclei were counted in Fiji ¹⁸¹.

4.4.9 Tissue harvesting for in-vivo collateral artery endothelial planar cell polarization.

For analysis of the spatial variation of endothelial cell planar polarization in the gracilis collateral arteries, whole gracilis muscles were immunolabeled for smooth muscle alpha-actin, the Golgi apparatus, and the nucleus. The Golgi apparatus was chosen over the more widely reported microtubule organizing center (MTOC)^{182–184} due to its larger size in order to aid identification in the situation of decreased resolution and clarity when imaging thick (>100µm) tissues using confocal microscopy. The Golgi apparatus, which colocalizes with the MTOC ¹⁸⁵, has previously been shown to serve as a functional marker of endothelial cell planar polarization ¹⁸⁶. Pre-ligation and 24 hours after femoral artery ligation, mice were euthanized, and the abdominal aorta was cannulated. The lower body was then perfused with 2% heparinized saline with 2mmol/L adenosine and 0.1mmol/L papaverine to clear and vasodilate the downstream vasculature at a constant rate of 1mL/min (PHD2000, Harvard Apparatus) and then fixed with 2% paraformaldehyde solution for 30 minutes. Tissues were then flushed with PBS and perfused with an antibody and blocking solution consisting of PBS, 2% BSA, 10% NGS, and 0.015% saponin and containing anti-smooth muscle α -actin-FITC (1:400 1A4 clone, A5691, Sigma Aldrich), rabbit anti-giantin (1:500, ab24586 Abcam Inc), and 5µmol/L Draq 5 (62251, Thermo Scientific Inc). This perfusion step was found necessary to ensure adequate penetration of the giantin antibody to the

collateral artery endothelial cells. After 60 minutes, muscles were removed and further incubated overnight at 4°C in an antibody solution consisting of PBS, 2% BSA, 10% NGS, and 1% TritonX100 and containing anti-smooth muscle alpha actin-FITC (1:400 1A4 clone, Sigma-Aldrich), rabbit anti-giantin (1:500, ab24586, Abcam Inc), and 5µmol/L Draq 5. Muscles were then washed and incubated overnight at 4°C in a secondary antibody solution consisting of PBS, 2% BSA, and 1% TritonX100 and containing goat anti-FITC Alexa 488 (1:200 A11090, Life Technologies Inc), goat anti-rabbit IgG Alexa 555 (1:200, A21428 Life Technologies Inc), and 5µmol/L Draq 5. Muscles were then washed and cleared in a series of 50% glycerol in PBS and then 90% glycerol in PBS overnight at 4°C. Cleared muscles were then mounted between two coverslips using 500 µm thick spacers (645501, Grace Bio-Labs Inc). Muscles were then imaged on a Nikon TE2000 C1 laser-scanning confocal microscope with a 20x oil lens immediately upstream of the first visible transverse arteriole branch off of the anterior and posterior collateral arteries extending from the muscular branch and saphenous arteries and at the midpoint of the anterior and posterior collateral arteries.

4.4.10 Regional analysis of hypoxia.

A femoral arterial ligation and sham procedure were performed as previously described on C57BL/6 mice. 24 hours post ligation, mice were anesthetized (i.p 120 mg/kg ketamine, 12 mg/kg xylazine, and 0.08 mg/kg atropine) then injected i.p. with 60mg/kg pimonidazole-HCl (Hypoxypoint, Burlington, MA). After 20 minutes, mice were euthanized with an overdose of pentobarbital. The heart was cannulated and perfused with cold 2% heparinized saline with 2mmol/L adenosine (16404, Fisher Scientific) to clear and vasodilate the downstream vasculature at a constant rate of 4mL/min (PHD2000, Harvard Apparatus) and then fixed with cold 4% paraformaldehyde solution (19943, Affymetrix). Gracilis muscles and liver sections were removed and further fixed in 4% PFA + 0.1% saponin for 20 minutes at room temperature. Tissues were then washed in PBS with 1% Triton-X overnight. Tissues were then cut and paraffin embedded

for cross sectional analysis at the muscular branch and saphenous artery entrance regions to the collateral arteries. Sections (5µm thickness) of paraffin embedded muscle from the muscular and saphenous regions were rehydrated and subjected to heat mediated antigen retrieval for 20 min in a citrate based antigen retrieval buffer (H-3300; Vector Laboratories). Slides were blocked and then incubated with anti-pimonidazole-HCl-FITC primary antibody (1:200, Hypoxyprobe) for 45 minutes at room temperature. Slides were washed then incubated with an 633 labeled anti-FITC secondary antibody (clone 1F8-1E4, Sigma, 1:400), Cy3-anti-SMA (1A4 clone, Sigma, 1:1000), and 10nmol/L SYTOX green nuclear stain (S7020, Life Technologies Inc) for 45 minutes at room temperature. Slides were washed and then sealed with Prolong Gold (Life Technologies). The entire cross-section for each region (encompassing both the anterior and posterior heads of the gracilis muscle) was imaged at 20x magnification on a Nikon TE2000 C1 laser-scanning confocal microscope and individual fields of view were stitched together (Photoshop CS2, Adobe Systems Inc). Integrated fluorescence intensity (mean gray value x area) was determined in cropped (256x256 pixels) fields of view encompassing the collateral vessels in each region from previously randomized and de-identified montaged images.

4.4.11 Human umbilical vein endothelial cell culture.

Human umbilical vein endothelial cells (HUVECs) purchased from Cell Applications Inc., VEC Technologies Inc. (Rensselaer, NY), and Lonza were thawed and maintained on 0.1% gelatin coated flasks in M-199 medium (Lonza), supplemented with 10% fetal bovine serum (Life Technologies Inc, Grand Island, NY), 100U/mL penicillin-G + 100ug/ml streptomycin (Life Technologies Inc) , 2mmol/L L-glutamine (Life Technologies Inc), 5ug/ml endothelial cell growth supplement (Biomedical Technologies, Stoughton, MA), and 10ug/ml heparin (Sigma Aldrich Inc). For each set of experimental comparisons, cells were used from the same company and cell line, in their third subculture passage.

4.4.12 In-vitro exposure of endothelial cells to simulated ligation shear stress.

HUVECs were plated on cell culture grade plastic dishes coated with 0.1% gelatin and grown to confluence. A cone and plate flow apparatus¹⁸⁷, which maintains cells at 5% CO₂ and 37°C, was used to induce a shear stress protocol. The applied shear stress protocol consisted of a 24 hour preconditioning period at a steady of 15 dyne/cm² and then either increased to 30 dynes/cm² (non-reversed), increased to 30 dynes/cm² and reversed in direction (reversed), or held constant at 15 dynes/cm² (control). Fresh culture media consisting of M199 with 4% dextran from *Leuconostoc* spp (Sigma Aldrich, Mr ~500,000), 2% fetal bovine serum, 100U/mL penicillin-G + 100ug/ml streptomycin, 2mmol/L L-glutamine, 5ug/ml endothelial cell growth supplement, and 10ug/ml heparin was added to cells before exposure to shear stress and was continuously exchanged throughout the duration in the cone and plate apparatus.

4.4.13 HUVEC RNA isolation, qRT-PCR, and microarray gene expression profiling.

For RT-PCR and cDNA microarray assays, total RNA was extracted using the PureLink total RNA purification system (Life Technologies Inc). RNA concentration and purity was confirmed with a NanoDrop spectrophotometer for RT-PCR and by Agilent Bioanalyzer. Each replicate consisted of three plates split from the same culture. The three plates were then run in tandem, under one of the three separate shear conditions.

For microarray analysis, 4 replicates were collected for each condition at 6 hours after simulated FAL. RNA amplification, labeling, hybridization with Human Gene 1.0ST oligo microarrays (Affymetrix), quality control, and raw data acquisition were performed by the University of Virginia Biomolecular Research facility and data analysis by the University of Virginia Bioinformatics Core facility. All preprocessing and analysis was done using R version 2.15.0. CEL files were imported using the affy package, version 1.34.0. Expression intensities were summarized, normalized, and transformed using Robust Multiarray Average (RMA) algorithm¹⁸⁸. Probesets were annotated using the bioconductor annotation package

hugene10sttranscriptcluster.db version 8.0.1, using the annotate package, version 1.34.0. Probesets not mapping to an Entrez gene were excluded (probesets mapping to RIKEN genes were not excluded). For examining differential gene expression, a linear model with empirical-Bayes moderated standard errors was fit using the limma package in R. The BioConductor package arrayQualityMetrics was used to perform quality assessment on the preprocessed, summarized, normalized, transformed, filtered data. The expression dataset is publically available at GEO (<http://www.ncbi.nlm.nih.gov/geo/> (GSE 46248)). Heat maps were created using the gplots package in R (<http://CRAN.R-project.org/package=gplots>). Gene ontology was assessed through the gene ontology enrichment analysis and visualization tool (GOrilla)¹⁸⁹. Biological context was analyzed by Ingenuity Pathway Analysis (<http://www.ingenuity.com/>) for functional gene clustering and function.

For quantitative reverse transcriptase PCR (qRT-PCR), total RNA was reverse transcribed using the iScript cNDA synthesis kit (Bio-Rad, Hercules, CA). RT-PCR was performed on CCL2 (forward 5'-CCAGCAGCAAGTGTCCCAAAG -3' reverse 5'-TGCTTGTCCAGGTGGTCCATG-3'), eNOS (forward 5'-CTCCATTAAGAGGAGCGGCTC-3', reverse 5'-CTAAGCTGGTAGGTGCCTGTG-3'), E-selectin (forward 5'-AATCCCAGTTTGTGAAGCTTTCCA-3', reverse 5'-GCCAGAAGCACTAGGAAGACAATT-3'), ICAM (forward 5'-TCGCTATGGCTCCCAGCAGC-3', reverse 5'-TTCCGGTTGTTCCCAGGCAGG-3'), KLF2 (forward 5'-GCTGAGTGAACCCATCCTGCC-3', reverse 5'-CGCTGTTGAGGTCGTCGTCG-3'), KLF4 (forward 5'-GGCCAGAATTGGACCCGGTGTAC-3', reverse 5'-CTGCCTTTGCTGACGCTGATGA-3'), and VCAM (forward 5'-GTTTGTGTCAGGCTAAGTTACATATTGATGA-3' reverse 5'-GGGCAACATTGACATAAAGTGTTT-3'), with SYBR Green (Roche Applied Sciences) on a CFX96 Real Time Detection System (Biorad). Expression was normalized to β 2-microglobulin (forward 5'-AGCATTCGGGCCGAGATGTCT-3', reverse 5'-CTGCTGGATGACGTGAGTAAACCT-3') which is endogenously expressed and is not altered by

many stimuli including shear stress ⁴⁴. Normalized expression was quantified using the comparative $2^{\Delta\Delta Ct}$ method.

4.4.14 Immunofluorescence labeling for HUVEC planar cell polarity.

After exposure to our shear stress protocol, cells were fixed in 4% PFA for 10 minutes at room temperature, blocked with PBS + 0.1% saponin + 2% BSA + 5% normal goat serum for 45 minutes at room temperature, and then incubated in primary antibody solution containing Vibrant Dyl (1:200, Life Technologies Inc) or CD31 (1:200, 89C2, Cell Signaling Technology, Danvers, MA), Draq5 (5 μ mol/L, Thermo Scientific Inc), and either rabbit-anti-giantin (1:1000, ab24586, Abcam Inc) or rabbit-anti-pericentrin (1:500, ab4448, Abcam Inc). Cells were washed three times in PBS+0.1% saponin then incubated in goat-anti-rabbit Alexafluor 488 (1:500, Life Technologies) secondary antibody solution for 45 minutes. Cells were washed twice in PBS, then twice in 50:50 PBS: glycerol, and then in 10:90 PBS: glycerol prior to cover slip mounting with Prolong Gold (Life Technologies). Plates were allowed to cure overnight then were imaged using a Nikon TE2000 C1 laser scanning confocal microscope. The relative location of the nucleus to the Golgi apparatus or MTOC from three independent sets of experimental conditions, each an average of three representative fields of view (for a total of nine images per experimental condition), was determined by a blinded, independent observer.

4.4.15 Data analysis of endothelial cell planar polarity.

For analysis of endothelial orientation with respect to flow, maximum intensity projections of collateral arteries (for whole mount analysis) or fields of view (for HUVEC plates) were indicated with flow direction then de-identified for blinded analysis. Peri-nuclear location of the Golgi apparatus or MTOC was determined with respect to flow direction and nuclear position ([Figure 4.1B-C](#) and [Supplemental Figure 4.4](#)).

4.4.16 HUVEC western blot and NF- κ B activity assays.

HUVECs were lysed in MAPK buffer (63.5mM Tris-HCL pH 6.8, 2% w/v SDS, 10% glycerol, 50mM DTT, 0.01% bromophenol blue). Total protein was collected and lysates resolved on a 7.5% SDS-PAGE gel and blotted on a nitrocellulose membrane. Primary antibodies [ICAM-1 (R&D Systems, 1:750), pS1177-eNOS (BD Biosciences, 1:750), α -tubulin (Sigma, 1:1000) were incubated overnight at 4C. A LICOR Odyssey imager was used for blot image acquisition and densitometry analysis.

To determine NF- κ B activity by luciferase reporter activity, endothelial cells were infected with adenovirus containing NF- κ B luciferase reporter (Vector Biolabs, Philadelphia, PA; Cat. No. 1740, 1:5000) 24 hours prior to shear stress. Luciferase reporter activity was assessed using the Promega Luciferase Assay System per manufacturer's instructions.

4.4.17 siRNA transfection in HUVECs

Twenty-four hours prior to exposure of HUVECs to flow conditions, HUVECs were plated without antibiotics on 0.1% gelatin coated plates in serum-free M199 (Life Technologies) supplemented with 2mmol/L L-glutamine. After cells were allowed to adhere for 2 hours after plating, cells were transfected with either 120pmol of ON-TARGETplus SMARTpool human ICAM-1 siRNA (L-003502-00-0005, GE Dharmacon, Lafayette, CO) or 120pmol of ON-TARGETplus non-targeting siRNA (D-001810-10-05, GE Dharmacon) in 52 μ L of Oligofectamine transfection reagent (Life Technologies) and 6.8mL Opti-MEM media (Life Technologies) for 5 hours at 37C. After 5 hours, plates were flooded with 8mL of M199 media without antibiotics supplemented with 10% fetal bovine serum + L-glutamine + 5ug/ml endothelial cell growth supplement (Biomedical Technologies, Stoughton, MA), and 10ug/ml heparin (Sigma Aldrich Inc). 24 hours post-transfection this solution was aspirated off and normal flow media was applied. Validation of transfection was performed on HUVEC plates not exposed to shear stress but in culture for the same duration (54 hours post-transfection) via ICAM-1 western blotting.

4.4.18 Monocyte adhesion functional assay

Human derived monocytes (THP-1 cell line) were purchased from the ATCC. Monocytes were unthawed and maintained in RPMI 1640 (11875-093, Life Technologies Inc) + 10% fetal bovine serum (Life Technologies Inc) + 0.05mM β -mercaptoethanol per ATCC culture instructions. Monocytes sub-cultured once cell density approached 800,000 cells/mL. Cells were used between passages 2 – 6.

Prior to the adhesion assay, cells were counted to obtain 3,000,000 cells / plate of HUVECs. Cells were pelleted, washed with PBS, pelleted, and then re-suspended in serum-free RPMI media at 1,000,000 cells/mL. Thawed calcein AM was added at 1ug/ml and incubated with cells for 15 minutes at 37°C. After 15 minutes, the reaction was stopped by adding excess serum-free RPMI to the cell solution then pelleted. Cells were washed once with serum-free M199 media, pelleted, and then re-suspended in serum-free M199 at 500,000 cells/mL. Immediately following completion of flow exposure to HUVECs, flow media was removed by aspiration. HUVECs were quickly washed with serum-free M199 media. This media was then aspirated off and 6mL of serum-free M199 + monocytes (3,000,000 / plate) were added to and incubated with HUVECs for 30 minutes at 37°C. Following the 30 minutes, cells were washed twice with PBS to remove unbound monocytes. Adhered monocytes and HUVECs were fixed with 4% PFA for 10 minutes followed by two washes with PBS. Cover slips were mounted with Prolong Gold (Life Technologies Inc). Plates were then imaged using a Nikon TE2000 C1 laser scanning confocal microscope. Nine randomly selected FOVs per condition for 4 independent experiments were obtained. Images were de-identified and randomized in MATLAB. Images were converted to 8-bit images, set to an equivalent threshold, and bound monocytes were quantified using Fiji's "Analyze Particles" tool (20 μ m² minimum particle size). Results were centered on the mean of all conditions within each independent experiment.

4.5 Results

4.5.1 Planar polarization confirms endothelial cell responsiveness to predicted flow directions

Femoral arterial ligation (FAL), performed as previously described¹⁷⁶, was used to induce arteriogenesis in the gracilis adductor muscle collateral arteries. In agreement with previous studies^{179,180}, perfusion measurements of the plantar surface of the foot indicated moderate ischemia immediately post-FAL, followed by a return to full perfusion by day 7 post-FAL (**Supplemental Figure 4.1**). The position of the ligation along the femoral artery was chosen to yield a change in blood flow direction and magnitude along the length of the two collateral arteries in this muscle. Pre-ligation, blood flows toward a convergence point in the center of the gracilis muscle via the muscular branch artery (also known as the lateral caudal femoral artery) and via the saphenous artery (**Figure 4.1A**). FAL causes a decrease in downstream pressure, resulting in increased flow through the gracilis collaterals and reversed flow direction in those collateral segments near the saphenous artery (**Figure 4.1A**). Using transillumination laser speckle flowmetry (LSF), we recently determined that shear stress magnitude increases 2-fold in both the muscular and saphenous collateral entrance regions 30 minutes post-FAL. Additionally, we confirmed the predicted flow directions in this ligation scheme through observation of circulating fluorescent microspheres during intravital imaging¹⁷⁶.

To further confirm endothelial cell responsiveness to the change in flow direction, we characterized endothelial cell planar polarization (PCP) in the gracilis collateral arteries by examination of the perinuclear position of the Golgi apparatus (GA) with respect to predicted flow direction both pre-FAL and 24hrs post-FAL (**Figure 4.1B-E**). At baseline, endothelial cells at the collateral entrance regions were primarily polarized toward their respective upstream directions (**Figure 4.1F, D**), while the central regions of the gracilis collateral arteries showed no significant polarization. By 24 hours post-FAL, however, most of the endothelial cells in both the central and

saphenous entrance regions repolarized toward the muscular branch artery, instead of the saphenous artery (**Figure 4.1B, E**).

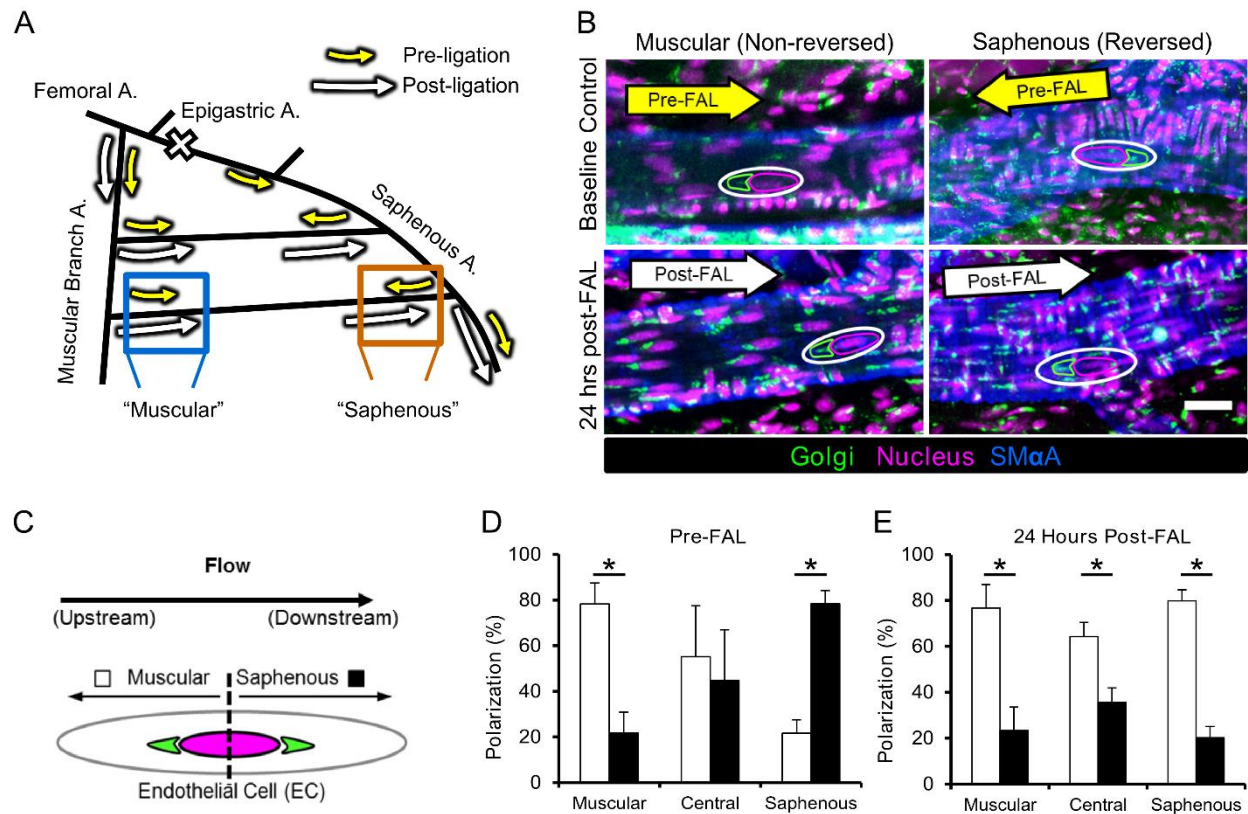


Figure 4.1. Collateral artery endothelial cells repolarize in response to reversed shear stress after FAL.

A) Schematic of the primary gracilis adductor collateral flow pathways after femoral arterial ligation (FAL). The femoral artery is ligated just distal to the epigastric artery thereby creating a change in flow direction at the saphenous branch entrance region. Arrows indicate the direction and magnitude of blood flow pre- (yellow) and post- (white) FAL. Flow magnitude increases in both the muscular branch and saphenous entrance regions, while flow direction also changes in the saphenous region. **B)** Representative images of collateral regions immunolabeled for the Golgi apparatus (anti-giantin, outlined in green), the position of which with respect to the nucleus (Draq5, outline in magenta) was used to determine planar polarization, a marker of endothelial response to flow direction. Images are oriented such that the muscular branch is toward the left and the saphenous artery is toward the right. Arrows indicate blood flow direction. (Scale bar=25 μ m). **C)** Diagram depicting the method used to quantify polarization. Golgi apparatus (green) position with respect to the nucleus (magenta) was used to classify EC polarization as toward either the saphenous (black bars) or muscular branch (white bars) arteries. **D)** Bar graph of pre-FAL EC planar polarization. ECs in the entrance regions show upstream polarization, while those central region show no directional bias (n=4). **E)** Bar graph of 24 hour post-FAL EC planar polarization. ECs in all regions show upstream polarization toward the muscular branch entrance region (n=4). *p<0.05 between muscular and saphenous polarization within the given region. Data are mean \pm SEM.

4.5.2 Arteriogenesis is enhanced in collateral artery segments exposed to reversed flow after FAL.

To determine if reversed flow affects arteriogenesis, we measured lumenal collateral diameter in the muscular branch and saphenous artery entrance regions using vascular casting ([Figure 4.2A](#)). After 24 hours, neither region demonstrated significant lumenal expansion compared to the unligated control limb. By day 3, however, both the saphenous (reversed) and muscular (non-reversed) regions underwent significant ($p < 0.001$ and $p = 0.04$ respectively) lumenal expansion compared to unligated controls ($58.8 \pm 8.5\%$ and $19.9 \pm 4.7\%$ increases respectively). Furthermore, the saphenous (i.e. flow-reversed) segment began to exhibit a significant ($p = 0.004$) enhancement in lumenal diameter when compared to the non-reversed muscular branch. Lumenal diameter in both reversed and non-reversed regions increased further by day 7 post-ligation ($93.7 \pm 9.1 \mu\text{m}$ and $70.7 \pm 6.1 \mu\text{m}$ within saphenous and muscular branch regions respectively), but thereafter remained constant through 12 weeks post-FAL ($91.6 \pm 3.3 \mu\text{m}$ and $75.2 \pm 5.2 \mu\text{m}$). At both 1 and 12 weeks post-FAL, lumenal diameter was significantly greater in the flow-reversed saphenous region when compared to the non-reversed muscular branch region ($p = 0.01$) ([Figure 4.2B](#)). The time course of arteriogenesis matched well with the laser Doppler reperfusion measurements ([Supplemental Figure 4.1](#)), where resting foot perfusion returned to baseline around 5 days post-ligation, with no further increases in reperfusion.

Cross-sectional analysis of the collateral artery entrance regions was used to confirm whole-mount diameter measurements and determine whether wall mass was also increased in flow reversed segments ([Figure 4.2C](#)). Both reversed and non-reversed regions showed significantly increased lumenal diameter, wall area, and wall thickness versus their respective unligated controls at 7 days post-FAL ([Figure 4.2C-F](#)). In confirmation of the whole mount vascular cast

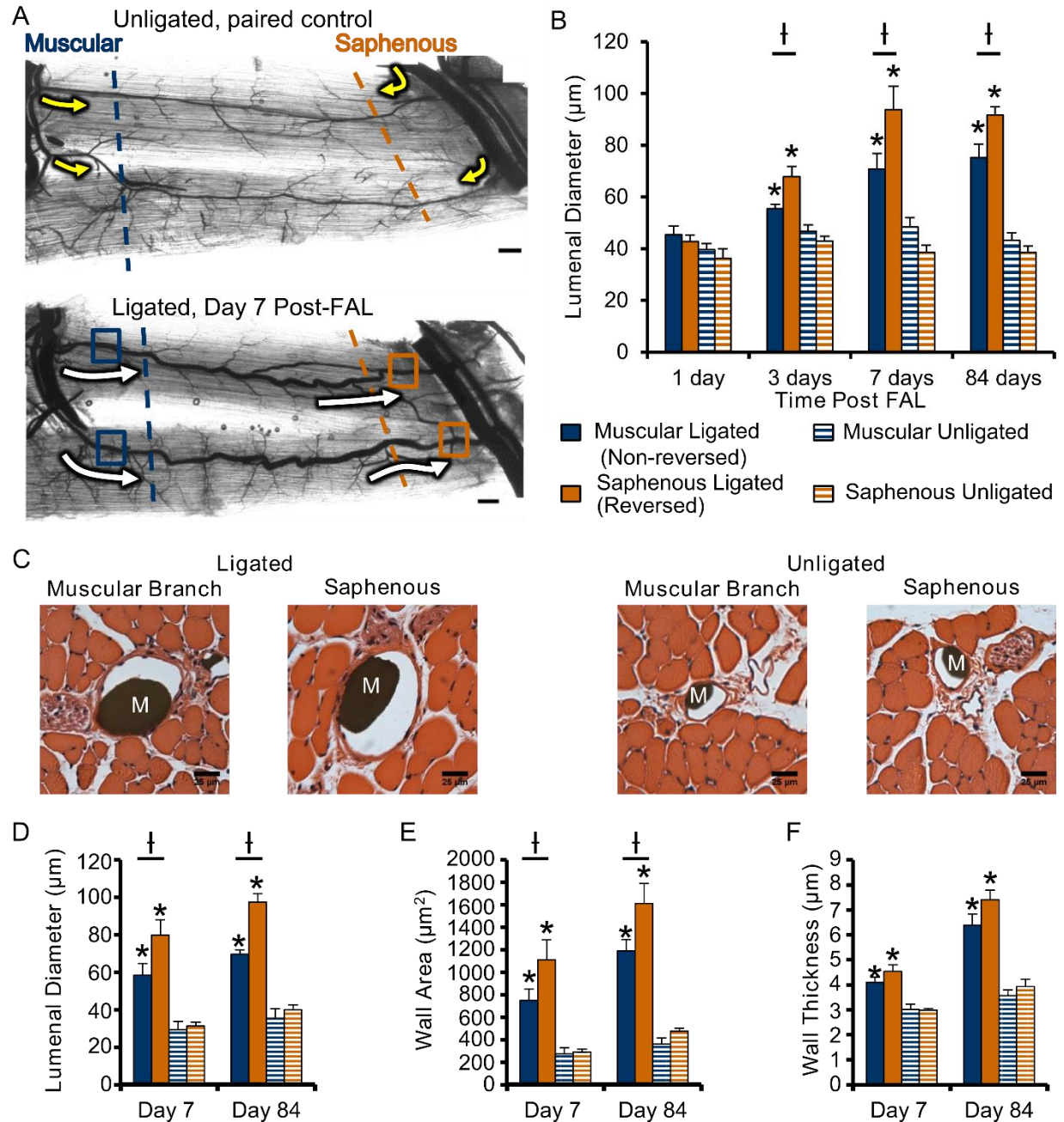


Figure 4.2. Gracilis collateral artery regions exposed to reversed flow exhibit enhanced arteriogenesis after FAL.

A) Representative vascular cast images of gracilis collateral arteries from unligated sham control (top) and FAL-treated (bottom) mice. Arrows indicate the direction and relative magnitude of blood flow pre- (yellow) and post- (white) FAL. Dashed lines indicate the collateral artery region (muscular=blue; saphenous=orange) and approximate location where the muscles were cut for regional cross-sectional analysis. Boxes indicate location at which luminal diameters were measured **B)** Bar graph of collateral artery luminal diameter at both the non-reversed (muscular branch, blue) and flow-reversed (saphenous, orange) entrance regions. (n=6-7 mice per day). **C)** Representative H&E stained cross-sections of gracilis muscles. Microfil casting material (M) is evident in artery lumens. **D-F)** Bar graphs of cross sectional luminal diameter, wall area, and wall thickness (n=6-7 mice per day). *p<0.05 between ligated and unligated within the given region at the specified time-point; †p<0.05 between regions (i.e. saphenous vs. muscular) at the specified time-point. Data are mean \pm SEM.

analysis, we observed an enhancement of luminal diameter in the flow-reversed saphenous region ($36.7 \pm 2.3\%$ vs. non-reversed muscular region, $p < 0.01$) at day 7. Wall area in the flow reversed region was also significantly increased at day 7 when compared to the non-reversed region ($47.9 \pm 5.8\%$, $p < 0.05$). These significant increases in luminal diameter and wall area in flow-reversed regions were maintained up to 12 weeks after FAL ([Figure 4.2D-E](#)).

4.5.3 FAL does not elicit regional differences in hypoxia in gracilis adductor muscles.

We next examined whether hypoxia in the gracilis adductor muscle could be contributing to the observed spatial differences in arteriogenesis between the flow reversed and non-reversed regions. Twenty-four hours post-FAL, we observed no regional differences in gracilis muscle hypoxia as determined by pimonidazole-HCl immunolabeling ([Supplemental Figure 4.2A-C](#)). Other indicators of tissue hypoxia, namely muscle fiber atrophy ([Supplemental Figure 4.2E](#)) and angiogenesis ([Supplemental Figure 4.2F](#)), were also found to be unchanged in the flow-reversed saphenous region when compared to both non-reversed muscular branch regions and unligated controls.

4.5.4 Amplified arteriogenesis in flow-reversed segments occurs independent of position.

To determine if enhanced arteriogenesis in response to reversed flow can occur in other collateral regions, we employed a muscular branch ligation (MBL) scheme that creates reversed flow in the muscular branch collateral region, instead of in the saphenous region ([Supplemental Figure 4.3A](#)). Reversed flow direction was confirmed via reorientation of the perinuclear position of the Golgi apparatus toward the saphenous entrance region ([Supplemental Figure 4.3B-C](#)). Flow-reversed collateral segments in the muscular branch region exhibited significant luminal growth when compared to non-reversed segments in the saphenous region at 14 days post-MBL ($36.2 \pm 4.9\%$ vs. non-reversed, $p < 0.01$) ([Supplemental Figure 4.3D-E](#)).

4.5.5 HUVECs exhibit directional responsiveness to simulated femoral artery ligation.

To investigate the influence of FAL-elicited hemodynamic changes on EC signaling, HUVECS were exposed to biomimetic changes in relative shear stress magnitude and/or direction, as previously by determined by transillumination LSF¹⁷⁶ (**Figure 4.3A**). A value of 15 dynes/cm² shear stress was chosen as a baseline shear stress¹⁹⁰. Preconditioning for 24 hours at this baseline shear stress was used to establish endothelial cell alignment and PCP, thereby mimicking the in-vivo baseline state. FAL was then simulated by a step-wise 100% increase in shear stress, in either the same direction or in the opposite direction, to mimic shear stress changes occurring in the muscular branch (non-reversed) and saphenous artery (reversed) entrance regions, respectively (**Figure 4.3A**). Consistent with in-vivo observations, HUVECs aligned with the flow direction and showed an upstream polarization of the GA with respect to the nucleus in control plates maintained at 15 dynes/cm². Upstream polarization was maintained (at 2 hours) or enhanced (at 6 hours) with a non-reversed, step-wise increase in shear stress (**Supplemental Figure 4.4**). However, when shear direction was reversed, endothelial cells transitioned from the PCP induced by preconditioning toward the new upstream direction within 6 hours (**Supplemental Figure 4.4**). Using HUVECS, we confirmed that GA perinuclear position matches well with MTOC perinuclear position (**Supplemental Figure 4.4**). These data demonstrate sensitivity to directional change in shear stress in HUVECs similar to that seen in-vivo, with complete re-orientation of PCP toward the new upstream direction within 6 hours after simulated FAL.

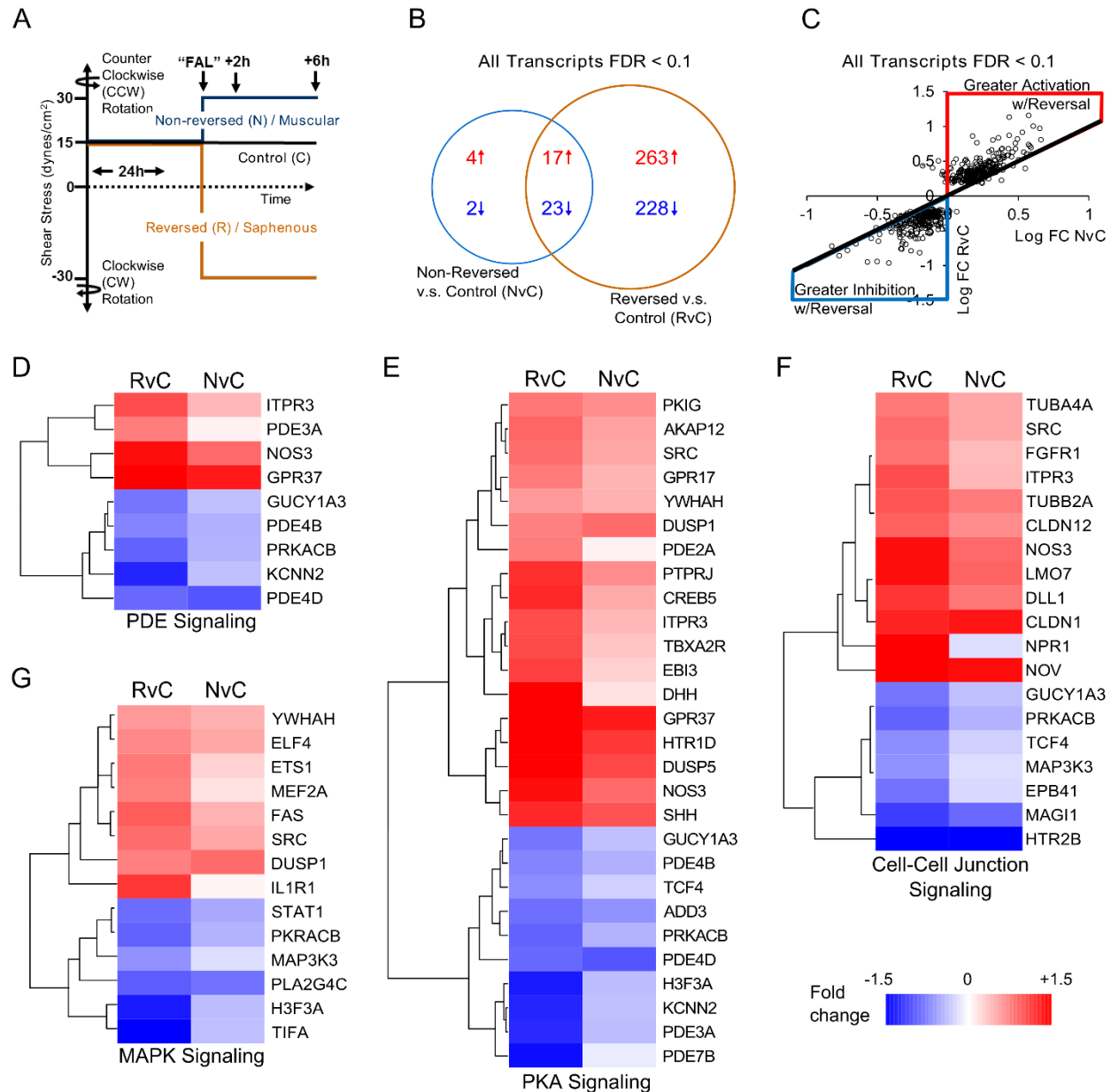


Figure 4.3. Genome-wide analysis indicates that reversed flow broadly enhances the arteriogenic transcriptional profile.

A) Schematic depicting shear stress conditions applied to HUVECs to simulate reversed (saphenous) and non-reversed (muscular) regions. HUVECs were preconditioned for 24 hours at 15 dynes/cm². Shear stress was then increased (or kept constant in the Control group) to 30 dynes/cm² in the same or opposite direction. **B)** Venn diagram of Affymetrix ST 1.0 human cDNA array data (n=4) comparing significantly altered transcripts (FDR<0.1) in non-reversed vs. control (NvC) conditions to those significantly altered with reversed direction vs. control (RvC). Red text and arrows=upregulated; Blue text and arrows=downregulated. **C)** Scatterplot showing gene expression changes between RvC and NvC conditions, red region=greater up-regulation in RvC; blue region=greater down-regulation in RvC; black line=equal RvC and NvC. **D-G)** Heatmaps grouped along significantly altered canonical pathways (cell-cell junctional signaling, protein kinase A signaling, MAP kinase signaling, and phosphodiesterase signaling) activated in both RvC and NvC conditions. Similar patterns of activation were observed between the conditions, but to a greater degree in the reversed flow condition.

4.5.6 Reversed flow broadly enhances the arteriogenic transcriptional profile.

To then comprehensively determine how a change shear stress magnitude, coupled with a change in flow direction, activates pro-arteriogenic endothelial cell mechanosignaling pathways, we performed genome-wide, microarray transcriptional analysis on HUVECs exposed to the simulated femoral arterial ligation (FAL) shear stress protocol ([Figure 4.3A](#)). The 6 hour post-FAL time-point was chosen because PCP reorientation is complete and robust transcriptional changes in response to a stepwise shear stress increase have been previously reported¹⁹¹. Using a false discovery rate (FDR) for significance of <0.10 obtained through the Robust Multiarray Average (RMA) algorithm, HUVECs exposed to reversed flow showed an ~10-fold greater number of transcripts (reversed versus control, RvC, [Supplemental Table 4.4](#)) compared to HUVECs exposed to increased shear stress magnitude only (non-reversed versus control, NvC, [Supplemental Table 4.5](#)) ([Figure 4.3B](#)). While reversed flow induced significant changes in more transcripts, the genes altered by a shear stress increase alone (NvC) demonstrated a similar expression pattern as those also exposed to reversed shear stress direction (RvC). When the expression of the 537 genes with $FDR < 0.1$ (in NvC and/or RvC comparisons) was compared in both NvC and RvC groups, 97.4% were altered in the same expression direction; i.e. genes that were up-regulated in reversed conditions were also up-regulated in non-reversed conditions and vice versa ([Figure 4.3C](#)). Interestingly, within this overlap, 93.9% of genes were altered to a greater degree in the reversed condition than in the non-reversed condition ([Figure 4.3C](#)). Of the 2.6% of genes exhibiting regulation in opposing directions between reversed and non-reversed conditions, all had a fold change <0.1 and an $FDR > 0.88$ in the non-reversed group. With the changes of expression occurring in similar directions from the control state, there were no significant differences between reversed and non-reversed expression levels with an $FDR < 0.20$. An *a priori* selection of 7 genes was used to validate the microarray results through real-time quantitative PCR ([Table 4.1](#)). All genes showed similar expression patterns and significance between microarray and RT-PCR measurements. However, the increased sensitivity of RT-PCR

yielded significant differences between reversed and non-reversed conditions for ICAM-1, eNOS, and KLF2, all of which are known to play key roles in arteriogenesis^{56,180,192} and are established as being sensitive to arterial levels of shear stress^{52,55,187,193–201}.

Table 4.1. Comparison of microarray genes to RT-PCR analyses for selected genes known to mediate arteriogenesis

Entrez Symbol	Gene Name	Comparison	RT-PCR		Microarray			
			Log ₂ Change	Fold	Log ₂ Change	Fold	p-value	FDR
NOS3	nitric oxide synthase 3 (endothelial cell)	RvC	1.17 ± 0.49 *†		0.47 ± 0.13		2.03 e-5	0.011
		NvC	0.30 ± 0.44		0.29 ± 0.13		1.09 e-3	0.207
ICAM1	intercellular adhesion molecule 1	RvC	0.92 ± 0.25 *†		0.15 ± 0.12		0.031	0.331
		NvC	0.49 ± 0.44		0.10 ± 0.12		0.114	0.640
VCAM1	vascular cell adhesion molecule 1	RvC	0.23 ± 0.78		-0.22 ± 0.29		0.161	0.641
		NvC	-0.67 ± 0.43 *		-0.66 ± 0.29		9.86 e-4	0.203
KLF2	Kruppel-like factor 2 (lung)	RvC	0.84 ± 0.31 *†		0.33 ± 0.11		1.30 e-4	0.025
		NvC	0.43 ± 0.25 *		0.26 ± 0.11		7.47 e-4	0.176
KLF4	Kruppel-like factor 4 (gut)	RvC	0.95 ± 0.35 *		0.47 ± 0.13		1.86 e-5	0.010
		NvC	0.53 ± 0.33 *		0.26 ± 0.13		2.06 e-3	0.261
SELE	selectin E	RvC	-0.86 ± 0.63 *		-0.86 ± 0.32		2.57 e-4	0.032
		NvC	-0.94 ± 0.51 *		-0.77 ± 0.32		6.35 e-4	0.157
CCL2	chemokine (C-C motif) ligand 2	RvC	-0.69 ± 0.37 *		-0.19 ± 0.11		5.53 e-3	0.153
		NvC	-0.38 ± 0.32 *		-0.08 ± 0.11		0.168	0.706

Data represents RT-PCR (n=8/group) and microarray analysis (n=4/group). RvC, reversed versus control. NvC non-reversed versus control. *, indicates p<0.05 significance versus control RT-PCR, †, indicates significance p<0.05 of reversed v non-reversed by RT-PCR expression levels. Uncertainty in PCR is mean +/- standard deviation for microarray mean +/- 95% confidence

Initial assessment of activated molecular functions was conducted through gene ontology analysis¹⁸⁹ to assess over-representation of molecular pathways. The 500 most significantly regulated genes based on p-value ranking for increased shear stress, with and without reversed flow, as compared to control were used to investigate the broad functional processes involved in both conditions ([Supplemental Table 4.1](#)). Oxidoreductase activity was the only significantly enriched molecular function in the case of the non-reversed increased shear stress ([Supplemental Figure 4.5A](#)). However, with the addition of a change in shear stress direction, there was activation of multiple molecular functions including: reelin receptor activity, RNA pol II

promoter transcription factors, cAMP phosphodiesterase activity, and GTPase regulation ([Supplemental Figure 4.5B](#), [Supplemental Table 4.1](#)).

4.5.7 NFκB as a predicted upstream regulator of gene expression patterns in flow-reversed conditions

Additional function annotation, clustering, and analysis of predicted upstream regulators were performed with the Ingenuity Pathways Analysis software. Analysis of predicted upstream transcriptional regulators for all genes with FDR<0.1 identified many of the known signaling pathways involved in arteriogenesis including activation of the NFκB pathway^{202–204} ([Table 4.2](#)) as well as growth factors [e.g. VEGF^{205,206}, HGF^{207,208}, TGFβ⁷¹, FGF2^{209,210}], MAPK signaling^{49,211,212}, and PI3K signaling²¹³ ([Supplemental Table 4.2](#)). Across all of these signaling pathways and upstream regulators, a clear activation was only apparent under the reversed flow condition.

Further clustering of expression changes of all genes with FDR<0.1 along canonical pathways showed activation of several key pathways known to be involved in arteriogenesis, including cGMP signaling^{180,214}, protein kinase A signaling^{215,216}, MAPK signaling^{49,211,212}, and cell-cell junction signaling^{50,51} ([Figure 4.3D-G](#), [Supplemental Table 4.3](#)). HUVECs exposed to a reversed flow showed much stronger activation of these canonical pathways versus those exposed to non-reversed conditions ([Supplemental Table 4.3](#)).

Table 4.2. NFκB is a predicted upstream regulator of gene expression patterns in HUVECs exposed to flow reversed conditions

<i>Upstream Regulator</i>	<i>Reversed v Control</i>		<i>Non-reversed v Control</i>	
	<i>Activation Z-Score</i>	<i>p-value overlap</i>	<i>Activation Z-Score</i>	<i>p-value overlap</i>
I. NFκB Pathway				
phorbol myristate acetate (activator PKC and NFκB)	2.767	1.35E-03		
NFKBIA	2.273	2.56E-02		4.95E-02
RELA	1.85	1.54E-02		
NFκB (complex)	1.47	3.99E-03		
IKBKB	1.272	6.94E-06		1.22E-02
All matching upstream regulators fitting into the defined groups with activation z-score >1.0				

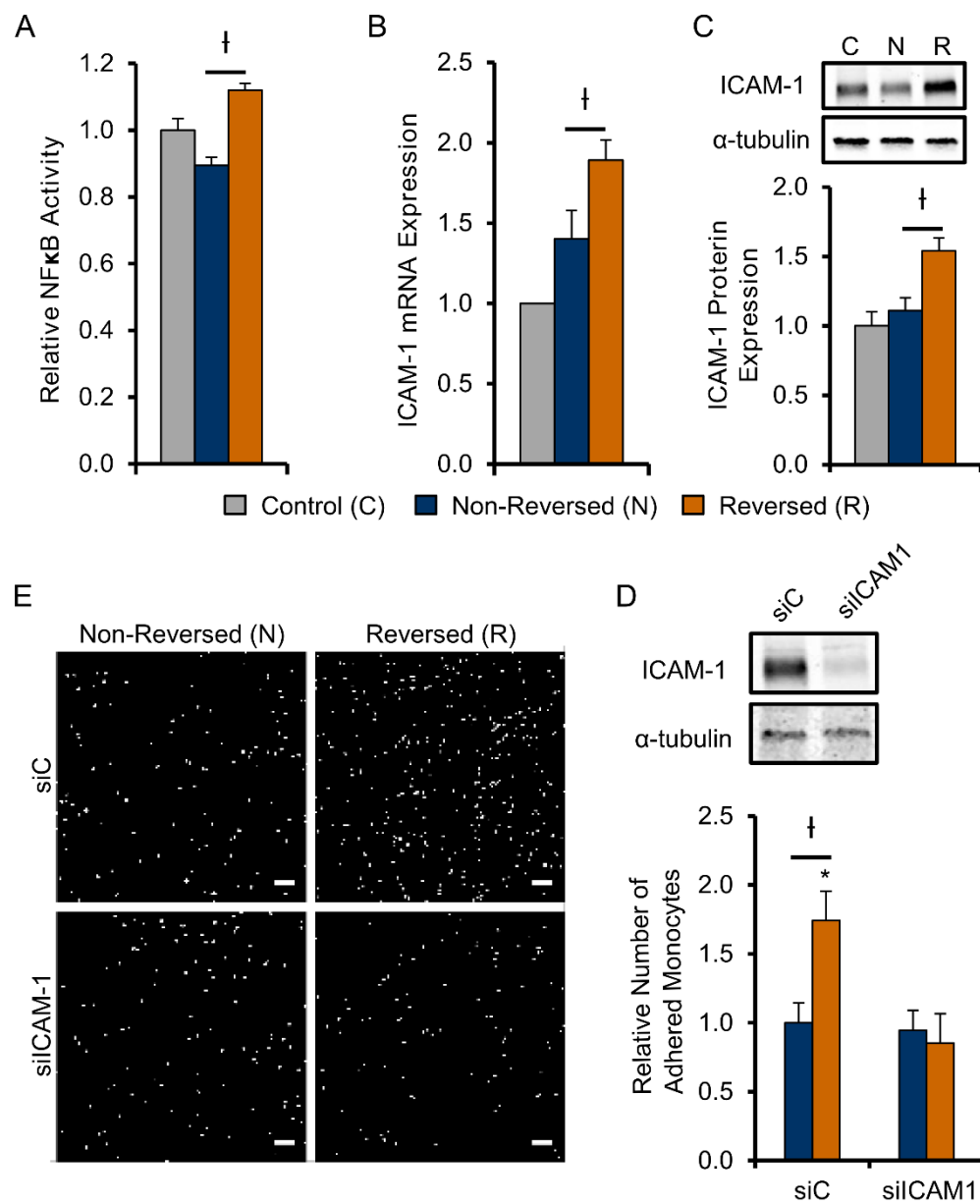


Figure 4.4. Reversed flow enhances monocyte adhesion in-vitro in an ICAM-1 dependent manner. **A)** NFκB activity (n=3) relative to control (C, gray) in HUVECs exposed to reversed (R, orange) and non-reversed (N, blue) shear conditions 1 hour after simulated FAL in-vitro ([Figure 4.3A](#)). **B, C)** ICAM-1 mRNA expression by RT-PCR (n=8) and protein expression (n=4) in HUVECs relative to control 6 hours after simulated FAL. **D)** Bar graph quantifying relative number of adhered monocytes in each condition **E)** Representative FOVs of THP-1 monocytes adhered to HUVECs exposed to reversed and non-reversed conditions transfected with either ICAM-1 siRNA (siICAM-1) or non-targeting control (siC) (Scale bar=100μm). †p<0.05 between reversed (R) and non-reversed (N); *p<0.05 between siC and siICAM-1 for given flow condition. Data are mean ± SEM.

4.5.8 Amplified arteriogenesis in flow-reversed collaterals depends on ICAM-1.

One pathway of particular interest from our Ingenuity Pathway Analysis of upstream regulators (Table 4.2) was the NFκB-ICAM-1 pathway. NFκB is a mechanosensitive transcription factor that regulates arteriogenesis^{204,217} through ICAM-1^{55,218} dependent monocyte/macrophage recruitment⁵⁶. To further investigate the NFκB- ICAM-1 pathway, we confirmed increased NFκB activity in HUVECs 1 hour after exposure to our in vitro simulated FAL, using a luciferase reporter assay (Figure 4.4A). Moreover, ICAM-1 mRNA expression was already shown to be increased (35%) under reversed flow conditions as determined from our *a priori* RT-PCR screen of known pro-arteriogenic genes (Table 4.1, Figure 4.4B). Western blotting confirmed its up-regulation (38.5%) at the protein level 6 hours after (Figure 4.4C). Additionally, reversed flow led to increased pro-arteriogenic function in-vitro as determined by increased monocyte adhesion to flow-conditioned HUVECs (Figure 4.4D-F). Furthermore, using a siRNA knockdown of ICAM-1, this increase in monocyte adhesion was determined to be ICAM-1 dependent (Figure 4.4D-F). We also determined there was over a 2-fold increase in pericollateral Mac3⁺ macrophages 3 days post-FAL in collateral segments of C57BL/6 mice that experienced reversed flow (6.53 ± 1.00 and 3.12 ± 0.47 cells in reversed and non-reversed pericollateral regions, respectively), as seen in (Figure 4.5A-B). This increase in pericollateral macrophage density was attenuated in flow-reversed segments of ICAM-1^{-/-} mice as there was no significant difference in reversed vs. non-reversed collateral segments (2.33 ± 0.44 and 1.67 ± 0.31 cells in reversed and non-reversed pericollateral regions, respectively, $p=0.34$) (Figure 4.5A-B).

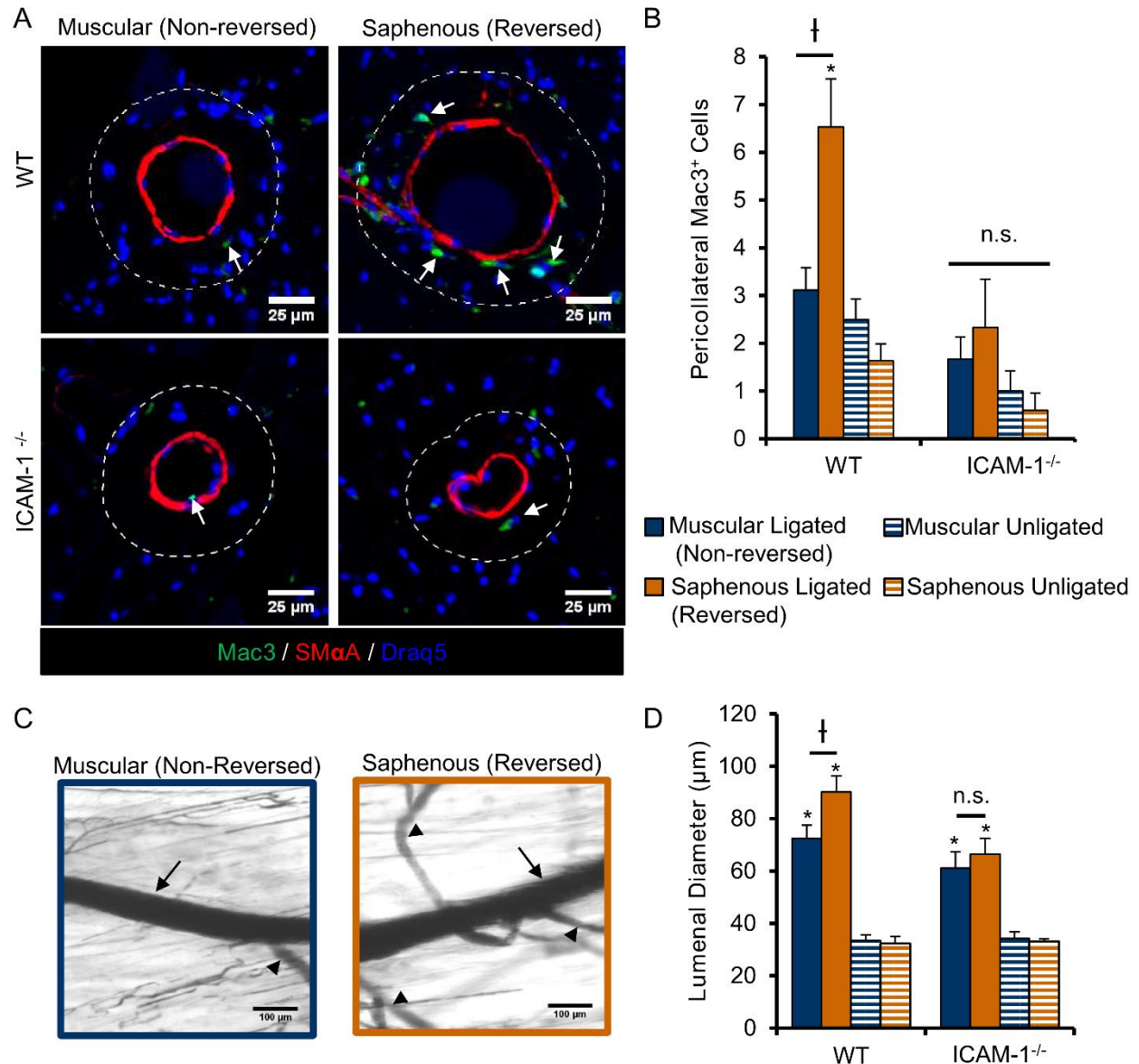


Figure 4.5. ICAM-1 is necessary for enhanced macrophage recruitment and amplified arteriogenesis in collateral segments exposed to a reversed flow.

A) Representative cross-sections of gracilis collateral artery regions in WT C57BL/6 and ICAM-1^{-/-} mice 3 days post-FAL immunolabeled for macrophage marker, Mac3 (green) and smooth muscle alpha actin (red). Dotted line indicates pericollateral region (25μm from vessel wall) used for quantification. Arrows indicate Mac3⁺ cells. (Scale bar=50μm) **B)** Bar graph of pericollateral Mac3⁺ cells. (n=4-5). **C)** Representative vascular cast images from ICAM-1^{-/-} mice 14 days post-FAL from both muscular and saphenous regions. (Scale bar=100μm). Arrows indicate the measured collateral artery while arrowheads indicate transverse arterioles. **D)** Bar graph of regional luminal diameter for both WT and ICAM-1^{-/-} mice (n=6). *p<0.05 between ligated and unligated within the given region; †p<0.05 between regions (saphenous versus muscular) within the given treatment (ligated or unligated). Data are mean ± SEM.

Based on these findings, we next tested whether ICAM-1 was necessary for amplified arteriogenesis in flow-reversed collateral segments in-vivo by applying FAL to ICAM-1^{-/-} mice. There were no significant differences between ICAM-1 null mice and WT in diameters of collateral segments in unligated limbs. The muscular, non-reversed collateral segments in ICAM-1^{-/-} mice were not significantly different than those in WT mice ($p=0.11$). However, deletion of ICAM-1 reduced the amplified collateral growth that occurs in collateral segments of WT mice exposed to a reversed flow ($p=0.017$). Importantly, in these ICAM-1^{-/-} mice, we also observed no significant differences in diameter between reversed and non-reversed collateral segments at 14 days post-FAL (66.5 ± 5.95 and 61.2 ± 6.05 respectively, $p=0.48$). Therefore the amplified arteriogenesis that occurs in flow reversed segments of WT mice (1.24 ± 0.12 fold-change, reversed vs. non-reversed) is attenuated in ICAM-1 null mice (1.08 ± 0.14 fold-change, reversed vs. non-reversed), demonstrating that ICAM-1 is necessary for the amplified response in segments exposed to reversed flow direction (**Figure 4.5C-D**).

Our transcriptional profiling data and *a priori* RT-PCR screen also suggested a potential role for the KLF2/eNOS pathway. We first determined that KLF2 and eNOS mRNA expression were enhanced by 33% and 83%, respectively, in HUVECs exposed to FAL-simulated reversed flow (**Supplemental Figure 4.6A-B**). Phosphorylated (S1177) eNOS protein expression was also increased under reversed flow conditions (**Supplemental Figure 4.6C**). To then test whether eNOS was required for amplified arteriogenesis in flow-reversed collateral segments in-vivo, we applied FAL to eNOS^{-/-} mice. When all regional measurements of collateral growth are binned together, we observe a 17% decrease in arteriogenesis in eNOS^{-/-} mice compared to wild-type (eNOS^{-/-} $67.67\pm3.38\mu\text{m}$; C57BL/6: $81.37\pm4.54\mu\text{m}$; $p<0.05$) (**Supplemental Figure 4.6E**). If each collateral region is analyzed separately, luminal diameter in non-reversed, muscular collateral artery segments was significantly reduced in eNOS^{-/-} mice compared to wild-type mice (eNOS^{-/-} $52.4\pm4.1\mu\text{m}$; C57BL/6: $72.5\pm5.0\mu\text{m}$, $p<0.05$), but not in the flow reversed, saphenous segments (eNOS^{-/-} $82.6\pm3.6\mu\text{m}$; C57BL/6: $90.2\pm6.2\mu\text{m}$, $p = 0.463$) (**Supplemental Figure 4.6F**). However,

when each region was normalized to its respective unligated control, amplified luminal growth in flow reversed segments was maintained in eNOS^{-/-} mice, indicating that this enhanced remodeling response is independent of eNOS ([Supplemental Figure 4.6G](#)).

4.6 Discussion

We report here a comprehensive, genome-wide, and direct mapping of mechanotransductive endothelial cell signaling pathway activation to a uniquely amplified and sustained in-vivo arteriogenesis response. We first used endothelial cell planar polarization as a marker to confirm endothelial cell responsiveness to the change in flow direction in the gracilis adductor collateral arteries following femoral arterial ligation ([Figure 4.1](#)). We then determined that collateral artery segments that are exposed to both an increase in shear stress magnitude and a reversed flow direction exhibit markedly amplified arteriogenesis when compared to collateral artery segments exposed to increased shear stress magnitude alone ([Figure 4.2](#)). Genome-wide transcriptional profiling of HUVECs exposed to a biomimetic “reversed-flow + increased shear stress magnitude” waveform yielded a ~10-fold increase in significantly regulated transcripts when compared to HUVECs exposed to increased shear-stress alone. Indeed, this stimulus acts as a broad amplifier of transcriptional activation ([Figure 4.3](#)), including a set of potent arteriogenesis regulators (eNOS, ICAM-1, and KLF-2) that were then confirmed by RT-PCR ([Table 4.1](#)). Further, Ingenuity Pathways Analysis indicated activation of a number of important canonical arteriogenesis pathways and upstream regulators, notably NFκB ([Table 4.2](#)). After confirming that the NFκB-ICAM-1 pathway was activated in HUVECs exposed to reversed flow, we showed the increased monocyte adhesion to HUVECs exposed to reversed flow was abrogated by knockdown of ICAM-1 ([Figure 4.4](#)). Finally, we demonstrated that enhanced pericollateral Mac3⁺ macrophage density and amplified arteriogenesis in flow-reversed collateral segments of WT mice was attenuated in ICAM-1^{-/-} mice, indicating that this amplified arteriogenic response is ICAM-1 dependent ([Figure 4.5](#)).

4.6.1 Reversed flow as an independent stimulus leading to amplified arteriogenesis.

Our ability to link amplified arteriogenesis to a unique hemodynamic stimulus (i.e. reversed flow with increase shear stress magnitude) was facilitated by the development of a laser speckle flowmetry approach for mouse hindlimb collaterals¹⁷⁶. We developed that approach because, despite the known importance of hemodynamic stimuli in driving collateral development, there was a surprising lack of quantitative data on the hemodynamic changes within these arteries. This is likely due to both the small size of the arteries (<100 μm) and the fact that different surgical models elicit arteriogenesis along different collateral pathways³⁶. Using laser speckle flowmetry¹⁷⁶, we determined the occurrence of at least three distinct hemodynamic conditions in these collateral vessels: a non-reversed increase in shear stress near the feeding entrance to the collateral loop, an increase in shear stress from low/oscillating flow to sustained high shear stress at the central anastomotic region, and an increase in shear stress but in a reversed direction at the downstream outlet back into the occluded arterial tree. In this study, we only considered the two entrance regions because they experience the same step increase in relative shear stress magnitude after FAL, thereby permitting isolation of the influence of reversed flow.

Nonetheless, we also had to consider that hypoxia in flow reversed regions could be contributing to amplified arteriogenesis. Indeed, previous studies using saphenous artery excision models that elicit severe ischemia have suggested a role for hypoxia and metabolic signaling in the arteriogenic response^{219,220} and observed spatial differences in capillary density in the adductor muscles as a marker of ischemic response²²¹. Thus, we examined the potential role of hypoxia in eliciting spatial differences in arteriogenesis between the flow reversed and non-reversed regions. In our study, pimonidazole-HCl immunolabeling revealed no signs of regional differences in hypoxia at 24 hours post-FAL ([Supplemental Figure 4.2A-C](#)). Consistent with previous findings for the gracilis muscle using a similar, milder (i.e. far less ischemic) FAL

scheme¹⁶⁸, there was no evidence of angiogenesis in either the muscular branch or saphenous artery regions ([Supplemental Figure 4.2F](#)). As another indirect measure of tissue ischemia, muscle fiber size in the gracilis muscle showed no evidence of atrophy in either the muscular branch or saphenous artery regions ([Supplemental Figure 4.2E](#)). Thus, our results are consistent with previous studies using similar hindlimb models in which arteriogenesis proceeds independent of a hypoxic stimulus^{168,222,223}.

Additionally, to determine if reversed flow can elicit amplified arteriogenesis independent of longitudinal position along a given collateral, we employed the MBL model to induce reversed flow in the muscular branch entrance region, instead of in the saphenous region ([Supplemental Figure 4.3](#)). With this ligation scheme, we observed both endothelial cell repolarization and amplified arteriogenesis in the muscular branch region of the collaterals, thereby establishing that this amplified arteriogenesis response is indeed not unique to the saphenous collateral region. In all, we conclude that reversed flow is a novel, independent stimulus for arteriogenesis.

4.6.2 Endothelial cell sensing of shear stress magnitude and reversed direction.

One motivation for the current study is that the endothelial response to increased shear stress from a pre-conditioned baseline state is not well-studied. In perhaps the most closely related study, a nearly 20x reduction in the number of genes that are sensitive to a step-wise increase in shear stress from a pre-conditioned baseline was observed when compared to a step change from static conditions (i.e. 86 versus 1838)¹⁹¹. Our data matches this previous study well, as only 48 genes were significantly altered (FDR<0.1) at 6 hours after a non-reversed 100% step increase in shear stress. This implies that gene expression changes induced by the application of laminar shear stress from static culture are not wholly predictive of gene expression changes occurring in the more physiological scenario of a step increase in shear stress from a non-zero baseline¹⁹¹.

Studies incorporating non-reciprocating directional flow changes indicate that shear stress reversal from baseline has a disproportionate impact on responses such as permeability²²⁴, which is a hallmark in the initiation of arteriogenesis³⁷, and intracellular calcium²²⁵. Because preconditioned, flow-adapted endothelial cells align with flow direction and incline their cell-cell junctions to reduced tension, they experience a dramatic increase in cell to cell tension when faced with a sudden reversed flow. This leads to a disproportionate response in endothelial cell signaling²²⁵. Interestingly, a step change in shear stress magnitude from a preconditioned level of 15 dyne/cm² to a very low level of 2.5 dynes/cm² with reversed flow direction elicits a disproportionately larger transcriptional response (of a similar pattern) than a step increase in shear stress (+10 dynes/cm²) in the same direction²²⁶. Our data demonstrate that adding reversed flow to a 2x increase in shear stress magnitude elicits a 10-fold increase in transcriptional activation. Moreover, in addition to broadly modulating the endothelial shear stress response, a change in flow direction relative to an endothelial cell's morphological and cytoskeletal axes can stimulate activation of distinct pathways²²⁷. Together, these data suggest that EC responsiveness to altered shear stress is highly dependent on initial conditions. For the specific case of shear signaling for arteriogenesis, consideration of the initial hemodynamic conditions across a given collateral network is especially significant.

4.6.3 Endothelial cell repolarization and signaling for amplified arteriogenesis.

In this study, endothelial cell planar polarization was used simply as a marker of endothelial cell responsiveness to a change in flow direction. To date there has been no direct functional link between endothelial planar (re)polarization and arteriogenesis; however our results offer an opportunity to explore this linkage. Indeed many molecular pathways that are activated by reversed flow in our study, such as small GTPase signaling ([Supplemental Figure 4.5](#)) and ICAM-1 ([Figure 4.4](#)), regulate both planar cell polarization^{182,228–230} and arteriogenesis^{49,56,231}, raising the hypothesis that endothelial cell polarization may play a significant role in collateral

artery remodeling. However, the functional consequence(s) of endothelial cell repolarization remains to be determined and future work could investigate the mechanistic role(s) of endothelial planar polarization in arteriogenesis.

4.6.4 Complex role of eNOS signaling in arteriogenesis.

Our transcriptional profiling and qRT-PCR studies led us to hypothesize that ICAM-1 and eNOS are important regulators of amplified arteriogenesis in flow-reversed collaterals. Here, we demonstrated ICAM-1 is necessary for enhanced monocyte/macrophage recruitment and augmented arteriogenesis in flow-reversed collateral segments. Together, these results are consistent with the previously demonstrated vital role for ICAM-1 in arteriogenesis through its regulation of monocyte/macrophage recruitment⁵⁶.

While our ICAM-1^{-/-} studies show attenuation of this amplified arteriogenic response, our eNOS^{-/-} studies do not. The role of eNOS and/or NO in arteriogenesis is fairly well-studied, yet still difficult to interpret. While eNOS and NO regulate arteriogenesis in more severe excision hindlimb models^{232,233} and in training models²³⁴, no significant defects in arteriogenesis were reported for eNOS^{-/-} mice three weeks after induction of a less ischemic femoral ligation model²³⁵. For our data set, if luminal diameters at either end of the collateral are averaged, we observed a moderate decrease in arteriogenesis in eNOS^{-/-} mice compared to wild-type. Given that eNOS can affect the baseline network configuration and maintenance¹⁸⁰, we normalized the diameters of the ligated muscular branch and saphenous regions to their respective unligated controls (**Supplemental Figure 4.6G**). Using this analysis, we observe that the enhanced arteriogenesis caused by reversed flow is eNOS independent potentially due to the ability to compensate for the loss of eNOS with other NOS subtypes.

4.6.5 Implications for understanding shear stress set-point.

Finally, our results may have important implications for our understanding of the so-called homeostatic “set-point” for constant shear stress in the arterial circulation. In 1926, Murray put

forth his “principle of minimum work”, a consequence of which is that shear stress is maintained at a relatively constant level throughout the arterial vasculature⁸⁶. In support of this concept, there appears to be a homeostatic wall shear stress magnitude (i.e. set-point) at which endothelial cells become quiescent and vessels maintain a steady state luminal diameter²³⁶. Little is known, however, about how this set-point is achieved or maintained at the molecular signaling level. In our FAL model, if we assume Poiseuille flow, apply mass conservation, and consider that the luminal diameter at the distal end (i.e. saphenous region) of the collateral is 22% greater than the luminal diameter in the proximal end (i.e. muscular branch region) at 12 weeks post-FAL (Figure 4.2B), we estimate that the new steady-state shear stress in the saphenous region is reduced by at least 45% from pre-FAL levels. Thus, in essence, the reversed flow stimulus effectively resets the set-point for constant shear stress. We posit that further examination of this response could uncover molecular regulators of the shear stress set-point and/or provide clues for generating sustained therapeutic arteriogenic responses via set-point adjustment(s).

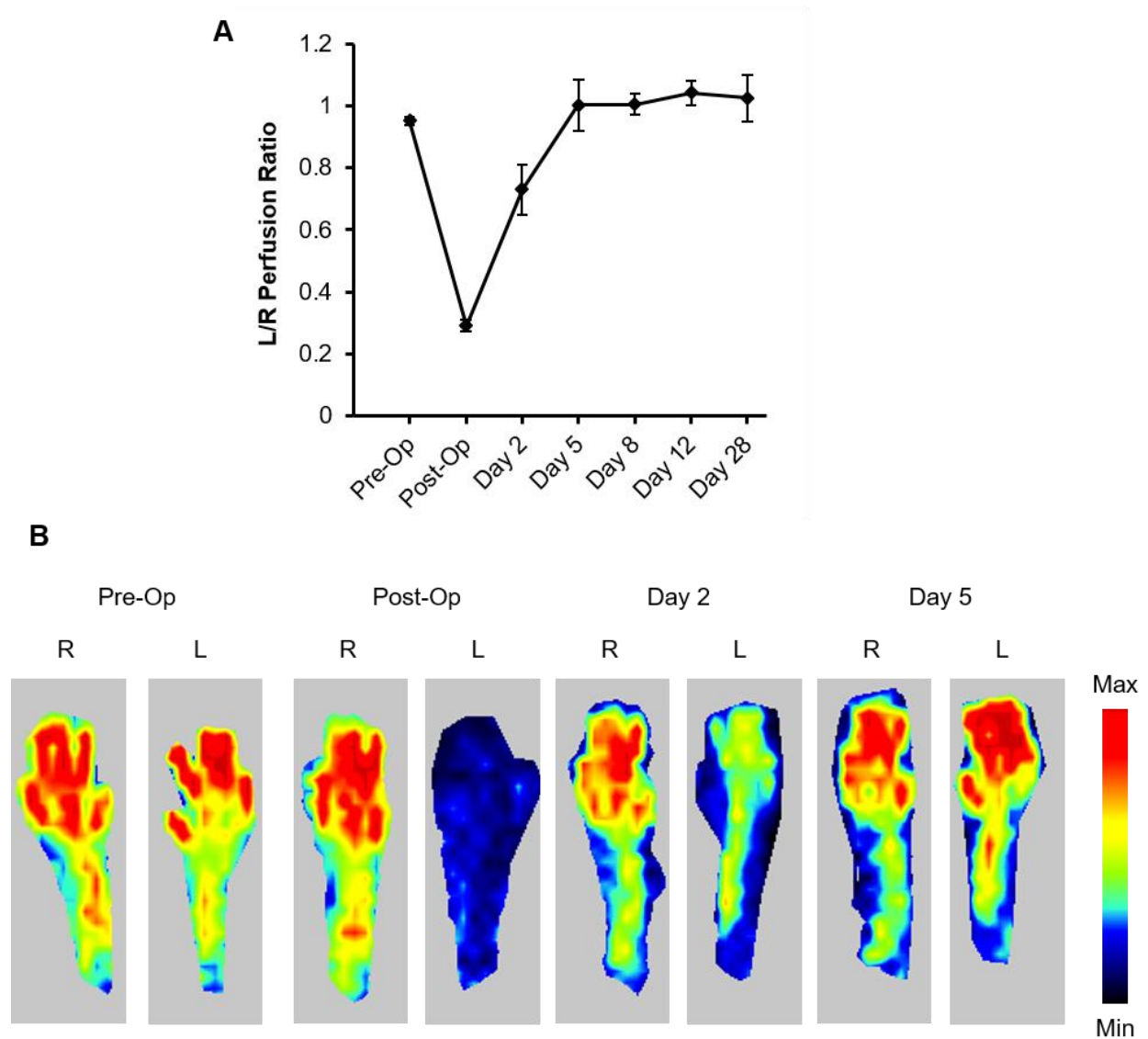
4.7 Acknowledgements

The authors would like to thank Dr. Stephen Turner (University of Virginia Bioinformatics Core) for help in processing and analysis of the microarray data and the University of Virginia Research Histology Core (under the direction of Sheri VanHoose) for histological tissue processing. The authors would also like to thank Dr. Brett Blackman for material support and guidance.

4.8 Sources of Funding

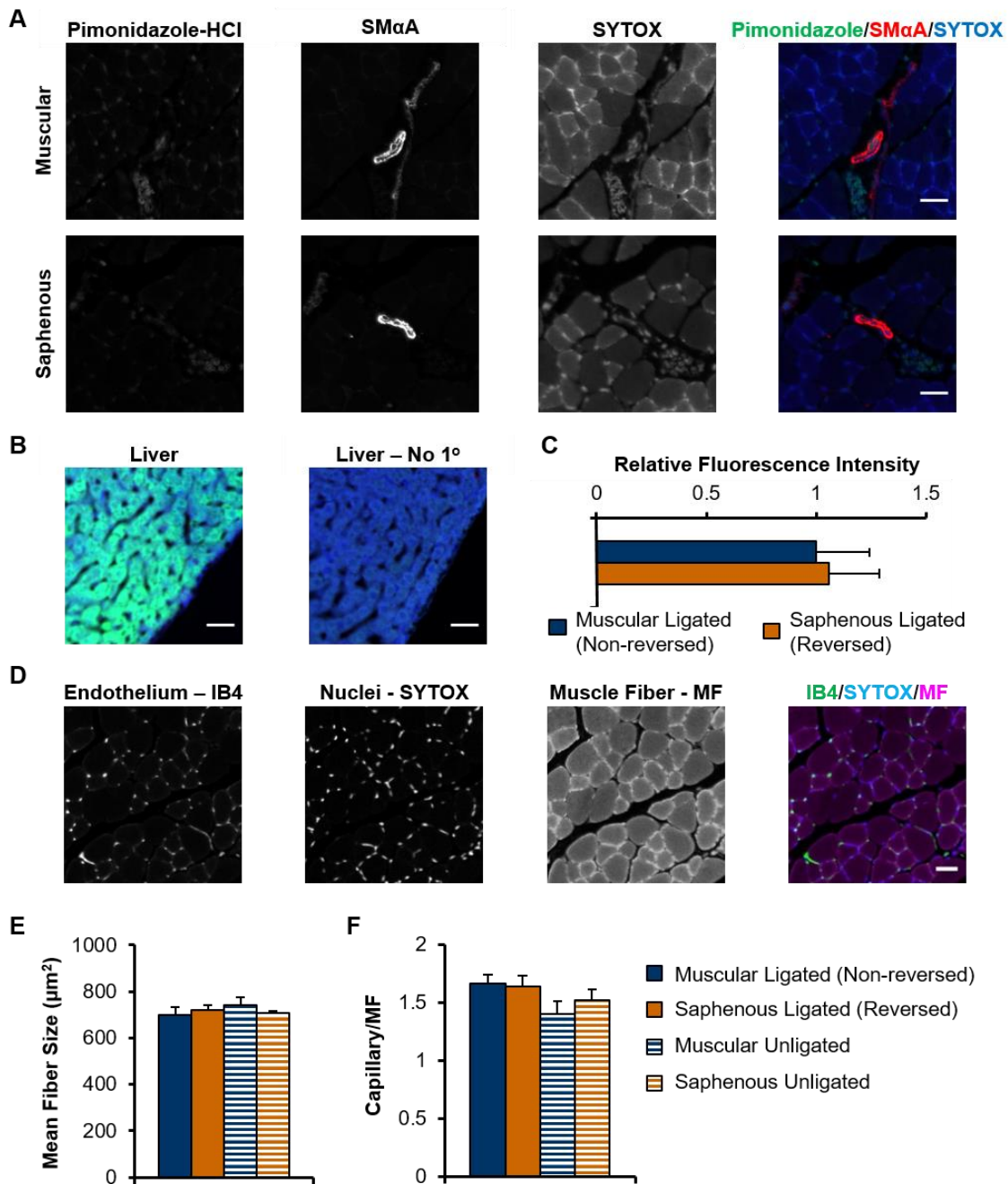
This material is based upon work supported by the National Science Foundation Graduate Research Fellowship Program under Grant No. NSF DGE-1315231 (JLH). Additional funding sources: American Heart Association awards 09PRE2060385 (JKM) and 10GRNT3490001 (RJP), and NIH grants T32-GM007267 (JKM), T32-HL007284 (JKM and JLH), R21-HL098632 (RJP).

4.9 Supplemental Figures



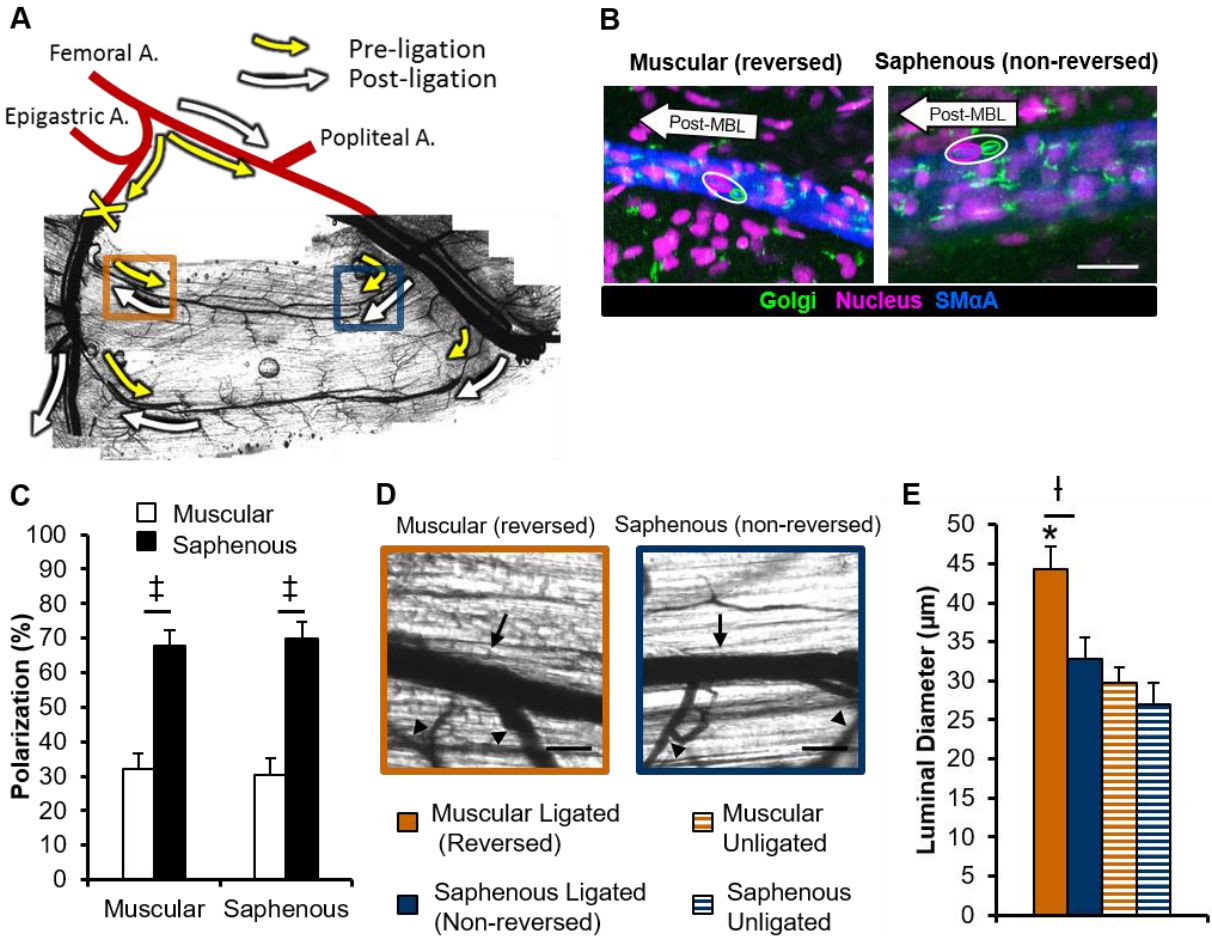
Supplemental Figure 4.1. Laser Doppler perfusion recovery curve.

A) Laser Doppler perfusion measurements show mild ischemia in distal hindlimb immediately post-FAL. Perfusion is restored by day 5 post-FAL ($n = 5$). Data are mean \pm SEM. **B)** Representative images of measured foot perfusion in the ligated (L) and unligated (R) legs. Data are mean \pm SEM.



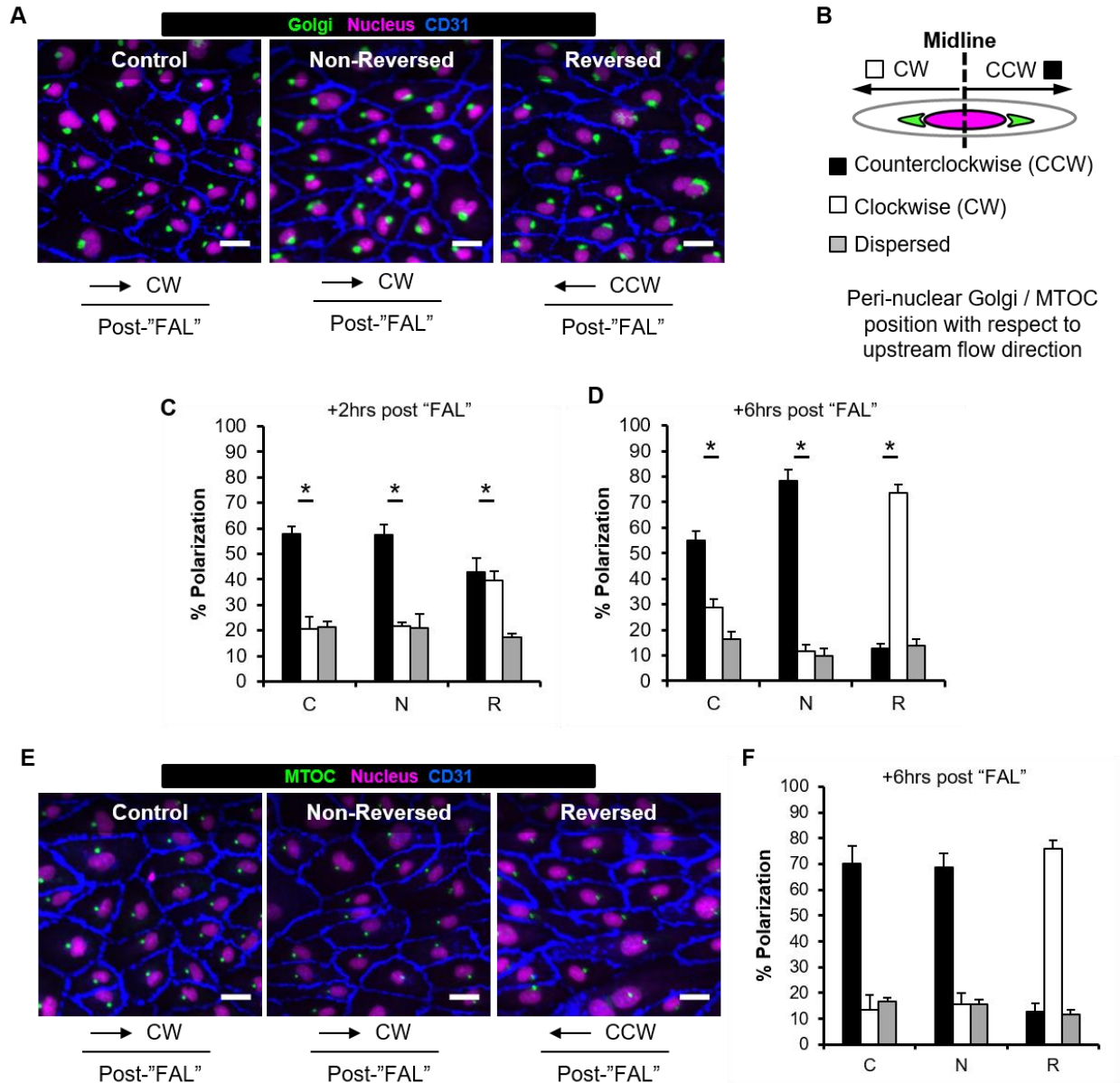
Supplemental Figure 4.2. Regional characterization of hypoxia, muscle fiber size, and capillary density in mouse gracilis muscle.

A) Representative paired fields of view of the gracilis muscles immunolabeled for pimonidazole-HCl to detect regions of hypoxia ($\text{pO}_2 < 10\text{mmHg}$) 24 hours post-FAL. Scale bars=25 μm . **B)** Liver cross-sections with and without primary anti-pimonidazole-HCl antibody were used as positive and negative immunolabeling controls. Scale bars=25 μm . **C)** Bar graph of relative fluorescence intensity 24 hours post-FAL indicates no significant differences in regional hypoxia ($n = 4$). **D)** Representative FOV of a gracilis muscle cross-section stained for capillaries (isolectin B4). Scale bar=25 μm . Tissue auto-fluorescence provided endogenous contrast for identifying individual muscle fibers. **E)** At 7 days post-FAL, there was no evidence of muscle atrophy or **F)** capillary to muscle fiber (MF) ratio to between ligated and unligated limbs in either region ($n = 8$). Data are mean \pm SEM.



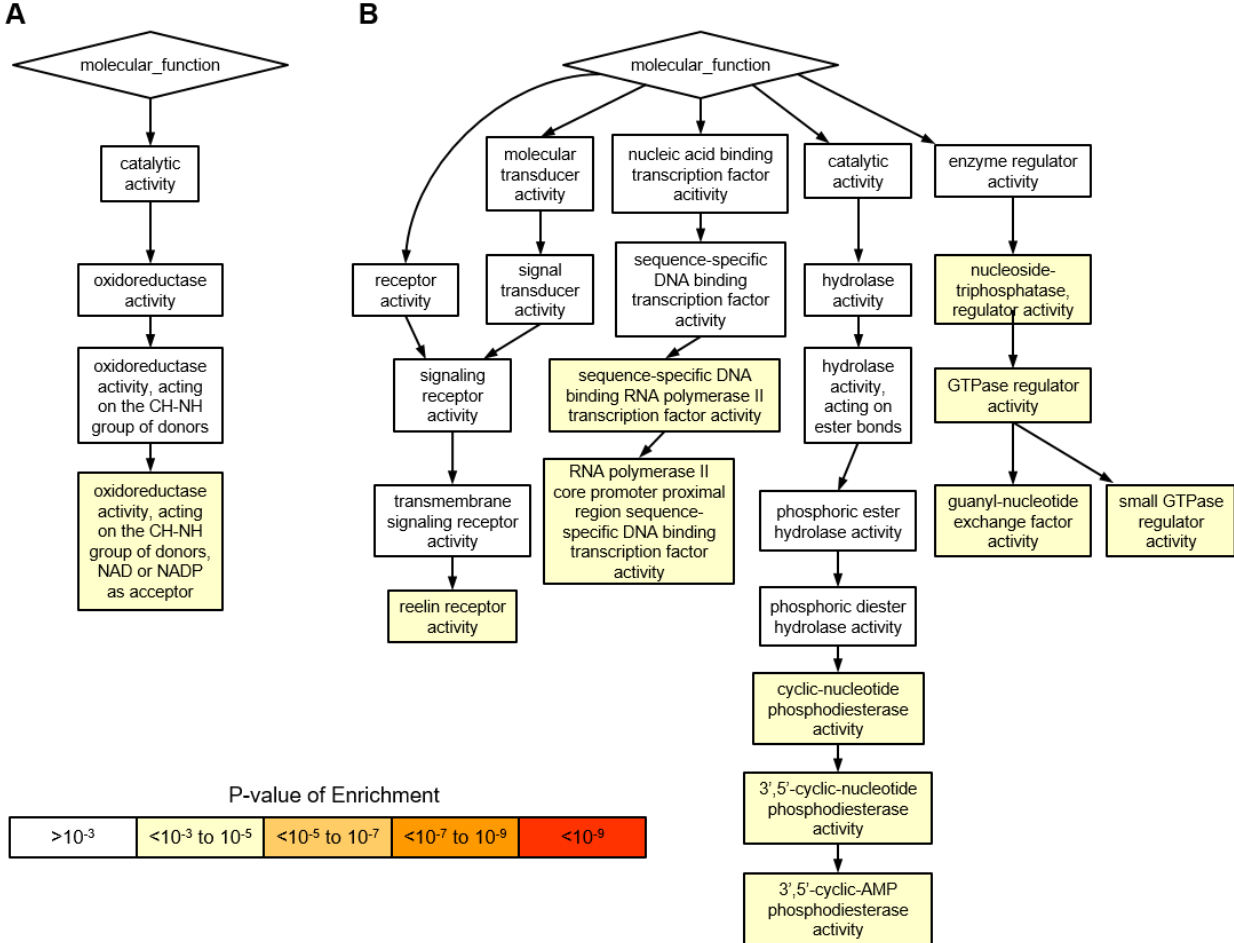
Supplemental Figure 4.3. Arteriogenesis in gracilis collateral artery segments exposed to a reversed flow after muscular branch ligation.

A) Schematic of the primary gracilis adductor collateral flow pathways after muscular branch ligation (MBL). The muscular branch feed artery is ligated just distal to the epigastric artery bifurcation thereby creating a change in flow direction at the muscular branch entrance region. The femoral and popliteal arteries are indicated for reference. Arrows indicate the direction and magnitude of blood flow both pre- (yellow) and post- (white) MBL. Boxes indicate location at which luminal diameters were measured (reversed muscular branch entrance region=orange; non-reversed saphenous entrance region=blue). **B)** Representative images of each collateral region immunolabeled for the Golgi apparatus to determine planar polarization. Images are oriented such that the muscular branch is toward the left and the saphenous artery is toward the right and arrows indicate blood flow direction post-FAL. (Scale bar = 25 μ m). **C)** Bar graph of EC planar polarization 24 hours post-MBL. ECs in all regions show upstream polarization toward the saphenous branch entrance region (n=3). **D)** Representative vascular cast images from remodeled gracilis collateral arteries 14 days post-MBL (Scale bar=50 μ m). Arrows indicate measured collateral artery while arrowheads indicate transverse arterioles. **E)** Bar graph of regional luminal diameter 14 days post-MBL (n=6). *p<0.05 between ligated and unligated within the given region; †p<0.05 between regions (saphenous versus muscular) within the given treatment (ligated or unligated). ‡p<0.05 between total upstream versus downstream polarization within the given flow condition. Data are mean \pm SEM.



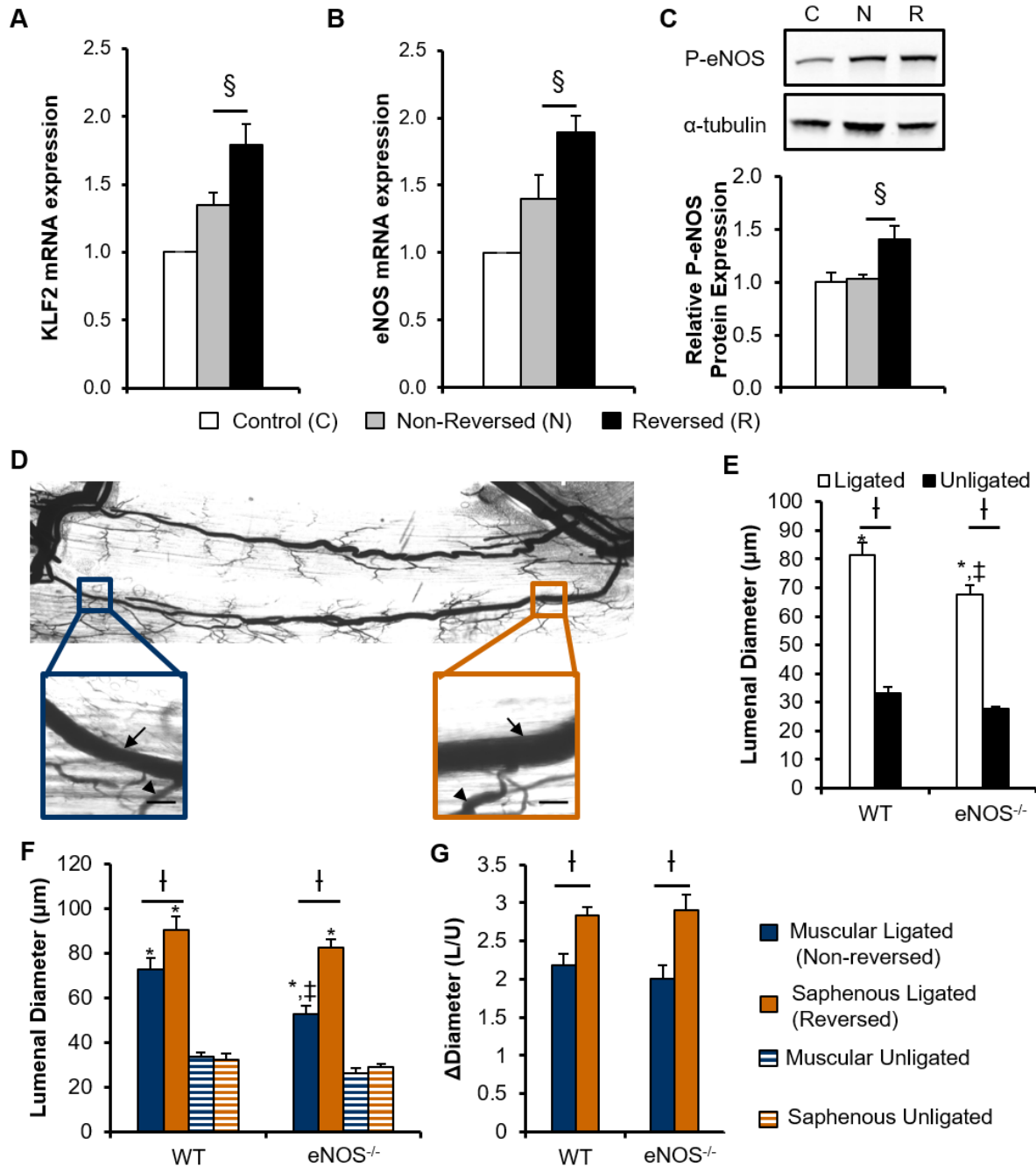
Supplemental Figure 4.4. HUVECs repolarize in response to directional change in shear stress induced by simulated FAL.

A) Representative images of HUVEC planar polarization assessed by the perinuclear position of the Golgi apparatus with respect to the pre-conditioning shear direction (see Fig 3A) at 6 hours after simulated FAL (Scale bar=25 μ m). Arrows indicate flow direction after simulated FAL (n=3). **B)** Diagram depicting the method used to quantify of polarization. Golgi apparatus (green) position with respect to the nucleus (magenta) was used to classify EC polarization as toward either the saphenous (black bars) or muscular branch (white bars) arteries. Golgi that were circum-nuclear and without preferential orientation were classified as dispersed **C)** Bar graph of HUVEC planar polarization at 2 hours after simulated FAL. (n=3). **D)** Bar graph of HUVEC planar polarization at 6 hours after simulated FAL. **E)** Representative images of perinuclear position of the MTOC with respect to pre-conditioning shear direction to confirm HUVEC repolarization with reversed shear stress. **F)** Bar graph showing degree of polarization at 6 hours after simulated FAL (n=3-4). *p<0.05 between upstream and downstream polarization within the given flow condition. Data are mean \pm SEM.



Supplemental Figure 4.5. Gene ontology clustering architecture of microarray expression in non-reversed and reversed flow waveforms.

Clustering of over-represented molecular functions for the 500 top transcripts as ranked by p-value was performed. **A)** Visual depiction of the changes seen with non-reversed increase in shear stress compared to control after 6 hours after simulated FAL. Only one significant molecular function is over-represented. **B)** Visual depiction of the changes seen with an increase in shear stress plus reversed direction compared to control after 6 hours after simulated FAL. Numerous pathways are over-represented. Of particular interest, cAMP PDE activity suggests involvement of PKA and Akt signaling, while the increased activity in small GTPases suggests involvement of cytoskeletal reorganization.



Supplemental Figure 4.6. Amplified arteriogenesis in flow reversed segments does not require eNOS.

A,B) KLF2 and eNOS mRNA expression by RT-PCR (n=8) and **C)** phosphorylated eNOS (Ser1177) protein expression (n=4) relative to control in HUVECs exposed to reversed or non-reversed shear conditions 6 hours after simulated FAL. **D)** Representative vascular cast image from gracilis collateral arteries of eNOS^{-/-} mice 14 days post-FAL, with insets from both muscular and saphenous regions. Arrows indicate measured collateral artery while arrowheads indicate transverse arterioles. Inset scale bar = 100 microns. **E-G)** Bar graphs of binned (all regions) luminal diameter, regional luminal diameter, and fold change of ligated diameter (L) from unligated control (U) for both wild-type (WT) and eNOS^{-/-} mice (n=6). *p<0.05 between ligated and unligated; †p<0.05 between saphenous and muscular regions; ‡p<0.05 between WT and eNOS^{-/-}. §p<0.05 between reversed (R) and non-reversed (N) conditions in vitro. Data are mean ± SEM.

4.10 Supplemental Tables

Supplemental Table 4.1. Gene ontology analysis for over-representation of molecular function

Description	P-value	FDR q-value	Enrichment Score	Enriched Genes in Pathway
A. Non-reversed v Control				
oxidoreductase activity, acting on the CH-NH group of donors, NAD or NADP as acceptor	6.66E-04	1.00E+00	9.57	AASS, MTHFR, PYCR1, MTHFD2
B. Reversed v Control				
3',5'-cyclic-AMP phosphodiesterase activity	8.29E-05	3.22E-01	15.42	PDE4D, PDE4B, PDE3A, PDE7B
nucleoside-triphosphatase regulator activity	1.07E-04	2.07E-01	2.25	ARHGAP18, RAPGEF5, CYTH1, TBC1D2, GRPEL1, PREX2, ARHGAP29, TBC1D22B, KIAA1244, HTR2B, SYDE2, STARD8, SIPA1L3, PLEKHG5, RGL1, TBCK, RASA4, PLEKHG1, PSD3, ARHGAP28, DNMBP, RASGEF1B, ARHGEF37, SH2D3C, TBXA2R, DOCK11
GTPase regulator activity	1.73E-04	2.25E-01	2.23	ARHGAP18, RAPGEF5, CYTH1, TBC1D2, PREX2, ARHGAP29, TBC1D22B, KIAA1244, HTR2B, SYDE2, STARD8, SIPA1L3, PLEKHG5, RGL1, TBCK, RASA4, PLEKHG1, PSD3, ARHGAP28, DNMBP, RASGEF1B, ARHGEF37, SH2D3C, TBXA2R, DOCK11
small GTPase regulator activity	2.07E-04	2.01E-01	2.53	RASA4, RAPGEF5, PLEKHG1, CYTH1, TBC1D2, PSD3, PREX2, ARHGAP29, TBC1D22B, KIAA1244, RASGEF1B, DNMBP, HTR2B, ARHGEF37, SYDE2, TBCK, PLEKHG5, RGL1, DOCK11
guanyl-nucleotide exchange factor activity	2.45E-04	1.91E-01	3.01	RAPGEF5, CYTH1, PLEKHG1, PSD3, PREX2, KIAA1244, DNMBP, RASGEF1B, ARHGEF37, SH2D3C, TBXA2R, RGL1, PLEKHG5, DOCK11
3',5'-cyclic-nucleotide phosphodiesterase activity	3.25E-04	2.10E-01	8.03	PDE4D, PDE4B, PDE3A, PDE2A, PDE7B
RNA polymerase II core promoter proximal region sequence-specific DNA binding transcription factor activity	3.53E-04	1.96E-01	4.08	RCOR1, NR4A1, CREB5, PLSCR1, KLF4, DACH1, TCF4, SOX4, ARNTL
cyclic-nucleotide phosphodiesterase activity	3.97E-04	1.93E-01	7.71	PDE4D, PDE4B, PDE3A, PDE2A, PDE7B
sequence-specific DNA binding RNA polymerase II transcription factor activity	5.28E-04	2.28E-01	2.58	RCOR1, NR4A1, RARB, DACH1, TCF4, NR1D2, KLF11, ARNTL, STAT1, CREB5, PLSCR1, FOXN2, KLF4, SOX4, MEF2A, FOXN3
reelin receptor activity	6.72E-04	2.61E-01	38.55	VLDLR, LRP8

Represents gene ontology clustering from top 500 genes from each group as ranked by p-value

Supplemental Table 4.2. Additional predicted upstream regulators of gene expression patterns seen with reversed and non-reversed flow waveforms

<i>Upstream Regulator</i>	<i>Reversed v Control</i>		<i>Non-reversed v Control</i>	
	<i>Activation Z-Score</i>	<i>p-value overlap</i>	<i>Activation Z-Score</i>	<i>p-value overlap</i>
A. MAPK Pathways				
Mek (group)	2.215	3.50E-02		
RAF1	2.037	2.62E-05		9.31E-04
ERK1/2	1.912	3.05E-02		
MAPK14	1.793	2.50E-02		3.38E-02
MAP3K1	1.513	1.65E-02		6.70E-03
ERK	1.418	5.74E-03		
P38 MAPK	1.403	2.72E-04		
U0126	-2.336	2.24E-05		
(inhibitor of MEK 1/2)				
PD98059	-3.215	6.65E-05	-0.577	1.91E-02
(inhibitor of MEK 1)				
B. Growth Factors				
HGF	5.243	1.87E-13		
Vegf (group)	4.955	1.81E-15		
EGF	2.407	7.47E-05		
PDGF BB	2.33	1.78E-02		1.76E-02
FGF1	2.18	8.10E-03		
EGR2	2.178	1.41E-02		
FGF2	2.11	1.68E-05		
TGFBR2	1.969	3.76E-02		
ERBB2	1.849	1.55E-03		
VEGFA	1.84	1.74E-04		
TGFB3	1.134	5.48E-03		
Tgf beta (group)	1.07	9.46E-03		
MET	1	4.26E-03		
tyrphostin AG 1478	-1.04	1.40E-02		
(inhibitor of EGFR1)				
CTGF	-1.134	2.39E-03		1.01E-02
C. PI3K/AKT Pathway				
Akt	1.941	3.40E-02		
PI3K (complex)	1.714	1.43E-02		
Ca2+	1.191	4.45E-07		
LY294002	-1.12	2.25E-04		4.99E-02
(inhibitor of PI3K)				
wortmannin	-2.007	8.01E-02		
(inhibitor of PI3K)				
D. Cytokines				
IL13	2.493	1.46E-01		
CXCL12	1.542	2.26E-02		
IL3	1.342	2.20E-02		
Ifn (group)	1.305	1.19E-03		
IL1RN	1.195	1.47E-02		
IL1A	1.115	2.82E-04		
TNF	0.062	1.03E-10	1.236	8.23E-05
IFNA1/IFNA13	-1	1.52E-02		
Tnf (family)	-1.089	5.67E-03		
IL27	-1.277	8.09E-03		
IFNA2	-1.564	1.20E-02		
IFNB1	-1.665	2.75E-03		
TNFSF10	-1.715	2.22E-02		

All matching upstream regulators fitting into the defined groups with activation | z-score | >1.0

Supplemental Table 4.3. Ingenuity Pathways Analysis significant canonical pathways

Pathway	P-value	Ratio	Molecules
A. Reversed v Control			
Cellular Effects of Sildenafil (Viagra)	1.17E-03	7.8E-02	PRKACB, PDE2A, KCNN2, GUCY1A3, GPR37, PDE3A, ACTA2, ITPR3, PDE4B, NOS3, PDE4D
Corticotropin Releasing Hormone Signaling	1.45E-03	7.46E-02	PRKACB, SHH, GUCY1A3, BDNF, NPR1, ITPR3, MEF2A, NR4A1, CREB5, NOS3
tRNA Splicing	2.45E-03	1.19E-01	PDE2A, PDE7B, PDE3A, PDE4B, PDE4D
Protein Kinase A Signaling	5.37E-03	5.29E-02	PRKACB, AKAP12, SHH, TCF4, PDE2A, H3F3A/H3F3B, YWHAH, PDE3A, PDE4B, CREB5, NOS3, PDE4D, DHH, DUSP5, ADD3, PDE7B, PTPRJ, DUSP1, ITPR3, EBI3
cAMP-mediated signaling	6.17E-03	6.36E-02	AKAP12, PRKACB, SRC, GPR17, PDE2A, PDE7B, DUSP1, PDE3A, TBXA2R, HTR1D, PDE4B, PDE4D, CREB5, PKIG
p38 MAPK Signaling	6.46E-03	7.89E-02	H3F3A/H3F3B, TIFA, DUSP1, PLA2G4C, MEF2A, IL1R1, CREB5, STAT1, FAS
Gap Junction Signaling	1.55E-02	5.85E-02	PRKACB, SRC, HTR2B, NOV, GUCY1A3, NPR1, ACTA2, TUBB2A, ITPR3, TUBA4A
Sertoli Cell-Sertoli Cell Junction Signaling	1.58E-02	5.7E-02	PRKACB, SRC, EPB41, CLDN12, GUCY1A3, CLDN1, ACTA2, TUBB2A, TUBA4A, NOS3, MAP3K3
Relaxin Signaling	1.91E-02	5.77E-02	PRKACB, PDE2A, PDE7B, GUCY1A3, PDE3A, NPR1, PDE4B, NOS3, PDE4D
β-alanine Degradation I	3.09E-02	1.11E-01	ALDH6A1
All-trans-decaprenyl Diphosphate Biosynthesis	3.09E-02	2E-01	PDSS1
Epithelial Adherens Junction Signaling	3.31E-02	6.16E-02	SRC, DLL1, TCF4, MAGI1, LMO7, FGFR1, ACTA2, TUBB2A, TUBA4A
ERK5 Signaling	3.55E-02	7.94E-02	SRC, YWHAH, MEF2A, CREB5, MAP3K3
FGF Signaling	3.98E-02	6.82E-02	FGFR3, FGF16, FGF18, FGFR1, FGF12, CREB5
G-Protein Coupled Receptor Signaling	4.37E-02	4.89E-02	PRKACB, SRC, GPR17, PDE2A, HTR2B, PDE7B, DUSP1, PDE3A, TBXA2R, HTR1D, PDE4B, PDE4D, CREB5
Cardiac β-adrenergic Signaling	4.47E-02	5.33E-02	PRKACB, AKAP12, PDE2A, PDE7B, PDE3A, PDE4B, PDE4D, PKIG
Aryl Hydrocarbon Receptor Signaling	4.57E-02	5.03E-02	SRC, NCOA7, CCND3, NFIA, RARB, ALDH6A1, FAS, MCM7
ERK/MAPK Signaling	4.68E-02	5.03E-02	PRKACB, ETS1, SRC, ELF4, H3F3A/H3F3B, YWHAH, DUSP1, PLA2G4C, CREB5, STAT1
B. Non-reversed v Control			
UDP-D-xylose and UDP-D-glucuronate Biosynthesis	5.13E-03	1.43E-01	UGDH
Sphingomyelin Metabolism	1.51E-02	7.14E-02	SGMS2
VDR/RXR Activation	1.70E-02	2.47E-02	MXD1, THBD
G-Protein Coupled Receptor Signaling	2.45E-02	1.13E-02	HTR2B, DUSP1, PDE4D
Hematopoiesis from Multipotent Stem Cells	3.02E-02	8.33E-02	KITLG
Colanic Acid Building Blocks Biosynthesis	3.02E-02	2.94E-02	UGDH
p38 MAPK Signaling	3.09E-02	1.75E-02	DUSP1, PLA2G4C
Leukotriene Biosynthesis	3.31E-02	4E-02	MGST2
The Visual Cycle	3.55E-02	3.7E-02	DHRS3
Glutathione Redox Reactions I	3.80E-02	4.55E-02	MGST2

CDP-diacylglycerol Biosynthesis I	3.80E-02	3.7E-02	AGPAT9
Extrinsic Prothrombin Activation Pathway	4.07E-02	5E-02	THBD
Phosphatidylglycerol Biosynthesis II (Non-plastidic)	4.07E-02	3.03E-02	AGPAT9
Aldosterone Signaling in Epithelial Cells	4.90E-02	1.27E-02	DUSP1, DNAJB9

Supplemental Table 4.4. All differentially regulated genes between reversed versus control conditions with FDR<0.10

<i>Gene Name</i>	<i>Entrez ID</i>	<i>Symbol</i>	<i>Log₂ FC</i>	<i>± 95% C.I.</i>	<i>FDR</i>
A. Upregulated Genes					
neutrophil cytosolic factor 2	4688	NCF2	1.157	0.293	7.72E-03
semaphorin 7A, GPI membrane anchor (John Milton Hagen blood group)	8482	SEMA7A	1.133	0.221	1.96E-03
thrombomodulin	7056	THBD	1.002	0.127	1.91E-04
1-acylglycerol-3-phosphate O-acyltransferase 9	84803	AGPAT9	0.971	0.184	1.96E-03
parathyroid hormone-like hormone	5744	PTH LH	0.914	0.216	6.37E-03
chemokine (C-C motif) ligand 20	6364	CCL20	0.870	0.353	4.73E-02
chemokine-like receptor 1	1240	CMKLR1	0.860	0.292	2.58E-02
ADAM metalloproteinase with thrombospondin type 1 motif, 4	9507	ADAMTS4	0.836	0.204	6.37E-03
ADAM metalloproteinase with thrombospondin type 1 motif, 9	56999	ADAMTS9	0.820	0.217	9.70E-03
serpin peptidase inhibitor, clade B (ovalbumin), member 2	5055	SERP INB2	0.810	0.356	6.22E-02
RasGEF domain family, member 1B	153020	RASGEF1B	0.803	0.372	7.46E-02
stanniocalcin 1	6781	STC1	0.765	0.306	4.43E-02
nephroblastoma overexpressed	4856	NOV	0.756	0.129	1.40E-03
kelch repeat and BTB (POZ) domain containing 8	84541	KBTD8	0.737	0.114	7.39E-04
KIT ligand	4254	KITLG	0.718	0.205	1.12E-02
fermitin family member 3	83706	FERMT3	0.695	0.316	7.04E-02
diacylglycerol lipase, alpha	747	DAGLA	0.682	0.198	1.21E-02
sema domain, immunoglobulin domain (Ig), transmembrane domain (TM) and short cytoplasmic domain, (semaphorin) 4B	10509	SEMA4B	0.679	0.125	1.96E-03
RCAN family member 3	11123	RCAN3	0.675	0.338	9.89E-02
ras homolog family member F (in filopodia)	54509	RHOF	0.671	0.240	3.10E-02
insulin induced gene 1	3638	INSIG1	0.660	0.164	7.23E-03
heparanase	10855	HPSE	0.635	0.255	4.50E-02
leucine rich repeat (in FLII) interacting protein 1	9208	LRRFIP1	0.629	0.267	5.57E-02
ADAM metalloproteinase with thrombospondin type 1 motif, 1	9510	ADAMTS1	0.629	0.265	5.51E-02
dual specificity phosphatase 5	1847	DUSP5	0.616	0.139	5.04E-03
angiopoietin-like 4	51129	ANGPTL4	0.610	0.276	6.94E-02
paraneoplastic Ma antigen 2	10687	PNMA2	0.603	0.255	5.54E-02
carbonic anhydrase XIII	377677	CA13	0.601	0.213	3.10E-02
dedicator of cytokinesis 11	139818	DOCK11	0.585	0.223	3.69E-02

G protein-coupled receptor, family C, group 5, member A	9052	GPRC5A	0.583	0.253	5.95E-02
plasminogen activator, urokinase receptor	5329	PLAUR	0.583	0.147	7.72E-03
FH2 domain containing 1	85462	FHDC1	0.568	0.138	6.37E-03
5-hydroxytryptamine (serotonin) receptor 1D, G protein-coupled	3352	HTR1D	0.563	0.271	8.71E-02
G protein-coupled receptor 37 (endothelin receptor type B-like)	2861	GPR37	0.562	0.241	5.71E-02
very low density lipoprotein receptor	7436	VLDLR	0.547	0.261	8.48E-02
grainyhead-like 1 (Drosophila)	29841	GRHL1	0.547	0.129	6.37E-03
UDP-N-acetyl-alpha-D-galactosamine:polypeptide N-acetylgalactosaminyltransferase 12 (GalNAc-T12)	79695	GALNT12	0.545	0.260	8.48E-02
neurotensin receptor 1 (high affinity)	4923	NTSR1	0.544	0.130	6.37E-03
Rap guanine nucleotide exchange factor (GEF) 5	9771	RAPGEF5	0.541	0.139	7.72E-03
desert hedgehog	50846	DHH	0.531	0.170	1.97E-02
pleckstrin homology domain containing, family G (with RhoGef domain) member 1	57480	PLEKHG1	0.523	0.117	4.79E-03
fibroblast growth factor 18	8817	FGF18	0.523	0.185	3.10E-02
Ras association (RalGDS/AF-6) and pleckstrin homology domains 1	65059	RAPH1	0.522	0.149	1.14E-02
fibroblast growth factor 16	8823	FGF16	0.520	0.200	3.77E-02
protocadherin 12	51294	PCDH12	0.508	0.163	1.97E-02
solute carrier family 35, member E4	339665	SLC35E4	0.506	0.144	1.12E-02
carbohydrate (chondroitin 6) sulfotransferase 3	9469	CHST3	0.503	0.213	5.57E-02
natriuretic peptide receptor A/guanylate cyclase A (atrionatriuretic peptide receptor A)	4881	NPR1	0.503	0.188	3.37E-02
chromosome 3 open reading frame 55	152078	C3orf55	0.498	0.141	1.12E-02
TSC22 domain family, member 3	1831	TSC22D3	0.489	0.171	2.93E-02
family with sequence similarity 134, member B	54463	FAM134B	0.487	0.181	3.23E-02
TBC1 domain family, member 2	55357	TBC1D2	0.485	0.161	2.28E-02
solute carrier organic anion transporter family, member 4C1	353189	SLCO4C1	0.485	0.193	4.28E-02
small nucleolar RNA, H/ACA box 1	677792	SNORA1	0.482	0.237	9.51E-02
LIM domain 7	4008	LMO7	0.477	0.171	3.10E-02
ADAM metallopeptidase domain 19	8728	ADAM19	0.476	0.139	1.21E-02
nitric oxide synthase 3 (endothelial cell)	4846	NOS3	0.474	0.131	1.08E-02
Kruppel-like factor 4 (gut)	9314	KLF4	0.473	0.129	1.02E-02
small cell adhesion glycoprotein	57228	SMAGP	0.469	0.113	6.37E-03
StAR-related lipid transfer (START) domain containing 8	9754	STARD8	0.465	0.126	1.02E-02
interleukin 11	3589	IL11	0.456	0.153	2.48E-02

cytochrome b5 reductase 2	51700	CYB5R2	0.456	0.221	8.98E-02
CASK interacting protein 2	57513	CASKIN2	0.455	0.128	1.12E-02
solute carrier family 7 (amino acid transporter light chain, L system), member 5	8140	SLC7A5	0.454	0.215	8.17E-02
GTP cyclohydrolase 1	2643	GCH1	0.454	0.224	9.51E-02
ephrin-B1	1947	EFNB1	0.453	0.178	4.15E-02
olfactory receptor, family 2, subfamily A, member 9 pseudogene	441295	OR2A9P	0.444	0.207	7.57E-02
odz, odd Oz/ten-m homolog 3 (Drosophila)	55714	ODZ3	0.441	0.143	2.02E-02
platelet-derived growth factor alpha polypeptide	5154	PDGFA	0.441	0.162	3.22E-02
myelin protein zero-like 3	196264	MPZL3	0.436	0.157	3.14E-02
OTU domain, ubiquitin aldehyde binding 2	78990	OTUB2	0.434	0.140	2.02E-02
claudin 1	9076	CLDN1	0.433	0.217	9.84E-02
versican	1462	VCAN	0.431	0.195	6.89E-02
sprouty homolog 4 (Drosophila)	81848	SPRY4	0.430	0.200	7.47E-02
tumor necrosis factor receptor superfamily, member 9	3604	TNFRSF9	0.427	0.133	1.74E-02
KIAA1522	57648	KIAA1522	0.426	0.116	1.02E-02
sonic hedgehog	6469	SHH	0.424	0.177	5.45E-02
cAMP responsive element binding protein 5	9586	CREB5	0.424	0.134	1.90E-02
meningioma (disrupted in balanced translocation) 1	4330	MN1	0.423	0.139	2.22E-02
potassium channel, subfamily K, member 1	3775	KCNK1	0.417	0.144	2.72E-02
epithelial mitogen homolog (mouse)	255324	EPGN	0.411	0.163	4.31E-02
BCL2-antagonist/killer 1	578	BAK1	0.408	0.186	7.04E-02
protein tyrosine phosphatase, receptor type, J	5795	PTPRJ	0.407	0.137	2.48E-02
LY6/PLAUR domain containing 5	284348	LYPD5	0.406	0.149	3.21E-02
Kruppel-like factor 8	11279	KLF8	0.404	0.197	9.01E-02
methylenetetrahydrofolate dehydrogenase (NADP+ dependent) 2, methenyltetrahydrofolate cyclohydrolase	10797	MTHFD2	0.404	0.153	3.51E-02
basic, immunoglobulin-like variable motif containing	54841	BIVM	0.403	0.174	5.88E-02
UDP-GlcNAc:betaGal beta-1,3-N-acetylglucosaminyltransferase 2	10678	B3GNT2	0.400	0.152	3.56E-02
zinc finger protein 467	168544	ZNF467	0.397	0.156	4.13E-02
delta-like 1 (Drosophila)	28514	DLL1	0.396	0.156	4.15E-02
cell division cycle 6 homolog (S. cerevisiae)	990	CDC6	0.393	0.143	3.14E-02
interleukin 1 receptor, type I	3554	IL1R1	0.392	0.171	6.01E-02
tensin 1	7145	TNS1	0.391	0.152	4.05E-02
delta/notch-like EGF repeat containing	92737	DNER	0.388	0.187	8.76E-02

mixed lineage kinase domain-like	197259	MLKL	0.385	0.182	8.22E-02
small nucleolar RNA, C/D box 50B	692088	SNORD50B	0.383	0.189	9.54E-02
gasdermin C	56169	GSDMC	0.383	0.178	7.47E-02
chemokine (C-C motif) receptor-like 2	9034	CCRL2	0.383	0.170	6.43E-02
plasminogen activator, urokinase	5328	PLAU	0.381	0.160	5.51E-02
Kruppel-like factor 11	8462	KLF11	0.380	0.107	1.12E-02
coagulation factor II (thrombin) receptor-like 3	9002	F2RL3	0.377	0.135	3.10E-02
Epstein-Barr virus induced 3	10148	EBI3	0.376	0.169	6.75E-02
microtubule-associated protein 1A	4130	MAP1A	0.374	0.135	3.14E-02
DnaJ (Hsp40) homolog, subfamily B, member 9	4189	DNAJB9	0.374	0.131	2.93E-02
zinc finger protein 589	51385	ZNF589	0.373	0.144	3.86E-02
zinc finger protein 643	65243	ZNF643	0.373	0.178	8.45E-02
ankyrin repeat domain 20 family, member A3	441425	ANKRD20A3	0.371	0.159	5.66E-02
low density lipoprotein receptor-related protein 8, apolipoprotein e receptor	7804	LRP8	0.369	0.164	6.59E-02
chromosome 14 open reading frame 43	91748	C14orf43	0.368	0.175	8.43E-02
pantothenate kinase 2	80025	PANK2	0.368	0.171	7.47E-02
KIAA1199	57214	KIAA1199	0.367	0.132	3.14E-02
proline rich 5 like	79899	PRR5L	0.366	0.139	3.56E-02
ganglioside induced differentiation associated protein 1	54332	GDAP1	0.365	0.166	7.04E-02
EPH receptor A4	2043	EPHA4	0.364	0.134	3.22E-02
tribbles homolog 1 (Drosophila)	10221	TRIB1	0.363	0.131	3.14E-02
fibroblast growth factor 12	2257	FGF12	0.360	0.152	5.51E-02
HEG homolog 1 (zebrafish)	57493	HEG1	0.359	0.125	2.90E-02
sphingomyelin synthase 2	166929	SGMS2	0.359	0.100	1.12E-02
spectrin repeat containing, nuclear envelope family member 3	161176	SYNE3	0.358	0.139	3.92E-02
FERM domain containing 3	257019	FRMD3	0.358	0.126	3.03E-02
CXXC finger protein 5	51523	CXXC5	0.357	0.137	3.70E-02
NEDD4 binding protein 2	55728	N4BP2	0.356	0.161	6.89E-02
chromosome X open reading frame 23	256643	CXorf23	0.354	0.160	6.89E-02
thromboxane A2 receptor	6915	TBXA2R	0.354	0.143	4.57E-02
Kruppel-like factor 13	51621	KLF13	0.354	0.159	6.87E-02
zinc finger, MIZ-type containing 1	57178	ZMIZ1	0.353	0.113	1.97E-02
chromosome 15 open reading frame 26	161502	C15orf26	0.352	0.126	3.10E-02
laminin, alpha 5	3911	LAMA5	0.352	0.131	3.36E-02

inositol 1,4,5-trisphosphate receptor, type 3	3710	ITPR3	0.351	0.110	1.81E-02
endonuclease domain containing 1	23052	ENDOD1	0.349	0.151	5.89E-02
sushi domain containing 1	64420	SUSD1	0.346	0.144	5.22E-02
heat shock 70kD protein 12B	116835	HSPA12B	0.346	0.139	4.50E-02
Niemann-Pick disease, type C1	4864	NPC1	0.344	0.137	4.26E-02
FIC domain containing	11153	FICD	0.344	0.150	6.01E-02
sprouty-related, EVH1 domain containing 1	161742	SPRED1	0.343	0.169	9.61E-02
fibroblast growth factor receptor 3	2261	FGFR3	0.340	0.145	5.66E-02
lysophosphatidic acid receptor 5	57121	LPAR5	0.340	0.119	3.00E-02
ring finger protein 125, E3 ubiquitin protein ligase	54941	RNF125	0.340	0.149	6.29E-02
smoothelin	6525	SMTN	0.339	0.099	1.21E-02
4 solute carrier family 36 (proton/amino acid symporter), member	120103	SLC36A4	0.339	0.170	9.97E-02
leucine rich repeat (in FLII) interacting protein 1	9208	LRRFIP1	0.339	0.134	4.19E-02
zinc finger, AN1-type domain 2A	90637	ZFAND2A	0.338	0.096	1.12E-02
mucosa associated lymphoid tissue lymphoma translocation gene 1	10892	MALT1	0.338	0.124	3.22E-02
lipocalin 6	158062	LCN6	0.336	0.157	7.58E-02
calicin	881	CCIN	0.335	0.144	5.71E-02
tubulin, beta 2A class IIa	7280	TUBB2A	0.335	0.157	7.67E-02
glucoside xylosyltransferase 1	283464	GXYLT1	0.331	0.122	3.23E-02
long intergenic non-protein coding RNA 341	79686	LINC00341	0.329	0.112	2.59E-02
Kruppel-like factor 2 (lung)	10365	KLF2	0.328	0.112	2.58E-02
alkaline ceramidase 3	55331	ACER3	0.327	0.121	3.23E-02
apolipoprotein L domain containing 1	81575	APOLD1	0.324	0.130	4.39E-02
non imprinted in Prader-Willi/Angelman syndrome 1	123606	NIPA1	0.324	0.089	1.02E-02
TATA box binding protein (TBP)-associated factor, RNA polymerase I, A, 48kDa	9015	TAF1A	0.324	0.128	4.21E-02
UDP-N-acetyl-alpha-D-galactosamine:polypeptide N-acetylgalactosaminyltransferase 4 (GalNAc-T4)	8693	GALNT4	0.323	0.107	2.28E-02
zinc finger protein 185 (LIM domain)	7739	ZNF185	0.323	0.148	7.17E-02
G protein-coupled receptor 132	29933	GPR132	0.322	0.121	3.38E-02
chromosome 5 open reading frame 48	389320	C5orf48	0.322	0.115	3.10E-02
chromosome 8 open reading frame 48	157773	C8orf48	0.319	0.128	4.43E-02
Fas (TNF receptor superfamily, member 6)	355	FAS	0.319	0.118	3.23E-02
ubiquitin carboxyl-terminal esterase L3 (ubiquitin thiolesterase)	7347	UCHL3	0.318	0.115	3.14E-02

G protein-coupled receptor 4	2828	GPR4	0.316	0.137	5.90E-02
solute carrier family 41, member 2	84102	SLC41A2	0.315	0.115	3.14E-02
EF-hand calcium binding domain 4B	84766	EFCAB4B	0.315	0.143	6.95E-02
cryptochrome 1 (photolyase-like)	1407	CRY1	0.314	0.128	4.86E-02
claudin 12	9069	CLDN12	0.312	0.144	7.46E-02
ubiquitin specific peptidase 12	219333	USP12	0.312	0.149	8.49E-02
Rho family GTPase 3	390	RND3	0.310	0.130	5.47E-02
SRY (sex determining region Y)-box 13	9580	SOX13	0.310	0.114	3.22E-02
pleckstrin homology domain containing, family H (with MyTH4 domain) member 2	130271	PLEKHH2	0.308	0.110	3.10E-02
pleckstrin homology domain containing, family A member 6	22874	PLEKHA6	0.308	0.118	3.68E-02
heat shock protein 70kDa family, member 13	6782	HSPA13	0.308	0.139	6.89E-02
signal peptide, CUB domain, EGF-like 1	80274	SCUBE1	0.307	0.143	7.47E-02
SH2 domain containing 3C	10044	SH2D3C	0.305	0.121	4.21E-02
uncharacterized LOC388022	388022	LOC388022	0.305	0.097	1.97E-02
glutamine-fructose-6-phosphate transaminase 2	9945	GFPT2	0.303	0.146	8.76E-02
A kinase (PRKA) anchor protein 12	9590	AKAP12	0.301	0.138	7.06E-02
pleckstrin homology domain containing, family M (with RUN domain) member 1	9842	PLEKHM1	0.300	0.139	7.46E-02
fibronectin type III and SPRY domain containing 1-like	83856	FSD1L	0.299	0.114	3.69E-02
small nucleolar RNA, H/ACA box 45	677826	SNORA45	0.297	0.137	7.32E-02
G protein-coupled receptor 83	10888	GPR83	0.294	0.125	5.57E-02
aquaporin 3 (Gill blood group)	360	AQP3	0.293	0.120	4.90E-02
ACAH3104	1E+08	LOC100128816	0.292	0.139	8.38E-02
retinoblastoma binding protein 8	5932	RBBP8	0.291	0.122	5.48E-02
discoidin domain receptor tyrosine kinase 2	4921	DDR2	0.291	0.126	5.89E-02
small nucleolar RNA, C/D box 14E	85391	SNORD14E	0.289	0.139	8.71E-02
OAF homolog (Drosophila)	220323	OAF	0.288	0.136	8.22E-02
v-src sarcoma (Schmidt-Ruppin A-2) viral oncogene homolog (avian)	6714	SRC	0.288	0.116	4.50E-02
intermediate filament family orphan 2	126917	IFFO2	0.287	0.137	8.38E-02
family with sequence similarity 214, member B	80256	FAM214B	0.286	0.139	9.01E-02
PDZ and LIM domain 4	8572	PDLIM4	0.285	0.120	5.48E-02
homer homolog 1 (Drosophila)	9456	HOMER1	0.285	0.102	3.14E-02
PDZ and LIM domain 3	27295	PDLIM3	0.284	0.111	4.13E-02
ABI family, member 3	51225	ABI3	0.284	0.123	5.89E-02

vacuolar protein sorting 37 homolog B (<i>S. cerevisiae</i>)	79720	VPS37B	0.283	0.130	7.28E-02
SH3 and PX domains 2A	9644	SH3PXD2A	0.283	0.141	9.73E-02
pleckstrin homology domain containing, family G (with RhoGef domain) member 5	57449	PLEKHG5	0.283	0.123	5.95E-02
potassium voltage-gated channel, subfamily G, member 1	3755	KCNG1	0.283	0.129	7.05E-02
hexokinase 2	3099	HK2	0.282	0.122	5.82E-02
pleckstrin and Sec7 domain containing 3	23362	PSD3	0.281	0.106	3.45E-02
TEA domain family member 4	7004	TEAD4	0.280	0.134	8.53E-02
pleckstrin and Sec7 domain containing 3	23362	PSD3	0.279	0.124	6.59E-02
transient receptor potential cation channel, subfamily C, member 1	7220	TRPC1	0.278	0.095	2.58E-02
interferon stimulated exonuclease gene 20kDa	3669	ISG20	0.276	0.102	3.22E-02
mannosyl (alpha-1,6-)-glycoprotein beta-1,2-N-acetylglucosaminyltransferase	4247	MGAT2	0.276	0.136	9.51E-02
fibroblast growth factor receptor 1	2260	FGFR1	0.275	0.114	5.22E-02
lysophosphatidylcholine acyltransferase 4	254531	LPCAT4	0.274	0.135	9.44E-02
cardiotrophin-like cytokine factor 1	23529	CLCF1	0.271	0.125	7.25E-02
thrombospondin, type I, domain containing 4	79875	THSD4	0.271	0.120	6.43E-02
golgi SNAP receptor complex member 2	9570	GOSR2	0.268	0.098	3.17E-02
thrombospondin, type I, domain containing 1	55901	THSD1	0.267	0.112	5.51E-02
family with sequence similarity 126, member A	84668	FAM126A	0.266	0.114	5.78E-02
protein kinase (cAMP-dependent, catalytic) inhibitor gamma	11142	PKIG	0.266	0.116	6.01E-02
actin filament associated protein 1-like 1	134265	AFAP1L1	0.265	0.117	6.43E-02
small nucleolar RNA, C/D box 54	26795	SNORD54	0.263	0.119	6.89E-02
v-ets erythroblastosis virus E26 oncogene homolog 1 (avian)	2113	ETS1	0.262	0.132	9.97E-02
tubulin, alpha 4a	7277	TUBA4A	0.262	0.119	6.97E-02
G protein-coupled receptor 17	2840	GPR17	0.260	0.110	5.57E-02
JAZF zinc finger 1	221895	JAZF1	0.258	0.128	9.73E-02
cyclin D3	896	CCND3	0.257	0.110	5.78E-02
phosphodiesterase 2A, cGMP-stimulated	5138	PDE2A	0.255	0.110	5.88E-02
myocyte enhancer factor 2A	4205	MEF2A	0.253	0.113	6.78E-02
ATP-binding cassette, sub-family G (WHITE), member 2	9429	ABCG2	0.252	0.110	5.94E-02
REST corepressor 1	23186	RCOR1	0.252	0.106	5.51E-02
armadillo repeat containing 7	79637	ARMC7	0.250	0.125	9.94E-02
STE20-like kinase	9748	SLK	0.250	0.093	3.23E-02
dual specificity phosphatase 1	1843	DUSP1	0.250	0.103	5.19E-02

chromodomain helicase DNA binding protein 9	80205	CHD9	0.250	0.124	9.62E-02
5 UDP-GlcNAc:betaGal beta-1,3-N-acetylglucosaminyltransferase	84002	B3GNT5	0.249	0.114	7.06E-02
nuclear receptor subfamily 4, group A, member 1	3164	NR4A1	0.247	0.101	4.86E-02
prenyl (decaprenyl) diphosphate synthase, subunit 1	23590	PDSS1	0.246	0.118	8.53E-02
ATPase, Ca++ transporting, plasma membrane 4	493	ATP2B4	0.246	0.122	9.63E-02
family with sequence similarity 40, member B	57464	FAM40B	0.243	0.113	7.47E-02
lysophosphatidylcholine acyltransferase 1	79888	LPCAT1	0.242	0.104	5.80E-02
GrpE-like 1, mitochondrial (E. coli)	80273	GRPEL1	0.242	0.101	5.48E-02
ST3 beta-galactoside alpha-2,3-sialyltransferase 1	6482	ST3GAL1	0.241	0.105	5.98E-02
epithelial membrane protein 3	2014	EMP3	0.241	0.116	8.78E-02
dual specificity phosphatase 7	1849	DUSP7	0.241	0.096	4.37E-02
3 human immunodeficiency virus type I enhancer binding protein	59269	HIVEP3	0.237	0.101	5.57E-02
E74-like factor 4 (ets domain transcription factor)	2000	ELF4	0.235	0.111	8.23E-02
aryl hydrocarbon receptor nuclear translocator-like	406	ARNTL	0.234	0.100	5.75E-02
mannosyl (alpha-1,3-)-glycoprotein beta-1,4-N-acetylglucosaminyltransferase, isozyme A	11320	MGAT4A	0.231	0.104	6.89E-02
Ras interacting protein 1	54922	RASIP1	0.231	0.115	9.77E-02
fem-1 homolog b (C. elegans)	10116	FEM1B	0.228	0.109	8.31E-02
N-myc downstream regulated 1	10397	NDRG1	0.228	0.111	8.96E-02
kinesin family member C1	3833	KIFC1	0.226	0.102	6.88E-02
ATPase type 13A3	79572	ATP13A3	0.226	0.095	5.51E-02
solute carrier family 33 (acetyl-CoA transporter), member 1	9197	SLC33A1	0.226	0.112	9.73E-02
MAX dimerization protein 1	4084	MXD1	0.225	0.108	8.49E-02
Ras-like without CAAX 1	6016	RIT1	0.225	0.095	5.51E-02
family with sequence similarity 65, member A	79567	FAM65A	0.224	0.107	8.38E-02
pleckstrin homology domain containing, family M (with RUN domain) member 1 pseudogene	440456	PLEKHM1P	0.223	0.096	5.82E-02
suppressor of cytokine signaling 1	8651	SOCS1	0.223	0.099	6.53E-02
ring finger protein 149	284996	RNF149	0.223	0.092	5.20E-02
collagen, type XIII, alpha 1	1305	COL13A1	0.220	0.110	9.77E-02
G protein-coupled receptor kinase 5	2869	GRK5	0.220	0.100	7.04E-02
signal-induced proliferation-associated 1 like 3	23094	SIPA1L3	0.220	0.108	9.31E-02
fibrillin 1	2200	FBN1	0.219	0.100	7.06E-02
RAS p21 protein activator 4	10156	RASA4	0.218	0.100	7.10E-02

Fc receptor-like A	84824	FCRLA	0.217	0.108	9.61E-02
potassium voltage-gated channel, Shaw-related subfamily, member 4	3749	KCNC4	0.215	0.092	5.66E-02
ATPase, H+ transporting, lysosomal 34kDa, V1 subunit D	51382	ATP6V1D	0.213	0.103	8.78E-02
ZNF625-ZNF20 readthrough	1.01E+08	ZNF625-ZNF20	0.213	0.107	9.94E-02
B-cell CLL/lymphoma 9-like	283149	BCL9L	0.212	0.098	7.46E-02
inositol(myo)-1(or 4)-monophosphatase 1	3612	IMPA1	0.211	0.104	9.45E-02
zinc finger and BTB domain containing 43	23099	ZBTB43	0.210	0.102	8.90E-02
peripheral myelin protein 22	5376	PMP22	0.209	0.099	8.38E-02
protein kinase-like protein Sgk196	84197	SGK196	0.208	0.104	9.89E-02
asparagine-linked glycosylation 5, dolichyl-phosphate beta-glucosyltransferase homolog (S. cerevisiae)	29880	ALG5	0.204	0.096	7.84E-02
Bardet-Biedl syndrome 7	55212	BBS7	0.203	0.101	9.61E-02
forkhead box N2	3344	FOXN2	0.202	0.094	7.47E-02
KIAA1244	57221	KIAA1244	0.202	0.098	9.01E-02
interleukin 20 receptor beta	53833	IL20RB	0.201	0.089	6.43E-02
tyrosine 3-monooxygenase/tryptophan 5-monooxygenase activation protein, eta polypeptide	7533	YWHAH	0.201	0.092	7.06E-02
patatin-like phospholipase domain containing 8	50640	PNPLA8	0.196	0.096	9.30E-02
transcription elongation factor B (SIII), polypeptide 1 (15kDa, elongin C)	6921	TCEB1	0.196	0.097	9.75E-02
Meis homeobox 3 pseudogene 1	4213	MEIS3P1	0.193	0.093	8.82E-02
cytohesin 1	9267	CYTH1	0.190	0.088	7.40E-02
alpha 1,4-galactosyltransferase	53947	A4GALT	0.187	0.092	9.44E-02
SERTA domain containing 2	9792	SERTAD2	0.185	0.090	9.21E-02
family with sequence similarity 160, member A2	84067	FAM160A2	0.184	0.092	9.77E-02

B. Downregulated Genes

ubiquitin D	10537	UBD	-0.967	0.478	9.61E-02
ADP-ribosyltransferase 4 (Dombrock blood group)	420	ART4	-0.951	0.185	1.96E-03
microRNA 146a	406938	MIR146A	-0.945	0.252	1.00E-02
selectin E	6401	SELE	-0.861	0.319	3.23E-02
endothelin 1	1906	EDN1	-0.816	0.231	1.12E-02
retinoic acid receptor, beta	5915	RARB	-0.791	0.298	3.47E-02
guanylate binding protein 4	115361	GBP4	-0.783	0.239	1.52E-02
chromosome 15 open reading frame 54	400360	C15orf54	-0.764	0.294	3.77E-02
ets variant 1	2115	ETV1	-0.760	0.205	1.02E-02

5-hydroxytryptamine (serotonin) receptor 2B, G protein-coupled	3357	HTR2B	-0.724	0.292	4.56E-02
multiple C2 domains, transmembrane 1	79772	MCTP1	-0.696	0.201	1.17E-02
guanylate binding protein 2, interferon-inducible	2634	GBP2	-0.691	0.195	1.12E-02
raftlin family member 2	130132	RFTN2	-0.689	0.177	7.72E-03
phosphatidylinositol-3,4,5-trisphosphate-dependent Rac exchange factor 2	80243	PREX2	-0.661	0.200	1.52E-02
sestrin 3	143686	SESN3	-0.652	0.155	6.37E-03
chemokine (C-X-C motif) receptor 4	7852	CXCR4	-0.614	0.245	4.36E-02
Rho GTPase activating protein 28	79822	ARHGAP28	-0.613	0.200	2.16E-02
tumor necrosis factor (ligand) superfamily, member 10	8743	TNFSF10	-0.613	0.219	3.10E-02
Rho GTPase activating protein 18	93663	ARHGAP18	-0.612	0.165	1.02E-02
epidermal growth factor receptor pathway substrate 8	2059	EPS8	-0.595	0.152	7.72E-03
NADPH oxidase 4	50507	NOX4	-0.581	0.191	2.22E-02
leucine-rich repeats and immunoglobulin-like domains 3	121227	LRIG3	-0.570	0.223	4.13E-02
protein phosphatase 1, regulatory subunit 16B	26051	PPP1R16B	-0.561	0.141	7.68E-03
GTPase, IMAP family member 4	55303	GIMAP4	-0.558	0.188	2.48E-02
dachshund homolog 1 (Drosophila)	1602	DACH1	-0.555	0.116	2.95E-03
Rho family GTPase 1	27289	RND1	-0.552	0.175	1.90E-02
histone cluster 1, H2ai	8329	HIST1H2AI	-0.551	0.116	2.95E-03
microtubule associated tumor suppressor 1	57509	MTUS1	-0.533	0.156	1.21E-02
microRNA 100	406892	MIR100	-0.532	0.197	3.23E-02
NUAK family, SNF1-like kinase, 1	9891	NUAK1	-0.526	0.198	3.47E-02
BCL2-like 11 (apoptosis facilitator)	10018	BCL2L11	-0.518	0.148	1.12E-02
solute carrier family 40 (iron-regulated transporter), member 1	30061	SLC40A1	-0.517	0.155	1.40E-02
TRAF-interacting protein with forkhead-associated domain	92610	TIFA	-0.515	0.187	3.14E-02
chromosome 11 open reading frame 82	220042	C11orf82	-0.512	0.219	5.66E-02
growth differentiation factor 6	392255	GDF6	-0.482	0.213	6.34E-02
family with sequence similarity 117, member B	150864	FAM117B	-0.479	0.100	2.95E-03
phosphodiesterase 7B	27115	PDE7B	-0.476	0.169	3.10E-02
Cdk5 and Abl enzyme substrate 1	91768	CABLES1	-0.474	0.144	1.52E-02
microRNA 199a-2	406977	MIR199A2	-0.473	0.140	1.30E-02
SH3-domain GRB2-like (endophilin) interacting protein 1	84251	SGIP1	-0.471	0.168	3.10E-02
microRNA 34a	407040	MIR34A	-0.469	0.170	3.14E-02
phosphoinositide-3-kinase interacting protein 1	113791	PIK3IP1	-0.469	0.227	8.87E-02
KAT8 regulatory NSL complex subunit 1-like	151050	KANSL1L	-0.462	0.213	7.33E-02

programmed cell death 4 (neoplastic transformation inhibitor)	27250	PDCD4	-0.462	0.089	1.96E-03
butyrophilin, subfamily 3, member A1	11119	BTN3A1	-0.460	0.122	9.92E-03
dehydrogenase/reductase (SDR family) member 3	9249	DHRS3	-0.457	0.154	2.48E-02
H3 histone, family 3A	3020	H3F3A	-0.452	0.169	3.34E-02
aminoadipate-semialdehyde synthase	10157	AASS	-0.451	0.177	4.15E-02
R-spondin 3	84870	RSPO3	-0.447	0.137	1.53E-02
zinc finger protein 704	619279	ZNF704	-0.440	0.195	6.43E-02
microRNA 216a	406998	MIR216A	-0.438	0.184	5.48E-02
histone cluster 1, H2bg	8339	HIST1H2BG	-0.437	0.133	1.52E-02
brain-derived neurotrophic factor	627	BDNF	-0.436	0.142	2.05E-02
interferon induced with helicase C domain 1	64135	IFIH1	-0.434	0.156	3.14E-02
myotubularin related protein 4	9110	MTMR4	-0.434	0.121	1.12E-02
SATB homeobox 1	6304	SATB1	-0.432	0.177	4.90E-02
transmembrane protein 144	55314	TMEM144	-0.431	0.178	5.14E-02
apolipoprotein L, 3	80833	APOL3	-0.429	0.145	2.54E-02
potassium intermediate/small conductance calcium-activated channel, subfamily N, member 2	3781	KCNN2	-0.429	0.214	9.84E-02
nuclear receptor subfamily 1, group D, member 2	9975	NR1D2	-0.429	0.124	1.18E-02
latexin	56925	LXN	-0.425	0.190	6.72E-02
histone cluster 1, H3e	8353	HIST1H3E	-0.421	0.127	1.50E-02
phosphodiesterase 3A, cGMP-inhibited	5139	PDE3A	-0.419	0.207	9.61E-02
nuclear factor I/A	4774	NFIA	-0.418	0.164	4.13E-02
chromosome 5 open reading frame 4	10826	C5orf4	-0.417	0.168	4.50E-02
Sp4 transcription factor	6671	SP4	-0.417	0.141	2.48E-02
nuclear receptor coactivator 7	135112	NCOA7	-0.414	0.145	3.00E-02
DnaJ (Hsp40) homolog, subfamily B, member 4	11080	DNAJB4	-0.413	0.123	1.31E-02
apolipoprotein B mRNA editing enzyme, catalytic polypeptide-like 3F	200316	APOBEC3F	-0.413	0.145	3.00E-02
phospholipid scramblase 4	57088	PLSCR4	-0.412	0.130	1.90E-02
butyrophilin, subfamily 3, member A3	10384	BTN3A3	-0.410	0.150	3.21E-02
cell division cycle associated 7-like	55536	CDCA7L	-0.408	0.172	5.51E-02
caspase recruitment domain family, member 16	114769	CARD16	-0.407	0.171	5.48E-02
pre-B-cell leukemia homeobox 1	5087	PBX1	-0.407	0.185	7.04E-02
KIAA1958	158405	KIAA1958	-0.406	0.190	7.74E-02
tropomodulin 1	7111	TMOD1	-0.406	0.184	6.89E-02

inositol polyphosphate-4-phosphatase, type II, 105kDa	8821	INPP4B	-0.406	0.184	6.97E-02
cysteine-rich, angiogenic inducer, 61	3491	CYR61	-0.399	0.142	3.10E-02
F-box protein 32	114907	FBXO32	-0.399	0.142	3.10E-02
butyrophilin, subfamily 3, member A2	11118	BTN3A2	-0.399	0.101	7.72E-03
regulatory factor X, 2 (influences HLA class II expression)	5990	RFX2	-0.398	0.161	4.66E-02
GTPase, IMAP family member 8	155038	GIMAP8	-0.398	0.176	6.43E-02
yippee-like 1 (Drosophila)	29799	YPEL1	-0.394	0.154	4.07E-02
actin, alpha 2, smooth muscle, aorta	59	ACTA2	-0.393	0.111	1.12E-02
protein phosphatase 1, regulatory subunit 3B	79660	PPP1R3B	-0.391	0.133	2.58E-02
guanylate binding protein 7	388646	GBP7	-0.390	0.126	2.01E-02
yippee-like 3 (Drosophila)	83719	YPEL3	-0.387	0.130	2.48E-02
SLAIN motif family, member 1	122060	SLAIN1	-0.385	0.186	8.78E-02
GATS protein-like 1	389523	GATSL1	-0.385	0.123	1.97E-02
transmembrane protein 140	55281	TMEM140	-0.385	0.117	1.52E-02
protein phosphatase 1, regulatory subunit 9A	55607	PPP1R9A	-0.384	0.113	1.23E-02
dimethylarginine dimethylaminohydrolase 1	23576	DDAH1	-0.384	0.137	3.10E-02
exocyst complex component 6	54536	EXOC6	-0.383	0.163	5.57E-02
mastermind-like 2 (Drosophila)	84441	MAML2	-0.383	0.133	2.84E-02
KIAA0922	23240	KIAA0922	-0.380	0.143	3.45E-02
membrane associated guanylate kinase, WW and PDZ domain containing 1	9223	MAGI1	-0.380	0.145	3.73E-02
serum deprivation response	8436	SDPR	-0.379	0.128	2.48E-02
histone cluster 1, H2bf	8343	HIST1H2BF	-0.372	0.158	5.57E-02
C-type lectin domain family 14, member A	161198	CLEC14A	-0.371	0.120	2.02E-02
pyruvate dehydrogenase kinase, isozyme 4	5166	PDK4	-0.370	0.164	6.43E-02
neuronal regeneration related protein homolog (rat)	9315	NREP	-0.367	0.167	7.06E-02
Cbl proto-oncogene, E3 ubiquitin protein ligase B	868	CBLB	-0.365	0.117	2.01E-02
myeloid/lymphoid or mixed-lineage leukemia (trithorax homolog, Drosophila); translocated to, 3	4300	MLLT3	-0.363	0.141	3.98E-02
zinc finger protein 48	197407	ZNF48	-0.361	0.104	1.14E-02
guanosine monophosphate reductase	2766	GMPR	-0.359	0.098	1.02E-02
DLGAP1 antisense RNA 1	649446	DLGAP1-AS1	-0.358	0.149	5.39E-02
FK506 binding protein 5	2289	FKBP5	-0.352	0.136	3.97E-02
zinc finger, CCHC domain containing 18	644353	ZCCHC18	-0.351	0.152	5.94E-02
transcription factor Dp-2 (E2F dimerization partner 2)	7029	TFDP2	-0.351	0.085	6.37E-03

homeobox A6	3203	HOXA6	-0.344	0.151	6.10E-02
LYR motif containing 1	57149	LYRM1	-0.342	0.135	4.15E-02
SRY (sex determining region Y)-box 4	6659	SOX4	-0.341	0.152	6.66E-02
GA binding protein transcription factor, beta subunit 1	2553	GABPB1	-0.341	0.124	3.14E-02
TRIM6-TRIM34 readthrough	445372	TRIM6-TRIM34	-0.338	0.169	9.89E-02
guanylate binding protein 1, interferon-inducible	2633	GBP1	-0.336	0.132	4.15E-02
ribonucleoprotein, PTB-binding 2	55225	RAVER2	-0.335	0.162	8.96E-02
SMAD family member 1	4086	SMAD1	-0.333	0.142	5.66E-02
lysophosphatidic acid receptor 6	10161	LPAR6	-0.329	0.157	8.49E-02
kinesin family member 18A	81930	KIF18A	-0.328	0.164	9.77E-02
CCR4-NOT transcription complex, subunit 6-like	246175	CNOT6L	-0.327	0.151	7.36E-02
MDS1 and EVI1 complex locus	2122	MECOM	-0.326	0.134	4.91E-02
sterile alpha motif domain containing 13	148418	SAMD13	-0.325	0.137	5.51E-02
aldehyde dehydrogenase 6 family, member A1	4329	ALDH6A1	-0.322	0.116	3.14E-02
solute carrier family 25, member 30	253512	SLC25A30	-0.321	0.117	3.14E-02
phospholipase A2, group IVC (cytosolic, calcium-independent)	8605	PLA2G4C	-0.320	0.100	1.81E-02
kelch-like 13 (Drosophila)	90293	KLHL13	-0.319	0.132	5.21E-02
TBC1 domain family, member 22B	55633	TBC1D22B	-0.313	0.141	6.81E-02
family with sequence similarity 84, member B	157638	FAM84B	-0.312	0.144	7.33E-02
vestigial like 3 (Drosophila)	389136	VGLL3	-0.312	0.155	9.77E-02
centrosomal protein 19kDa	84984	CEP19	-0.311	0.156	9.94E-02
protein kinase, cAMP-dependent, catalytic, beta	5567	PRKACB	-0.308	0.121	4.15E-02
solute carrier family 2 (facilitated glucose transporter), member 12	154091	SLC2A12	-0.307	0.148	8.71E-02
mitochondria-localized glutamic acid-rich protein	84709	MGARP	-0.305	0.111	3.14E-02
golgi phosphoprotein 3-like	55204	GOLPH3L	-0.305	0.135	6.43E-02
DIS3 mitotic control homolog (S. cerevisiae)-like	115752	DIS3L	-0.305	0.111	3.17E-02
zinc finger protein 610	162963	ZNF610	-0.303	0.097	1.97E-02
carnitine O-octanoyltransferase	54677	CROT	-0.303	0.142	7.86E-02
Rho GTPase activating protein 29	9411	ARHGAP29	-0.301	0.121	4.50E-02
Rho guanine nucleotide exchange factor (GEF) 37	389337	ARHGEF37	-0.301	0.124	5.20E-02
regulatory factor X, 5 (influences HLA class II expression)	5993	RFX5	-0.300	0.109	3.14E-02
family with sequence similarity 43, member A	131583	FAM43A	-0.300	0.127	5.57E-02
family with sequence similarity 149, member B1	317662	FAM149B1	-0.296	0.133	6.80E-02
phosphodiesterase 4D, cAMP-specific	5144	PDE4D	-0.296	0.117	4.20E-02

G protein-coupled receptor 125	166647	GPR125	-0.294	0.122	5.19E-02
sideroflexin 2	118980	SFXN2	-0.292	0.135	7.46E-02
phospholipid scramblase 1	5359	PLSCR1	-0.291	0.095	2.22E-02
chromosome 10 open reading frame 114	399726	C10orf114	-0.290	0.106	3.17E-02
proline-rich nuclear receptor coactivator 1	10957	PNRC1	-0.290	0.107	3.23E-02
ral guanine nucleotide dissociation stimulator-like 1	23179	RGL1	-0.288	0.107	3.23E-02
zinc finger and SCAN domain containing 16	80345	ZSCAN16	-0.288	0.129	6.64E-02
forkhead box N3	1112	FOXP3	-0.288	0.109	3.56E-02
signal transducer and activator of transcription 1, 91kDa	6772	STAT1	-0.287	0.116	4.50E-02
ER membrane protein complex subunit 2	9694	EMC2	-0.287	0.121	5.51E-02
KIAA1107	23285	KIAA1107	-0.287	0.113	4.17E-02
long intergenic non-protein coding RNA 478	388815	LINC00478	-0.287	0.119	5.22E-02
homeobox A4	3201	HOXA4	-0.285	0.143	9.97E-02
G protein-coupled receptor 146	115330	GPR146	-0.285	0.121	5.57E-02
SH3 domain containing 19	152503	SH3D19	-0.285	0.119	5.45E-02
adducin 3 (gamma)	120	ADD3	-0.285	0.124	6.01E-02
Rho-related BTB domain containing 3	22836	RHOBTB3	-0.285	0.141	9.62E-02
ST6 beta-galactosamide alpha-2,6-sialyltransferase 1	6480	ST6GAL1	-0.285	0.109	3.68E-02
uracil-DNA glycosylase	7374	UNG	-0.284	0.126	6.43E-02
dynamitin binding protein	23268	DNMBP	-0.284	0.097	2.64E-02
hydroxysteroid (17-beta) dehydrogenase 7	51478	HSD17B7	-0.284	0.112	4.17E-02
WD repeat domain, phosphoinositide interacting 1	55062	WIPI1	-0.283	0.132	7.47E-02
histone cluster 1, H3h	8357	HIST1H3H	-0.283	0.105	3.23E-02
methylcrotonoyl-CoA carboxylase 1 (alpha)	56922	MCCC1	-0.282	0.093	2.22E-02
NADH dehydrogenase (ubiquinone) 1 alpha subcomplex, 2, 8kDa	4695	NDUFA2	-0.280	0.126	6.89E-02
leucine-rich repeats and immunoglobulin-like domains 1	26018	LRIG1	-0.280	0.100	3.10E-02
WW domain binding protein 1-like	54838	WBP1L	-0.279	0.101	3.14E-02
ubiquitin specific peptidase 28	57646	USP28	-0.279	0.109	4.15E-02
syntrophin binding protein 4	252983	STXBP4	-0.278	0.132	8.29E-02
translocase of inner mitochondrial membrane 8 homolog B (yeast)	26521	TIMM8B	-0.276	0.135	9.20E-02
erythrocyte membrane protein band 4.1 (elliptocytosis 1, RH-linked)	2035	EPB41	-0.276	0.135	9.39E-02
chromosome 6 open reading frame 141	135398	C6orf141	-0.275	0.132	8.61E-02
caspase 2, apoptosis-related cysteine peptidase	835	CASP2	-0.274	0.125	7.04E-02

histone cluster 1, H4d	8360	HIST1H4D	-0.274	0.121	6.43E-02
guanylate cyclase 1, soluble, alpha 3	2982	GUCY1A3	-0.271	0.118	5.97E-02
histone cluster 1, H3d	8351	HIST1H3D	-0.270	0.110	4.86E-02
zinc finger and SCAN domain containing 2	54993	ZSCAN2	-0.269	0.095	3.10E-02
Bcl2 modifying factor	90427	BMF	-0.269	0.117	6.01E-02
cyclin M3	26505	CNNM3	-0.266	0.104	4.13E-02
kinesin family member 13A	63971	KIF13A	-0.265	0.102	3.76E-02
Rho guanine nucleotide exchange factor (GEF) 28	64283	ARHGEF28	-0.263	0.102	3.88E-02
OMA1 zinc metallopeptidase homolog (S. cerevisiae)	115209	OMA1	-0.262	0.120	7.06E-02
t-complex 11 (mouse)-like 2	255394	TCP11L2	-0.261	0.102	4.13E-02
tumor protein p53 inducible nuclear protein 1	94241	TP53INP1	-0.260	0.118	7.00E-02
KIAA1328	57536	KIAA1328	-0.258	0.118	7.06E-02
family with sequence similarity 63, member A	55793	FAM63A	-0.256	0.119	7.47E-02
TBC1 domain containing kinase	93627	TBCK	-0.256	0.093	3.14E-02
CREB3 regulatory factor	153222	CREBRF	-0.255	0.110	5.80E-02
RAB30, member RAS oncogene family	27314	RAB30	-0.254	0.121	8.29E-02
integrator complex subunit 8	55656	INTS8	-0.254	0.104	5.00E-02
family with sequence similarity 198, member B	51313	FAM198B	-0.253	0.110	5.90E-02
chromosome 17 open reading frame 28	283987	C17orf28	-0.250	0.123	9.53E-02
microRNA 93	407050	MIR93	-0.250	0.111	6.43E-02
transmembrane protein 117	84216	TMEM117	-0.249	0.118	8.18E-02
minichromosome maintenance complex component 7	4176	MCM7	-0.249	0.092	3.23E-02
leucine rich repeat containing 8 family, member B	23507	LRRC8B	-0.249	0.102	4.93E-02
apolipoprotein B mRNA editing enzyme, catalytic polypeptide-like 3F	200316	APOBEC3F	-0.248	0.113	7.05E-02
DnaJ (Hsp40) homolog, subfamily C, member 6	9829	DNAJC6	-0.243	0.102	5.51E-02
TRAF family member-associated NFKB activator	10010	TANK	-0.241	0.120	9.77E-02
phosphodiesterase 4B, cAMP-specific	5142	PDE4B	-0.241	0.115	8.54E-02
ring finger protein 44	22838	RNF44	-0.240	0.120	9.77E-02
phosphofructokinase, muscle	5213	PFKM	-0.240	0.108	6.80E-02
opsin 3	23596	OPN3	-0.240	0.090	3.46E-02
solute carrier family 35, member E2B	728661	SLC35E2B	-0.240	0.120	9.97E-02
HMG-box transcription factor 1	26959	HBP1	-0.239	0.104	5.97E-02
dystrophin	1756	DMD	-0.237	0.100	5.51E-02
tripartite motif containing 5	85363	TRIM5	-0.237	0.086	3.14E-02

CTD (carboxy-terminal domain, RNA polymerase II, polypeptide A) small phosphatase 2	10106	CTDSP2	-0.236	0.115	9.01E-02
histone cluster 1, H2ag	8969	HIST1H2AG	-0.236	0.116	9.32E-02
filamin A interacting protein 1	27145	FILIP1	-0.235	0.109	7.42E-02
XRCC6 binding protein 1	91419	XRCC6BP1	-0.234	0.115	9.20E-02
solute carrier family 1 (neuronal/epithelial high affinity glutamate transporter, system Xag), member 1	6505	SLC1A1	-0.234	0.118	9.98E-02
ankyrin repeat domain 50	57182	ANKRD50	-0.232	0.099	5.66E-02
zinc finger protein 254	9534	ZNF254	-0.231	0.111	8.49E-02
family with sequence similarity 111, member A	63901	FAM111A	-0.230	0.110	8.49E-02
LIM and senescent cell antigen-like domains 3	96626	LIMS3	-0.230	0.108	7.99E-02
kelch-like 23 (Drosophila)	151230	KLHL23	-0.229	0.112	9.20E-02
uridine phosphorylase 1	7378	UPP1	-0.229	0.099	5.81E-02
NMDA receptor regulated 2	79664	NARG2	-0.229	0.103	6.89E-02
polymerase (DNA directed), beta	5423	POLB	-0.228	0.097	5.57E-02
synovial sarcoma, X breakpoint 2	6757	SSX2	-0.227	0.097	5.59E-02
transcription factor 4	6925	TCF4	-0.224	0.105	7.92E-02
PDZ and LIM domain 5	10611	PDLIM5	-0.224	0.104	7.47E-02
sestrin 1	27244	SESN1	-0.223	0.093	5.45E-02
SEC14 and spectrin domains 1	91404	SESTD1	-0.222	0.090	4.63E-02
stearoyl-CoA desaturase 5	79966	SCD5	-0.221	0.102	7.26E-02
myeloid/lymphoid or mixed-lineage leukemia (trithorax homolog, Drosophila); translocated to, 1	4298	MLLT1	-0.221	0.110	9.72E-02
methionine adenosyltransferase II, beta	27430	MAT2B	-0.221	0.106	8.50E-02
synapse defective 1, Rho GTPase, homolog 2 (C. elegans)	84144	SYDE2	-0.220	0.104	7.97E-02
zinc finger protein 260	339324	ZNF260	-0.220	0.110	9.84E-02
chromosome 2 open reading frame 27A	29798	C2orf27A	-0.219	0.108	9.71E-02
eukaryotic translation initiation factor 2 alpha kinase 4	440275	EIF2AK4	-0.216	0.094	6.01E-02
mitogen-activated protein kinase 3	4215	MAP3K3	-0.215	0.106	9.44E-02
synuclein, alpha (non A4 component of amyloid precursor)	6622	SNCA	-0.211	0.097	7.17E-02
centrosomal protein 41kDa	95681	CEP41	-0.209	0.096	7.06E-02
mex-3 homolog B (C. elegans)	84206	MEX3B	-0.209	0.094	6.80E-02
ubiquitin specific peptidase 49	25862	USP49	-0.206	0.092	6.75E-02
SEC14-like 1 (S. cerevisiae)	6397	SEC14L1	-0.202	0.100	9.69E-02
nuclear mitotic apparatus protein 1	4926	NUMA1	-0.201	0.098	9.01E-02
uncharacterized LOC441204	441204	LOC441204	-0.199	0.099	9.77E-02

ATP/GTP binding protein-like 5	60509	AGBL5	-0.198	0.090	7.06E-02
family with sequence similarity 115, member C	285966	FAM115C	-0.197	0.089	6.78E-02
hematopoietic prostaglandin D synthase	27306	HPGDS	-0.194	0.097	9.77E-02
Hermansky-Pudlak syndrome 3	84343	HPS3	-0.193	0.093	8.85E-02
cysteine conjugate-beta lyase, cytoplasmic	883	CCBL1	-0.190	0.088	7.47E-02
adaptor-related protein complex 3, mu 2 subunit	10947	AP3M2	-0.190	0.092	8.96E-02
GRAM domain containing 1A	57655	GRAMD1A	-0.185	0.090	9.20E-02
damage-specific DNA binding protein 2, 48kDa	1643	DDB2	-0.184	0.090	9.08E-02

Supplemental Table 4.5. All differentially regulated genes between non-reversed versus control conditions with FDR<0.10

<i>Gene Name</i>	<i>Entrez ID</i>	<i>Symbol</i>	<i>Log₂ FC</i>	<i>± 95% C.I.</i>	<i>FDR</i>
A. Upregulated Genes					
1-acylglycerol-3-phosphate O-acyltransferase 9	84803	AGPAT9	0.652	0.184	6.61E-02
thrombomodulin	7056	THBD	0.606	0.127	1.63E-02
carbonic anhydrase XIII	377677	CA13	0.588	0.213	9.97E-02
KIT ligand	4254	KITLG	0.581	0.205	9.97E-02
kelch repeat and BTB (POZ) domain containing 8	84541	KBTBD8	0.571	0.114	1.63E-02
cell division cycle 6 homolog (<i>S. cerevisiae</i>)	990	CDC6	0.549	0.143	6.13E-02
nephroblastoma overexpressed	4856	NOV	0.478	0.129	6.13E-02
sema domain, immunoglobulin domain (Ig), transmembrane domain (TM) and short cytoplasmic domain, (semaphorin) 4B	10509	SEMA4B	0.429	0.125	6.61E-02
odz, odd Oz/ten-m homolog 3 (<i>Drosophila</i>)	55714	ODZ3	0.394	0.143	9.97E-02
DnaJ (Hsp40) homolog, subfamily B, member 9	4189	DNAJB9	0.388	0.131	9.97E-02
Rap guanine nucleotide exchange factor (GEF) 5	9771	RAPGEF5	0.385	0.139	9.97E-02
MAX dimerization protein 1	4084	MXD1	0.380	0.108	6.61E-02
pleckstrin homology domain containing, family G (with RhoGef domain) member 1	57480	PLEKHG1	0.368	0.117	7.90E-02
pentraxin 3, long	5806	PTX3	0.362	0.129	9.97E-02
forkhead box F1	2294	FOXF1	0.346	0.124	9.97E-02
smoothelin	6525	SMTN	0.333	0.099	6.61E-02
UDP-glucose 6-dehydrogenase	7358	UGDH	0.327	0.118	9.97E-02
small cell adhesion glycoprotein	57228	SMAGP	0.317	0.113	9.97E-02
KIAA1024	23251	KIAA1024	0.307	0.097	7.90E-02
sphingomyelin synthase 2	166929	SGMS2	0.291	0.100	9.97E-02
dual specificity phosphatase 1	1843	DUSP1	0.290	0.103	9.97E-02
B. Downregulated Genes					
5-hydroxytryptamine (serotonin) receptor 2B, G protein-coupled	3357	HTR2B	-0.823	0.292	9.97E-02
microRNA 519a-2	574500	MIR519A2	-0.717	0.215	6.61E-02
guanylate binding protein 4	115361	GBP4	-0.712	0.239	9.97E-02
guanylate binding protein 2, interferon-inducible	2634	GBP2	-0.651	0.195	6.61E-02
ADP-ribosyltransferase 4 (Dombrock blood group)	420	ART4	-0.570	0.185	8.69E-02
dehydrogenase/reductase (SDR family) member 3	9249	DHRS3	-0.508	0.154	6.70E-02
sestrin 3	143686	SESN3	-0.492	0.155	7.90E-02

Rho family GTPase 1	27289	RND1	-0.483	0.175	9.97E-02
microRNA 199a-2	406977	MIR199A2	-0.477	0.140	6.61E-02
butyrophilin, subfamily 3, member A1	11119	BTN3A1	-0.453	0.122	6.13E-02
DLGAP1 antisense RNA 1	649446	DLGAP1-AS1	-0.419	0.149	9.97E-02
apolipoprotein L, 3	80833	APOL3	-0.411	0.145	9.97E-02
G protein-coupled receptor 146	115330	GPR146	-0.375	0.121	8.69E-02
microsomal glutathione S-transferase 2	4258	MGST2	-0.373	0.134	9.97E-02
transmembrane protein 140	55281	TMEM140	-0.369	0.117	7.90E-02
guanylate binding protein 7	388646	GBP7	-0.367	0.126	9.97E-02
histone cluster 1, H2ai	8329	HIST1H2AI	-0.343	0.116	9.97E-02
protein phosphatase 1, regulatory subunit 9A	55607	PPP1R9A	-0.335	0.113	9.97E-02
KIAA1107	23285	KIAA1107	-0.334	0.113	9.97E-02
phosphodiesterase 4D, cAMP-specific	5144	PDE4D	-0.333	0.117	9.97E-02
zinc finger protein 610	162963	ZNF610	-0.326	0.097	6.61E-02
transcription factor Dp-2 (E2F dimerization partner 2)	7029	TFDP2	-0.319	0.085	6.13E-02
phospholipase A2, group IVC (cytosolic, calcium-independent)	8605	PLA2G4C	-0.278	0.100	9.97E-02
guanosine monophosphate reductase	2766	GMPR	-0.272	0.098	9.97E-02
sestrin 1	27244	SESN1	-0.265	0.093	9.97E-02

5 DNMT1-dependent DNA hypermethylation constrains arteriogenesis by augmenting shear stress set-point

Authors: Joshua L. Heuslein, Catherine M. Gorick, Ji Song, Richard J. Price. *In preparation.*

5.1 Abstract

Objective: Collateral arteriogenesis is initiated by increased shear stress and is thought to continue until shear stress is returned to its original “set-point”. It follows that shear stress set-point is critical in determining arteriogenic capacity. Nonetheless, the molecular mechanism(s) through which shear stress set-point is established by endothelial cells (ECs) are essentially unstudied. Here, we tested the hypothesis that DNMT1-dependent EC DNA methylation regulates arteriogenic capacity via adjustments to shear stress set-point.

Approach and Results: Previously, we reported that collateral artery segments exposed to a non-reversed increase in shear stress magnitude display limited arteriogenic capacity when compared to segments exposed to reversed flow direction. Here, using 5-mC immunolabeling, we first demonstrated that these non-reversed collateral segments exhibit a 70% increase in global DNA methylation in-vivo. Then, we applied flow waveforms, biomimetic of those leading to either amplified arteriogenic capacity (i.e. reversed flow) or constrained arteriogenic capacity (i.e. non-reversed flow) in-vivo, to ECs in-vitro, and performed both reduced representation bisulfite sequencing (RRBS) and mRNA-sequencing. ECs exposed to the non-reversed waveform exhibited increased DNMT1 expression, genome-wide hypermethylation of significantly regulated gene promoters (>70%), and a DNMT1-dependent reduction in pro-arteriogenic monocyte adhesion. This led us to test whether DNMT1 regulates arteriogenic capacity in-vivo. We found that, in non-reversed collateral artery segments, DNMT1 inhibition rescued arteriogenic capacity ($70.9 \pm 7.9 \mu\text{m}$ vs. $50.1 \pm 3.4 \mu\text{m}$, $p \leq 0.05$, $n=6$) and returned shear stress back to its original set point.

Conclusions: We conclude that, although shear stress initiates arteriogenesis, it also elicits an EC DNA hypermethylation response that inhibits endothelial mechanosensing (i.e. it augments shear stress set-point). In turn, this augmented shear stress set-point constrains the arteriogenic capacity of the vessel. This epigenetic effect could have important bearing on both endogenous collateralization and therapeutic arteriogenesis in peripheral arterial disease (PAD) patients.

5.2 Abbreviations

PAD	peripheral arterial disease
FAL	femoral arterial ligation
EC	endothelial cell
HUVEC	human umbilical vein endothelial cell
DNMT1	DNA methyltransferase 1
RRBS	reduced representation bisulfite sequencing
DMR	differential methylated region
5AZA	5-Aza-2'-deoxycytidine
HRM	high resolution melting
LSF	laser speckle flowmetry

5.3 Introduction

Collateral arteriogenesis, the growth of existing arterial vessels to a larger diameter, is a fundamental adaptive response that is often critical for the perfusion and survival of tissues downstream of chronic arterial occlusion(s). Arterial occlusion(s) create steep pressure gradients and increased flow along collateral arterial pathways bypassing the occlusion(s). The resulting increase in shear stress acting on the endothelium initiates a highly coordinated signaling cascade, ultimately resulting in the outward growth of the collateral vessel^{37,39}. Outward luminal

growth is hypothesized to continue until normalization to the original shear stress level (i.e. the shear stress “set-point”) has been achieved^{39,41,80,81}.

However, in addition to shear stress magnitude, other hemodynamic factors can also influence arteriogenesis. Indeed, we have recently demonstrated that collateral artery segments exposed to both a 2-fold increase in shear stress magnitude and reversed flow direction (i.e. “reversed” flow) following femoral arterial ligation (FAL) exhibit amplified arteriogenesis, whereas segments experiencing just a 2-fold increase in shear stress magnitude (i.e. “non-reversed”) exhibit a more constrained extent of arteriogenesis²³⁷. Furthermore, this difference in arteriogenic capacity was maintained up to 12-weeks following FAL. Importantly, these collateral artery segments start at the same basal diameter and shear stress magnitude prior to FAL, suggesting that shear stress set-point may be altered due to differential hemodynamics post-FAL.

Though critical in determining ultimate arteriogenic capacity, the molecular mechanism(s) involved in establishing and maintaining the shear stress set-point remain unknown. Epigenetic mechanisms, such as DNA methylation, histone modifications, and noncoding RNA regulation, could be a way for local hemodynamics to regulate long-term gene expression changes¹⁰². Of these epigenetic mechanisms, DNA methylation is considered the most stable^{100,103}. DNA is methylated at a cytosine base pair, most often at a CpG dinucleotide (CpG site)¹⁰³. Methylation of CpG sites in the promoter region of a gene is commonly associated with repression of gene expression^{110–112}. DNA methylation occurs through the activity of DNA methyltransferases (DNMTs), particularly DNMT1 post-development^{98,104,105}. Recently, DNA methylation has been shown to differentially regulate flow-mediated endothelial gene expression through DNMT1^{238–241}, though the role of DNA methylation in the regulation of arteriogenesis has not been explored. Here, using our previous observations of differential arteriogenic capacity within collateral artery segments in-vivo, we tested the central hypothesis that an augmented shear stress set-point constrains arteriogenic capacity via DNMT1-dependent endothelial cell DNA hypermethylation.

5.4 Materials and Methods

5.4.1 Mice.

All animal protocols were approved by the Institutional Animal Care and Use Committee at the University of Virginia (Protocol 3814) and conformed to all regulations for animal use outlined in the American Heart Association Guidelines for the Use of Animals in Research. Male C57BL/6 mice and Balb/c were purchased from Charles River Laboratory (Wilmington, MA). All animals were housed in the animal facilities at the University of Virginia. C57BL/6 mice were used for all studies unless otherwise noted.

5.4.2 Femoral arterial ligation model.

We used a previously detailed femoral artery ligation (FAL) scheme^{167,237,242} that produces consistent arteriogenesis in the collateral arteries of the gracilis adductor muscles^{29,30,177–180,237}, along with minimal heterogeneity in the baseline collateral structure and known changes in flow direction from baseline. Male mice, (10-12 and 20-21 weeks of age for C57BL/6 and Balb/c, respectively), were anesthetized (i.p 120 mg/kg ketamine, 12 mg/kg xylazine, and 0.08 mg/kg atropine), depilated, and prepped for aseptic surgery. On the left leg, an incision was made directly above and along the femoral artery, which was gently dissected from the femoral vein and nerve between the bifurcation of the superior epigastric artery and popliteal artery. Two 6.0 silk sutures were placed immediately distal to the epigastric artery, which served as the origin of the muscular branch artery in all mice, and the artery segment between the two ligatures was then severed with micro dissecting scissors. The surgical site was then closed with 5.0 prolene sutures. A sham surgery, wherein the femoral artery was exposed but not ligated, was performed on the right hindlimb (i.e. on the other leg). Animals received one injection of buprenorphine for analgesia at the time of surgery and a second dose 8-12 hours later.

5.4.3 5AZA treatment.

5-aza-2'-deoxycytidine (5AZA) (Sigma, #A3656) was reconstituted in DMSO to a stock concentration of 0.25mg/μl. Each day immediately before use, stock 5AZA was diluted to 1.25μg/μl and DMSO to 0.01% DMSO in sterile saline. Both solutions were then passed through a 0.22μm sterile syringe filter. Mice were treated daily with an i.p. injection of 0.1mg/kg 5AZA in sterile saline or 0.01% DMSO in a total volume of 100μl.

5.4.4 Quantification of global DNA methylation by high resolution melting (HRM).

Methylation of genomic repeat elements, such as LINE1, have been used as markers of global gDNA methylation^{100,243,244}. LINE1 methylation in the peripheral blood was therefore used as an indicator of the efficacy of our 5AZA treatment protocol on DNA methylation in-vivo. Peripheral blood (100-150μl) was collected retro-orbitally with heparinized capillary tubes from mice 7 days after beginning daily 5AZA or DMSO i.p. injections. Genomic DNA was immediately extracted using the Quick-gDNA MiniPrep kit (Zymo Research, #D3006) and gDNA (80ng) underwent bisulfite conversion using the EZ-DNA Methylation-Gold kit (Zymo Research, #D5005) according to manufacturer's instructions. PCR and HRM analysis were adapted from a previously determined protocol²⁴³. Briefly, modified DNA was diluted to 10ng/μl with nuclease-free water. A 20μl reaction mix of 20ng bisulfite modified DNA and a final concentration of 1x EpiTect HRM Master Mix (Qiagen, #59445), 0.75μM LINE1 forward primer (5'-GTTGAGGTAGTATTTTGTGTGGGT-3'), 0.75μM LINE1 reverse primer (5'-TCCAAAACTATCAAATTCTCTAACAC-3'), and nuclease-free water. PCR cycling conditions for LINE1 were 95°C for 5 minutes followed by 40 cycles of 95°C for 20s then 55°C for 30s then 72°C for 20s. Melt analysis occurred from 60-90 °C rising by 0.1 °C/5s. PCR and HRM was performed on a CFX96 Real Time Detection System (Biorad) and each sample was run in duplicate.

Differences in DNA methylation as detected by HRM were quantified by the Net Temperature Shift (NTS) as previously calculated²⁴³. Briefly, the NTS was calculated as average distance between the normalized melt curves of experimental samples from a universal methylated positive control (Zymo Research, #D5012) where a more negative NTS indicates a less methylated sample. For LINE1, the two normalization regions used were between 72-73°C and 82-83°C.

5.4.5 Tissue harvesting for whole mount vascular casting and cross sectional analysis.

For analysis of luminal diameters in the gracilis collateral arteries and to enable sectioning at specific regions, vascular casting was performed using an opaque polymer that allows for accurate luminal diameter measurements¹⁷⁹. After femoral artery ligation, mice were anesthetized (i.p 120 mg/kg ketamine, 12 mg/kg xylazine, and 0.08 mg/kg atropine), euthanized via an overdose of pentobarbital, and then the abdominal aorta was cannulated. The lower body was then perfused with 7mL of 2% heparinized saline with 2mmol/L adenosine (16404, Fisher Scientific, Pittsburg, PA) and 0.1mmol/L papaverine (P3510, Sigma Aldrich, St Louis, MO) to clear and vasodilate the downstream vasculature at a constant rate of 1mL/min (PHD2000, Harvard Apparatus). Once perfused, we waited 5 minutes to enable vasodilation. Tissues were then perfused with 3mL of 4% paraformaldehyde solution (19943, Affymetrix, Cleveland, OH) at 1mL/min and allowed to fix for 10 minutes. The lower body was then perfused with 0.8mL of Microfil® casting agent (FlowTech, Inc, Carver, Massachusetts) at a constant pressure of 100mmHg. Viscosity of Microfil® was adjusted to minimize transport across capillaries. After curing for 1.5 hours at room temperature, gracilis muscles were dissected free and then cleared in 50% glycerol in phosphate buffered saline (PBS) overnight. Cleared tissues were mounted between two coverslips using 500 µm thick spacers (645501, Grace Bio-Labs Inc) to keep constant thickness between muscles. Muscles were imaged using transmitted light at 4x

magnification on a Nikon TE200 inverted microscope with a CCD camera (Quantifier, Optronics Inc). Individual fields of view were montaged together (Photoshop CS2, Adobe Systems Inc).

For analysis of lumenal diameters from intact gracilis collateral whole mounts (i.e. vascular casting), collateral entrance regions were defined according to the following method. A cropped portion (560 μm x 560 μm) of the montaged image (previously randomized and de-identified) was taken of the collateral artery at the first visible branch point of a terminal arteriole from the primary collateral as it extended from either the muscular branch or saphenous artery as previously described²³⁷. After each cropped image region was taken, all images were randomized and de-identified. The mean diameter was then taken from 4-5 separate diameter measurements along the length of cropped portion of the collateral artery.

After imaging, muscles were rehydrated, cut, and then paraffin embedded for cross sectional analysis at the muscular branch and saphenous artery entrance regions to the collateral arteries. Resulting cross sections were re-hydrated and immunolabeled for 5-methylcytosine (84 days post-FAL) or H&E stained for collateral artery structure analysis (day 28 post-FAL).

5.4.6 Immunofluorescence labeling of 5-methylcytidine.

Sections (5 μm thickness) of paraffin embedded muscle from the muscular and saphenous regions were rehydrated and subjected to heat mediated antigen retrieval for 20 minutes in a citrate based antigen retrieval buffer (Vector Laboratories, Burlingame, CA; H-3300). After cooling, tissues were encircled with a hydrophobic barrier pen and blocked with PBS+0.1% saponin+ 2% bovine serum albumin (Jackson ImmunoResearch) for 1 hour at room temperature. Tissues were then incubated overnight at 4°C with anti-5-methylcytidine (1:100, BI-MECY, Eurogentec) and rat anti-CD31 (1:75, SZ31, Dianova). Following primary antibody incubation, slides were washed in PBS then incubated with DRAQ5 (a nuclear marker), a donkey-anti-mouse Cy3 F_{ab} (1:200, Jackson ImmunoResearch), and a goat-anti-rat-488 secondary antibody (1:200, Jackson ImmunoResearch) for 1 hour at room temperature. Following incubation, slides were washed again in PBS, mounted

with Prolong Gold (Life Technologies) to minimize photobleaching, allowed to cure overnight, and imaged using a Nikon TE2000 C1 laser scanning confocal microscope with a 20x oil objective. All settings were held constant throughout imaging. Cropped fields of view (200µm x 200µm) encompassing the collaterals in each region were randomized and de-identified. The collateral diameter, collateral cross-sectional area, and the integrated density of 5-methylcytidine with an individual cross-section were determined in Fiji¹⁸¹. For each mouse, mean collateral diameter, cross-sectional area, and integrated density was calculated from the average of the two primary gracilis collateral arteries, with two immunolabeled sections per collateral artery for a total of 4 images per mouse.

5.4.7 Cross sectional analysis of collateral artery structure.

Sections (5µm thickness) of paraffin embedded muscle from the muscular and saphenous regions were labeled for H&E. Individual fields of view encompassing the collateral vessels were imaged with a 40x water objective on a Zeiss inverted microscope (Zeiss Axioskop, Thornwood, NY) with a CCD camera (Quantifier, Optronics Inc). All images were randomized and de-identified prior to analysis. Lumenal diameter, wall area, and wall thickness were determined using Fiji¹⁸¹.

5.4.8 Human umbilical vein endothelial cell culture.

Human umbilical vein endothelial cells (HUVECs) purchased from VEC Technologies Inc. (Rensselaer, NY) were thawed and maintained on 0.1% gelatin coated flasks in M-199 medium (Lonza, Basel, Switzerland), supplemented with 10% fetal bovine serum (Life Technologies Inc, Grand Island, NY), 100U/mL penicillin-G + 100ug/ml streptomycin (Life Technologies Inc), 2mmol/L L-glutamine (Life Technologies Inc), 5ug/ml endothelial cell growth supplement (Biomedical Technologies, Stoughton, MA), and 10ug/ml heparin (Sigma Aldrich, St. Louis, MO). For each set of experimental comparisons, cells were used from the same cell line between subculture passages 2-3.

5.4.9 *In vitro* exposure of endothelial cells to biomimetic shear stress waveforms.

HUVECs were plated on cell culture grade plastic dishes coated with 0.1% gelatin and grown to confluence. A cone and plate flow apparatus¹⁸⁷, which maintains cells at 5% CO₂ and 37°C, was used to induce a shear stress protocol. The applied shear stress protocol consisted of a 24 hour preconditioning period at a steady of 15 dyne/cm², which was then either increased to 30 dynes/cm² (non-reversed flow) or increased to 30 dynes/cm² and reversed in direction (reversed flow) to simulate relative hemodynamics previously quantified in our in-vivo FAL model¹⁷⁶. Fresh culture media consisting of M199 with 4% dextran from *Leuconostoc* spp (Sigma Aldrich, M_r ~500,000), 2% fetal bovine serum, 100U/mL penicillin-G + 100ug/ml streptomycin, 2mmol/L L-glutamine, 5ug/ml endothelial cell growth supplement, and 10ug/ml heparin was added to cells before exposure to shear stress and was continuously exchanged throughout the duration in the cone and plate apparatus.

5.4.10 HUVEC RNA isolation and qRT-PCR.

Total RNA was extracted using the PureLink total RNA purification system using the on-column DNase protocol (Life Technologies Inc) according to manufacturer's instructions. RNA concentration and purity was determined with a NanoDrop spectrophotometer in duplicate. For quantitative reverse transcriptase PCR (qRT-PCR), 500ng of total RNA was reverse transcribed using the iScript cDNA synthesis kit (Bio-Rad, Hercules, CA). A reaction mixture of 12.5ng of reverse transcribed cDNA, DNMT1 forward primer (TGCCAGCTGAGCGTGGTGGT), DNMT1 reverse primer (GCATGCGGGCAGCCACCAAT), and FastStart SYBR Green (Roche Applied Sciences) underwent qRT-PCR on a CFX96 Real Time Detection System (Biorad). Expression was normalized to β 2-microglobulin (forward 5'-AGCATTCGGGCCGAGATGTCT-3', reverse 5'-CTGCTGGATGACGTGAGTAAACCT-3') which is endogenously expressed and is not altered by many stimuli including shear stress⁴⁴. Normalized expression was quantified using the comparative 2 ^{$\Delta\Delta C_t$} method.

5.4.11 Reduced representation bisulfite sequencing (RRBS) and mRNA sequencing.

Total gDNA and total RNA were extracted from flow-exposed HUVECs using the Quick-gDNA MiniPrep kit (Zymo Research, Irvine, CA, #D3006) and the Quick-RNA MiniPrep kit (Zymo Research, #R1054) according to manufacturer's instructions. Total gDNA and total RNA concentration and purity were determined with a NanoDrop spectrophotometer in duplicate. Both gDNA and RNA were isolated from the same plate of cells for each condition within an experiment. Purified genomic DNA and purified total RNA isolated from flow-exposed HUVECs were pooled from 2 independent flow experiments. Pooled gDNA samples were sent to Zymo Research where DNA fragmentation, library preparation, bisulfite conversion, next-generation sequencing, and bioinformatics were performed. Pooled RNA samples were also sent to Zymo Research where they performed mRNA sequencing (mRNA-Seq). HiSeq 50bp singleton reads from RNA-Seq were first adaptor trimmed and then analyzed using the TopHat and Cufflinks software. TopHat (v2.2.0) was used for alignment of short read to the human genome hg19. Cufflinks (v2.2.0) was used to transcript assembly and differential expression. CommeRbund (v2.0.0) was used for visualization of differential analysis. Default parameters were used in all instances.

5.4.12 RRBS Analysis.

RRBS next-generation sequencing reads were mapped to the "Feb. 2009 (GRCh37/hg19)" genome assembly by Zymo Research. The %CpG methylation was calculated as the percent of methylated CpG sites per total CpG sites in a given differentially methylated region (DMR) with $\geq 10\times$ CpG coverage in a given DMR. Significance was determined using a Fisher's exact test then applying a Benjamini-Hochberg procedure to find false discovery rate (FDR). DMRs with $\geq 10\times$ CpG coverage in their promoter regions (transcription start site $\pm 1\text{kb}$) were considered significant if $\text{FDR} < 0.1$ and the absolute value of %CpG methylation of a DMR in N minus the %CpG methylation of a DMR in R was $\geq 10\%$ ([Supplemental Table 5.3](#)). We then compared this

list of significant DMRs with our mRNA-Seq dataset to determine genes with relative gene expression changes that correspond to their methylation status between shear stress conditions, i.e. identify genes up-regulated in N conditions that also have a significantly hypomethylated promoter region as well as genes that are down-regulated in N conditions that have hypermethylated promoter regions compared to in R conditions ([Supplemental Table 5.4](#) & [Supplemental Table 5.5](#)). Only genes demonstrating this relative gene expression-methylation correlation were used for gene ontology analysis using MSigDB²⁴⁵ from the Broad Institute.

5.4.13 Transillumination laser speckle imaging and shear stress analysis.

Transillumination laser speckle imaging was performed as previously described¹⁷⁶. Briefly, 28-days after femoral arterial ligation, mice were anesthetized (i.p 120 mg/kg ketamine, 12 mg/kg xylazine, and 0.08 mg/kg atropine), depilated, and prepped for aseptic surgery. On the left leg (ligated leg), an incision was made above and along the femoral artery such that a window of skin was dissected free and retracted directly above the superficial adductor muscles. Exposed tissue was superfused throughout the procedure and during imaging with a warmed solution of Tris-CaCl₂ (0.1g/L CaCl₂) with 2mmol/L adenosine (16404, Fisher Scientific) and 0.1mmol/L papaverine (P3510, Sigma Aldrich). To image the gracilis muscle, the mouse was placed supine on an intravital microscope stage (Zeiss Axioskop). A 30mW, 658nm laser diode (LPM658-30, Newport Corporation, Irvine, CA) was coupled to a fiber optic cable and placed beneath the mouse in a trans-illumination orientation. A cooled, monochrome CCD camera (Optonics Quantifier, Goleta, CA) was used to acquire the raw speckle images using a 4x air objective (Zeiss Acroplan LD NA=0.1). The objective and camera were chosen to ensure satisfaction of the Nyquist sampling criteria of at least 2 pixels per individual speckle.²⁹ An objective mounted fiber optic light guide allowed for brightfield imaging to enable luminal diameter measurements (A08650, Schott Inc., Elmsford, NY). For each field of view, a sequence of 20 12-bit raw speckle images was acquired with a 5ms exposure time to capture average velocity over multiple cardiac cycles.

All processing of raw speckle images was performed using Fiji¹⁸¹ as described previously¹⁷⁶. Briefly, raw speckle images were converted to laser speckle flow index maps, removing any images with excessive motion artifact. To then account for the influence of whole background tissue variations, the processed flow images were normalized to median background intensity. Individual flow images were then merged into larger two-dimensional maps using Adobe Photoshop (CS2, Adobe Systems Inc., San Jose, CA). Finally, to allow for comparison of velocity change across experiments vessel speckle intensity (SI) was normalized to the background tissue according to Eq. 1 to obtain the normalized speckle index (NSI).

$$NSI = \frac{SI_{\text{vessel}}}{SI_{\text{background}}} - 1$$

(5.1)

Blood velocity analysis of laser speckle images was limited to defined muscular branch and saphenous collateral artery regions and assumed Poiseuille flow. The mean speckle shear rate (SSR) in each region was calculated using the normalized speckle index and vessel diameter (D) according to Eq. 2:

$$SSR \propto \frac{NSI}{D}$$

(5.2)

5.4.14 siRNA transfection in HUVECs.

Twenty-four hours prior to exposure of HUVECs to flow conditions, HUVECs were plated without antibiotics on 0.1% gelatin coated plates in serum-free M199 (Life Technologies) supplemented with 10% fetal bovine serum, 2mmol/L L-glutamine, 5ug/ml endothelial cell growth supplement (Biomedical Technologies, Stoughton, MA), and 10ug/ml heparin (Sigma Aldrich Inc). After cells were allowed to adhere for 2 hours after plating, cells were transfected with either 120pmol of

ON-TARGETplus SMARTpool human DNMT1 siRNA (GE Dharmacon, Lafayette, CO, L-004605-00-0005,) or 120pmol of ON-TARGETplus non-targeting siRNA (GE Dharmacon, D-001810-10-05) in 52µL of Oligofectamine transfection reagent (Life Technologies) and 6.8mL Opti-MEM media (Life Technologies) for 5 hours at 37°C. After 5 hours, plates were flooded with 8mL of M199 media without antibiotics supplemented with 10% fetal bovine serum + L-glutamine + 5ug/ml endothelial cell growth supplement (Biomedical Technologies, Stoughton, MA), and 10ug/ml heparin (Sigma Aldrich Inc). 24 hours post-transfection this solution was aspirated off and normal flow media was applied. Validation of transfection was performed on HUVEC plates (54 hours post-transfection) via DNMT1 western blotting.

5.4.15 Western blot analysis.

HUVECs were lysed in RIPA buffer (Sigma-Aldrich, #R0278) with protease inhibitor (Sigma, 1:50, #P8340). Samples were then cleared for 30 minutes at 4°C under constant agitation. Samples were centrifuged for 1 minute at 10,000g, the supernatant was collected, and a Pierce BCA assay (ThermoFisher Scientific, #23225) was used to determine total protein concentration. Samples were diluted 1:1 in 2x Laemmli sample buffer (Biorad, #1610737) with β-mercaptoethanol (1:200) and boiled for 10 minutes. Equal protein was loaded onto a 10% SDS-PAGE gel and blotted on a nitrocellulose membrane. After transfer, membranes were blocked for 1 hour at room temperature with Odyssey Blocking Buffer (LICOR, Lincoln, NB, #927-40000) and then incubated with primary antibodies overnight at 4°C. Western blots were performed by using primary antibodies directed against DNMT1 (Abcam, 1:1000, ab92314) and GAPDH (EMD Millipore, 0.0625µg/mL, #AB2302). Secondary antibodies were purchased from LICOR and used at a 1:10,000 dilution. A LICOR Odyssey imager was used for blot image acquisition and densitometry analysis.

5.4.16 Monocyte adhesion functional assay.

Human derived monocytes (THP-1 cell line) were purchased from the ATCC. Monocytes were unthawed and maintained in RPMI 1640 (Life Technologies, #11875-093) + 10% fetal bovine serum (Life Technologies Inc) + 0.05mM β -mercaptoethanol per ATCC culture instructions. Monocytes sub-cultured once cell density approached 800,000 cells/mL. Cells were used between passages 2 – 6.

Prior to the adhesion assay, cells were counted to obtain 3,000,000 cells / plate of HUVECs. Cells were pelleted, washed with PBS, pelleted, and then re-suspended in serum-free RPMI media at 1,000,000 cells/mL. Thawed calcein AM was added at 1ug/ml and incubated with cells for 15 minutes at 37°C. After 15 minutes, the reaction was stopped by adding excess serum-free RPMI to the cell solution then pelleted. Cells were washed once with serum-free M199 media, pelleted, and then re-suspended in serum-free M199 at 500,000 cells/mL. Immediately following completion of flow exposure to HUVECs, flow media was removed by aspiration. HUVECs were quickly washed with serum-free M199 media. This media was then aspirated off and 6mL of serum-free M199 + monocytes (3,000,000 / plate) were added to and incubated with HUVECs for 30 minutes at 37°C. Following the 30 minutes, cells were washed twice with PBS to remove unbound monocytes. Adhered monocytes and HUVECs were fixed with 4% PFA for 10 minutes followed by two washes with PBS. Cover slips were mounted with Prolong Gold (Life Technologies). Plates were then imaged using a Nikon TE2000 C1 laser scanning confocal microscope. Randomly selected FOVs (8-9) per condition for 3 independent experiments were obtained. Images were then deidentified and randomized in MATLAB. Images were converted to 8-bit images, set to an equivalent threshold, and bound monocytes were quantified using Fiji's "Analyze Particles" tool (20 μ m² minimum particle size). Results were centered on the mean of all conditions within each independent experiment.

5.4.17 Statistical Analyses.

All results are reported as mean \pm standard error of the mean (SEM), unless otherwise noted. All data were first tested for normality and equal variance. Statistical significance was then assessed by a Student's *t* test or a two-way ANOVA followed by a Holm-Sidak multiple comparisons test, unless otherwise noted (SigmaStat 3.5, Systat Inc). Significance was assessed at $p < 0.05$.

5.5 Results

5.5.1 Collateral artery segments exhibiting limited arteriogenic capacity exhibit hypermethylated DNA 12-weeks after FAL.

Using an FAL model identical to that employed previously by our group to demonstrate differential arteriogenesis at either end of gracilis collateral arteries ([Figure 5.1A](#)), we first sought to determine if these two collateral artery regions displayed differential EC DNA methylation. To this end, we immunolabeled collateral artery cross-sections for 5-methylcytosine, a marker of DNA methylation, along with endothelial cell (CD31) and nuclear (DRAQ5) counter-labels ([Figure 5.1B](#)). These cross sections confirmed our previous findings²³⁷ that muscular (non-reversed) collateral artery regions experience limited arteriogenesis when compared to saphenous (reversed) regions 12-weeks post-FAL ([Figure 5.1C-D](#)). We also found there was a >1.7 -fold increase in circumference-normalized 5-methylcytosine expression in muscular (non-reversed) segments ([Figure 5.1B, F](#)). These results demonstrate that collateral segments exposed to a non-reversed increase in shear stress magnitude exhibit DNA hypermethylation which correlates to limited long-term arteriogenic capacity.

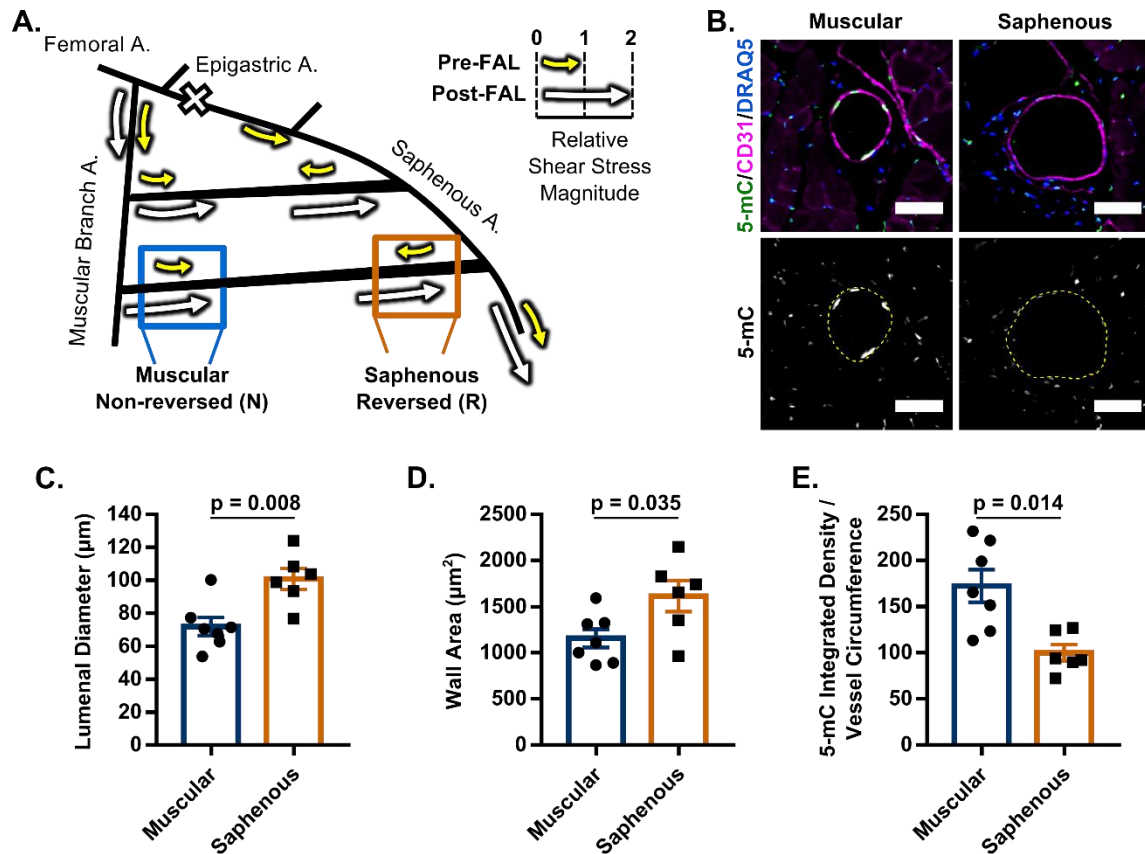


Figure 5.1. Gracilis collateral arteries exposed to a non-reversed increase in shear stress magnitude exhibit limited arteriogenic capacity and hypermethylated DNA.

A) Schematic of the primary gracilis adductor collateral flow pathways after femoral arterial ligation (FAL). Arrows indicate the direction and magnitude of blood flow pre- (yellow) and post- (white) FAL. The femoral artery is ligated just distal to the epigastric artery such that some collateral segments ("muscular") experience a 2-fold increase in shear stress magnitude ("non-reversed" flow), while other segments ("saphenous") are exposed to both a 2-fold increase in shear stress magnitude and reversed flow direction ("reversed" flow). **B)** Representative cross-sections of gracilis collateral regions in C57BL/6 mice 12 weeks post-FAL immunolabeled with 5-methylcytosine (5-mC, green), CD31 (ECs, magenta), and DRAQ5 (nuclei, blue) (Scale bar = 50µm). Dotted yellow line indicates vessel wall. **C-E)** Bar graphs of luminal diameter, collateral wall area, and 5-mC vessel density (total 5-mC per vessel circumference) for both muscular (non-reversed, blue) and saphenous (reversed, orange) regions 12 weeks post-FAL (n=6-7). $p < 0.05$, Student's *t* test. Data are mean \pm SEM.

5.5.2 ECs exposed to a non-reversed increase in shear stress magnitude exhibit augmented DNMT1 expression

To further investigate the influence of these FAL-elicited hemodynamic changes on endothelial cell (EC) DNA methylation, human umbilical vein endothelial cells (HUVECs) were exposed to flow waveforms biomimetic of those experienced by collateral arteries following FAL in-vivo¹⁷⁶ (Figure 5.2A). Briefly, ECs were preconditioned for 24 hours at 15 dynes/cm² to establish basal

endothelial cell alignment and planar cell polarity, thereby mimicking the in-vivo baseline state. A femoral arterial ligation (FAL) was then simulated by a step-wise 100% increase in shear stress, in either the same direction or in the opposite direction, to mimic shear stress changes occurring in the muscular branch (non-reversed flow) and saphenous artery (reversed flow) entrance regions, respectively ([Figure 5.2A](#)). We examined DNMT1 mRNA expression by qRT-PCR 1-hour and 6-hours after our simulated FAL, finding it was transiently increased by ~25% after 1-hour in HUVECs exposed to non-reversed flow, but was unchanged in reversed flow conditions ([Figure 5.2B](#)). DNMT1 mRNA expression returned to basal level by 6-hours after simulated FAL ([Figure 5.2B](#)).

5.5.3 Altered genome-wide DNA methylation patterns in ECs exposed to a arteriogenic shear stress waveforms in-vitro

To then determine how these biomimetic waveforms affect global DNA methylation patterns, we exposed HUVECs to these same flow waveforms. Six hours after simulated FAL, we isolated both genomic DNA (gDNA) and total RNA and performed both reduced representation bisulfite sequencing (RRBS) and mRNA-sequencing (mRNA-seq) on these samples, respectively. Both data sets were mapped to the hg19 human genome assembly (GRCh37/hg19, NCBI, Feb. 2009) and showed a similar degree of coverage between our non-reversed and reversed datasets ([Supplemental Table 5.1](#) and [Supplemental Table 5.2](#)). Additionally, there was a similar degree of total CpG and promoter CpG coverage in both non-reversed and reversed datasets ([Supplemental Figure 5.1](#)).

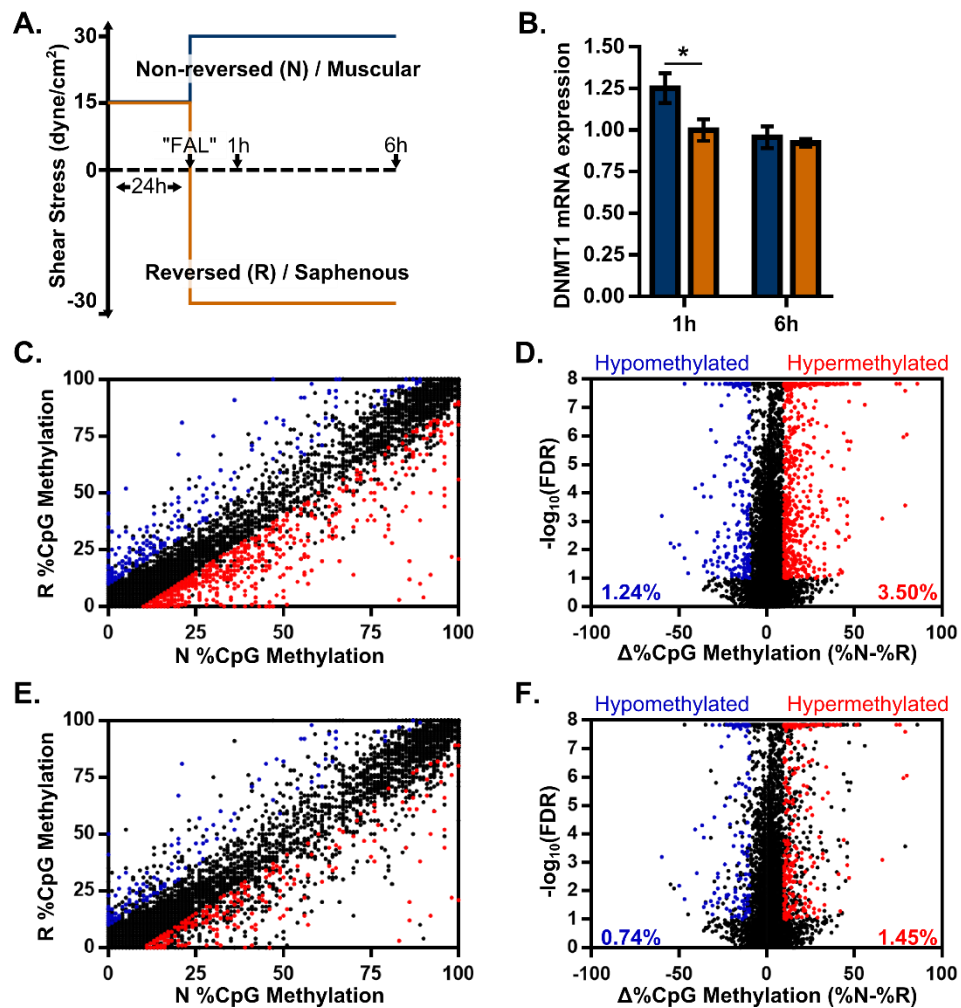


Figure 5.2. ECs exposed to a non-reversed increase in shear stress magnitude exhibit augmented DNMT1 expression and altered genome-wide DNA methylation patterns in-vitro.

A) Schematic depicting biomimetic shear stress conditions applied to HUVECs to simulate non-reversed/muscular (N, blue) and reversed/saphenous (R, orange) regions. **B)** Bar graph of DNMT1 mRNA expression in each flow condition 1-hour or 6-hours post simulated FAL (n=8 for 1hr and n=6 for 6hr). *p<0.05 between reversed and non-reversed within a time-point, Student's t-test. Data are mean ± SEM. **C-D)** Scatter plot and Volcano plot of all DMRs in a gene promoter region (17,227 total). Significant DMRs were designated as hypomethylated (blue, 213 total) or hypermethylated (red, 603 total) with respect to the non-reversed condition ([Supplemental Table 5.3](#)). FDR = false discovery rate. **E-F)** Using our mRNA-Seq dataset, we further filtered this list of significantly hyper- and hypomethylated genes (816 total genes) to contain only those with gene expression changes between non-reversed and reversed conditions in the expected direction based on their change in promoter methylation [i.e. genes that were down-regulated and had a hypermethylated promoter (red, 250 genes) or were up-regulated and had a hypomethylated promoter (blue, 127 genes) in non-reversed versus reversed conditions ([Supplemental Table 5.4](#), [Supplemental Table 5.5](#)).

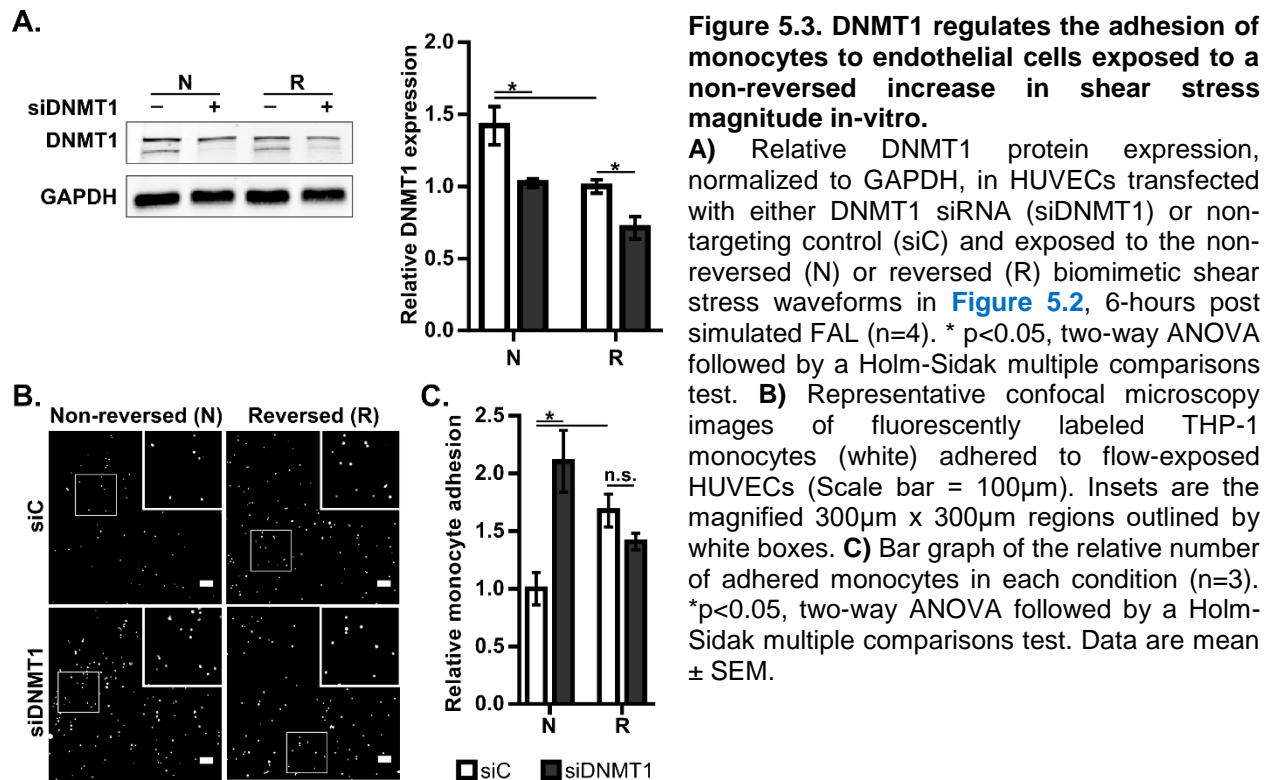
To characterize global DNA methylation changes between non-reversed (N) and reversed (R) data sets in genomic regions, we analyzed the CpG methylation in promoter (transcription start site \pm 1kb), exon, and intron regions. From our RRBS analysis, only read regions with at least 10x CpG read coverage (henceforth termed differentially methylated regions or DMRs) and mRNA expression in both non-reversed and reversed datasets were selected for further analysis. Intron regions displayed a higher degree of CpG methylation compared to exon or promoter regions; however, exon regions displayed the highest mean methylation density within a DMR, consistent with a previous study²⁴¹ (**Supplemental Table 5.2A-B**). Average methylation across gene regions was similar for both non-reversed and reversed data sets. However, when we considered only significantly different (FDR<0.1) DMRs, we observed global hypermethylation in non-reversed conditions compared to reversed conditions, across all gene regions (**Supplemental Table 5.2C-D**). Expectedly, we observed that the degree of promoter methylation inversely correlated with raw gene expression levels on a global scale (**Supplemental Table 5.3**).

As numerous studies have shown that DNA methylation in the promoter region regulates transcription¹⁰⁹, we focused on DNA methylation differences within gene promoters. We found that 4.74% (816/17,227) of DMRs in promoter regions have a \geq | 10% | difference in CpG methylation and an FDR<0.1 between non-reversed and reversed conditions (**Supplemental Table 5.3**). Of these 816 genes, 73.9% (603/816) were hypermethylated in non-reversed compared to reversed conditions (**Figure 5.2C-D**, red). To determine which mechanosensitive genes demonstrate a correlation between relative gene expression and promoter DNA methylation status, we further filtered this list of 816 genes to contain only genes with expression changes in the expected direction based on their change on promoter methylation [i.e. genes that were down-regulated and had a hypermethylated promoter in non-reversed vs. reversed conditions and vice versa] (**Supplemental Table 5.4**). We found that 66.3% of these genes (250/377) were hypermethylated and down-regulated compared to 33.7% (127/377) that were up-regulated and hypomethylated in non-reversed vs. reversed conditions (**Figure 5.2E-F**,

[Supplemental Table 5.4](#) & [Supplemental Table 5.5](#)). We then performed gene ontology analysis on these 377 genes to identify overrepresented pathways ([Supplemental Table 5.6](#)). Cellular metabolism, nucleic acid metabolism, and transcription processes were among the most significantly regulated pathways but a number of additional pathways were overrepresented including protein metabolism, MAPK signaling, apoptosis, cellular localization and transport, and signal transduction

5.5.4 DNMT1 regulates the adhesion of monocytes to endothelial cells exposed to a non-reversed increase in shear stress magnitude in-vitro.

We next sought to determine whether DNMT1 regulates monocyte adhesion to endothelial cells, which is a required step in the arteriogenesis cascade^{52,56,58,60,62,246}. HUVECs were transfected with DNMT1 siRNA (siDNMT1) or non-targeting control (siC) and subjected to the biomimetic shear stress waveforms. DNMT1 expression was increased >40% in HUVECs exposed to non-reversed compared to reversed shear stress waveforms in siC-treated conditions ([Figure 5.3A](#)). This corresponded to a 60% reduction in monocyte adhesion ($p=0.023$) to HUVECs exposed to the non-reversed shear stress waveform ([Figure 5.3B-C](#)). Knockdown of DNMT1 significantly ($p=0.002$) increased monocyte adhesion to HUVECs exposed to the non-reversed waveform compared to siC, while there was no significant effect on HUVECs exposed to the reversed waveform ([Figure 5.3B-C](#)).



5.5.5 The arteriogenic capacity of non-reversed collateral artery segments is restored by DNMT1 inhibition.

Our observations led us to test the hypothesis that arteriogenic capacity can be rescued in non-reversed collateral artery segments by reversing DNA hypermethylation through DNMT1 inhibition. As outlined in [Figure 5.4A](#), we performed FALs on C57BL/6 mice and allowed them to recover for two weeks, which is sufficient time for collaterals to achieve steady-state diameters in this model²³⁷. We then treated mice with daily i.p. injections of 0.1mg/kg 5-Aza-2'-deoxycytidine (5AZA) or 0.1% DMSO vehicle control for an additional two weeks ([Figure 5.4A](#)). 5AZA is a nucleoside analog that preferentially targets DNMT1 via ubiquitin-dependent proteasomal degradation²⁴⁷. 5AZA treatment was shown to be effective in reducing global DNA methylation after only one week by high resolution melting (HRM) ([Figure 5.4B](#)).

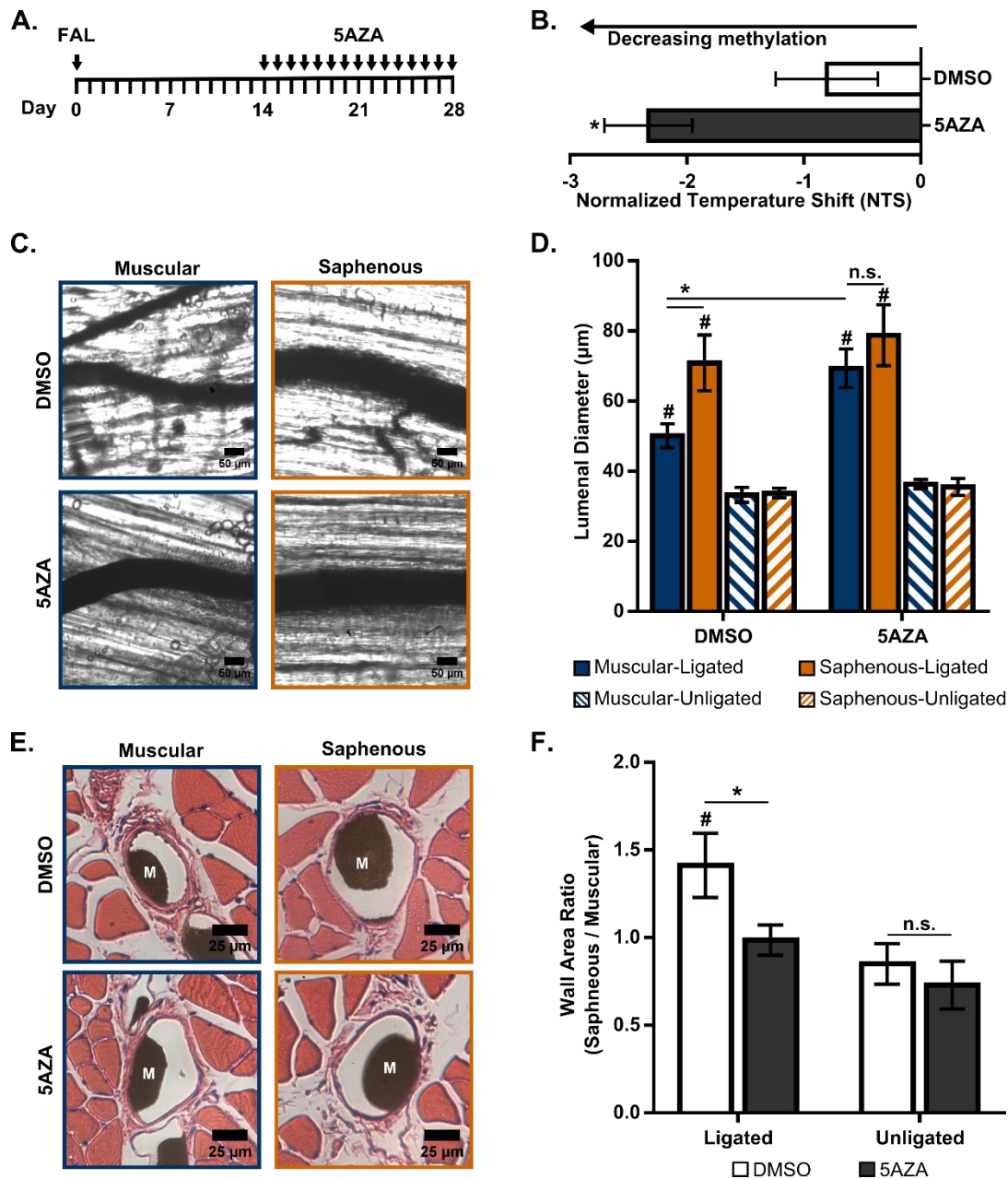


Figure 5.4. The arteriogenic capacity of non-reversed collateral artery segments is restored by DNMT1 inhibition.

A) Experimental treatment time-course. Femoral arterial ligation (FAL) is performed on Day 0. On day 14, mice begin receiving daily i.p. injections of DMSO or 5-Aza-2'-deoxycytidine (5AZA) until day 28. **B)** Bar graph of normalized temperature shift (NTS) determined by high resolution melting (HRM) of LINE1 repeat elements after 7 days treatment (n=6). * $p < 0.05$ between DMSO and 5AZA, Student's t-test. **C)** Representative vascular cast images from muscular (non-reversed) and saphenous (reversed) collateral artery regions 28 days post-FAL from C57BL/6 mice treated according to (B) (Scale Bar = 50 μm). **D)** Bar graph of regional luminal diameter in DMSO or 5AZA treated mice. * $p < 0.05$; # $p < 0.01$ between ligated and unligated within the given region. Two-way ANOVA followed by a Holm-Sidak multiple comparisons test. **E)** Representative H&E stained cross-sections of gracilis collateral artery regions in DMSO and 5AZA treated mice at day 28 post-FAL (Scale bar = 25 μm). Microfil casting material (M) is evident in artery lumen. **F)** Bar graph of wall area ratio of saphenous:muscular collateral regions. # $p < 0.01$ between ligated and unligated for a given treatment; * $p < 0.05$ between DMSO and 5AZA treated mice; Two-way ANOVA followed by a Holm-Sidak multiple comparisons test. Data are mean \pm SEM.

Vascular casting was used to determine collateral artery diameter in both muscular (non-reversed) and saphenous (reversed) regions 28 days post-FAL. Consistent with previous results (Figure 5.1 C and Heuslein et al.²³⁷), we observed limited arteriogenesis in muscular (non-reversed) compared to saphenous (reversed) collateral artery segments in DMSO-treated vehicle control mice. However, DNMT1 inhibition increased the arteriogenic capacity of non-reversed collateral segments by >40%, while there was no significant ($p=0.33$) effect on reversed segments (Figure 5.4 C-D). Cross-sections were used to determine collateral wall area, a metric that further indicated that the differential arteriogenic capacity along the collateral length in DMSO-treated mice was normalized by DNMT1 inhibition (Figure 5.4 E-F). Of note, we observed similar results in FAL-treated Balb/c mice (Supplemental Figure 5.6). Here, DNMT1 inhibition increased arteriogenic capacity by ~44% in non-reversed segments, while there was no effect on reversed segments ($p=0.163$), indicating that this response is not limited to the C57BL/6 strain.

5.5.6 Shear stress set-point is re-established in non-reversed collateral artery segments by DNMT1 inhibition

Finally, we sought to determine if DNMT1-dependent DNA hypermethylation alters non-reversed collateral artery shear stress set-point. Mice were treated with 5AZA or DMSO according to Figure 5.4 A. Relative changes in collateral artery shear rates were then determined by transillumination laser speckle flowmetry (LSF)¹⁷⁶ 28 days post-FAL. Interestingly, in DMSO-treated vehicle control mice, shear stress remained elevated (~2.5-fold) in muscular (non-reversed) collateral segments, while it was restored to pre-FAL levels in saphenous (reversed) segments (Figure 5.5). DNMT1 inhibition restored shear stress in non-reversed segments to pre-FAL levels, whereas there was no significant effect on reversed segments (Figure 5.5).

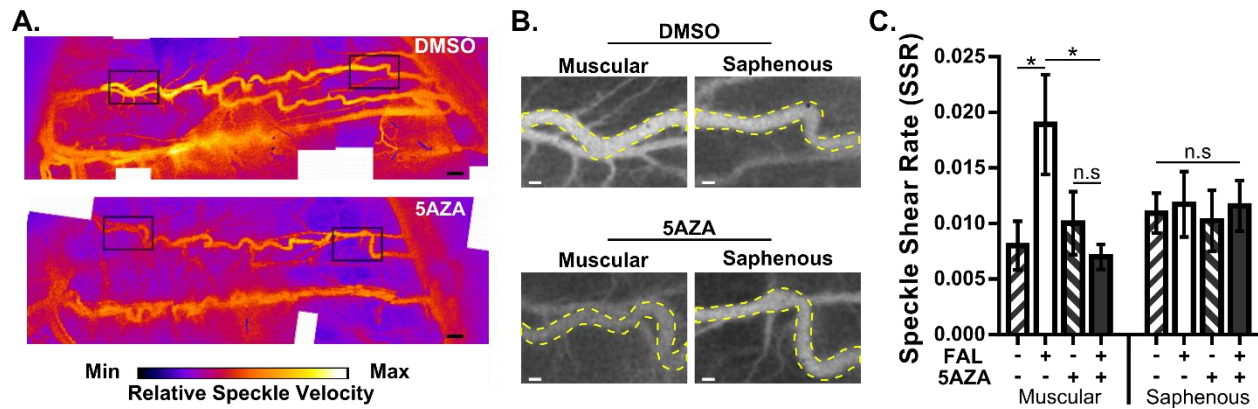


Figure 5.5. Shear stress set-point in non-reversed collateral artery segments is restored by DNMT1 inhibition.

A) Representative relative speckle velocity maps across the primary gracilis muscle collateral pathways 28 days post-FAL in C57BL/6 mice treated with DMSO and 5AZA according to [Figure 5.4A](#). (Scale bar = 500µm). **B)** Greyscale images of the 300pixel X 200pixel boxed regions shown in (A) for both the muscular (non-reversed, left) and saphenous (reversed, right) collateral regions. (Scale bar = 100µm). Dotted line indicates collateral artery ROI used for analysis. **C)** Bar graph of regional speckle shear rate in DMSO and 5AZA treated mice (n=6 for DMSO, n=5 for 5AZA). *p<0.05, n.s. = not significant. Student's t-test. Data are mean ± SEM.

5.6 Discussion

In this study, we tested the hypothesis that DNMT1-dependent EC DNA methylation regulates arteriogenic capacity via adjustments to shear stress set-point. Previously, we demonstrated that collateral artery segments exposed to a non-reversed increase in shear stress magnitude display limited arteriogenic capacity when compared to segments exposed to reversed flow direction. Here, we first determined that these non-reversed collateral segments exhibit global DNA hypermethylation in-vivo. We then applied flow waveforms, biomimetic of those leading to either amplified arteriogenic capacity (i.e. reversed flow) or constrained arteriogenic capacity (i.e. non-reversed flow) in-vivo, to ECs in-vitro, and performed both RRBS and mRNA-sequencing. ECs exposed to the non-reversed waveform exhibited increased DNMT1 expression, genome-wide hypermethylation of significantly regulated gene promoters, and a DNMT1-dependent reduction in pro-arteriogenic monocyte adhesion. Together, this led us to next test whether DNMT1 regulates arteriogenic capacity in-vivo. We ascertained that, in non-reversed collateral artery segments, DNMT1 inhibition rescued arteriogenic capacity and returned the elevated shear stress

in these segments back to its original set point. Collectively, these results demonstrate that DNMT1-dependent DNA hypermethylation constrains arteriogenesis by dampening EC mechanosensing, which effectively augments shear stress set-point. The epigenetic regulation of shear stress set-point may therefore have critical impact on both endogenous and therapeutic arteriogenesis in patients with PAD.

5.6.1 Mapping the EC mechanosensitive DNA methylation to differential arteriogenic capacity

The significance of epigenetics in vascular biology, with roles as regulators of molecular signaling known to drive physiology and as potential therapeutic targets to treat disease, is now well-recognized^{98,99,103}. Both histone modifications and microRNAs regulate flow-mediated EC gene expression^{248–254} and arteriogenesis^{144,151,155,162,163}; however, DNA methylation has only recently been shown to regulate flow-mediated EC gene expression in any context^{238–241}. Moreover, to our knowledge, the role of DNMT1-mediated DNA methylation in arteriogenesis has not been previously studied.

Our study directly maps EC mechanosensitive DNA methylation to differential, sustained arteriogenesis responses. Additionally, by using both RRBS and mRNA-sequencing, we were able to determine mechanosensitive genes whose expression correlated to gene promoter DNA methylation status. Gene ontology analysis of these genes identified a number of pathways crucial for EC mechanotransduction and arteriogenesis, including several metabolism, transcription, MAPK signaling, and cell transport pathways^{43,73}. Of note, SIRT4 was involved in a number of these significantly overrepresented pathways ([Supplemental Figure 5.5](#)). SIRT4 has been shown to disrupt the NFκB pathway whereby overexpression of SIRT4 in ECs abrogates NFκB nuclear translocation and decreases expression of pro-inflammatory cytokines (IL-1β, IL-6, and IL-8), MMP-9, and ICAM-1²⁵⁵. As we also previously reported ECs exposed to non-reversed shear stress waveforms exhibited decreased NFκB-ICAM-1 activity²³⁷ and because the NFκB-ICAM-1

pathway is crucial for arteriogenesis^{56,237,256}, flow-dependent regulation of SIRT4 could be of particular interest.

Additionally, earlier studies examining flow-mediated EC DNA methylation identified Homeobox transcription factors (e.g. HOXA5) as differentially regulated in atheroprone conditions^{239,241}. HOX transcription factors are considered “master regulators” as they regulate EC proliferation, migration, differentiation, morphogenesis, and permeability during development and vascular remodeling processes²⁵⁷. Interestingly, we found HOXB3 to be among the genes down-regulated (decreased 25%) and hypermethylated (20% vs. 0.1% methylation) in non-reversed compared to reversed conditions ([Supplemental Table 5.4](#)). As HOXB3 regulates EC activation and promotes angiogenesis²⁵⁸, our results are consistent with the hypothesis that hypermethylation of the HOXB3 promoter decreases its expression, thereby limiting EC activation and arteriogenic potential of collateral artery segments.

5.6.2 The role of DNMT1 in flow-mediated endothelial inflammation is dependent on hemodynamic context

Monocyte adhesion to an activated endothelium is required for collateral artery growth^{52,56,58,60,62,246,68}. Here, we used a monocyte adhesion assay, which has been previously used to examine flow-mediated EC function^{237,239,259,260}, to determine the role of endothelial DNMT1 expression in regulating this essential step in arteriogenesis. Our results showed increased DNMT1 expression and limited monocyte adhesion to ECs exposed to the non-reversed shear stress waveform. Monocyte adhesion to ECs under non-reversed conditions was enhanced with DNMT1 inhibition but not under reversed conditions, indicating an anti-inflammatory role for DNMT1 that is dependent on hemodynamic context. In contrast, DNMT1 has been shown to also promote EC inflammation in HUVECs exposed to atheroprone flow conditions demonstrated by a DNMT1-dependent increase in monocyte adhesion²³⁹. However, our pro-arteriogenic flow conditions, which include a laminar flow pre-conditioning phase, are very

different from oscillatory, atheroprone conditions²³⁹, further supporting the idea that DNMT1's role in endothelial inflammation is dependent on hemodynamic context. Furthermore, exposure to atheroprone conditions led to a chronic increase in DNMT1 expression²³⁹, whereas our results suggest a transient increase in DNMT1 expression. This adaptive, instead of chronic, response may contribute to context-dependent role of DNMT1 on monocyte adhesion to ECs.

5.6.3 Molecular regulation of collateral artery shear stress set-point

Finally, we have determined that DNMT1-dependent DNA methylation regulates, at least in part, long-term arteriogenic capacity and shear stress set-point. The concept of an arterial homeostatic wall shear stress magnitude (i.e. shear stress set-point) at which vessels maintain a steady-state lumenal diameter⁸⁵ arises from Murray's principle of minimum work⁸⁶. Outward collateral artery growth is therefore hypothesized to stop once normalization to the shear stress set-point has been achieved^{39,41,80,81}. Premature normalization to the shear stress set-point has been a predominant rationalization for the failure of collateral arteries to realize full arteriogenic capacity, frequently reaching only 30-40% of the maximal conductance⁴⁹. However, our results indicate that shear stress actually remains elevated in collateral artery segments exhibiting limited arteriogenic capacity. In essence, EC DNA hypermethylation prevents these collaterals from continuing to increase in diameter; therefore, shear stress remains chronically elevated. Yet, when DNMT1-dependent DNA methylation is inhibited, these collaterals become re-sensitized to their elevated shear stress and are able to resume the arteriogenic process until the original set-point is achieved (**Figure 5.6**). This response appears to require a basal level of DNA methylation as there was no effect of DNMT1 inhibition on collateral artery segments that were not hypermethylated.

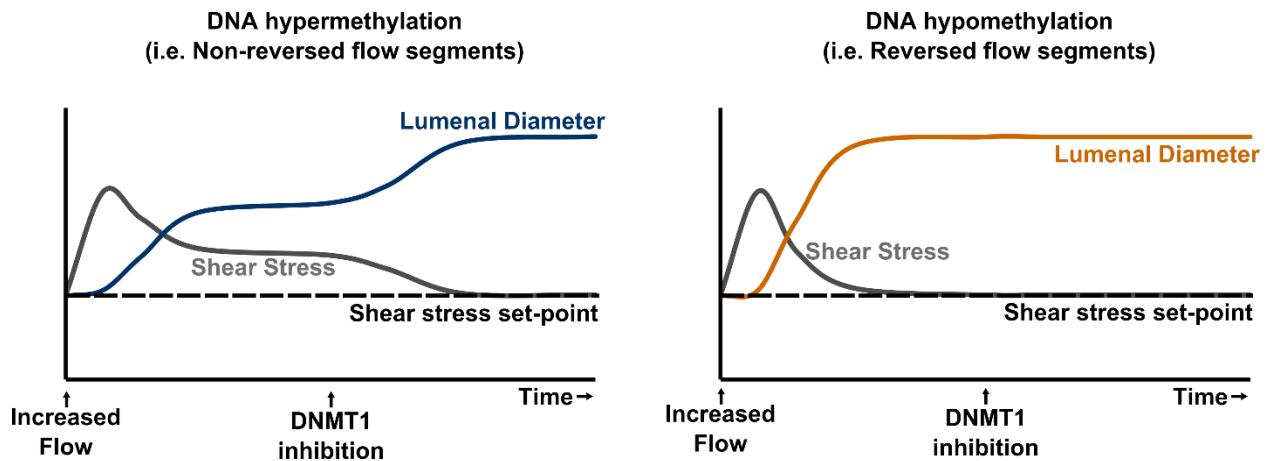


Figure 5.6. Summary of DNMT1-dependent regulation of arteriogenic capacity and shear stress set-point in gracilis adductor collateral arteries following FAL.

There are several other studies that have reported an altered set-point following arterial adaptation. To this end, a left-right carotid anastomosis was used to induce an acute increase in blood flow in the common carotid artery mature and weanling rabbits. Two months later, shear stress remained augmented in mature rabbits due to a lack of compensatory arterial enlargement, whereas weanling rabbits exhibited significant diameter enlargement, enabling for shear stress to normalize to the set-point⁸³. This age-dependent remodeling was also observed in rats in which ligation of the left internal and external carotid arteries increased right carotid blood flow by 46%. After 4-weeks, the right carotid outer diameter increased and shear stress returned to initial values in juvenile but not adult rats⁹⁴. The constrained arterial remodeling and augmented shear stress set-point of aged animals is strikingly similar to the phenotype we observed in non-reversed collateral segments. Given that age alters DNA methylation¹²³, together, these results would be consistent with the hypothesis that acutely increased shear stress yields incomplete arterial remodeling and augmented shear stress set-point due to DNA hypermethylation.

5.6.4 Clinical perspective

Given our results, modulation of the shear stress set-point by DNMT1 inhibition could represent a therapeutic strategy for treating arterial occlusive diseases. By focusing on the molecular mechanisms regulating the maturation stage of arteriogenesis, as opposed to initiation and growth

stages, such an approach could better account for the chronic nature of arterial occlusive diseases in humans. To this end, we didn't begin DNMT1 inhibition until 2-weeks after FAL. Though a few previous studies have demonstrated increased arteriogenic capacity after such a delayed treatment^{58,66,261}, ours is the first to demonstrate an epigenetic mechanism. DNMT1 inhibition may also be clinically advantageous because it appears to avoid the so-called "Janus phenomenon", which refers to the conundrum created by the fact that pro-arteriogenic therapies also tend to promote atherosclerosis²⁶². To this point, DNMT1 inhibition with 5AZA reverses DNA hypermethylation induced by atheroprone shear stress^{239,240} and reduces atherosclerotic plaque size²³⁹. Ultimately, because shear-stress induced changes in DNMT1 expression markedly affect both atherosclerosis and arteriogenic capacity, DNMT1 may represent an interesting target for PAD therapy.

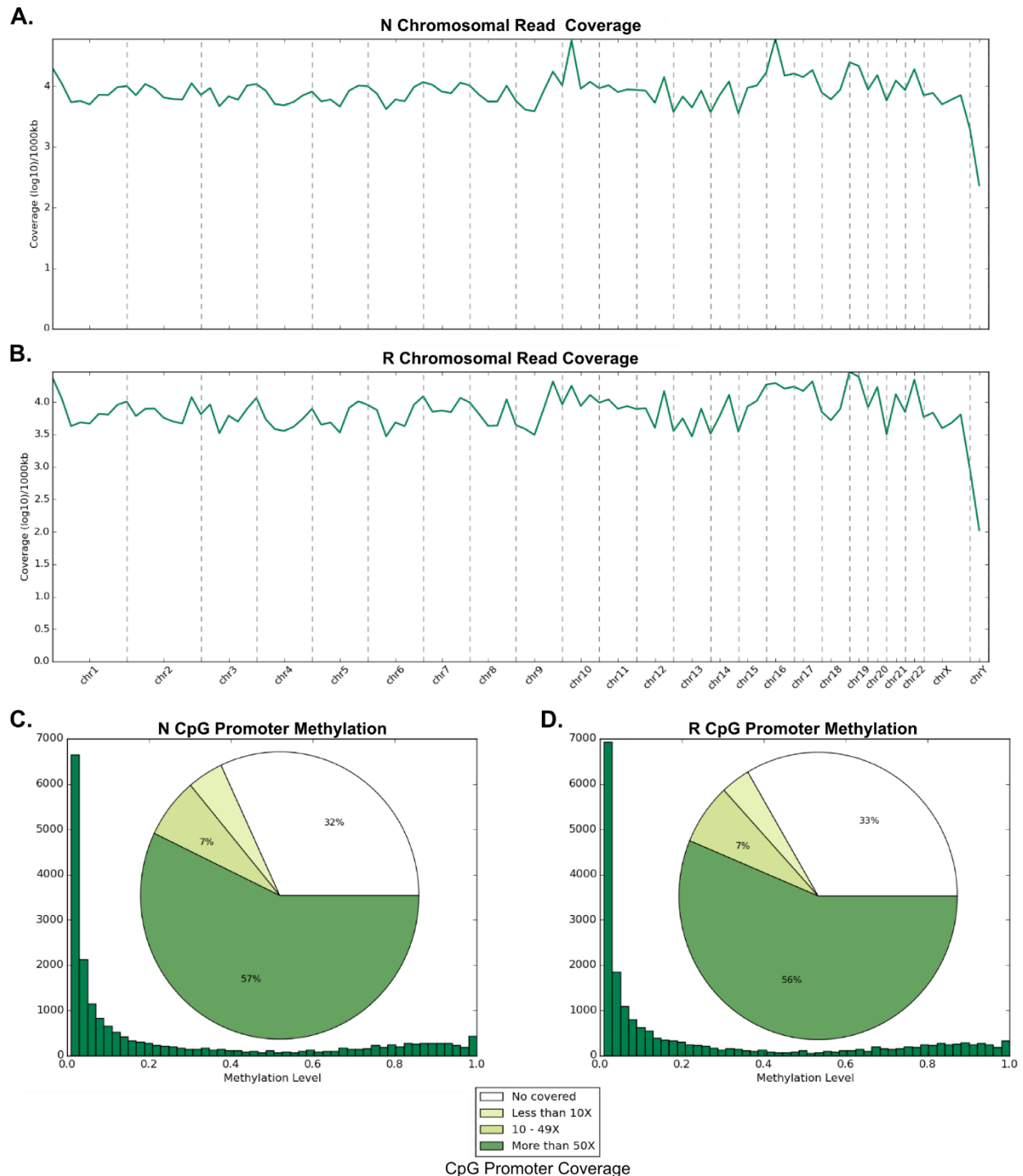
5.7 Acknowledgements

The authors would like to thank the University of Virginia Research Histology Core (under the direction of Sheri VanHoose) for histological tissue processing.

5.8 Sources of Funding

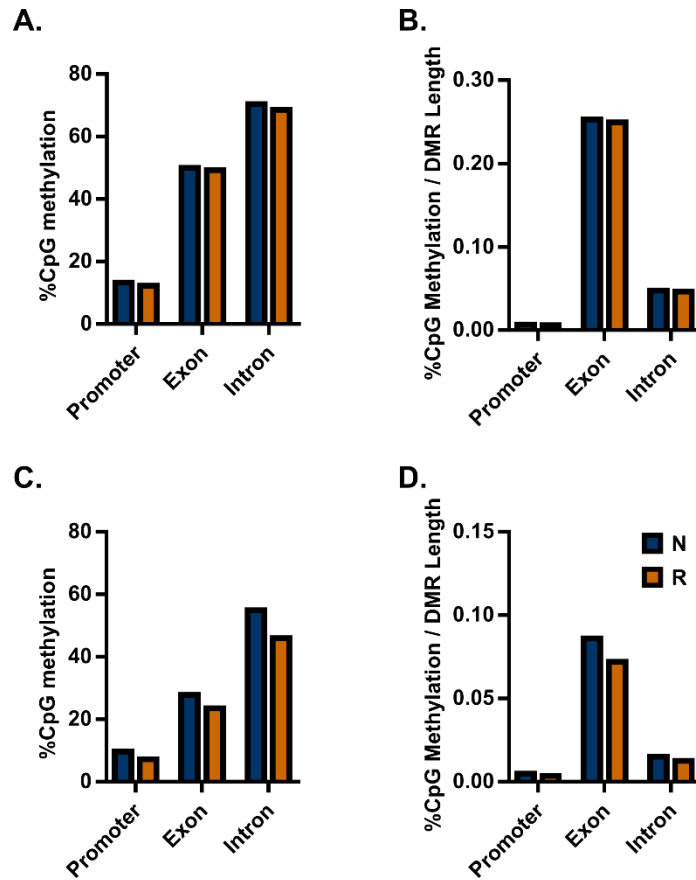
Supported by NIH R03 EB017927 and R01 EB020147. JLH was supported by National Science Foundation Graduate Research Fellowship Program Grant No. NSF DGE-1315231.

5.9 Supplemental Figures



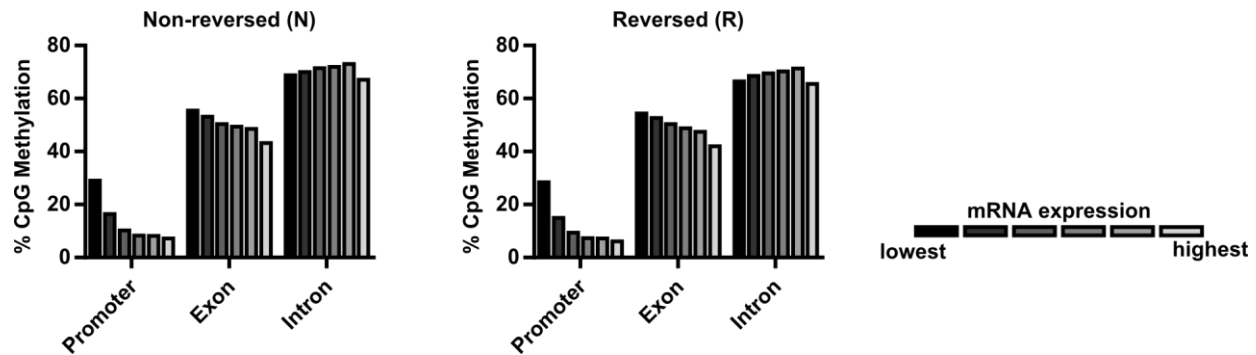
Supplemental Figure 5.1. Similar degree of methylation coverage in HUVECs exposed to biomimetic shear stress waveforms.

A-B) Representation of methylation read coverage by chromosome across the genome for HUVECs exposed to non-reversed (N) and reversed (R) shear stress waveforms **C-D)** Pie charts of CpG site coverage and histograms of methylation level in gene promoter region in HUVECs exposed to non-reversed (N) and reversed (R) shear stress waveforms.



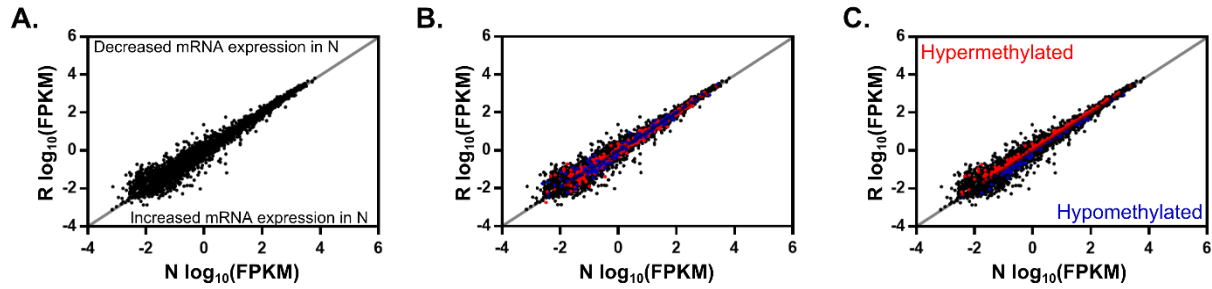
Supplemental Figure 5.2. DNA methylation across different gene regions.

A-B) Mean %CpG methylation (#methylated CpG sites / total CpG sites in given DMR) and mean %CpG methylation normalized by DMR length in promoter, exon, and intron gene regions for all DMRs with $\geq 10\times$ CpG coverage in a given DMR. **C-D)** Mean %CpG methylation and mean %CpG methylation normalized to DMR length in promoter, exon, and intron gene regions for all DMRs with $\geq 10\times$ CpG coverage in a given DMR and $FDR < 0.1$ between HUVECs exposed to non-reversed (blue) and reversed (orange) shear stress waveforms.



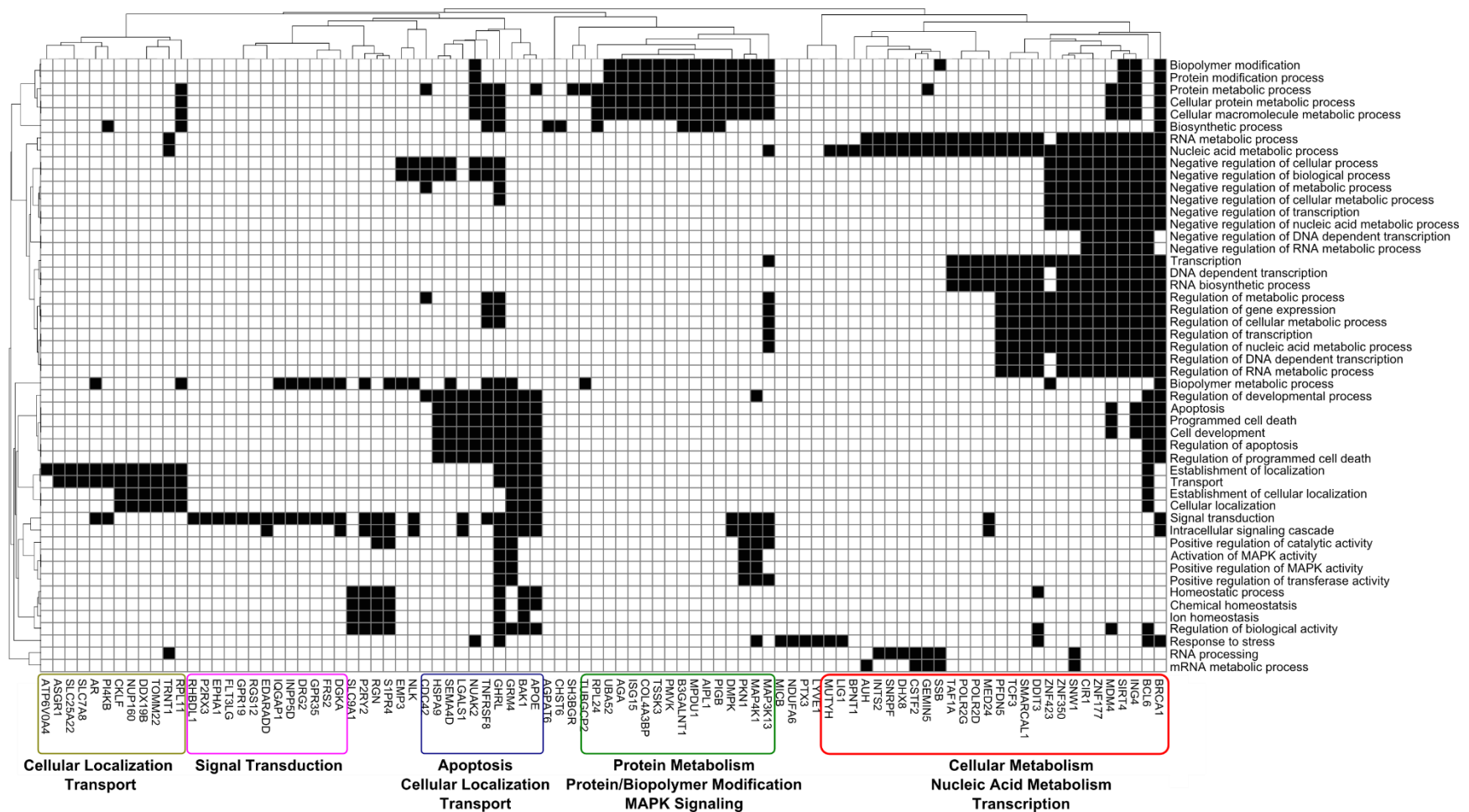
Supplemental Figure 5.3. DNA methylation negatively correlates to mRNA expression in gene promoter regions.

Raw mRNA expression (FPKM) from HUVECs exposed to either non-reversed/N or reversed/R shear stress waveforms was ordered from lowest mRNA expression to highest and divided into six, equal sized bins. Mean %CpG methylation was determined for each bin within the promoter, exon, and intron gene regions. Only DMRs with $\geq 10\times$ CpG coverage were included in the analysis. FPKM = fragments per kilobase of transcript per million mapped reads.



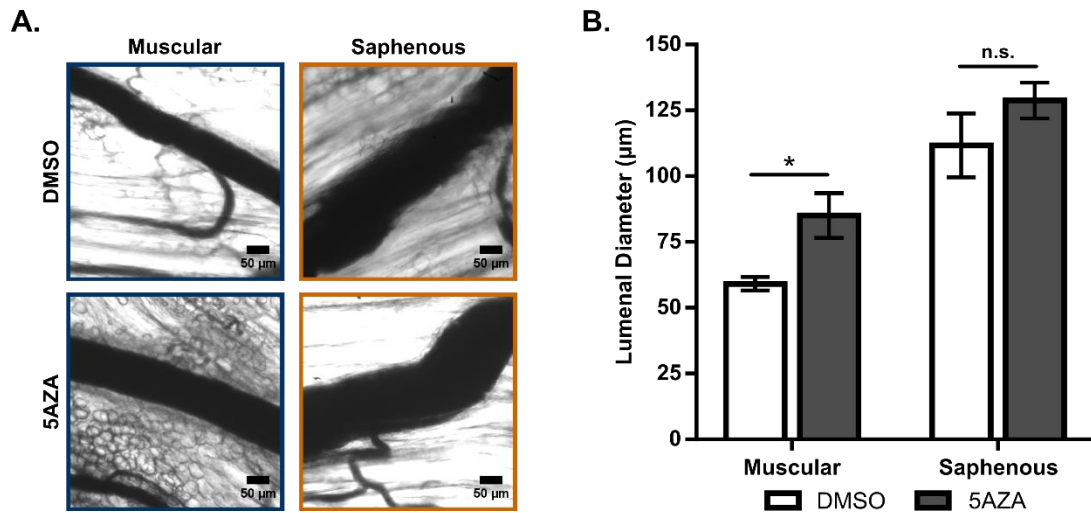
Supplemental Figure 5.4. Genome-wide mRNA expression patterns in HUVECs exposed to arteriogenesis biomimetic shear stress waveforms.

A-C) HUVECs were exposed to biomimetic shear stress waveforms, RNA was isolated 6-hours post-FAL, and genome-wide mRNA expression was determined by mRNA-sequencing. Scatter plots indicate relative expression of each gene represented in both non-reversed (N) and reversed (R) conditions and contained in our RRBS dataset (17,227 total). **A)** Indicates all genes corresponding to promoter regions of genes with a methylation ratio difference $\geq |0.10|$ and $FDR < 0.1$ between non-reversed and reversed conditions. **B)** Contains all 17,227 genes, where genes with significantly hypermethylated promoters (in N relative to R) are red and hypomethylated genes are blue, corresponding to [Supplemental Table 5.3](#). **C)** All 17,227 genes, where significantly hyper- or hypomethylated genes are also downregulated or upregulated, respectively, in N relative to R, corresponding to [Supplemental Table 5.4](#) and [Supplemental Table 5.5](#). FPKM = fragments per kilobase of transcript per million mapped reads.



Supplemental Figure 5.5. Top 50 most significantly overrepresented gene ontology (GO) biological processes.

Heat map of the top 50 significantly overrepresented biological process GO terms (columns) for genes with differential changes in expression corresponding to significantly different CpG promoter methylation in non-reversed vs. reversed conditions (i.e. genes that were down-regulated and had a hypermethylated promoter or were up-regulated and had a hypomethylated promoter in non-reversed versus reversed conditions) as listed in [Supplemental Table 5.4](#) and [Supplemental Table 5.5](#). Black indicates the presence of a gene in a GO process whereas white indicates its absence. Only genes present in at least one GO process are shown.



Supplemental Figure 5.6. DNMT1 inhibition also restores the arteriogenic capacity of non-reversed collateral artery segments in Balb/c mice

A) Representative vascular cast images from muscular (non-reversed) and saphenous (reversed) collateral artery regions 28 days post-FAL from Balb/c mice treated according to [Figure 5.4A](#). (Scale Bar = 50µm). **B)** Bar graph of regional luminal diameter in DMSO or 5AZA treated mice. * $p < 0.05$ between DMSO and 5AZA treated mice; Two-way ANOVA followed by a Holm-Sidak multiple comparisons test. Data are mean \pm SEM.

5.10 Supplemental Tables

Supplemental Table 5.1. Summary of total number of reads, mapping ratio, and CpG coverage in RRBS datasets.

Label	Species	Seq Type	Total Read #	Mapped Read #	Mapping Ratio	Unique CpG	CpG Coverage (X)	Bisulfite Conversion Rate
N	human (hg19)	MiniSeq	34,206,095	15,411,220	45.05%	7,126,531	7	98.24%
R	human (hg19)	MiniSeq	23,777,663	13,438,821	56.52%	7,269,847	7	99.21%

Supplemental Table 5.2. Summary of total number of reads, mapped reads, and mapping ratio for mRNA-seq datasets.

Label	Species	Seq Type	Total Read Count	Total Read Count After QC	Mapped Read Count	Mapping Ratio
N	human (hg19)	mRNASeq	93,600,141	91,395,543	86,700,087	94.90%
R	human (hg19)	mRNASeq	85,738,933	83,771,202	79,624,282	95.00%

Supplemental Table 5.3. All DMRs corresponding to the promoter regions of genes with a methylation ratio difference $\geq |0.10|$ and $FDR < 0.1$ between non-reversed and reversed conditions

gene name	R methylation %	N methylation %	methylation % difference (N-R)	methylation adjusted Pvalue	mRNASeq Nvalue	mRNASeq Rvalue	mRNASeq Log2FC
EPS8L3	81	21	-60	6.33E-04	0.03	0.01	1.90
DSCR8	91	36	-55	5.92E-03	0.22	0.28	-0.36
MAB21L2	100	47	-53	8.13E-03	0.01	0.07	-2.72
EGFLAM	50	0	-50	6.61E-03	0.77	0.39	0.98
C8orf74	52	5	-47	1.44E-08	0.01	0.03	-1.55
MICB	67	20	-47	1.94E-02	8.63	5.20	0.73
AQP4-AS1	75	30	-45	6.69E-02	0.13	0.16	-0.38
BPNT1	41	0	-41	6.95E-05	27.27	24.52	0.15
POM121L9P	98	58	-40	2.38E-03	0.02	0.01	1.59
ITGBL1	92	55	-37	4.98E-05	0.89	0.65	0.47
PLCH2	81	45	-36	1.33E-04	0.04	0.02	1.30
SYNPO2L	92	56	-36	3.69E-02	0.16	0.13	0.36
PMEPA1	35	0	-35	1.44E-08	14.44	17.10	-0.24
BTBD16	100	65	-35	2.46E-02	0.11	0.41	-1.90
CSAD	83	48	-35	2.73E-02	9.61	7.18	0.42
NRG1	100	66	-34	5.92E-02	29.29	34.46	-0.23
SLC22A15	33	1	-32	5.96E-07	0.01	0.01	-1.18
POTEF	95	63	-32	1.38E-04	0.02	0.02	-0.51
ACOT2	82	50	-32	2.29E-02	0.87	0.46	0.91
ACP5	57	26	-31	1.48E-08	46.28	30.30	0.61
CCDC74B- AS1	94	63	-31	3.27E-02	0.12	0.11	0.11
C9orf153	74	43	-31	6.69E-02	0.09	0.07	0.39
CD79B	71	41	-30	2.58E-05	0.38	0.34	0.16
KIAA1549L	80	50	-30	4.65E-03	4.04	4.36	-0.11
LAMB3	95	65	-30	1.18E-02	10.22	8.45	0.27
LAMB3	95	65	-30	1.18E-02	10.22	8.45	0.27
PAPOLB	52	23	-29	1.60E-06	0.00	0.02	-2.59
METTL5	48	20	-28	2.43E-03	66.99	63.77	0.07
ZNF503-AS1	33	5	-28	3.35E-03	0.38	0.20	0.93
RGS12	31	3	-28	8.09E-03	29.65	28.00	0.08
PLEKHB1	60	32	-28	2.61E-02	2.43	2.29	0.09
KCNK2	69	41	-28	3.75E-02	0.09	0.13	-0.49
PDGFB	41	13	-28	9.14E-02	3.77	4.11	-0.13
EZH1	45	18	-27	1.47E-08	13.01	10.64	0.29
ZNF423	92	65	-27	1.89E-02	2.56	2.41	0.08
CCDC152	46	20	-26	8.49E-08	1.33	1.11	0.26
GGT1	34	9	-25	2.79E-02	74.25	78.80	-0.09
SLC13A3	25	1	-24	1.44E-08	0.07	0.09	-0.34
MPDU1	52	28	-24	1.02E-05	44.96	44.47	0.02
PRKACA	54	30	-24	1.18E-03	67.05	61.07	0.13
FGL2	35	11	-24	7.45E-03	0.04	0.05	-0.21
TOMM22	23	0	-23	1.44E-08	75.48	58.83	0.36
PLA2G4C	36	13	-23	5.39E-06	18.51	39.81	-1.11
LINC00672	88	65	-23	1.42E-02	0.32	0.25	0.34
KLK10	26	3	-23	1.61E-02	0.37	0.32	0.22
GGT1	30	7	-23	1.85E-02	74.25	78.80	-0.09

DAND5	59	36	-23	4.23E-02	0.31	0.20	0.67
ZNF597	49	27	-22	1.48E-08	1.27	1.51	-0.25
DRG2	33	11	-22	3.61E-08	10.53	10.52	0.00
ERAL1	22	0	-22	1.97E-03	41.46	49.11	-0.24
CPVL	33	11	-22	3.62E-03	0.07	0.11	-0.76
SPIN3	42	20	-22	1.37E-02	1.37	1.01	0.44
CSTF2T	23	2	-21	1.44E-08	9.50	8.92	0.09
INPP5D	23	2	-21	1.44E-08	60.83	48.65	0.32
HELB	46	25	-21	5.02E-06	1.03	0.93	0.14
RAX2	83	62	-21	4.50E-05	0.03	0.03	0.01
MSL3	40	19	-21	5.74E-05	86.41	96.78	-0.16
PKN1	56	35	-21	5.04E-02	59.22	41.39	0.52
RNF166	28	8	-20	1.44E-08	16.37	15.28	0.10
CLASRP	26	6	-20	1.44E-08	27.58	25.50	0.11
ITGAM	74	54	-20	6.76E-02	0.03	0.09	-1.51
BPIFB1	80	60	-20	8.40E-02	0.11	0.11	0.03
NAA60	46	27	-19	1.87E-08	105.11	95.31	0.14
SIRT4	47	28	-19	2.69E-04	0.79	0.68	0.21
RBMX2	37	18	-19	2.48E-02	22.84	22.56	0.02
NLRP11	68	49	-19	4.81E-02	0.00	0.00	-0.23
ZC3H4	18	0	-18	1.44E-08	15.21	10.06	0.60
ATHL1	31	13	-18	1.65E-08	3.98	3.19	0.32
S1PR4	24	6	-18	1.94E-06	0.23	0.12	0.90
HPRT1	38	20	-18	6.50E-06	31.01	35.05	-0.18
RGN	65	47	-18	1.12E-04	0.18	0.06	1.51
COMMD6	29	11	-18	7.77E-03	98.08	105.99	-0.11
RCN3	95	77	-18	8.90E-03	82.51	39.28	1.07
SLC7A8	28	10	-18	1.12E-02	2.60	2.49	0.06
SPC24	31	13	-18	1.67E-02	6.08	5.49	0.15
SLC6A10P	95	77	-18	4.42E-02	0.00	0.02	-2.87
SERPINA4	82	64	-18	7.75E-02	0.10	0.06	0.58
STYX	17	0	-17	1.44E-08	26.56	25.30	0.07
MED1	22	5	-17	3.94E-05	19.87	20.22	-0.03
SPON2	38	21	-17	1.30E-03	0.19	0.28	-0.60
MAP4K1	26	9	-17	2.84E-03	0.93	0.54	0.79
PCDHB3	48	31	-17	1.91E-02	0.04	0.02	1.26
C8orf44	17	1	-16	1.44E-08	14.52	12.54	0.21
PHF14	20	4	-16	1.45E-08	20.98	21.22	-0.02
HEXB	17	1	-16	1.47E-08	410.11	529.01	-0.37
TTC38	19	3	-16	1.52E-08	12.85	12.93	-0.01
PLEKHG6	30	14	-16	1.55E-08	0.34	0.12	1.47
PLEKHG6	30	14	-16	1.55E-08	0.34	0.12	1.47
SPAG4	24	8	-16	1.67E-08	1.89	1.20	0.66
RGMA	28	12	-16	1.12E-06	0.01	0.01	-0.28
APOE	17	1	-16	1.63E-06	4.60	4.09	0.17
TMEM209	52	36	-16	1.07E-03	1.92	1.17	0.71
TCF3	34	18	-16	3.92E-03	71.64	55.68	0.36
DBNDD2	95	79	-16	4.39E-03	14.96	17.62	-0.24
C1orf86	27	11	-16	3.81E-02	4.82	4.10	0.24
PKD1L1	76	60	-16	7.03E-02	1.48	1.20	0.30
AMPD2	70	54	-16	7.53E-02	41.20	35.57	0.21
CALD1	42	26	-16	8.38E-02	571.85	513.31	0.16
PPID	16	1	-15	1.52E-08	47.81	64.65	-0.44
ZNF493	15	0	-15	2.03E-08	5.54	5.51	0.01

BAK1	21	6	-15	8.76E-05	3.54	2.95	0.27
BDKRB2	25	10	-15	2.31E-03	0.03	0.13	-2.21
RPL38	24	9	-15	2.94E-03	2612.63	3092.61	-0.24
ANKRD33	35	20	-15	3.71E-03	0.09	0.07	0.42
SLCO1A2	100	85	-15	7.77E-03	0.10	0.24	-1.30
ASGR1	73	58	-15	4.08E-02	3.04	2.98	0.03
LPIN2	15	1	-14	1.44E-08	2.38	8.63	-1.86
TAB1	14	0	-14	1.44E-08	5.50	8.00	-0.54
DKKL1	19	5	-14	1.47E-08	0.17	0.12	0.46
DKKL1	19	5	-14	1.47E-08	0.17	0.12	0.46
BRCA1	18	4	-14	1.74E-06	5.17	5.14	0.01
ZNF207	27	13	-14	9.74E-06	168.27	171.22	-0.03
PHF17	14	0	-14	9.24E-05	13.84	12.17	0.19
MBNL3	26	12	-14	1.25E-04	0.67	0.73	-0.12
MED24	14	0	-14	2.69E-04	52.08	47.89	0.12
OCRL	20	6	-14	4.18E-04	16.60	13.84	0.26
SYCE1L	97	83	-14	2.29E-02	16.68	14.18	0.23
C12orf36	93	79	-14	9.90E-02	0.14	0.04	1.94
AGPAT6	13	0	-13	1.44E-08	68.63	66.13	0.05
DGCR14	15	2	-13	1.44E-08	4.17	4.07	0.04
IDUA	13	0	-13	1.52E-08	8.72	5.44	0.68
SNX29	17	4	-13	1.07E-05	5.30	5.94	-0.17
USP16	28	15	-13	2.24E-05	15.29	15.39	-0.01
ADAM32	30	17	-13	3.37E-05	1.50	1.52	-0.02
DMPK	23	10	-13	4.92E-04	39.58	37.02	0.10
TCEB3B	97	84	-13	2.64E-03	0.01	0.01	-0.06
PCYT1B	19	6	-13	6.38E-03	0.07	0.10	-0.46
SLC5A4	100	87	-13	1.42E-02	0.10	0.08	0.33
DMKN	14	1	-13	2.24E-02	0.09	0.05	0.78
C1QTNF1	35	22	-13	3.09E-02	0.46	0.22	1.06
MUTYH	13	0	-13	4.32E-02	4.19	4.03	0.06
TOE1	13	0	-13	4.32E-02	3.62	3.14	0.21
NRN1L	68	55	-13	5.14E-02	34.26	35.66	-0.06
FTLP10	94	81	-13	6.78E-02	0.04	0.11	-1.50
LINC00574	13	0	-13	8.23E-02	0.13	0.12	0.10
RFESD	12	0	-12	1.44E-08	0.57	0.22	1.35
RFESD	12	0	-12	1.44E-08	0.57	0.22	1.35
PI4KB	13	1	-12	1.47E-08	31.10	26.02	0.26
PI4KB	13	1	-12	1.47E-08	31.10	26.02	0.26
TSSK3	20	8	-12	1.67E-08	0.53	0.48	0.16
EDARADD	12	0	-12	3.66E-08	0.20	0.16	0.29
SUMO2	28	16	-12	2.15E-06	441.13	338.71	0.38
RHBDL1	27	15	-12	4.01E-06	0.13	0.10	0.50
SUGT1P3	25	13	-12	5.12E-06	1.39	2.47	-0.83
MARS	47	35	-12	4.05E-05	90.69	97.27	-0.10
SNAPC5	21	9	-12	4.51E-04	30.90	31.57	-0.03
MRPL28	20	8	-12	2.57E-03	39.19	34.56	0.18
KBTBD7	39	27	-12	3.96E-03	2.99	2.59	0.21
FXVD2	88	76	-12	1.89E-02	15.81	24.14	-0.61
MORN3	91	79	-12	6.08E-02	0.67	0.45	0.58
APOBEC3D	12	0	-12	7.81E-02	11.13	9.90	0.17
C19orf33	47	35	-12	8.20E-02	39.79	40.11	-0.01
CKS1B	12	0	-12	8.87E-02	5.51	5.85	-0.09
SHC1	12	0	-12	8.87E-02	202.71	208.14	-0.04

ASL	14	3	-11	1.44E-08	70.34	67.45	0.06
ERICH1	13	2	-11	1.51E-08	37.35	23.08	0.69
TUBGCP2	22	11	-11	1.55E-08	15.68	12.74	0.30
GP1BB	16	5	-11	1.57E-08	8.91	9.43	-0.08
ARC	21	10	-11	1.64E-08	0.02	0.06	-2.00
CRISPLD2	11	0	-11	2.32E-08	2.74	2.11	0.38
RASSF1	12	1	-11	7.16E-07	5.10	5.37	-0.07
P2RY2	16	5	-11	7.63E-07	1.54	1.44	0.10
P2RY2	16	5	-11	7.63E-07	1.54	1.44	0.10
RGPD2	100	89	-11	1.51E-05	0.08	0.09	-0.24
PMVK	13	2	-11	3.89E-05	7.59	6.70	0.18
MSL3	38	27	-11	3.12E-04	86.41	96.78	-0.16
RBP5	23	12	-11	4.10E-04	0.87	0.87	0.00
FLT3LG	22	11	-11	5.74E-04	782.26	935.32	-0.26
ZC4H2	26	15	-11	5.96E-04	8.73	8.31	0.07
C20orf196	15	4	-11	7.96E-04	2.89	2.91	-0.01
MSL3	39	28	-11	8.02E-04	86.41	96.78	-0.16
MGAT5B	21	10	-11	1.27E-03	0.15	0.08	0.91
SPON2	24	13	-11	1.34E-03	0.19	0.28	-0.60
KCNH2	34	23	-11	8.19E-03	0.02	0.03	-0.34
ZNF177	21	10	-11	1.51E-02	10.72	9.81	0.13
MYADM	22	11	-11	1.86E-02	32.83	34.40	-0.07
ZNF682	37	26	-11	2.03E-02	1.07	0.90	0.26
HYPK	19	8	-11	2.37E-02	304.92	347.00	-0.19
AR	24	13	-11	2.86E-02	2.56	2.19	0.23
MYO1H	99	88	-11	3.22E-02	0.09	0.30	-1.79
DNAJC8	51	40	-11	3.70E-02	113.66	116.81	-0.04
NUP160	27	16	-11	4.44E-02	37.20	35.05	0.09
BDNF	13	2	-11	4.61E-02	2.82	3.05	-0.11
LYNX1	67	56	-11	9.05E-02	4.97	5.21	-0.07
EIF4G1	12	2	-10	1.44E-08	193.74	209.84	-0.12
GRM4	13	3	-10	1.51E-08	0.00	0.00	0.08
HMBS	12	2	-10	2.40E-08	5.93	6.03	-0.02
IRF7	20	10	-10	2.64E-08	1.87	2.87	-0.62
LGALS1	10	0	-10	6.26E-08	1405.19	820.91	0.78
LZTS2	11	1	-10	1.93E-07	10.24	10.10	0.02
USP39	16	6	-10	2.29E-07	55.11	72.89	-0.40
C2orf68	16	6	-10	2.29E-07	7.45	6.91	0.11
CREB3L1	12	2	-10	1.10E-06	1.10	1.01	0.12
ASL	18	8	-10	2.56E-06	70.34	67.45	0.06
FAM57B	11	1	-10	2.91E-06	0.11	0.14	-0.42
TNK1	14	4	-10	7.13E-06	0.16	0.56	-1.84
RGMA	18	8	-10	1.33E-05	0.01	0.01	-0.28
NOP2	12	2	-10	1.17E-04	24.14	22.62	0.09
CCDC78	21	11	-10	2.50E-04	0.10	0.07	0.57
THUMPD1	20	10	-10	2.81E-04	29.93	34.48	-0.20
NFRKB	18	8	-10	2.62E-03	5.75	6.45	-0.17
POC5	24	14	-10	2.71E-03	6.05	4.78	0.34
TTC25	30	20	-10	6.50E-03	0.13	0.07	0.78
NUP210L	41	31	-10	7.33E-03	0.04	0.04	-0.03
WDR38	29	19	-10	1.48E-02	0.05	0.05	0.10
DDX43	96	86	-10	1.49E-02	0.26	0.17	0.63
JDP2	98	88	-10	2.33E-02	3.98	5.75	-0.53
POM121L10P	89	79	-10	3.81E-02	0.06	0.06	-0.15

SEMA4D	99	89	-10	4.39E-02	4.05	3.11	0.38
TRIM72	41	31	-10	4.91E-02	0.04	0.04	-0.23
CD320	71	61	-10	5.49E-02	25.89	23.20	0.16
PKP3	59	49	-10	5.49E-02	0.18	0.09	1.04
WBSCR27	38	28	-10	9.71E-02	0.13	0.19	-0.50
ADPGK-AS1	4	14	10	1.44E-08	1.01	1.25	-0.31
PDLIM5	3	13	10	1.44E-08	46.85	54.30	-0.21
KIAA1598	1	11	10	1.44E-08	1.42	1.52	-0.10
KLC4	1	11	10	1.44E-08	11.20	11.40	-0.03
KLC4	1	11	10	1.44E-08	11.20	11.40	-0.03
POLR3H	1	11	10	1.44E-08	10.20	9.57	0.09
POLR3H	1	11	10	1.44E-08	10.20	9.57	0.09
MRPL2	1	11	10	1.44E-08	30.42	27.23	0.16
DEGS1	6	16	10	1.44E-08	147.47	120.36	0.29
SLC12A6	4	14	10	1.44E-08	20.84	23.38	-0.17
TRNT1	6	16	10	1.46E-08	26.46	31.82	-0.27
PITPNA	5	15	10	1.47E-08	106.60	108.69	-0.03
WDR85	7	17	10	1.48E-08	8.45	6.47	0.39
VKORC1	9	19	10	1.52E-08	55.52	42.57	0.38
ZNF707	8	18	10	1.57E-08	5.34	4.73	0.17
SSB	2	12	10	1.57E-08	654.63	681.75	-0.06
NLK	7	17	10	1.60E-08	18.02	18.78	-0.06
B3GALNT1	9	19	10	1.67E-08	7.45	8.31	-0.16
CXXC1	6	16	10	1.76E-08	28.92	22.11	0.39
TSPAN15	3	13	10	8.05E-08	34.23	30.63	0.16
C12orf29	2	12	10	9.87E-08	10.01	9.63	0.06
UBA52	9	19	10	2.17E-07	365.84	531.97	-0.54
SDHC	12	22	10	2.99E-07	42.94	46.05	-0.10
C11orf92	6	16	10	1.63E-06	0.08	0.09	-0.29
SNRNP35	15	25	10	2.32E-06	10.38	5.57	0.90
HCG11	8	18	10	7.14E-06	2.54	2.32	0.13
ZFR	7	17	10	8.39E-06	42.36	47.72	-0.17
C9orf3	10	20	10	1.28E-05	44.26	43.18	0.04
CCDC103	3	13	10	6.69E-05	6.99	5.36	0.38
PTGDS	8	18	10	6.81E-05	18.31	13.32	0.46
CORO1B	18	28	10	1.19E-04	51.78	37.39	0.47
STIL	9	19	10	1.24E-04	2.96	2.74	0.11
PPP1R14A	13	23	10	1.75E-04	6.36	7.54	-0.25
ZFYVE26	8	18	10	2.62E-04	18.97	15.73	0.27
KCNJ11	12	22	10	3.43E-04	0.11	0.06	0.84
STX6	10	20	10	5.54E-04	28.34	26.31	0.11
ZNF552	18	28	10	5.73E-04	0.24	0.46	-0.95
PAIP2	10	20	10	6.26E-04	200.32	160.85	0.32
GYPC	12	22	10	9.27E-04	1.17	1.08	0.11
MAPK15	11	21	10	1.08E-03	0.05	0.02	1.49
RPL11	15	25	10	1.36E-03	917.46	985.09	-0.10
TRAPPC12	12	22	10	1.50E-03	17.57	18.98	-0.11
KLHL12	37	47	10	1.74E-03	11.53	11.68	-0.02
ZNF391	13	23	10	1.95E-03	1.04	0.44	1.25
MAP3K13	11	21	10	2.04E-03	9.80	10.21	-0.06
FAM215A	18	28	10	2.74E-03	0.07	0.14	-0.98
LHB	20	30	10	2.89E-03	0.03	0.03	0.16
KCNJ11	23	33	10	3.04E-03	0.11	0.06	0.84
BTBD2	29	39	10	3.62E-03	23.13	35.63	-0.62

SYNE4	19	29	10	4.06E-03	4.57	3.64	0.33
DHX8	23	33	10	4.26E-03	15.44	15.56	-0.01
FBXW4P1	77	87	10	5.56E-03	0.23	0.28	-0.26
PDHA1	22	32	10	5.85E-03	155.70	162.93	-0.07
CWF19L1	18	28	10	6.65E-03	11.89	11.96	-0.01
ELAC1	11	21	10	7.78E-03	79.22	69.68	0.19
OIP5-AS1	12	22	10	7.78E-03	28.34	17.94	0.66
AIPL1	70	80	10	1.02E-02	0.11	0.12	-0.03
RIBC2	41	51	10	1.48E-02	0.34	0.47	-0.48
SMC1B	41	51	10	1.48E-02	0.02	0.02	-0.03
FGFBP3	0	10	10	1.67E-02	0.18	0.07	1.30
LAPTM5	3	13	10	1.75E-02	59.38	53.75	0.14
PAFAH2	2	12	10	2.73E-02	6.94	3.98	0.80
CPLX3	14	24	10	2.79E-02	0.02	0.04	-0.93
PCDHGC4	38	48	10	2.80E-02	44.63	44.34	0.01
EXOC7	50	60	10	2.85E-02	44.66	54.64	-0.29
KIF20B	6	16	10	3.22E-02	4.68	3.57	0.39
ZNF165	18	28	10	3.33E-02	0.22	0.29	-0.35
GHITM	22	32	10	4.18E-02	117.28	115.52	0.02
PTP4A3	89	99	10	4.48E-02	2.51	2.57	-0.03
SPESP1	75	85	10	4.92E-02	3.15	2.05	0.62
NOX5	75	85	10	4.92E-02	3.15	2.05	0.62
TBPL2	43	53	10	5.75E-02	0.76	0.48	0.67
ISLR	78	88	10	6.20E-02	0.03	0.03	-0.05
ZDHHHC9	28	38	10	7.65E-02	14.97	18.54	-0.31
LIMS2	9	19	10	8.73E-02	18.41	16.73	0.14
MED11	7	17	10	9.21E-02	4.32	5.14	-0.25
RP1L1	90	100	10	9.46E-02	0.44	0.26	0.78
ZNF808	2	13	11	1.44E-08	16.48	25.19	-0.61
MIS18BP1	0	11	11	1.44E-08	14.50	20.73	-0.52
IQGAP1	3	14	11	1.44E-08	248.25	307.74	-0.31
FLT3LG	0	11	11	1.44E-08	782.26	935.32	-0.26
GMNN	0	11	11	1.44E-08	22.50	17.67	0.35
MCU	2	13	11	1.47E-08	18.85	19.38	-0.04
AUH	4	15	11	1.47E-08	6.69	6.75	-0.01
VPS11	8	19	11	1.55E-08	27.65	24.21	0.19
LAMP1	9	20	11	1.90E-08	258.24	234.38	0.14
XPO4	5	16	11	1.95E-08	6.71	6.76	-0.01
CHST7	26	37	11	2.07E-08	4.57	4.10	0.15
ANKRD30BL	27	38	11	2.34E-08	0.04	0.07	-0.91
FGFRL1	13	24	11	2.41E-08	4.36	3.94	0.15
IKBKE	0	11	11	5.88E-08	10.37	7.64	0.44
CDC42	4	15	11	2.51E-07	185.16	192.43	-0.06
ZSWIM3	2	13	11	1.09E-06	1.08	1.18	-0.12
C3orf55	9	20	11	1.47E-06	9.52	9.75	-0.03
EMR2	2	13	11	2.21E-06	0.18	0.22	-0.34
USP51	19	30	11	4.29E-06	1.23	0.92	0.41
PIH1D3	24	35	11	6.35E-06	0.08	0.09	-0.23
ZNF560	18	29	11	1.77E-05	0.00	0.00	-0.22
GGACT	6	17	11	2.08E-05	1.56	1.20	0.38
NLRX1	8	19	11	6.05E-05	1.27	0.97	0.39
PSMB4	14	25	11	1.23E-04	89.62	80.22	0.16
CEND1	10	21	11	1.33E-04	0.28	0.19	0.60
TMEM218	10	21	11	1.63E-04	18.41	13.72	0.42

TMEM218	10	21	11	1.63E-04	18.41	13.72	0.42
RNF8	7	18	11	2.32E-04	29.41	30.97	-0.07
TGDS	13	24	11	2.55E-04	4.97	4.86	0.03
RGAG4	23	34	11	2.72E-04	0.52	0.43	0.28
FOXO4	8	19	11	3.07E-04	4.45	3.31	0.42
CDK20	7	18	11	3.99E-04	0.41	0.44	-0.09
CCM2	4	15	11	4.77E-04	41.58	30.78	0.43
AMMECR1	16	27	11	5.11E-04	5.61	5.56	0.02
MSN	24	35	11	8.21E-04	283.85	304.74	-0.10
AGA	6	17	11	9.90E-04	12.45	15.11	-0.28
PTPLAD2	27	38	11	1.10E-03	4.87	5.90	-0.28
ZMYND10	19	30	11	1.47E-03	0.07	0.06	0.33
SNRPF	11	22	11	2.89E-03	91.74	114.33	-0.32
TLE2	12	23	11	3.43E-03	22.37	19.69	0.18
RAD51D	27	38	11	5.73E-03	8.49	9.87	-0.22
RAD9A	40	51	11	1.25E-02	3.72	2.38	0.64
PIWIL1	60	71	11	1.33E-02	0.06	0.04	0.74
ZNF551	30	41	11	1.38E-02	8.81	7.22	0.29
LPIN3	11	22	11	1.66E-02	0.14	0.17	-0.25
PPAPDC3	56	67	11	1.74E-02	0.36	0.31	0.19
FAM9C	81	92	11	2.02E-02	0.14	0.16	-0.19
GLUD2	18	29	11	2.42E-02	0.09	0.12	-0.38
TCTEX1D4	77	88	11	2.79E-02	0.20	0.16	0.32
ASIC2	46	57	11	5.88E-02	0.00	0.04	-3.22
ZNF492	45	56	11	6.60E-02	0.08	0.07	0.18
DNAH6	16	27	11	7.47E-02	0.01	0.05	-2.92
GON4L	34	45	11	8.31E-02	14.46	17.91	-0.31
PIGA	25	36	11	8.45E-02	3.85	2.88	0.42
MS4A10	82	93	11	8.49E-02	0.18	0.15	0.29
ADTRP	89	100	11	9.37E-02	14.26	14.84	-0.06
BCL2L14	81	92	11	9.88E-02	0.32	0.63	-0.96
PIWIL2	46	57	11	9.96E-02	0.13	0.13	-0.05
RNASEH1	7	19	12	1.44E-08	18.38	17.32	0.09
SNX33	4	16	12	1.44E-08	4.38	3.92	0.16
SRP14	1	13	12	1.44E-08	1089.93	942.41	0.21
ZNF771	1	13	12	1.44E-08	1.15	0.90	0.35
METTL13	6	18	12	1.44E-08	15.91	11.91	0.42
C6orf57	5	17	12	1.44E-08	5.46	3.87	0.50
ZNHIT6	2	14	12	1.44E-08	15.33	12.92	0.25
POLR3F	5	17	12	1.47E-08	11.01	12.78	-0.22
SNAPC1	10	22	12	1.57E-08	406.34	404.96	0.00
MAP7D3	17	29	12	1.60E-08	22.27	16.64	0.42
ACOT4	10	22	12	1.73E-08	0.03	0.03	-0.16
GNAS	31	43	12	2.51E-08	458.16	442.50	0.05
MCM5	27	39	12	3.67E-08	12.56	9.31	0.43
TMEM62	8	20	12	4.94E-08	30.43	35.77	-0.23
RHPN2	11	23	12	6.11E-08	1.55	1.56	-0.01
TCTN3	12	24	12	1.67E-06	56.15	52.02	0.11
EIF1AX	24	36	12	2.43E-06	56.38	47.36	0.25
RUFY1	5	17	12	2.95E-06	109.75	111.85	-0.03
MRPS25	7	19	12	7.02E-06	33.83	29.94	0.18
BLVRB	11	23	12	7.04E-06	12.40	14.19	-0.20
NHLRC1	18	30	12	7.90E-06	0.41	0.29	0.49
PHF16	16	28	12	1.42E-05	5.93	8.25	-0.48

PHF16	16	28	12	1.42E-05	5.93	8.25	-0.48
C16orf80	35	47	12	1.69E-04	68.93	72.29	-0.07
SMARCA1	8	20	12	2.02E-04	13.36	13.73	-0.04
SMARCA1	8	20	12	2.02E-04	13.36	13.73	-0.04
C1GALT1C1	36	48	12	2.36E-04	33.64	38.22	-0.18
MMADHC	0	12	12	3.32E-04	65.47	73.95	-0.18
CSTF2	36	48	12	6.15E-04	6.05	7.68	-0.35
KCNN3	9	21	12	8.37E-04	6.89	6.08	0.18
C14orf2	17	29	12	9.41E-04	283.38	220.43	0.36
SYCE2	43	55	12	1.10E-03	0.25	0.12	1.04
MAOA	30	42	12	1.15E-03	3.31	2.91	0.19
C2orf74	82	94	12	1.63E-03	40.17	44.10	-0.13
MDM4	27	39	12	3.48E-03	11.11	11.93	-0.10
BCL6	4	16	12	3.71E-03	6.69	6.92	-0.05
LY6K	67	79	12	9.63E-03	0.83	0.71	0.23
MED16	16	28	12	1.73E-02	10.24	7.71	0.41
DNAJC19	38	50	12	1.73E-02	30.36	23.15	0.39
DNAJC19	34	46	12	1.87E-02	30.36	23.15	0.39
CDHR5	72	84	12	2.84E-02	0.02	0.02	0.20
C1D	12	24	12	2.88E-02	16.36	13.16	0.31
TNFRSF25	45	57	12	3.60E-02	29.69	24.12	0.30
RHBDL2	9	21	12	6.21E-02	1.74	2.10	-0.27
PEX19	31	43	12	8.24E-02	96.70	79.61	0.28
DIO1	82	94	12	8.31E-02	0.06	0.07	-0.11
ALDH3B1	80	92	12	8.56E-02	0.29	0.18	0.71
EVI5L	79	91	12	9.86E-02	23.04	21.63	0.09
UBE2L6	0	13	13	1.44E-08	19.57	22.84	-0.22
MLH3	1	14	13	1.44E-08	5.17	5.83	-0.17
ING4	1	14	13	1.44E-08	33.56	35.69	-0.09
COA6	3	16	13	1.44E-08	28.20	29.70	-0.07
TBCCD1	1	14	13	1.44E-08	9.27	9.72	-0.07
C11orf48	2	15	13	1.44E-08	306.26	300.07	0.03
MKS1	0	13	13	1.44E-08	7.54	6.41	0.24
FOXRED2	29	42	13	1.91E-08	3.21	3.15	0.03
FOXRED2	30	43	13	2.30E-08	3.21	3.15	0.03
AMZ2P1	9	22	13	5.41E-08	6.21	5.71	0.12
CHST6	12	25	13	6.54E-08	0.06	0.11	-0.93
WIF1	23	36	13	2.36E-07	0.01	0.01	0.03
DNAJC15	8	21	13	2.46E-07	5.56	5.21	0.09
SERF2	15	28	13	4.74E-07	304.92	347.00	-0.19
IFFO1	14	27	13	6.39E-07	11.83	10.79	0.13
UBQLN2	16	29	13	1.13E-06	11.33	10.28	0.14
ANGEL2	9	22	13	2.44E-06	16.92	17.08	-0.01
TNFSF11	3	16	13	3.65E-06	0.01	0.01	-0.41
GANC	3	16	13	7.39E-06	13.30	13.94	-0.07
ZNF695	7	20	13	8.06E-06	2.38	2.13	0.16
ABCC10	9	22	13	8.90E-06	12.79	11.98	0.09
CCND3	9	22	13	1.16E-05	32.18	30.73	0.07
RINT1	10	23	13	2.48E-05	30.19	29.98	0.01
SSTR5	9	22	13	2.91E-05	0.10	0.01	2.97
TGFB111	5	18	13	4.61E-05	10.45	10.33	0.02
TGFB111	5	18	13	4.61E-05	10.45	10.33	0.02
TGFB111	5	18	13	6.50E-05	10.45	10.33	0.02
TAF1A	23	36	13	1.02E-04	2.19	3.27	-0.58

CYP11A1	8	21	13	1.40E-04	0.05	0.03	0.53
ZNF331	38	51	13	1.93E-04	3.57	2.98	0.26
USP18	9	22	13	2.21E-04	5.00	5.69	-0.19
C15orf26	5	18	13	2.59E-04	1.50	0.93	0.69
MAP2K3	1	14	13	4.89E-04	12.12	10.05	0.27
SFR1	0	13	13	5.81E-04	22.46	23.37	-0.06
SFR1	0	13	13	5.81E-04	22.46	23.37	-0.06
PEX14	18	31	13	9.82E-04	12.49	11.03	0.18
IZUMO1	27	40	13	1.22E-03	0.29	0.41	-0.52
DNALI1	18	31	13	2.12E-03	4.45	5.35	-0.27
RSPH10B	14	27	13	2.87E-03	0.18	0.38	-1.10
RSPH10B2	14	27	13	2.87E-03	0.04	0.06	-0.58
MIR202	63	76	13	3.90E-03	0.37	0.42	-0.20
NGFRAP1	26	39	13	4.76E-03	151.93	159.11	-0.07
PCDHGA2	24	37	13	8.40E-03	44.63	44.34	0.01
CAMKK2	58	71	13	9.04E-03	12.21	11.78	0.05
DDIT3	11	24	13	1.23E-02	5.17	5.66	-0.13
MFAP2	9	22	13	3.66E-02	114.38	150.38	-0.39
KLK6	59	72	13	5.26E-02	1.88	2.03	-0.11
CT45A6	81	94	13	6.60E-02	0.06	0.04	0.81
DAB2IP	24	37	13	7.52E-02	17.74	19.02	-0.10
LRRC36	3	17	14	1.44E-08	0.23	0.32	-0.47
CIR1	0	14	14	1.44E-08	32.00	38.12	-0.25
SCRN3	0	14	14	1.44E-08	23.96	27.89	-0.22
FRS2	1	15	14	1.44E-08	10.88	12.61	-0.21
PNPO	1	15	14	1.44E-08	47.87	55.37	-0.21
CARS	1	15	14	1.44E-08	15.79	17.60	-0.16
SNW1	5	19	14	1.44E-08	80.71	86.15	-0.09
SCAP	6	20	14	1.44E-08	11.47	11.46	0.00
MRP63	1	15	14	1.44E-08	7.54	7.52	0.00
RUFY2	1	15	14	1.44E-08	32.12	31.90	0.01
RUFY2	1	15	14	1.44E-08	32.12	31.90	0.01
HN1L	1	15	14	1.44E-08	171.21	156.30	0.13
PPT1	0	14	14	1.44E-08	99.58	80.88	0.30
PSMC1	1	15	14	1.44E-08	83.29	65.49	0.35
XKR9	0	14	14	1.44E-08	0.43	0.34	0.35
COPS3	4	18	14	1.44E-08	136.84	100.11	0.45
KCTD19	3	17	14	1.44E-08	1.31	0.88	0.59
LACTB2	0	14	14	1.44E-08	1.95	0.71	1.46
NDUFA6	5	19	14	1.52E-08	56.97	73.19	-0.36
COX8A	14	28	14	1.52E-08	49.36	45.00	0.13
PLK4	11	25	14	1.55E-08	4.44	2.41	0.88
CDC25B	8	22	14	1.63E-08	241.43	191.42	0.33
FAM71E1	10	24	14	1.79E-08	0.12	0.15	-0.30
EMC10	10	24	14	1.79E-08	48.33	17.51	1.46
LONRF3	24	38	14	2.21E-08	4.25	4.17	0.03
LRFN4	26	40	14	3.12E-08	2.48	2.21	0.17
FAM83D	13	27	14	3.90E-08	8.08	5.55	0.54
GATA2	33	47	14	4.12E-08	13.84	13.07	0.08
RNF113A	31	45	14	6.46E-08	6.27	5.73	0.13
NDUFA1	31	45	14	1.33E-07	70.69	78.72	-0.16
TCOF1	9	23	14	2.19E-07	19.21	18.95	0.02
KIAA1919	13	27	14	8.61E-07	2.65	2.60	0.03
GNAS	33	47	14	4.93E-06	458.16	442.50	0.05

TRIP4	13	27	14	5.73E-06	36.61	27.87	0.39
OXGR1	8	22	14	1.22E-05	0.05	0.02	1.11
RPSAP58	9	23	14	3.78E-05	0.75	0.74	0.00
NCMAP	8	22	14	4.37E-05	0.05	0.08	-0.65
SUMF1	25	39	14	3.60E-04	22.44	20.47	0.13
ALDH1L2	25	39	14	4.11E-04	0.34	0.29	0.22
EPHA1	33	47	14	1.06E-03	1.04	1.67	-0.68
MTIF2	4	18	14	1.23E-03	16.40	16.32	0.01
ZMAT1	32	46	14	1.85E-03	2.42	3.10	-0.36
ZCCHC4	22	36	14	3.13E-03	4.57	5.04	-0.14
PFDN5	52	66	14	7.59E-03	165.38	213.81	-0.37
GABRB3	45	59	14	7.66E-03	1.19	1.16	0.04
NEURL3	41	55	14	8.07E-03	0.03	0.01	2.08
PCDHA9	13	27	14	1.31E-02	0.88	0.67	0.39
PYCRL	36	50	14	2.15E-02	0.48	0.48	0.00
ANO4	17	31	14	4.60E-02	0.56	1.79	-1.69
PRND	35	49	14	8.78E-02	0.06	0.09	-0.54
PIGB	1	16	15	1.44E-08	9.07	10.53	-0.22
ZNF497	5	20	15	1.44E-08	1.91	1.49	0.36
FAM127B	13	28	15	5.65E-07	33.00	30.29	0.12
TOP1MT	24	39	15	5.95E-07	9.47	8.28	0.19
DGKA	10	25	15	7.82E-07	198.25	199.67	-0.01
GPR19	0	15	15	6.35E-06	0.13	0.32	-1.25
C9orf129	20	35	15	8.63E-06	0.05	0.14	-1.43
CALHM2	2	17	15	3.33E-05	35.25	30.30	0.22
MGARP	34	49	15	7.52E-05	62.54	63.24	-0.02
MTL5	27	42	15	1.86E-04	0.72	0.70	0.05
RUSC1	20	35	15	1.07E-03	7.78	7.27	0.10
KLC4	14	29	15	1.08E-03	11.20	11.40	-0.03
EID3	24	39	15	1.33E-03	1.30	1.95	-0.58
ZMAT4	9	24	15	4.69E-03	0.17	0.27	-0.64
C2orf50	56	71	15	4.90E-03	0.07	0.10	-0.54
MRVI1	70	85	15	1.14E-02	0.52	0.48	0.12
C1orf64	81	96	15	1.32E-02	0.08	0.10	-0.34
ZNF235	3	18	15	1.54E-02	5.76	5.89	-0.03
CARD14	56	71	15	2.64E-02	0.51	0.41	0.30
C19orf38	57	72	15	3.30E-02	0.17	0.14	0.22
LIG1	2	17	15	3.50E-02	0.97	2.31	-1.25
AQP7	53	68	15	6.55E-02	0.14	0.09	0.70
C11orf83	0	16	16	1.44E-08	2.48	3.10	-0.32
UFSP2	0	16	16	1.44E-08	71.39	84.81	-0.25
TMEM219	13	29	16	1.44E-08	28.20	28.97	-0.04
GIN51	1	17	16	1.44E-08	4.54	3.91	0.21
WDR66	5	21	16	1.44E-08	23.62	19.81	0.25
KPNA6	9	25	16	1.52E-08	28.25	21.96	0.36
C11orf70	7	23	16	1.52E-08	0.33	0.17	0.93
SET	2	18	16	1.60E-08	275.42	222.70	0.31
ZNF414	11	27	16	1.63E-08	3.94	3.86	0.03
ZNF726	21	37	16	1.84E-08	0.95	0.99	-0.07
SEPSECS	9	25	16	9.29E-08	3.84	3.66	0.07
RBMXL2	51	67	16	9.89E-08	0.17	0.16	0.07
PKD2L2	11	27	16	4.90E-07	0.65	0.82	-0.34
ZNF350	14	30	16	7.06E-07	6.13	11.48	-0.90
SMUG1	18	34	16	3.41E-06	6.35	5.63	0.17

UFC1	15	31	16	3.90E-06	120.85	88.13	0.46
HSDL2	3	19	16	5.77E-06	19.85	18.99	0.06
DYNLT3	16	32	16	7.12E-06	33.88	32.82	0.05
DUS3L	15	31	16	1.09E-05	6.30	4.87	0.37
MFSD5	5	21	16	1.09E-05	21.51	18.82	0.19
SYCE1	56	72	16	2.25E-05	0.57	0.25	1.20
HOXB8	12	28	16	2.28E-05	4.92	5.01	-0.02
ANO7	76	92	16	2.59E-04	0.70	0.57	0.30
KIAA1598	60	76	16	2.71E-04	1.42	1.52	-0.10
HEMK1	15	31	16	2.73E-04	1.37	1.44	-0.07
KCNE3	33	49	16	9.06E-04	0.06	0.10	-0.83
TOR1AIP2	10	26	16	1.28E-03	51.44	46.67	0.14
QPRT	69	85	16	2.23E-03	0.50	0.50	0.00
IGF2	77	93	16	3.13E-03	8.78	7.78	0.17
ISG15	51	67	16	4.76E-03	10.67	13.13	-0.30
RASAL3	52	68	16	1.64E-02	0.34	0.24	0.49
NEK8	29	45	16	1.84E-02	0.68	0.48	0.52
PAK6	22	38	16	2.05E-02	17.78	9.87	0.85
CAPN12	74	90	16	2.26E-02	13.78	12.26	0.17
SNAPC4	76	92	16	2.53E-02	2.77	1.86	0.57
SLC23A1	78	94	16	3.23E-02	0.15	0.11	0.34
IDI2-AS1	80	96	16	3.32E-02	0.04	0.04	-0.04
SLC38A7	13	29	16	4.59E-02	17.72	18.57	-0.07
MTO1	11	28	17	1.44E-08	21.26	26.76	-0.33
ATL3	0	17	17	1.44E-08	42.26	39.60	0.09
ZNF440	1	18	17	1.44E-08	4.24	3.89	0.12
NINL	2	19	17	1.44E-08	12.26	9.74	0.33
AKR1E2	17	34	17	1.46E-08	1.94	1.50	0.37
DLG3	19	36	17	1.52E-08	1.70	1.94	-0.19
SMUG1	17	34	17	5.07E-07	6.35	5.63	0.17
SYTL4	20	37	17	3.32E-06	356.86	227.69	0.65
SYTL4	20	37	17	3.32E-06	356.86	227.69	0.65
SOX30	27	44	17	6.21E-06	0.04	0.03	0.29
TGIF1	8	25	17	6.61E-06	30.13	24.18	0.32
BBS2	26	43	17	1.31E-04	90.58	81.61	0.15
POLR2G	41	58	17	3.21E-04	36.69	40.07	-0.13
EXOC7	23	40	17	5.72E-04	44.66	54.64	-0.29
CCDC58	14	31	17	8.36E-04	24.64	25.73	-0.06
JAK3	19	36	17	2.89E-03	0.20	0.15	0.47
IVD	4	21	17	3.17E-03	17.42	16.32	0.09
KCNE1L	47	64	17	4.83E-03	35.93	35.28	0.03
POGZ	81	98	17	2.27E-02	43.20	30.12	0.52
MORF4L2	3	20	17	2.55E-02	301.86	347.28	-0.20
C1orf168	69	86	17	5.04E-02	0.17	0.13	0.42
CNN1	26	43	17	6.16E-02	0.39	0.25	0.68
CCDC73	74	91	17	8.45E-02	3.61	4.21	-0.22
LCT	80	97	17	8.59E-02	0.00	0.00	0.87
SERF2	16	34	18	1.57E-08	304.92	347.00	-0.19
LARS	15	33	18	5.69E-08	122.66	129.09	-0.07
DNM1P46	12	30	18	1.52E-07	0.16	0.06	1.43
ZNF331	34	52	18	2.15E-07	3.57	2.98	0.26
EBPL	21	39	18	2.49E-07	18.18	17.40	0.06
POLR2D	20	38	18	4.74E-07	17.62	24.88	-0.50
C5orf63	9	27	18	1.48E-05	0.48	0.24	1.01

NHLRC4	40	58	18	2.85E-05	7.35	6.73	0.13
COX7A1	20	38	18	4.67E-05	5.18	10.00	-0.95
CECR1	11	29	18	4.67E-04	5.87	4.76	0.30
CLNS1A	15	33	18	6.44E-04	198.48	174.26	0.19
MKLN1	3	21	18	1.39E-02	18.39	17.39	0.08
MCTS1	18	36	18	1.55E-02	30.71	26.45	0.22
ZNF439	77	95	18	5.01E-02	0.40	0.35	0.17
NAP1L5	36	54	18	7.74E-02	4.00	4.13	-0.05
SATL1	63	81	18	8.61E-02	2.29	2.10	0.13
STARD8	13	32	19	1.44E-08	11.86	12.08	-0.03
ECSIT	21	40	19	1.47E-08	26.08	12.80	1.03
TCP11	30	49	19	1.52E-08	0.02	0.01	0.74
MAFG	68	87	19	1.57E-08	17.53	12.47	0.49
SSR4P1	31	50	19	1.62E-08	0.14	0.21	-0.58
RBM5	14	33	19	1.64E-08	312.40	296.50	0.08
FAM217B	27	46	19	1.87E-08	4.34	4.88	-0.17
CCDC19	15	34	19	3.38E-06	0.62	0.47	0.40
LRRC37A6P	19	38	19	4.49E-06	0.17	0.24	-0.48
REEP2	4	23	19	1.10E-05	2.15	1.32	0.70
ACBD4	0	19	19	1.97E-04	1.18	0.84	0.49
PLA2G6	22	41	19	1.37E-03	4.90	2.67	0.87
PLA2G6	22	41	19	1.37E-03	4.90	2.67	0.87
ZNF331	51	70	19	1.41E-03	3.57	2.98	0.26
ZNF331	51	70	19	1.41E-03	3.57	2.98	0.26
HOXB3	1	20	19	4.90E-03	5.12	6.78	-0.41
ZNF711	16	35	19	5.80E-03	7.58	6.58	0.20
SH3BGR	44	63	19	1.59E-02	2.03	2.06	-0.02
CHM	18	37	19	2.19E-02	17.05	16.25	0.07
CACNA2D4	56	75	19	3.02E-02	0.08	0.02	1.82
CEP85	13	33	20	1.44E-08	4.58	4.28	0.10
MYSM1	2	22	20	1.44E-08	15.49	13.92	0.15
TBL2	6	26	20	1.44E-08	12.16	10.49	0.21
RPS24	11	31	20	1.50E-08	2446.97	2193.85	0.16
ECSIT	24	44	20	1.51E-08	26.08	12.80	1.03
ZRSR2	9	29	20	1.52E-08	10.87	10.98	-0.01
COL4A3BP	1	21	20	1.52E-08	15.96	16.99	-0.09
ZXDB	23	43	20	1.55E-08	2.26	1.85	0.29
TTLL10	34	54	20	1.67E-08	0.30	0.12	1.33
CABYR	16	36	20	2.00E-07	2.47	1.91	0.37
HOXB5	39	59	20	7.20E-06	63.50	50.37	0.33
GPR35	64	84	20	4.56E-04	2.99	3.07	-0.04
INPP5F	45	65	20	7.75E-04	13.34	14.35	-0.11
RDH13	27	47	20	1.41E-03	0.77	0.43	0.85
CREBL2	0	20	20	2.22E-03	18.61	15.84	0.23
ZNF749	0	20	20	3.15E-03	13.20	12.87	0.04
COMT	67	87	20	2.84E-02	98.34	72.18	0.45
TSSC4	75	95	20	4.71E-02	6.96	4.30	0.70
SIPA1L1	80	100	20	8.53E-02	9.01	9.36	-0.06
TOMM20	5	26	21	1.44E-08	56.21	49.11	0.19
VILL	12	33	21	1.44E-08	1.75	1.43	0.29
GCAT	1	22	21	1.44E-08	1.93	1.16	0.74
MRPS22	16	37	21	1.52E-08	70.84	99.59	-0.49
STPG1	22	43	21	1.55E-08	8.50	12.38	-0.54
PSTK	1	22	21	1.55E-08	1.88	1.82	0.05

CCDC8	23	44	21	1.60E-08	0.03	0.03	0.00
FAM96A	13	34	21	7.54E-08	82.61	87.34	-0.08
CUEDC2	1	22	21	3.96E-07	27.78	31.40	-0.18
CABYR	22	43	21	6.00E-07	2.47	1.91	0.37
CBWD2	2	23	21	1.97E-06	5.73	6.26	-0.13
UBE2L3	14	35	21	9.09E-05	101.13	76.80	0.40
PAK6	13	34	21	3.10E-04	17.78	9.87	0.85
CLK2	31	52	21	2.53E-03	25.67	22.67	0.18
GHRL	49	70	21	3.94E-02	97.76	108.06	-0.14
SUSD2	66	87	21	5.03E-02	0.03	0.06	-1.03
C1orf198	7	29	22	1.44E-08	7.65	5.78	0.40
PUM1	7	29	22	1.44E-08	110.62	80.78	0.45
IL10RA	13	35	22	1.47E-08	2.31	3.39	-0.55
STOM	8	30	22	1.60E-08	301.47	266.40	0.18
PIGU	20	42	22	9.81E-08	27.67	26.12	0.08
LDLRAD4	26	48	22	2.78E-05	1.20	1.04	0.21
LDLRAD4	26	48	22	2.78E-05	1.20	1.04	0.21
ELN	12	34	22	3.41E-04	9.47	6.93	0.45
RGPD2	44	66	22	2.13E-03	0.08	0.09	-0.24
RGS4	4	26	22	6.93E-03	55.64	51.60	0.11
RGS4	4	26	22	6.93E-03	55.64	51.60	0.11
RGS4	4	26	22	6.93E-03	55.64	51.60	0.11
ZSCAN23	76	98	22	9.68E-03	0.23	0.43	-0.88
HMSD	14	36	22	1.79E-02	32.21	33.50	-0.06
KRT8	73	95	22	2.79E-02	84.31	101.27	-0.26
ABAT	8	30	22	4.97E-02	0.32	0.37	-0.18
TMPRSS6	67	89	22	5.98E-02	0.02	0.01	1.78
NSA2	8	31	23	1.47E-08	176.72	195.11	-0.14
ZMAT3	3	26	23	1.52E-08	62.84	52.54	0.26
VMA21	20	43	23	1.68E-08	24.56	22.91	0.10
GEMIN5	28	51	23	2.13E-06	6.55	7.35	-0.17
SPARC	21	44	23	3.67E-06	2342.55	2385.35	-0.03
UBE2L3	12	35	23	3.87E-06	101.13	76.80	0.40
ETV4	30	53	23	1.47E-05	3.25	4.36	-0.42
MGAT1	25	48	23	1.36E-04	36.02	28.16	0.36
MCTS1	18	41	23	1.81E-03	30.71	26.45	0.22
OC90	54	77	23	7.60E-02	0.80	1.13	-0.50
LINC00320	59	82	23	9.29E-02	0.07	0.03	1.36
PLEC	15	39	24	1.56E-08	35.07	27.76	0.34
ATP5J2	25	49	24	2.99E-07	389.08	433.24	-0.16
AARS	15	39	24	2.33E-06	52.17	48.55	0.10
HSD3B7	41	65	24	1.98E-04	0.78	0.66	0.24
RAPGEF1	72	96	24	3.49E-04	56.37	51.44	0.13
SCG5	42	66	24	2.10E-02	0.68	0.51	0.40
INS-IGF2	54	78	24	3.47E-02	8.78	7.78	0.17
INS	54	78	24	3.47E-02	8.78	7.78	0.17
P2RX3	67	91	24	3.57E-02	0.02	0.19	-3.44
MR1	40	64	24	3.64E-02	2.24	2.22	0.01
IFITM10	17	41	24	7.83E-02	61.13	46.32	0.40
ATF5	3	28	25	1.44E-08	12.77	8.74	0.55
ATF5	3	28	25	1.44E-08	12.77	8.74	0.55
TASP1	9	34	25	1.47E-08	2.91	3.38	-0.22
STPG1	32	57	25	2.08E-08	8.50	12.38	-0.54
MIR503	23	48	25	4.06E-07	3.89	3.39	0.20

MIR424	23	48	25	4.06E-07	3.89	3.39	0.20
XKRX	38	63	25	2.58E-06	0.03	0.01	1.56
RPL24	20	45	25	1.21E-05	913.12	1152.83	-0.34
LSG1	17	42	25	5.52E-05	51.45	50.61	0.02
FAM74A3	50	75	25	8.40E-05	0.35	0.04	3.10
SV2A	6	31	25	6.56E-04	0.16	0.20	-0.29
GPATCH2	28	53	25	5.50E-03	6.47	10.20	-0.66
SPATA17	28	53	25	5.50E-03	0.34	0.49	-0.51
RPAP1	61	86	25	2.52E-02	8.67	9.04	-0.06
SEC61A2	10	36	26	1.44E-08	7.47	10.53	-0.50
MRPS17	29	55	26	1.44E-08	63.91	55.15	0.21
ALKBH7	5	31	26	2.49E-07	3.86	3.92	-0.02
ZNF468	15	41	26	2.16E-05	5.89	6.96	-0.24
FAM101A	50	76	26	5.65E-04	55.48	48.24	0.20
C19orf21	47	73	26	1.40E-03	0.00	0.01	-0.88
HSPA9	22	49	27	1.44E-08	318.67	415.42	-0.38
DCAF8	3	30	27	1.44E-08	96.70	79.61	0.28
CAPS2	1	28	27	1.47E-08	0.49	0.54	-0.14
COIL	18	45	27	1.57E-08	11.05	9.17	0.27
PALM2	11	38	27	1.01E-07	284.69	216.88	0.39
NDN	23	50	27	1.12E-06	15.12	13.74	0.14
CFD	58	85	27	3.84E-06	0.10	0.10	0.00
LAS1L	52	79	27	1.01E-03	4.84	5.32	-0.14
RBBP9	13	40	27	3.45E-03	7.35	5.78	0.35
PPP1R2P3	36	63	27	4.26E-02	0.06	0.09	-0.68
MYT1L	61	88	27	5.91E-02	0.12	0.17	-0.55
CCDC106	16	44	28	1.44E-08	30.48	27.18	0.17
SMU1	9	37	28	1.55E-08	54.58	55.96	-0.04
GBAP1	8	36	28	5.85E-08	11.40	10.46	0.12
IFITM1	29	57	28	9.88E-02	96.29	88.64	0.12
BMPR1B	18	46	28	9.97E-02	0.68	0.64	0.10
GRAMD1C	2	31	29	1.44E-08	6.13	6.35	-0.05
CDKL3	27	56	29	3.39E-07	771.93	681.71	0.18
AMBRA1	16	45	29	6.63E-04	8.10	6.58	0.30
GFI1B	19	48	29	1.54E-03	0.10	0.07	0.64
TNFRSF8	47	76	29	8.20E-03	0.01	0.03	-1.63
ATP6V0A4	17	46	29	8.70E-02	0.02	0.09	-1.93
C1orf141	34	64	30	1.44E-08	0.02	0.04	-1.10
CKLF-CMTM1	35	65	30	1.28E-04	30.75	34.38	-0.16
CKLF	35	65	30	1.28E-04	30.75	34.38	-0.16
HHIPL2	66	96	30	4.79E-02	0.02	0.06	-1.25
GCFC2	1	32	31	1.44E-08	1.10	1.19	-0.12
APC2	4	35	31	8.53E-05	0.41	0.32	0.36
TMPRSS12	33	64	31	2.08E-04	0.05	0.03	0.71
DCAF8	3	35	32	1.44E-08	96.70	79.61	0.28
DCAF8	3	35	32	1.44E-08	96.70	79.61	0.28
DVL3	7	39	32	1.48E-08	24.04	21.47	0.16
C10orf11	9	41	32	5.61E-06	10.04	11.32	-0.17
TNFRSF1A	31	63	32	3.68E-04	210.02	172.32	0.29
MFSD4	10	42	32	4.90E-04	0.60	0.70	-0.22
FBXL22	29	61	32	7.10E-04	0.08	0.09	-0.07
PSMF1	63	96	33	5.96E-03	49.90	47.08	0.08
GBA	0	33	33	8.91E-03	103.23	93.11	0.15
GBA	0	33	33	8.91E-03	103.23	93.11	0.15

C12orf71	60	93	33	3.16E-02	0.01	0.08	-2.45
PC	38	71	33	5.08E-02	14.53	11.54	0.33
MYL4	23	56	33	8.42E-02	1.55	1.22	0.35
ANKRD20A5P	17	51	34	1.44E-08	0.14	0.19	-0.47
EXOSC5	8	42	34	1.44E-08	1.92	2.63	-0.46
FMO5	31	65	34	1.44E-08	1.33	1.32	0.01
ZNF878	21	55	34	1.44E-08	1.65	1.38	0.26
HOOK2	8	42	34	1.44E-08	9.77	7.90	0.31
MEG3	30	64	34	1.60E-08	40.71	33.61	0.28
MEG3	30	64	34	1.60E-08	40.71	33.61	0.28
DDX19B	22	56	34	4.40E-07	44.14	44.31	-0.01
HIF3A	5	39	34	4.00E-04	1.25	0.71	0.82
SETDB1	17	52	35	1.44E-08	21.03	20.94	0.01
DND1	35	70	35	1.57E-08	45.60	37.72	0.27
LYPD3	40	75	35	3.52E-06	0.01	0.11	-3.00
LIMK1	22	57	35	8.77E-04	11.62	9.79	0.25
KPTN	14	50	36	1.44E-08	0.47	0.58	-0.31
NAPA-AS1	14	50	36	1.44E-08	0.30	0.32	-0.08
ZNF70	13	49	36	1.44E-08	1.78	1.86	-0.06
ZNF615	0	36	36	1.44E-08	4.13	3.05	0.44
BSG	38	74	36	1.47E-08	256.20	194.09	0.40
CFP	43	79	36	7.96E-02	1.11	0.88	0.34
GMFG	50	87	37	1.12E-05	12.75	10.41	0.29
SLC22A17	38	76	38	1.44E-08	1.15	1.16	-0.01
TJP2	4	42	38	1.44E-08	46.09	42.79	0.11
RBM34	0	39	39	1.51E-08	123.18	128.23	-0.06
DDX1	1	41	40	1.44E-08	124.08	159.39	-0.36
KIAA1755	2	42	40	2.16E-03	0.04	0.03	0.62
RAB17	15	56	41	1.62E-04	0.77	0.39	1.00
ALG1L2	44	85	41	2.59E-03	0.18	0.35	-0.98
SNORA69	44	85	41	7.76E-03	7.84	3.33	1.24
GPR141	20	61	41	7.22E-02	0.18	0.10	0.87
HCCS	14	56	42	1.44E-08	30.54	34.21	-0.16
AIMP1	16	58	42	1.47E-08	38.94	35.05	0.15
AIMP1	16	58	42	1.47E-08	38.94	35.05	0.15
SLC1A5	42	84	42	2.64E-04	22.59	21.97	0.04
CLK3	50	92	42	5.19E-02	63.88	63.92	0.00
MSTO1	5	48	43	1.44E-08	5.02	4.72	0.09
GABPB2	11	54	43	1.44E-08	2.67	2.16	0.30
SELPLG	7	50	43	5.92E-02	0.78	0.74	0.08
ARHGAP6	0	43	43	6.18E-02	0.74	0.68	0.11
SLC19A3	36	80	44	1.44E-08	0.13	0.08	0.62
MAT2B	2	46	44	7.75E-07	112.95	110.35	0.03
CECR1	56	100	44	1.43E-05	5.87	4.76	0.30
ZFYVE27	52	96	44	1.62E-04	6.01	6.34	-0.08
GZF1	0	45	45	4.43E-03	5.19	5.05	0.04
RNASEH2A	20	66	46	1.44E-08	8.73	8.43	0.05
IFT172	34	80	46	1.50E-06	12.97	12.61	0.04
NR1H3	0	46	46	2.05E-04	2.64	2.35	0.17
WNT2B	4	50	46	6.40E-04	2.47	2.42	0.03
LYVE1	0	46	46	1.23E-03	107.15	114.96	-0.10
NCR1	49	96	47	6.15E-08	0.07	0.07	0.10
TRIM5	0	47	47	2.92E-06	72.47	66.35	0.13
CCM2L	10	57	47	3.50E-03	11.59	12.04	-0.05

PARP6	31	79	48	1.53E-06	58.49	55.67	0.07
TMEM177	1	51	50	1.44E-08	1.44	1.27	0.18
INTS2	38	89	51	1.47E-08	9.14	12.60	-0.46
PTX3	44	96	52	1.44E-08	107.71	114.02	-0.08
RNF125	28	81	53	1.44E-08	47.96	47.68	0.01
ABCB9	14	70	56	7.88E-08	2.64	1.98	0.42
C9orf117	20	86	66	8.11E-04	0.64	0.69	-0.11
SLC9A1	12	86	74	1.44E-08	25.16	29.17	-0.21
IQCD	22	98	76	1.44E-08	0.19	0.21	-0.17
SLC25A22	14	92	78	1.08E-06	3.14	3.31	-0.08
NUAK2	21	100	79	2.54E-08	0.29	0.42	-0.54
BTC	10	89	79	2.76E-04	0.22	0.17	0.39
EMP3	3	83	80	8.78E-07	848.00	949.45	-0.16
FOLH1	4	90	86	1.44E-08	1.06	0.96	0.15

Supplemental Table 5.4. All significantly hypermethylated promoter regions corresponding to genes that are down-regulated in non-reversed conditions compared to reversed conditions

gene name	R methylation %	N methylation %	methylation % difference (N-R)	methylation adjusted Pvalue	mRNASeq Nvalue	mRNASeq Rvalue	mRNASeq Log2FC
EMP3	3	83	80	8.78E-07	848.00	949.45	-0.16
NUAK2	21	100	79	2.54E-08	0.29	0.42	-0.54
SLC25A22	14	92	78	1.08E-06	3.14	3.31	-0.08
IQCD	22	98	76	1.44E-08	0.19	0.21	-0.17
SLC9A1	12	86	74	1.44E-08	25.16	29.17	-0.21
C9orf117	20	86	66	8.11E-04	0.64	0.69	-0.11
PTX3	44	96	52	1.44E-08	107.71	114.02	-0.08
INTS2	38	89	51	1.47E-08	9.14	12.60	-0.46
CCM2L	10	57	47	3.50E-03	11.59	12.04	-0.05
LYVE1	0	46	46	1.23E-03	107.15	114.96	-0.10
ZFYVE27	52	96	44	1.62E-04	6.01	6.34	-0.08
HCCS	14	56	42	1.44E-08	30.54	34.21	-0.16
CLK3	50	92	42	5.19E-02	63.88	63.92	0.00
ALG1L2	44	85	41	2.59E-03	0.18	0.35	-0.98
DDX1	1	41	40	1.44E-08	124.08	159.39	-0.36
RBM34	0	39	39	1.51E-08	123.18	128.23	-0.06
SLC22A17	38	76	38	1.44E-08	1.15	1.16	-0.01
KPTN	14	50	36	1.44E-08	0.47	0.58	-0.31
NAPA-AS1	14	50	36	1.44E-08	0.30	0.32	-0.08
ZNF70	13	49	36	1.44E-08	1.78	1.86	-0.06
LYPD3	40	75	35	3.52E-06	0.01	0.11	-3.00
ANKRD20A5P	17	51	34	1.44E-08	0.14	0.19	-0.47
EXOSC5	8	42	34	1.44E-08	1.92	2.63	-0.46
DDX19B	22	56	34	4.40E-07	44.14	44.31	-0.01
C12orf71	60	93	33	3.16E-02	0.01	0.08	-2.45
MFSD4	10	42	32	4.90E-04	0.60	0.70	-0.22
C10orf11	9	41	32	5.61E-06	10.04	11.32	-0.17
FBXL22	29	61	32	7.10E-04	0.08	0.09	-0.07
GCFC2	1	32	31	1.44E-08	1.10	1.19	-0.12
HHIPL2	66	96	30	4.79E-02	0.02	0.06	-1.25
C1orf141	34	64	30	1.44E-08	0.02	0.04	-1.10
CKLF-CMTM1	35	65	30	1.28E-04	30.75	34.38	-0.16
CKLF	35	65	30	1.28E-04	30.75	34.38	-0.16
ATP6V0A4	17	46	29	8.70E-02	0.02	0.09	-1.93
TNFRSF8	47	76	29	8.20E-03	0.01	0.03	-1.63
GRAMD1C	2	31	29	1.44E-08	6.13	6.35	-0.05
SMU1	9	37	28	1.55E-08	54.58	55.96	-0.04
PPP1R2P3	36	63	27	4.26E-02	0.06	0.09	-0.68
MYT1L	61	88	27	5.91E-02	0.12	0.17	-0.55
HSPA9	22	49	27	1.44E-08	318.67	415.42	-0.38
CAPS2	1	28	27	1.47E-08	0.49	0.54	-0.14
LAS1L	52	79	27	1.01E-03	4.84	5.32	-0.14
C19orf21	47	73	26	1.40E-03	0.00	0.01	-0.88
SEC61A2	10	36	26	1.44E-08	7.47	10.53	-0.50
ZNF468	15	41	26	2.16E-05	5.89	6.96	-0.24
ALKBH7	5	31	26	2.49E-07	3.86	3.92	-0.02

GPATCH2	28	53	25	5.50E-03	6.47	10.20	-0.66
STPG1	32	57	25	2.08E-08	8.50	12.38	-0.54
SPATA17	28	53	25	5.50E-03	0.34	0.49	-0.51
RPL24	20	45	25	1.21E-05	913.12	1152.83	-0.34
SV2A	6	31	25	6.56E-04	0.16	0.20	-0.29
TASP1	9	34	25	1.47E-08	2.91	3.38	-0.22
RPAP1	61	86	25	2.52E-02	8.67	9.04	-0.06
P2RX3	67	91	24	3.57E-02	0.02	0.19	-3.44
ATP5J2	25	49	24	2.99E-07	389.08	433.24	-0.16
OC90	54	77	23	7.60E-02	0.80	1.13	-0.50
ETV4	30	53	23	1.47E-05	3.25	4.36	-0.42
GEMIN5	28	51	23	2.13E-06	6.55	7.35	-0.17
NSA2	8	31	23	1.47E-08	176.72	195.11	-0.14
SPARC	21	44	23	3.67E-06	2342.55	2385.35	-0.03
ZSCAN23	76	98	22	9.68E-03	0.23	0.43	-0.88
IL10RA	13	35	22	1.47E-08	2.31	3.39	-0.55
KRT8	73	95	22	2.79E-02	84.31	101.27	-0.26
RGPD2	44	66	22	2.13E-03	0.08	0.09	-0.24
ABAT	8	30	22	4.97E-02	0.32	0.37	-0.18
HMSD	14	36	22	1.79E-02	32.21	33.50	-0.06
SUSD2	66	87	21	5.03E-02	0.03	0.06	-1.03
STPG1	22	43	21	1.55E-08	8.50	12.38	-0.54
MRPS22	16	37	21	1.52E-08	70.84	99.59	-0.49
CUEDC2	1	22	21	3.96E-07	27.78	31.40	-0.18
GHRL	49	70	21	3.94E-02	97.76	108.06	-0.14
CBWD2	2	23	21	1.97E-06	5.73	6.26	-0.13
FAM96A	13	34	21	7.54E-08	82.61	87.34	-0.08
CCDC8	23	44	21	1.60E-08	0.03	0.03	0.00
INPP5F	45	65	20	7.75E-04	13.34	14.35	-0.11
COL4A3BP	1	21	20	1.52E-08	15.96	16.99	-0.09
SIPA1L1	80	100	20	8.53E-02	9.01	9.36	-0.06
GPR35	64	84	20	4.56E-04	2.99	3.07	-0.04
ZRSR2	9	29	20	1.52E-08	10.87	10.98	-0.01
SSR4P1	31	50	19	1.62E-08	0.14	0.21	-0.58
LRRC37A6P	19	38	19	4.49E-06	0.17	0.24	-0.48
HOXB3	1	20	19	4.90E-03	5.12	6.78	-0.41
FAM217B	27	46	19	1.87E-08	4.34	4.88	-0.17
STARD8	13	32	19	1.44E-08	11.86	12.08	-0.03
SH3BGR	44	63	19	1.59E-02	2.03	2.06	-0.02
COX7A1	20	38	18	4.67E-05	5.18	10.00	-0.95
POLR2D	20	38	18	4.74E-07	17.62	24.88	-0.50
SERF2	16	34	18	1.57E-08	304.92	347.00	-0.19
LARS	15	33	18	5.69E-08	122.66	129.09	-0.07
NAP1L5	36	54	18	7.74E-02	4.00	4.13	-0.05
MTO1	11	28	17	1.44E-08	21.26	26.76	-0.33
EXOC7	23	40	17	5.72E-04	44.66	54.64	-0.29
CCDC73	74	91	17	8.45E-02	3.61	4.21	-0.22
MORF4L2	3	20	17	2.55E-02	301.86	347.28	-0.20
DLG3	19	36	17	1.52E-08	1.70	1.94	-0.19
POLR2G	41	58	17	3.21E-04	36.69	40.07	-0.13
CCDC58	14	31	17	8.36E-04	24.64	25.73	-0.06
ZNF350	14	30	16	7.06E-07	6.13	11.48	-0.90
KCNE3	33	49	16	9.06E-04	0.06	0.10	-0.83
PKD2L2	11	27	16	4.90E-07	0.65	0.82	-0.34

C11orf83	0	16	16	1.44E-08	2.48	3.10	-0.32
ISG15	51	67	16	4.76E-03	10.67	13.13	-0.30
UFSP2	0	16	16	1.44E-08	71.39	84.81	-0.25
KIAA1598	60	76	16	2.71E-04	1.42	1.52	-0.10
ZNF726	21	37	16	1.84E-08	0.95	0.99	-0.07
HEMK1	15	31	16	2.73E-04	1.37	1.44	-0.07
SLC38A7	13	29	16	4.59E-02	17.72	18.57	-0.07
IDI2-AS1	80	96	16	3.32E-02	0.04	0.04	-0.04
TMEM219	13	29	16	1.44E-08	28.20	28.97	-0.04
HOXB8	12	28	16	2.28E-05	4.92	5.01	-0.02
QPRT	69	85	16	2.23E-03	0.50	0.50	0.00
C9orf129	20	35	15	8.63E-06	0.05	0.14	-1.43
GPR19	0	15	15	6.35E-06	0.13	0.32	-1.25
LIG1	2	17	15	3.50E-02	0.97	2.31	-1.25
ZMAT4	9	24	15	4.69E-03	0.17	0.27	-0.64
EID3	24	39	15	1.33E-03	1.30	1.95	-0.58
C2orf50	56	71	15	4.90E-03	0.07	0.10	-0.54
C1orf64	81	96	15	1.32E-02	0.08	0.10	-0.34
PIGB	1	16	15	1.44E-08	9.07	10.53	-0.22
ZNF235	3	18	15	1.54E-02	5.76	5.89	-0.03
KLC4	14	29	15	1.08E-03	11.20	11.40	-0.03
MGARP	34	49	15	7.52E-05	62.54	63.24	-0.02
DGKA	10	25	15	7.82E-07	198.25	199.67	-0.01
ANO4	17	31	14	4.60E-02	0.56	1.79	-1.69
EPHA1	33	47	14	1.06E-03	1.04	1.67	-0.68
NCMAP	8	22	14	4.37E-05	0.05	0.08	-0.65
PRND	35	49	14	8.78E-02	0.06	0.09	-0.54
LRRC36	3	17	14	1.44E-08	0.23	0.32	-0.47
PFDN5	52	66	14	7.59E-03	165.38	213.81	-0.37
NDUFA6	5	19	14	1.52E-08	56.97	73.19	-0.36
ZMAT1	32	46	14	1.85E-03	2.42	3.10	-0.36
FAM71E1	10	24	14	1.79E-08	0.12	0.15	-0.30
CIR1	0	14	14	1.44E-08	32.00	38.12	-0.25
SCRN3	0	14	14	1.44E-08	23.96	27.89	-0.22
FRS2	1	15	14	1.44E-08	10.88	12.61	-0.21
PNPO	1	15	14	1.44E-08	47.87	55.37	-0.21
CARS	1	15	14	1.44E-08	15.79	17.60	-0.16
NDUFA1	31	45	14	1.33E-07	70.69	78.72	-0.16
ZCCHC4	22	36	14	3.13E-03	4.57	5.04	-0.14
SNW1	5	19	14	1.44E-08	80.71	86.15	-0.09
RSPH10B	14	27	13	2.87E-03	0.18	0.38	-1.10
CHST6	12	25	13	6.54E-08	0.06	0.11	-0.93
RSPH10B2	14	27	13	2.87E-03	0.04	0.06	-0.58
TAF1A	23	36	13	1.02E-04	2.19	3.27	-0.58
IZUMO1	27	40	13	1.22E-03	0.29	0.41	-0.52
TNFSF11	3	16	13	3.65E-06	0.01	0.01	-0.41
MFAP2	9	22	13	3.66E-02	114.38	150.38	-0.39
DNALI1	18	31	13	2.12E-03	4.45	5.35	-0.27
UBE2L6	0	13	13	1.44E-08	19.57	22.84	-0.22
MIR202	63	76	13	3.90E-03	0.37	0.42	-0.20
USP18	9	22	13	2.21E-04	5.00	5.69	-0.19
SERF2	15	28	13	4.74E-07	304.92	347.00	-0.19
MLH3	1	14	13	1.44E-08	5.17	5.83	-0.17
DDIT3	11	24	13	1.23E-02	5.17	5.66	-0.13

KLK6	59	72	13	5.26E-02	1.88	2.03	-0.11
DAB2IP	24	37	13	7.52E-02	17.74	19.02	-0.10
ING4	1	14	13	1.44E-08	33.56	35.69	-0.09
COA6	3	16	13	1.44E-08	28.20	29.70	-0.07
TBCCD1	1	14	13	1.44E-08	9.27	9.72	-0.07
GANC	3	16	13	7.39E-06	13.30	13.94	-0.07
NGFRAP1	26	39	13	4.76E-03	151.93	159.11	-0.07
SFR1	0	13	13	5.81E-04	22.46	23.37	-0.06
SFR1	0	13	13	5.81E-04	22.46	23.37	-0.06
ANGEL2	9	22	13	2.44E-06	16.92	17.08	-0.01
PHF16	16	28	12	1.42E-05	5.93	8.25	-0.48
PHF16	16	28	12	1.42E-05	5.93	8.25	-0.48
CSTF2	36	48	12	6.15E-04	6.05	7.68	-0.35
RHBDL2	9	21	12	6.21E-02	1.74	2.10	-0.27
TMEM62	8	20	12	4.94E-08	30.43	35.77	-0.23
POLR3F	5	17	12	1.47E-08	11.01	12.78	-0.22
BLVRB	11	23	12	7.04E-06	12.40	14.19	-0.20
C1GALT1C1	36	48	12	2.36E-04	33.64	38.22	-0.18
MMADHC	0	12	12	3.32E-04	65.47	73.95	-0.18
ACOT4	10	22	12	1.73E-08	0.03	0.03	-0.16
C2orf74	82	94	12	1.63E-03	40.17	44.10	-0.13
DIO1	82	94	12	8.31E-02	0.06	0.07	-0.11
MDM4	27	39	12	3.48E-03	11.11	11.93	-0.10
C16orf80	35	47	12	1.69E-04	68.93	72.29	-0.07
BCL6	4	16	12	3.71E-03	6.69	6.92	-0.05
SMARCA1	8	20	12	2.02E-04	13.36	13.73	-0.04
SMARCA1	8	20	12	2.02E-04	13.36	13.73	-0.04
RUFY1	5	17	12	2.95E-06	109.75	111.85	-0.03
RHPN2	11	23	12	6.11E-08	1.55	1.56	-0.01
ASIC2	46	57	11	5.88E-02	0.00	0.04	-3.22
DNAH6	16	27	11	7.47E-02	0.01	0.05	-2.92
BCL2L14	81	92	11	9.88E-02	0.32	0.63	-0.96
ANKRD30BL	27	38	11	2.34E-08	0.04	0.07	-0.91
ZNF808	2	13	11	1.44E-08	16.48	25.19	-0.61
MIS18BP1	0	11	11	1.44E-08	14.50	20.73	-0.52
GLUD2	18	29	11	2.42E-02	0.09	0.12	-0.38
EMR2	2	13	11	2.21E-06	0.18	0.22	-0.34
SNRPF	11	22	11	2.89E-03	91.74	114.33	-0.32
IQGAP1	3	14	11	1.44E-08	248.25	307.74	-0.31
GON4L	34	45	11	8.31E-02	14.46	17.91	-0.31
AGA	6	17	11	9.90E-04	12.45	15.11	-0.28
PTPLAD2	27	38	11	1.10E-03	4.87	5.90	-0.28
FLT3LG	0	11	11	1.44E-08	782.26	935.32	-0.26
LPIN3	11	22	11	1.66E-02	0.14	0.17	-0.25
PIH1D3	24	35	11	6.35E-06	0.08	0.09	-0.23
RAD51D	27	38	11	5.73E-03	8.49	9.87	-0.22
ZNF560	18	29	11	1.77E-05	0.00	0.00	-0.22
FAM9C	81	92	11	2.02E-02	0.14	0.16	-0.19
ZSWIM3	2	13	11	1.09E-06	1.08	1.18	-0.12
MSN	24	35	11	8.21E-04	283.85	304.74	-0.10
CDK20	7	18	11	3.99E-04	0.41	0.44	-0.09
RNF8	7	18	11	2.32E-04	29.41	30.97	-0.07
ADTRP	89	100	11	9.37E-02	14.26	14.84	-0.06
CDC42	4	15	11	2.51E-07	185.16	192.43	-0.06

PIWIL2	46	57	11	9.96E-02	0.13	0.13	-0.05
MCU	2	13	11	1.47E-08	18.85	19.38	-0.04
C3orf55	9	20	11	1.47E-06	9.52	9.75	-0.03
AUH	4	15	11	1.47E-08	6.69	6.75	-0.01
XPO4	5	16	11	1.95E-08	6.71	6.76	-0.01
FAM215A	18	28	10	2.74E-03	0.07	0.14	-0.98
ZNF552	18	28	10	5.73E-04	0.24	0.46	-0.95
CPLX3	14	24	10	2.79E-02	0.02	0.04	-0.93
BTBD2	29	39	10	3.62E-03	23.13	35.63	-0.62
UBA52	9	19	10	2.17E-07	365.84	531.97	-0.54
RIBC2	41	51	10	1.48E-02	0.34	0.47	-0.48
ZNF165	18	28	10	3.33E-02	0.22	0.29	-0.35
ZDHHC9	28	38	10	7.65E-02	14.97	18.54	-0.31
ADPGK-AS1	4	14	10	1.44E-08	1.01	1.25	-0.31
C11orf92	6	16	10	1.63E-06	0.08	0.09	-0.29
EXOC7	50	60	10	2.85E-02	44.66	54.64	-0.29
TRNT1	6	16	10	1.46E-08	26.46	31.82	-0.27
FBXW4P1	77	87	10	5.56E-03	0.23	0.28	-0.26
MED11	7	17	10	9.21E-02	4.32	5.14	-0.25
PPP1R14A	13	23	10	1.75E-04	6.36	7.54	-0.25
PDLIM5	3	13	10	1.44E-08	46.85	54.30	-0.21
ZFR	7	17	10	8.39E-06	42.36	47.72	-0.17
SLC12A6	4	14	10	1.44E-08	20.84	23.38	-0.17
B3GALNT1	9	19	10	1.67E-08	7.45	8.31	-0.16
TRAPPC12	12	22	10	1.50E-03	17.57	18.98	-0.11
RPL11	15	25	10	1.36E-03	917.46	985.09	-0.10
SDHC	12	22	10	2.99E-07	42.94	46.05	-0.10
KIAA1598	1	11	10	1.44E-08	1.42	1.52	-0.10
PDHA1	22	32	10	5.85E-03	155.70	162.93	-0.07
NLK	7	17	10	1.60E-08	18.02	18.78	-0.06
SSB	2	12	10	1.57E-08	654.63	681.75	-0.06
MAP3K13	11	21	10	2.04E-03	9.80	10.21	-0.06
ISLR	78	88	10	6.20E-02	0.03	0.03	-0.05
PTP4A3	89	99	10	4.48E-02	2.51	2.57	-0.03
PITPNA	5	15	10	1.47E-08	106.60	108.69	-0.03
AIPL1	70	80	10	1.02E-02	0.11	0.12	-0.03
SMC1B	41	51	10	1.48E-02	0.02	0.02	-0.03
KLC4	1	11	10	1.44E-08	11.20	11.40	-0.03
KLC4	1	11	10	1.44E-08	11.20	11.40	-0.03
KLHL12	37	47	10	1.74E-03	11.53	11.68	-0.02
DHX8	23	33	10	4.26E-03	15.44	15.56	-0.01
CWF19L1	18	28	10	6.65E-03	11.89	11.96	-0.01
BLVRB	11	23	12	7.04E-06	12.40	14.19	-0.20
DLG3	19	36	17	1.52E-08	1.70	1.94	-0.19
USP18	9	22	13	2.21E-04	5.00	5.69	-0.19
SERF2	15	28	13	4.74E-07	304.92	347.00	-0.19
SERF2	16	34	18	1.57E-08	304.92	347.00	-0.19
FAM9C	81	92	11	2.02E-02	0.14	0.16	-0.19
C1GALT1C1	36	48	12	2.36E-04	33.64	38.22	-0.18
CUEDC2	1	22	21	3.96E-07	27.78	31.40	-0.18
MMADHC	0	12	12	3.32E-04	65.47	73.95	-0.18
ABAT	8	30	22	4.97E-02	0.32	0.37	-0.18
IQCD	22	98	76	1.44E-08	0.19	0.21	-0.17
C10orf11	9	41	32	5.61E-06	10.04	11.32	-0.17

MLH3	1	14	13	1.44E-08	5.17	5.83	-0.17
ZFR	7	17	10	8.39E-06	42.36	47.72	-0.17
FAM217B	27	46	19	1.87E-08	4.34	4.88	-0.17
GEMIN5	28	51	23	2.13E-06	6.55	7.35	-0.17
SLC12A6	4	14	10	1.44E-08	20.84	23.38	-0.17
HCCS	14	56	42	1.44E-08	30.54	34.21	-0.16
EMP3	3	83	80	8.78E-07	848.00	949.45	-0.16
CKLF-CMTM1	35	65	30	1.28E-04	30.75	34.38	-0.16
CKLF	35	65	30	1.28E-04	30.75	34.38	-0.16
B3GALNT1	9	19	10	1.67E-08	7.45	8.31	-0.16
ACOT4	10	22	12	1.73E-08	0.03	0.03	-0.16
CARS	1	15	14	1.44E-08	15.79	17.60	-0.16
NDUFA1	31	45	14	1.33E-07	70.69	78.72	-0.16
ATP5J2	25	49	24	2.99E-07	389.08	433.24	-0.16
GHRL	49	70	21	3.94E-02	97.76	108.06	-0.14
NSA2	8	31	23	1.47E-08	176.72	195.11	-0.14
ZCCHC4	22	36	14	3.13E-03	4.57	5.04	-0.14
CAPS2	1	28	27	1.47E-08	0.49	0.54	-0.14
LAS1L	52	79	27	1.01E-03	4.84	5.32	-0.14
C2orf74	82	94	12	1.63E-03	40.17	44.10	-0.13
DDIT3	11	24	13	1.23E-02	5.17	5.66	-0.13
POLR2G	41	58	17	3.21E-04	36.69	40.07	-0.13
CBWD2	2	23	21	1.97E-06	5.73	6.26	-0.13
ZSWIM3	2	13	11	1.09E-06	1.08	1.18	-0.12
GCFC2	1	32	31	1.44E-08	1.10	1.19	-0.12
KLK6	59	72	13	5.26E-02	1.88	2.03	-0.11
C9orf117	20	86	66	8.11E-04	0.64	0.69	-0.11
TRAPPC12	12	22	10	1.50E-03	17.57	18.98	-0.11
DIO1	82	94	12	8.31E-02	0.06	0.07	-0.11
INPP5F	45	65	20	7.75E-04	13.34	14.35	-0.11
MDM4	27	39	12	3.48E-03	11.11	11.93	-0.10
RPL11	15	25	10	1.36E-03	917.46	985.09	-0.10
MSN	24	35	11	8.21E-04	283.85	304.74	-0.10
LYVE1	0	46	46	1.23E-03	107.15	114.96	-0.10
SDHC	12	22	10	2.99E-07	42.94	46.05	-0.10
DAB2IP	24	37	13	7.52E-02	17.74	19.02	-0.10
KIAA1598	1	11	10	1.44E-08	1.42	1.52	-0.10
KIAA1598	60	76	16	2.71E-04	1.42	1.52	-0.10
CDK20	7	18	11	3.99E-04	0.41	0.44	-0.09
SNW1	5	19	14	1.44E-08	80.71	86.15	-0.09
COL4A3BP	1	21	20	1.52E-08	15.96	16.99	-0.09
ING4	1	14	13	1.44E-08	33.56	35.69	-0.09
PTX3	44	96	52	1.44E-08	107.71	114.02	-0.08
FAM96A	13	34	21	7.54E-08	82.61	87.34	-0.08
ZFYVE27	52	96	44	1.62E-04	6.01	6.34	-0.08
NAPA-AS1	14	50	36	1.44E-08	0.30	0.32	-0.08
SLC25A22	14	92	78	1.08E-06	3.14	3.31	-0.08
COA6	3	16	13	1.44E-08	28.20	29.70	-0.07
RNF8	7	18	11	2.32E-04	29.41	30.97	-0.07
LARS	15	33	18	5.69E-08	122.66	129.09	-0.07
ZNF726	21	37	16	1.84E-08	0.95	0.99	-0.07
TBCCD1	1	14	13	1.44E-08	9.27	9.72	-0.07
C16orf80	35	47	12	1.69E-04	68.93	72.29	-0.07
HEMK1	15	31	16	2.73E-04	1.37	1.44	-0.07

GANC	3	16	13	7.39E-06	13.30	13.94	-0.07
SLC38A7	13	29	16	4.59E-02	17.72	18.57	-0.07
FBXL22	29	61	32	7.10E-04	0.08	0.09	-0.07
NGFRAP1	26	39	13	4.76E-03	151.93	159.11	-0.07
PDHA1	22	32	10	5.85E-03	155.70	162.93	-0.07
ZNF70	13	49	36	1.44E-08	1.78	1.86	-0.06
CCDC58	14	31	17	8.36E-04	24.64	25.73	-0.06
RPAP1	61	86	25	2.52E-02	8.67	9.04	-0.06
NLK	7	17	10	1.60E-08	18.02	18.78	-0.06
SSB	2	12	10	1.57E-08	654.63	681.75	-0.06
MAP3K13	11	21	10	2.04E-03	9.80	10.21	-0.06
ADTRP	89	100	11	9.37E-02	14.26	14.84	-0.06
RBM34	0	39	39	1.51E-08	123.18	128.23	-0.06
SFR1	0	13	13	5.81E-04	22.46	23.37	-0.06
SFR1	0	13	13	5.81E-04	22.46	23.37	-0.06
HMSD	14	36	22	1.79E-02	32.21	33.50	-0.06
SIPA1L1	80	100	20	8.53E-02	9.01	9.36	-0.06
CDC42	4	15	11	2.51E-07	185.16	192.43	-0.06
CCM2L	10	57	47	3.50E-03	11.59	12.04	-0.05
PIWIL2	46	57	11	9.96E-02	0.13	0.13	-0.05
GRAMD1C	2	31	29	1.44E-08	6.13	6.35	-0.05
BCL6	4	16	12	3.71E-03	6.69	6.92	-0.05
ISLR	78	88	10	6.20E-02	0.03	0.03	-0.05
NAP1L5	36	54	18	7.74E-02	4.00	4.13	-0.05
IDI2-AS1	80	96	16	3.32E-02	0.04	0.04	-0.04
MCU	2	13	11	1.47E-08	18.85	19.38	-0.04
SMARCA1	8	20	12	2.02E-04	13.36	13.73	-0.04
SMARCA1	8	20	12	2.02E-04	13.36	13.73	-0.04
TMEM219	13	29	16	1.44E-08	28.20	28.97	-0.04
SMU1	9	37	28	1.55E-08	54.58	55.96	-0.04
GPR35	64	84	20	4.56E-04	2.99	3.07	-0.04
C3orf55	9	20	11	1.47E-06	9.52	9.75	-0.03
PTP4A3	89	99	10	4.48E-02	2.51	2.57	-0.03
ZNF235	3	18	15	1.54E-02	5.76	5.89	-0.03
PITPNA	5	15	10	1.47E-08	106.60	108.69	-0.03
RUFY1	5	17	12	2.95E-06	109.75	111.85	-0.03
STARD8	13	32	19	1.44E-08	11.86	12.08	-0.03
AIPL1	70	80	10	1.02E-02	0.11	0.12	-0.03
SPARC	21	44	23	3.67E-06	2342.55	2385.35	-0.03
SMC1B	41	51	10	1.48E-02	0.02	0.02	-0.03
KLC4	1	11	10	1.44E-08	11.20	11.40	-0.03
KLC4	1	11	10	1.44E-08	11.20	11.40	-0.03
KLC4	14	29	15	1.08E-03	11.20	11.40	-0.03
HOXB8	12	28	16	2.28E-05	4.92	5.01	-0.02
ALKBH7	5	31	26	2.49E-07	3.86	3.92	-0.02
SH3BGR	44	63	19	1.59E-02	2.03	2.06	-0.02
KLHL12	37	47	10	1.74E-03	11.53	11.68	-0.02
MGARP	34	49	15	7.52E-05	62.54	63.24	-0.02
ZRSR2	9	29	20	1.52E-08	10.87	10.98	-0.01
ANGEL2	9	22	13	2.44E-06	16.92	17.08	-0.01
AUH	4	15	11	1.47E-08	6.69	6.75	-0.01
SLC22A17	38	76	38	1.44E-08	1.15	1.16	-0.01
DHX8	23	33	10	4.26E-03	15.44	15.56	-0.01
DGKA	10	25	15	7.82E-07	198.25	199.67	-0.01

XPO4	5	16	11	1.95E-08	6.71	6.76	-0.01
RHPN2	11	23	12	6.11E-08	1.55	1.56	-0.01
CWF19L1	18	28	10	6.65E-03	11.89	11.96	-0.01
DDX19B	22	56	34	4.40E-07	44.14	44.31	-0.01
QPRT	69	85	16	2.23E-03	0.50	0.50	0.00
CCDC8	23	44	21	1.60E-08	0.03	0.03	0.00
CLK3	50	92	42	5.19E-02	63.88	63.92	0.00

Supplemental Table 5.5. All significantly hypomethylated promoter regions corresponding to genes that are up-regulated in non-reversed conditions compared to reversed conditions

gene name	R methylation %	N methylation %	methylation % difference (N-R)	methylation adjusted Pvalue	mRNASeq Nvalue	mRNASeq Rvalue	mRNASeq Log2FC
EPS8L3	81	21	-60	0.000633	0.03	0.01	1.90
EGFLAM	50	0	-50	0.006606	0.77	0.39	0.98
MICB	67	20	-47	0.01945	8.63	5.20	0.73
BPNT1	41	0	-41	6.95E-05	27.27	24.52	0.15
POM121L9P	98	58	-40	0.002384	0.02	0.01	1.59
ITGBL1	92	55	-37	4.98E-05	0.89	0.65	0.47
SYNPO2L	92	56	-36	0.036867	0.16	0.13	0.36
PLCH2	81	45	-36	0.000133	0.04	0.02	1.30
CSAD	83	48	-35	0.02734	9.61	7.18	0.42
ACOT2	82	50	-32	0.022889	0.87	0.46	0.91
CCDC74B- AS1	94	63	-31	0.032704	0.12	0.11	0.11
C9orf153	74	43	-31	0.066878	0.09	0.07	0.39
ACP5	57	26	-31	1.48E-08	46.28	30.30	0.61
CD79B	71	41	-30	2.58E-05	0.38	0.34	0.16
LAMB3	95	65	-30	0.011814	10.22	8.45	0.27
LAMB3	95	65	-30	0.011814	10.22	8.45	0.27
METTL5	48	20	-28	0.002432	66.99	63.77	0.07
RGS12	31	3	-28	0.008089	29.65	28.00	0.08
PLEKHB1	60	32	-28	0.026128	2.43	2.29	0.09
ZNF503-AS1	33	5	-28	0.003345	0.38	0.20	0.93
ZNF423	92	65	-27	0.018858	2.56	2.41	0.08
EZH1	45	18	-27	1.47E-08	13.01	10.64	0.29
CCDC152	46	20	-26	8.49E-08	1.33	1.11	0.26
MPDU1	52	28	-24	1.02E-05	44.96	44.47	0.02
PRKACA	54	30	-24	0.00118	67.05	61.07	0.13
KLK10	26	3	-23	0.016083	0.37	0.32	0.22
LINC00672	88	65	-23	0.01419	0.32	0.25	0.34
TOMM22	23	0	-23	1.44E-08	75.48	58.83	0.36
DAND5	59	36	-23	0.042271	0.31	0.20	0.67
DRG2	33	11	-22	3.61E-08	10.53	10.52	0.00
SPIN3	42	20	-22	0.01372	1.37	1.01	0.44
RAX2	83	62	-21	4.50E-05	0.03	0.03	0.01
CSTF2T	23	2	-21	1.44E-08	9.50	8.92	0.09
HELB	46	25	-21	5.02E-06	1.03	0.93	0.14
INPP5D	23	2	-21	1.44E-08	60.83	48.65	0.32
PKN1	56	35	-21	0.05044	59.22	41.39	0.52
BPIFB1	80	60	-20	0.084018	0.11	0.11	0.03
RNF166	28	8	-20	1.44E-08	16.37	15.28	0.10
CLASRP	26	6	-20	1.44E-08	27.58	25.50	0.11
RBMX2	37	18	-19	0.024771	22.84	22.56	0.02
NAA60	46	27	-19	1.87E-08	105.11	95.31	0.14
SIRT4	47	28	-19	0.000269	0.79	0.68	0.21
SLC7A8	28	10	-18	0.011235	2.60	2.49	0.06
SPC24	31	13	-18	0.016683	6.08	5.49	0.15
ATHL1	31	13	-18	1.65E-08	3.98	3.19	0.32
SERPINA4	82	64	-18	0.077535	0.10	0.06	0.58

ZC3H4	18	0	-18	1.44E-08	15.21	10.06	0.60
S1PR4	24	6	-18	1.94E-06	0.23	0.12	0.90
RCN3	95	77	-18	0.008897	82.51	39.28	1.07
RGN	65	47	-18	0.000112	0.18	0.06	1.51
STYX	17	0	-17	1.44E-08	26.56	25.30	0.07
MAP4K1	26	9	-17	0.002836	0.93	0.54	0.79
PCDHB3	48	31	-17	0.019056	0.04	0.02	1.26
CALD1	42	26	-16	0.083803	571.85	513.31	0.16
APOE	17	1	-16	1.63E-06	4.60	4.09	0.17
C8orf44	17	1	-16	1.44E-08	14.52	12.54	0.21
AMPD2	70	54	-16	0.075339	41.20	35.57	0.21
C1orf86	27	11	-16	0.03815	4.82	4.10	0.24
PKD1L1	76	60	-16	0.07031	1.48	1.20	0.30
TCF3	34	18	-16	0.003922	71.64	55.68	0.36
SPAG4	24	8	-16	1.67E-08	1.89	1.20	0.66
TMEM209	52	36	-16	0.001065	1.92	1.17	0.71
PLEKHG6	30	14	-16	1.55E-08	0.34	0.12	1.47
PLEKHG6	30	14	-16	1.55E-08	0.34	0.12	1.47
ZNF493	15	0	-15	2.03E-08	5.54	5.51	0.01
ASGR1	73	58	-15	0.040817	3.04	2.98	0.03
BAK1	21	6	-15	8.76E-05	3.54	2.95	0.27
ANKRD33	35	20	-15	0.003708	0.09	0.07	0.42
BRCA1	18	4	-14	1.74E-06	5.17	5.14	0.01
MED24	14	0	-14	0.000269	52.08	47.89	0.12
PHF17	14	0	-14	9.24E-05	13.84	12.17	0.19
SYCE1L	97	83	-14	0.022915	16.68	14.18	0.23
OCRL	20	6	-14	0.000418	16.60	13.84	0.26
DKKL1	19	5	-14	1.47E-08	0.17	0.12	0.46
DKKL1	19	5	-14	1.47E-08	0.17	0.12	0.46
C12orf36	93	79	-14	0.098991	0.14	0.04	1.94
DGCR14	15	2	-13	1.44E-08	4.17	4.07	0.04
AGPAT6	13	0	-13	1.44E-08	68.63	66.13	0.05
MUTYH	13	0	-13	0.043238	4.19	4.03	0.06
DMPK	23	10	-13	0.000492	39.58	37.02	0.10
LINC00574	13	0	-13	0.082325	0.13	0.12	0.10
TOE1	13	0	-13	0.043238	3.62	3.14	0.21
SLC5A4	100	87	-13	0.014153	0.10	0.08	0.33
IDUA	13	0	-13	1.52E-08	8.72	5.44	0.68
DMKN	14	1	-13	0.022411	0.09	0.05	0.78
C1QTNF1	35	22	-13	0.030878	0.46	0.22	1.06
TSSK3	20	8	-12	1.67E-08	0.53	0.48	0.16
APOBEC3D	12	0	-12	0.078091	11.13	9.90	0.17
MRPL28	20	8	-12	0.002575	39.19	34.56	0.18
KBTBD7	39	27	-12	0.003955	2.99	2.59	0.21
PI4KB	13	1	-12	1.47E-08	31.10	26.02	0.26
PI4KB	13	1	-12	1.47E-08	31.10	26.02	0.26
EDARADD	12	0	-12	3.66E-08	0.20	0.16	0.29
SUMO2	28	16	-12	2.15E-06	441.13	338.71	0.38
RHBDL1	27	15	-12	4.01E-06	0.13	0.10	0.50
MORN3	91	79	-12	0.06079	0.67	0.45	0.58
RFESD	12	0	-12	1.44E-08	0.57	0.22	1.35
RFESD	12	0	-12	1.44E-08	0.57	0.22	1.35
RBP5	23	12	-11	0.00041	0.87	0.87	0.00
ASL	14	3	-11	1.44E-08	70.34	67.45	0.06

ZC4H2	26	15	-11	0.000596	8.73	8.31	0.07
NUP160	27	16	-11	0.044358	37.20	35.05	0.09
P2RY2	16	5	-11	7.63E-07	1.54	1.44	0.10
P2RY2	16	5	-11	7.63E-07	1.54	1.44	0.10
ZNF177	21	10	-11	0.015138	10.72	9.81	0.13
PMVK	13	2	-11	3.89E-05	7.59	6.70	0.18
AR	24	13	-11	0.02855	2.56	2.19	0.23
ZNF682	37	26	-11	0.020253	1.07	0.90	0.26
TUBGCP2	22	11	-11	1.55E-08	15.68	12.74	0.30
CRISPLD2	11	0	-11	2.32E-08	2.74	2.11	0.38
ERICH1	13	2	-11	1.51E-08	37.35	23.08	0.69
MGAT5B	21	10	-11	0.001269	0.15	0.08	0.91
LZTS2	11	1	-10	1.93E-07	10.24	10.10	0.02
ASL	18	8	-10	2.56E-06	70.34	67.45	0.06
GRM4	13	3	-10	1.51E-08	0.00	0.00	0.08
NOP2	12	2	-10	0.000117	24.14	22.62	0.09
WDR38	29	19	-10	0.014801	0.05	0.05	0.10
C2orf68	16	6	-10	2.29E-07	7.45	6.91	0.11
CREB3L1	12	2	-10	1.10E-06	1.10	1.01	0.12
CD320	71	61	-10	0.054866	25.89	23.20	0.16
POC5	24	14	-10	0.002707	6.05	4.78	0.34
SEMA4D	99	89	-10	0.043859	4.05	3.11	0.38
CCDC78	21	11	-10	0.00025	0.10	0.07	0.57
DDX43	96	86	-10	0.014869	0.26	0.17	0.63
LGALS1	10	0	-10	6.26E-08	1405.19	820.91	0.78
TTC25	30	20	-10	0.006495	0.13	0.07	0.78
PKP3	59	49	-10	0.054925	0.18	0.09	1.04

Supplemental Table 5.6. Top 50 significantly overrepresented biological process GO terms for genes with expression patterns corresponding to differential promoter methylation under arteriogenic shear stress waveforms

Gene Set Name	# Genes in Gene Set (K)	# Genes in Overlap (k)	k/K	p-value	FDR
BIOPOLYMER_METABOLIC_PROCESS	1684	98	0.06	2.52E-29	2.08E-26
NUCLEOBASENUCLEOSIDENUCLEOTIDE_AND_NUCLEIC_ACID_METABOLIC_PROCESS	1244	71	0.06	6.79E-21	2.80E-18
RNA_METABOLIC_PROCESS	841	54	0.06	2.57E-18	7.08E-16
PROTEIN_METABOLIC_PROCESS	1231	65	0.05	1.62E-17	3.35E-15
TRANSCRIPTION	753	45	0.06	2.44E-14	4.02E-12
CELLULAR_PROTEIN_METABOLIC_PROCESS	1117	55	0.05	9.61E-14	1.32E-11
TRANSCRIPTION_DNA_DEPENDENT	636	40	0.06	1.36E-13	1.45E-11
RNA_BIOSYNTHETIC_PROCESS	638	40	0.06	1.51E-13	1.45E-11
CELLULAR_MACROMOLECULE_METABOLIC_PROCESS	1131	55	0.05	1.58E-13	1.45E-11
REGULATION_OF_METABOLIC_PROCESS	799	44	0.06	7.76E-13	6.41E-11
SIGNAL_TRANSDUCTION	1634	66	0.04	2.63E-12	1.97E-10
BIOPOLYMER_MODIFICATION	650	37	0.06	2.07E-11	1.43E-09
BIOSYNTHETIC_PROCESS	470	31	0.07	2.38E-11	1.51E-09
REGULATION_OF_CELLULAR_METABOLIC_PROCESS	787	41	0.05	2.66E-11	1.57E-09
PROTEIN_MODIFICATION_PROCESS	631	36	0.06	3.65E-11	2.01E-09
NEGATIVE_REGULATION_OF_BIOLOGICAL_PROCESS	677	37	0.05	6.58E-11	3.39E-09
NEGATIVE_REGULATION_OF_METABOLIC_PROCESS	262	22	0.08	2.13E-10	9.84E-09
REGULATION_OF_GENE_EXPRESSION	673	36	0.05	2.15E-10	9.84E-09
TRANSCRIPTION_FROM_RNA_POLYMERASE_II_PROMOTER	457	29	0.06	2.59E-10	1.12E-08
NEGATIVE_REGULATION_OF_CELLULAR_PROCESS	646	35	0.05	2.73E-10	1.13E-08
INTRACELLULAR_SIGNALING_CASCADE	667	35	0.05	6.35E-10	2.50E-08
REGULATION_OF_NUCLEOBASENUCLEOSIDENUCLEOTIDE_AND_NUCLEIC_ACID_METABOLIC_PROCESS	618	33	0.05	1.27E-09	4.78E-08
NEGATIVE_REGULATION_OF_CELLULAR_METABOLIC_PROCESS	259	20	0.08	5.94E-09	2.13E-07
NEGATIVE_REGULATION_OF_NUCLEOBASENUCLEOSIDENUCLEOTIDE_AND_NUCLEIC_ACID_METABOLIC_PROCESS	211	18	0.09	7.23E-09	2.48E-07
REGULATION_OF_TRANSCRIPTION	566	30	0.05	8.50E-09	2.80E-07

TRANSPORT	795	36	0.05	1.70E-08	5.38E-07
REGULATION_OF_TRANSCRIPTIONDNA_DEPENDENT	461	26	0.06	2.43E-08	7.43E-07
REGULATION_OF_RNA_METABOLIC_PROCESS	471	26	0.06	3.73E-08	1.10E-06
CELLULAR_BIOSYNTHETIC_PROCESS	321	21	0.07	4.50E-08	1.24E-06
MACROMOLECULE_BIOSYNTHETIC_PROCESS	321	21	0.07	4.50E-08	1.24E-06
ESTABLISHMENT_OF_LOCALIZATION	870	37	0.04	5.33E-08	1.42E-06
CELLULAR_COMPONENT_ASSEMBLY	298	20	0.07	6.19E-08	1.60E-06
PROTEIN_AMINO_ACID_PHOSPHORYLATION	279	19	0.07	1.05E-07	2.62E-06
MACROMOLECULAR_COMPLEX_ASSEMBLY	280	19	0.07	1.11E-07	2.68E-06
POSITIVE_REGULATION_OF_BIOLOGICAL_PROCESS	709	32	0.05	1.14E-07	2.68E-06
POST_TRANSLATIONAL_PROTEIN_MODIFICATION	476	25	0.05	1.75E-07	4.00E-06
LIPID_METABOLIC_PROCESS	325	20	0.06	2.51E-07	5.60E-06
NEGATIVE_REGULATION_OF_TRANSCRIPTION	188	15	0.08	3.06E-07	6.64E-06
POSITIVE_REGULATION_OF_CELLULAR_PROCESS	668	30	0.04	3.14E-07	6.64E-06
LIPID_BIOSYNTHETIC_PROCESS	97	11	0.11	3.55E-07	7.32E-06
PHOSPHORYLATION	313	19	0.06	6.12E-07	1.23E-05
CELLULAR_LIPID_METABOLIC_PROCESS	255	17	0.07	6.55E-07	1.29E-05
CARBOXYLIC_ACID_METABOLIC_PROCESS	178	14	0.08	8.97E-07	1.72E-05
ORGANIC_ACID_METABOLIC_PROCESS	180	14	0.08	1.03E-06	1.92E-05
REGULATION_OF_MOLECULAR_FUNCTION	324	18	0.06	4.18E-06	7.67E-05
MAPKKK_CASCADE_GO_0000165	104	10	0.10	5.48E-06	9.83E-05
REGULATION_OF_PROTEIN_KINASE_ACTIVITY	155	12	0.08	6.30E-06	1.11E-04
REGULATION_OF_KINASE_ACTIVITY	157	12	0.08	7.18E-06	1.23E-04
POSITIVE_REGULATION_OF_TRANSFERASE_ACTIVITY	86	9	0.10	8.04E-06	1.35E-04
REGULATION_OF_CATALYTIC_ACTIVITY	276	16	0.06	8.31E-06	1.35E-04

6 Mechanosensitive microRNA-199a regulates perfusion recovery and collateral arteriogenesis in Balb/c mice following femoral arterial ligation

Authors: Joshua L. Heuslein, Ji Song, Richard J. Price. *In preparation*

6.1 Abstract

Objective: The luminal growth of collateral arteries that bypass arterial occlusions (i.e. arteriogenesis) is a fundamental shear stress-induced adaptation that may provide important clues for the treatment of peripheral arterial disease (PAD). MicroRNAs are key regulators of gene expression in vascular biology, but the explicit role of mechanosensitive miRNAs in regulating collateral arteriogenesis has not been studied. Here, we tested the hypothesis that a mechanosensitive microRNA, miR-199a, regulates perfusion recovery and collateral arteriogenesis following femoral arterial ligation (FAL) via control of monocyte recruitment and pro-arteriogenic gene expression.

Approach and Results: Previously, we reported that collateral artery segments exhibit either “moderate” or “amplified” arteriogenesis depending on the hemodynamics to which they are exposed post-FAL. Using a genome-wide approach, we examined comparative microRNA expression in endothelial cells (ECs) exposed to shear stress waveforms biomimetic of those leading to either a moderate or amplified arteriogenic response, in-vitro. We determined that microRNA-199a-5p (miR-199a), which was downregulated by ~40% in ECs exposed to the amplified arteriogenesis waveform, regulated the expression of genes (CCND1, CD44, IKK β) crucial for the pro-arteriogenic functions of EC proliferation and monocyte adhesion. We then tested whether miR-199a regulates arteriogenesis in-vivo. Following FAL in Balb/c mice, overexpression of miR-199a impaired both foot perfusion and arteriogenesis. In contrast, miR-199a inhibition elicited complete foot perfusion recovery, markedly augmented collateral

arteriogenesis (a 36% increase in diameter corresponding to a >3.4-fold increase in segment conductance), and improved gastrocnemius muscle tissue composition 21 days post-FAL. Furthermore, miR-199a-modulated pro-arteriogenic macrophage recruitment in proportion to the degree of collateral artery growth.

Conclusions: We have identified mechanosensitive miR-199a as a potent regulator of perfusion recovery and arteriogenesis after arterial occlusion. MicroRNA-199a may therefore represent a new target for the therapeutic stimulation of arteriogenesis and treatment of PAD.

6.2 Abbreviations

PAD	peripheral arterial disease
FAL	femoral arterial ligation
EC	endothelial cell
HUVEC	human umbilical vein endothelial cell
miRNA	microRNA

6.3 Introduction

Peripheral arterial disease (PAD) has become a global problem – it is estimated that over 202 million people worldwide have PAD³. PAD arises when atherosclerotic plaques block arteries in the lower limbs, thereby limiting blood flow to the distal tissue, ultimately leading to intermittent claudication or critical limb ischemia in severe cases. Many PAD patients are either not amenable to surgical intervention or receive little long term benefit from surgery⁴. Revascularization strategies to stimulate the growth of new capillaries from preexisting vessels (i.e. angiogenesis) or luminal expansion of pre-existing arteries (i.e. arteriogenesis) remain promising therapeutic options, despite their limited success to date³⁹. The stimulation of angiogenesis is important in PAD, as capillary density is reduced in these patients^{4,25,28}; however, it is also imperative to restore

the driving pressure to the distal tissue via luminal expansion (i.e. arteriogenesis) of collateral arteries bypassing the occlusion(s)^{26,29,30}.

We recently reported that a subset of collateral segments in the mouse hindlimb display remarkably permanent, amplified arteriogenesis after femoral arterial ligation (FAL)²³⁷.

Specifically, we showed that collateral artery segments exposed to both a 2-fold increase in shear stress magnitude and reversed flow direction (“reversed” flow) following FAL exhibit a ~30% increase in luminal diameter 12-weeks post-FAL compared to segments experiencing just a 2-fold increase in shear stress magnitude (“non-reversed” flow) (**Figure 6.1A**)¹⁷⁶.

Moreover, by applying shear stress waveforms biomimetic of these in-vivo hemodynamics to endothelial cells (ECs) in-vitro, we were able to generate a direct, comprehensive mapping of EC mechanosensitive signaling to differential arteriogenesis responses¹⁷⁶. Comparative analysis of EC mechano-signaling corresponding to these differential responses may enable for the discovery of novel regulators of arteriogenesis.

To this end, mature microRNAs (miRNAs) are now well-recognized as key regulators of vascular remodeling^{263,264}. MicroRNAs are ~22 nucleotide, non-coding RNAs that are endogenous regulators of gene expression¹¹⁷. Mature miRNA incorporates into the RNA-induced silencing complex (RISC) and then binds to a target mRNA, usually in the 3' untranslated region (UTR) of the mRNA¹¹⁸. MicroRNA binding acts to suppress target gene expression by inhibiting mRNA translation to protein or by promoting mRNA degradation¹¹⁹, depending on miRNA-target complementarity¹²⁰. Additionally, miRNAs are attractive as potential therapeutic targets as they are short, highly conserved, and can negatively regulate gene expression of multiple mRNA targets²⁶⁵. Several miRNAs have been implicated as regulators vascular growth, primarily angiogenesis in ischemic tissue, in response to arterial occlusion^{143,150,151,154,155,159,161,162,164}. However, the explicit role of miRNAs in collateral arteriogenesis remains unstudied. Here, we tested the hypothesis that mechanosensitive microRNA-199a regulates perfusion recovery and

collateral arteriogenesis following femoral arterial ligation (FAL) via control of monocyte recruitment and pro-arteriogenic gene expression.

6.4 Materials and Methods

6.4.1 Human umbilical vein endothelial cell culture.

Human umbilical vein endothelial cells (HUVECs) purchased from VEC Technologies Inc. (Rensselaer, NY) were thawed and maintained on 0.1% gelatin coated flasks in M-199 medium (Lonza, Basel, Switzerland), supplemented with 10% fetal bovine serum (Life Technologies Inc, Grand Island, NY), 100U/mL penicillin-G + 100ug/ml streptomycin (Life Technologies Inc), 2mmol/L L-glutamine (Life Technologies Inc), 5ug/ml endothelial cell growth supplement (Biomedical Technologies, Stoughton, MA), and 10ug/ml heparin (Sigma Aldrich, St. Louis, MO). For each set of experimental comparisons, cells were used from the same cell line between subculture passages 2-3.

6.4.2 *In vitro* exposure of endothelial cells to biomimetic shear stress waveforms.

HUVECs were plated on cell culture grade plastic dishes coated with 0.1% gelatin and grown to confluence. A cone and plate flow apparatus¹⁸⁷, which maintains cells at 5% CO₂ and 37°C, was used to induce a shear stress protocol. The applied shear stress protocol consisted of a 24 hour preconditioning period at a steady of 15 dyne/cm², which was then either increased to 30 dynes/cm² (non-reversed flow) or increased to 30 dynes/cm² and reversed in direction (reversed flow) to simulate relative hemodynamics previously quantified in our in-vivo FAL model¹⁷⁶. Fresh culture media consisting of M199 with 4% dextran from *Leuconostoc* spp (Sigma Aldrich, M, ~500,000), 2% fetal bovine serum, 100U/mL penicillin-G + 100ug/ml streptomycin, 2mmol/L L-glutamine, 5ug/ml endothelial cell growth supplement, and 10ug/ml heparin was added to cells before exposure to shear stress and was continuously exchanged throughout the duration in the cone and plate apparatus.

6.4.3 HUVEC microarray gene expression profiling.

Microarray analysis was performed as previously described and is publically available at GEO (<http://www.ncbi.nlm.nih.gov/geo/> (GSE46248)). Volcano plots were generated using the expression change and false discovery rates (FDR) from the RvN and RvC datasets, respectively.

6.4.4 Transfection of miRNA antagomirs and mimics in HUVECs.

Twenty-four hours prior to exposure of HUVECs to flow conditions, HUVECs were plated without antibiotics on 0.1% gelatin coated plates in serum-free M199 (Life Technologies Inc) supplemented with 10% fetal bovine serum, 2mmol/L L-glutamine, 5ug/ml endothelial cell growth supplement (Biomedical Technologies, Stoughton, MA), and 10ug/ml heparin (Sigma Aldrich Inc). After cells were allowed to adhere for 2 hours after plating, cells were transfected using Lipofectamine RNAiMax (Invitrogen, Carlsbad, CA) according to manufacturer's instructions. For inhibitor experiments, HUVECs were transfected with 20nM control or miR-199a-5p locked-nucleic acid (LNA) inhibitors (Power Inhibitors, Exiqon, Vedbaek, Denmark). For over-expression experiments, HUVECs were transfected with 20nM control or miR-199a-5p locked-nucleic acid (LNA) mimic (miRCURY LNA mimics, Exiqon).

6.4.5 HUVEC RNA isolation and qRT-PCR.

Total RNA was extracted using the PureLink total RNA purification system (Life Technologies Inc) using the on-column DNase protocol (Life Technologies Inc) according to manufacturer's instructions. RNA concentration and purity was determined with a NanoDrop spectrophotometer in duplicate.

For quantitative reverse transcriptase PCR (qRT-PCR), 500ng of total RNA was reverse transcribed using the miScript II reverse transcription kit (Qiagen, Hilden, Germany, #218160) with HiFlex buffer mix according to manufacturer's instructions. Following reverse transcription, RT-PCR was performed on 20ng cDNA using miScript SYBR Green PCR kit (Qiagen, #218073) and miScript Primer Assays (Qiagen) for U6 (#MS00033740), miR-199a-5p (#MS00006741),

miR-146a-5p (#MS00003535), and miR-29a (#MS00003262) on a CFX96 Real Time Detection System (Biorad). Normalized expression to U6 was quantified using the comparative $2^{\Delta\Delta Ct}$ method.

Target mRNA expression was assessed by qRT-PCR on 12.5ng reverse transcribed cDNA with FastStart SYBR Green (Roche Applied Sciences, Penzberg, Germany) on a CFX96 Real Time Detection System (Biorad, Hercules, CA). Primers used were as follows: CD44 (forward 5'-GCAGCCAACTTCCGAGGCAGC-3', reverse 5'-CGGAGGACGGGACGAGGATGG-3'), CCND1 (forward 5'-AACTACCTGGACCGCTTC-3', reverse 5'-GAGTTGTCTGGTGTAGATGC-3'), IKK β (forward 5'-GCCTGGGAAATGAAAGAGCG-3', reverse 5'-ATCTGCTCACCTGTTTCCTGA-3'), Expression was normalized to β 2-microglobulin (forward 5'-AGCATTCGGGCCGAGATGTCT-3', reverse 5'-CTGCTGGATGACGTGAGTAAACCT-3') which is endogenously expressed and is not altered by many stimuli including shear stress⁴⁴. Normalized expression was quantified using the comparative $2^{\Delta\Delta Ct}$ method.

6.4.6 Monocyte adhesion functional assay

Human derived monocytes (THP-1 cell line) were purchased from the ATCC. Monocytes were unthawed and maintained in RPMI 1640 (11875-093, Life Technologies Inc) + 10% fetal bovine serum (Life Technologies Inc) + 0.05mM β -mercaptoethanol per ATCC culture instructions. Monocytes sub-cultured once cell density approached 800,000 cells/mL. Cells were used between passages 2 – 6.

Prior to the adhesion assay, cells were counted to obtain 3,000,000 cells / plate of HUVECs. Cells were pelleted, washed with PBS, pelleted, and then re-suspended in serum-free RPMI media at 1,000,000 cells/mL. Thawed calcein AM was added at 1ug/ml and incubated with cells for 15 minutes at 37°C. After 15 minutes, the reaction was stopped by adding excess serum-free RPMI to the cell solution then pelleted. Cells were washed once with serum-free M199 media, pelleted, and then re-suspended in serum-free M199 at 500,000 cells/mL. Immediately following

completion of flow exposure to HUVECs, flow media was removed by aspiration. HUVECs were quickly washed with serum-free M199 media. This media was then aspirated off and 6mL of serum-free M199 + monocytes (3,000,000 / plate) were added to and incubated with HUVECs for 30 minutes at 37°C. Following the 30 minutes, cells were washed twice with PBS to remove unbound monocytes. Adhered monocytes and HUVECs were fixed with 4% PFA for 10 minutes followed by two washes with PBS. Cover slips were mounted with Prolong Gold (Life Technologies Inc). Plates were then imaged using a Nikon TE2000 C1 laser scanning confocal microscope. Nine randomly selected FOVs per condition for 4 independent experiments were obtained. Images were de-identified and randomized in MATLAB. Images were converted to 8-bit images, set to an equivalent threshold, and bound monocytes were quantified using Fiji's "Analyze Particles" tool (20 μm^2 minimum particle size). Results were centered on the mean of all conditions within each independent experiment.

6.4.7 Mice.

All animal protocols were approved by the Institutional Animal Care and Use Committee at the University of Virginia (Protocol 3814) and conformed to all regulations for animal use outlined in the American Heart Association Guidelines for the Use of Animals in Research. Balb/c mice were purchased from Charles River Laboratory (Wilmington, MA). All animals were housed in the animal facilities at the University of Virginia.

6.4.8 Femoral arterial ligation model.

We used a previously detailed femoral artery ligation (FAL) scheme^{167,237,242} that produces consistent arteriogenesis in the collateral arteries of the gracilis adductor muscles^{29,30,177–180,237}, along with minimal heterogeneity in the baseline collateral structure and with known changes in flow direction from baseline. Male mice, 10-12 weeks of age, were anesthetized (i.p 120 mg/kg ketamine, 12 mg/kg xylazine, and 0.08 mg/kg atropine), depilated, and prepped for aseptic surgery. On the left leg, an incision was made directly above and along the femoral artery, which

was gently dissected from the femoral vein and nerve between the bifurcation of the superior epigastric artery and popliteal artery. Two 6.0 silk sutures were placed immediately distal to the epigastric artery, which served as the origin of the muscular branch artery in all mice, and the artery segment between the two ligatures was then severed with micro dissecting scissors. The surgical site was then closed with 5.0 prolene sutures. A sham surgery, wherein the femoral artery was exposed but not ligated, was performed on the right hindlimb (i.e. on the other leg). Animals received one injection of buprenorphine for analgesia at the time of surgery and a second dose 8-12 hours later.

6.4.9 *In vivo* miR-199a antagomir treatment.

Anti-miR-199a-5p (5'-TAGTCTGAACACTGGG-3') and non-targeting control (5'-ACGTCTATACGCCCA-3') locked nucleic acid (LNA) oligonucleotides were purchased from Exiqon. Oligonucleotides were reconstituted in sterile TE buffer and stored at 1.2nmol/ μ l at -20°C. Prior to use, aliquots of oligonucleotides were thawed and diluted in sterile saline to a final concentration of 0.25nmol/ μ l. Immediately following FAL, 7.5nmol of oligonucleotide was injected into each (ligated and sham-operated) gracilis muscles.

6.4.10 *In vivo* miR-199a mimic treatment.

In-vivo ready miRVana miR-199a-5p (#4464070, MC10893) mimic and non-targeting control (#4464061) mimic were purchased from Ambion. Mimics (250nmol) were reconstituted in sterile nuclease-free water and stored at 0.5nmol/ μ l at -20°C. Prior to use, aliquots of oligonucleotides were thawed and diluted in sterile saline to a final concentration of 0.25nmol/ μ l. Immediately following FAL, 7.5nmol of oligonucleotide was injected into both ligated and sham-operated gracilis muscles.

6.4.11 Laser Doppler perfusion imaging.

For monitoring blood flow recovery and post-surgical ischemia, mice were anesthetized via 1.5% isoflurane under constant oxygen. Mice were placed in a prone position and the soles of the feet

were scanned (PeriCam PSI, PeriMed, Stockholm, Sweden). Mean foot perfusion was used to calculate relative perfusion ratio (ligated/unligated).

6.4.12 Tissue harvesting for miRNA and target expression.

Seven days after femoral artery ligation, mice were anesthetized (i.p 120 mg/kg ketamine, 12 mg/kg xylazine, and 0.08 mg/kg atropine) and euthanized via an overdose of pentobarbital. The left ventricle was cannulated with a 23-gauge catheter (right ventricle was carefully opened to act as a sink for perfusate) and the entire body was perfused with 7mL of Tris-CaCl₂ (0.1g/L CaCl₂) containing 2% heparin, 2mmol/L adenosine (16404, Fisher Scientific, Pittsburg, PA) and 0.1mmol/L papaverine (P3510, Sigma Aldrich, St Louis, MO) to clear and vasodilate the downstream vasculature at a constant rate of 1.5mL/min (PHD2000, Harvard Apparatus). Once perfused, we waited 5 minutes to enable vasodilation. The entire body was then perfused with 14mL Tris-CaCl₂ and both gracilis muscles dissected free, placed in RNAlater (Ambion), and stored at -20°C.

6.4.13 RNA isolation from tissues and qRT-PCR.

Excess RNAlater was removed from tissues. Tissues were then incubated in 450µl TRIzol reagent for 5 minutes at room temperature. Tissues were then placed on ice and homogenized using a power homogenizer (Omni International, Kennesaw, GA) in short bursts to avoid overheating. Following homogenization, an additional 550µl TRIzol reagent was added. Samples were incubated for another 5 minutes at room temperature to ensure complete lysis. 200µl of chloroform was added to each sample. Samples were then shaken vigorously for 15 seconds and incubated for 3 minutes at room temperature. Following this incubation, samples were centrifuged for 10 minutes at 12,000g at 4°C. The resulting aqueous layer was carefully removed, placed in a new RNA/DNase-free tube, and an equal volume of 70% ethanol was added to the same aqueous layer. RNA isolation then proceeded using the PureLink total RNA purification system (Life Technologies Inc) with the on-column DNase protocol (Life Technologies Inc) according to

manufacturer's instructions. RNA concentration and purity was determined with a NanoDrop spectrophotometer in duplicate.

For reverse transcription (Applied Biosystems, #4366596) and miR-199a-5p detection, TaqMan MicroRNA assays (Applied Biosystems, #4427975) were used. Quantitative real-time PCRs were done on an ABI Prism 7900 HT detection system (Applied Biosystems). Gene expression was normalized to RNU6 (Applied Biosystems, #4427975) and the relative expression was determined with the comparative $2^{-\Delta\Delta C_t}$ method.

6.4.14 Tissue harvesting for whole mount vascular casting and cross sectional analysis.

For analysis of luminal diameters in the gracilis collateral arteries and to enable sectioning at specific regions, vascular casting was performed using an opaque polymer that allows for accurate luminal diameter measurements¹⁷⁹. Twenty-one days after femoral artery ligation, mice were anesthetized (i.p 120 mg/kg ketamine, 12 mg/kg xylazine, and 0.08 mg/kg atropine), euthanized via an overdose of pentobarbital, and then the abdominal aorta was cannulated. The lower body was then perfused with 7mL of 2% heparinized saline with 2mmol/L adenosine (16404, Fisher Scientific) and 0.1mmol/L papaverine (P3510, Sigma Aldrich) to clear and vasodilate the downstream vasculature at a constant rate of 1mL/min (PHD2000, Harvard Apparatus). Once perfused, we waited 5 minutes to enable vasodilation. Tissues were then perfused with 3mL of 4% paraformaldehyde solution (19943, Affymetrix, Cleveland, OH) at 1mL/min and allowed to fix for 10 minutes. The lower body was then perfused with 0.8mL Microfil® casting agent (FlowTech, Inc, Carver, Massachusetts) at a constant pressure of 100mmHg. The viscosity of Microfil® was adjusted to minimize transport across capillaries. After curing for 1.5 hours at room temperature, gracilis muscles were dissected free and then cleared in 50% glycerol in phosphate buffered saline (PBS) overnight. Cleared tissues were mounted between two coverslips using 500 µm thick spacers (645501, Grace Bio-Labs Inc) to keep constant thickness between muscles. Muscles

were imaged using transmitted light at 4x magnification on a Nikon TE200 inverted microscope with a CCD camera (Quantifier, Optronics Inc). Individual fields of view were montaged together (Photoshop CS2, Adobe Systems Inc).

For analysis of lumenal diameters from intact gracilis collateral whole mounts (i.e. vascular casting), collateral entrance regions were defined according to the following method. A cropped portion (560 μm x 560 μm) of the montaged image (previously randomized and de-identified) was taken of the collateral artery at the first visible branch point of a terminal arteriole from the primary collateral as it extended from either the muscular branch or saphenous artery as previously described²³⁷. After each cropped image region was taken, all images were randomized and de-identified. The mean diameter was then taken from 4-5 separate diameter measurements along the length of cropped portion of the collateral artery.

After imaging, muscles were rehydrated, cut, and then paraffin embedded for cross sectional analysis at the muscular branch and saphenous artery entrance regions to the collateral arteries. Resulting cross sections were re-hydrated and immunolabeled for the macrophage marker Mac-3 (day 7 post-FAL) and H&E stained for collateral artery structure analysis (day 21 post-FAL).

6.4.15 Cross sectional analysis of collateral artery structure.

Sections (5 μm thickness) of paraffin embedded muscle from the muscular and saphenous regions were labeled for H&E. Individual fields of view encompassing the collateral vessels were imaged with a 40x water objective on a Zeiss inverted microscope (Zeiss Axioskop, Thornwood, NY) with a CCD camera (Quantifier, Optronics Inc). All images were randomized and de-identified prior to analysis. Lumenal diameter, wall area, and wall thickness were determined using Fiji¹⁸¹.

6.4.16 Immunofluorescence labeling of pericollateral Mac3⁺ cells.

Sections (5 μm thickness) of paraffin embedded muscle from the muscular and saphenous regions were rehydrated and subjected to heat mediated antigen retrieval for 10 minutes in a citrate based antigen retrieval buffer (Vector Laboratories, Burlingame, CA; H-3300). Slides were then

quenched of endogenous peroxidase activity with a 30 minute incubation in 3% H₂O₂, blocked, and labeled with rat-anti-Mac3 (1:100, M3/4 clone, 550292; BD Biosciences, San Jose, CA) overnight at 4°C. Slides were washed and incubated with a biotinylated sheep-anti-rat secondary antibody (Abcam, Cambridge, MA, ab6851, 1:500) for 1 hour at room temperature. Slides were washed and incubated with an avidin-biotin complex (Vectastain ABC solution, Vector Laboratories) for 30 minutes at room temperature. Slides were washed and incubated with a Tyramide Signal Amplification (TSA) reagent (Perkin Elmer, Waltham, MA; 1:50) for 10 minutes at room temperature. Slides were washed and incubated with streptavidin-488 (Life Technologies Inc, 1:500), Cy3-anti-SMA (1A4 clone, Sigma, 1:1000) and DRAQ5 (Thermo Scientific Inc, 1:1000). Slides were then mounted with Prolong Gold (Life Technologies Inc) to minimize photobleaching, allowed to cure overnight, and imaged using a Nikon TE2000 C1 laser scanning confocal microscope with a 20x oil objective. Cropped fields of view (512x512 pixels) encompassing the collaterals in each region were randomized and de-identified. The pericollateral region was outlined (25 microns around the vessel) and pericollateral Mac3⁺ nuclei were counted in Fiji¹⁸¹.

6.4.17 Cross sectional analysis for gastrocnemius muscle morphology.

Sections (5µm thickness) of paraffin embedded muscle from the gastrocnemius muscle were H&E labeled. Individual fields of view were imaged with a 10x objective on a Zeiss inverted microscope (Zeiss Axioskop) with a CCD camera (Quantifier, Optronics Inc). Individual fields of view were montaged together (Photoshop CS2, Adobe Systems Inc). All montaged images were randomized and de-identified prior to analysis. Muscle areas were manually outlined using Fiji¹⁸¹.

Tissue composition was classified into viable and non-viable, which were defined as:

1. Viable: fibers are present and have centrally located nuclei (regenerating) or fibers are comparable in size, organization, and structure to unligated control with peripheral nuclei (mature)³⁰

2. Non-viable: fibers lack nuclei, are rounded and dilated in appearance, have weak eosinophilic cytoplasm (necrotic) or where there is minimal presence of myoblasts and is dominated by fibrous matrix and adipose tissue (fibroadipose)³⁰

6.4.18 Cross sectional analysis for gastrocnemius capillary density.

Sections (5µm thickness) of paraffin embedded gastrocnemius muscles were deparaffinized, rehydrated, then blocked in Carbofree blocking solution (1:10, Vector Labs). Slides were then incubated with fluorophore conjugated primary antibody (isolectin-IB4-AlexFluor-647, 1:200, Life Technologies Inc) overnight at 4 °C. Nuclei were counterstained with Sytox green (500uM, Life Technologies Inc). Slides were washed and sealed with Prolong Gold (Life Technologies Inc) to minimize photobleaching. Individual fields of view were imaged with a Nikon TE2000 C1 laser scanning confocal microscope with a 10x objective and the same imaging parameters for all fields of view. Fields of view were then montaged together using Photoshop CS2 (Adobe Systems Inc). Muscle areas were manually outlined using Fiji¹⁸¹ and classified as either viable or non-viable tissue. The number of capillaries (Isolectin-B4⁺ vessels <25µm² in diameter) and muscle area (identified from autofluorescence) were determined in each montaged image view using a semi-automated Fiji image analysis.

6.4.19 Statistical analyses.

All results are reported as mean ± standard error of the mean (SEM), unless otherwise noted. All data were first tested for normality and equal variance. Statistical significance was then assessed by a Student's *t* test or a two-way ANOVA followed by a Holm-Sidak multiple comparisons test, unless otherwise noted (SigmaStat 3.5, Systat Inc). Significance was assessed at $p < 0.05$.

6.5 Results

6.5.1 Endothelial cell miRNA expression is regulated by shear stress waveforms biomimetic of collateral artery segments exhibiting differential arteriogenic responses.

To identify candidate miRNAs, we examined previously generated genome-wide cDNA microarray data (GSE46248)²³⁷ from ECs exposed to shear stress waveforms biomimetic of those measured in-vivo¹⁷⁶ in collateral artery segments exhibiting either moderate (muscular) or amplified (saphenous) arteriogenesis responses ([Figure 6.1A](#)). Briefly, human umbilical vein endothelial cells (HUVECs) were preconditioned for 24 hours at a baseline arterial shear stress (15 dynes/cm²)¹⁹⁰ to establish endothelial cell alignment, planar cell polarity, and steady-state signaling, thereby mimicking the in-vivo baseline state. A femoral arterial ligation (FAL) was then simulated by a step-wise 100% increase in shear stress, in either the same direction or in the opposite direction, to mimic shear stress changes occurring in the muscular branch (non-reversed flow) and saphenous artery (reversed flow) entrance regions, respectively ([Figure 6.1A-B](#)). Six hours after our simulated FAL, we isolated total RNA and performed genome-wide analysis using Affymetrix cDNA 1.0 ST microarrays. Genome-wide analysis identified a small subset of miRNA genes differentially regulated between reversed and non-reversed flow conditions ([Figure 6.1C](#), [Supplemental Table 6.1](#)). The expression of several candidate miRNAs (miR-199a-5p, miR-146a-5p, and miR-29a) was assessed by RT-qPCR both at 1-hour and 6-hours after simulated FAL to confirm microarray results. We found all these candidate miRNAs to be significantly downregulated (~40%) in HUVECs exposed to the reversed flow waveform 6-hours after simulated FAL ([Figure 6.1D-F](#)).

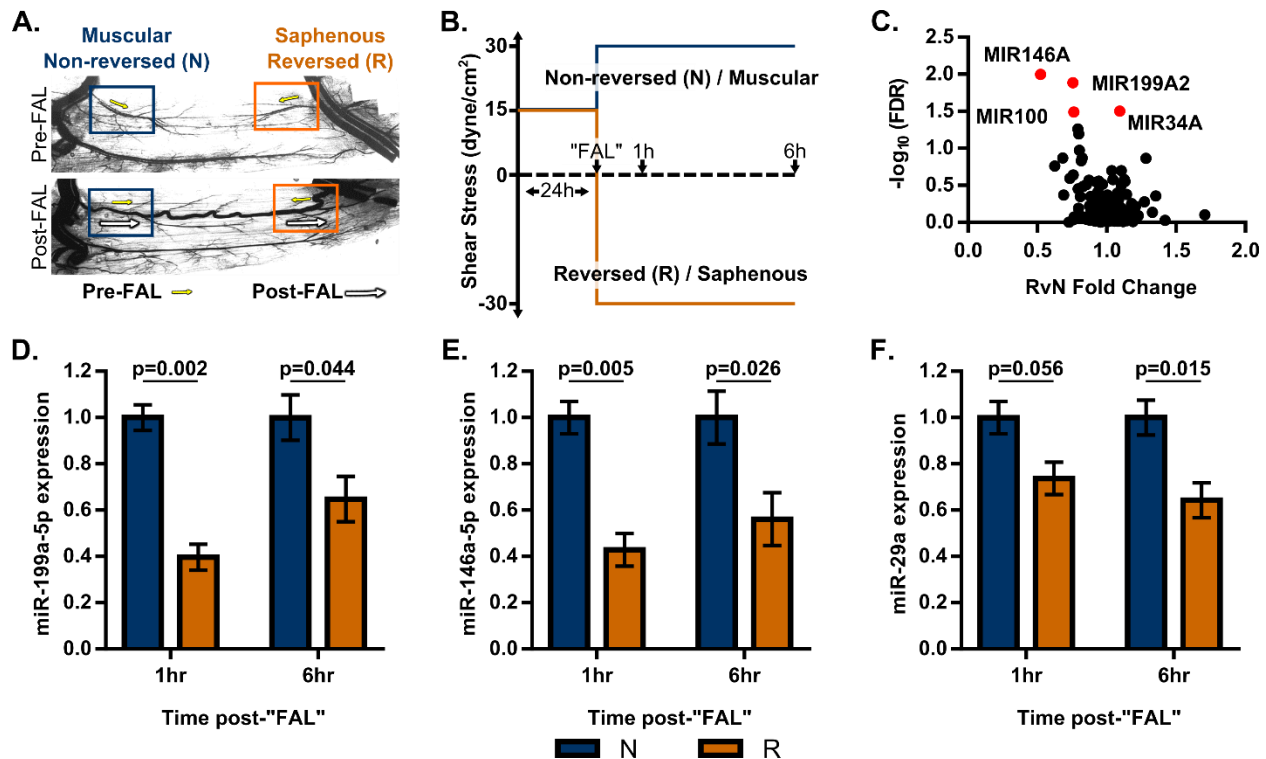


Figure 6.1. Endothelial cell miRNA expression is differentially regulated by shear stress waveforms biomimetic of collateral artery segments exhibiting varied arteriogenic responses.

A) Representative vascular cast images of gracilis adductor collaterals in Balb/c mice taken from unligated sham control (top) and day 21 post-femoral arterial ligation (FAL, bottom) groups. Arrows indicate direction and magnitude of blood flow pre- (yellow) and post- (white) FAL. The femoral artery is ligated just distal to the epigastric artery such that some collateral segments (“muscular”) experience a 2-fold increase in shear stress magnitude (“non-reversed” flow) while other segments (“saphenous”) are exposed to both a 2-fold increase in shear stress magnitude and reversed flow direction (“reversed” flow). Arteriogenesis is amplified in the flow-reversed, saphenous regions of collateral arteries. **B)** Schematic depicting biomimetic waveforms applied to HUVECs to simulate saphenous (reversed flow, R) and muscular (non-reversed flow, N) regions. **C)** Volcano plot of all microRNAs (miRNAs) on the Affymetrix ST 1.0 human microarray dataset ($n=4$) from Heuslein et al.²³⁷ HUVECs were exposed to the flow waveforms in (B). Gene expression was determined at 6 hours after simulated FAL. False discovery rate = FDR. Red dots indicate miRNAs with $FDR < 0.05$. **D-F)** Bar graphs of mature miR-199a-5p, miR-146a-5p, and miR-29a expression in HUVECs exposed to biomimetic shear stress conditions from (B) ($n=3-5$). Student’s *t*-test. Data are mean \pm SEM.

6.5.2 MicroRNA-199a negatively regulates pro-arteriogenic endothelial gene expression and monocyte adhesion to flow-exposed ECs in-vitro.

Of these candidate miRNAs, miR-199a-5p (henceforth denoted as miR-199a) was of particular interest as it is known to regulate mRNAs of several pathways necessary for arteriogenesis, including CD44^{266,267}, CCDN1²⁶⁸, and IKK β ²⁶⁹. We therefore sought to determine if miR-199a

regulates the expression of these pro-arteriogenic genes in ECs exposed to the biomimetic shear stress waveforms. HUVECs were transfected with 20nM miR-199a mimic, anti-miR-199a locked nucleic acid oligonucleotides, or respective non-targeting controls, 24 hours prior to shear stress exposure.

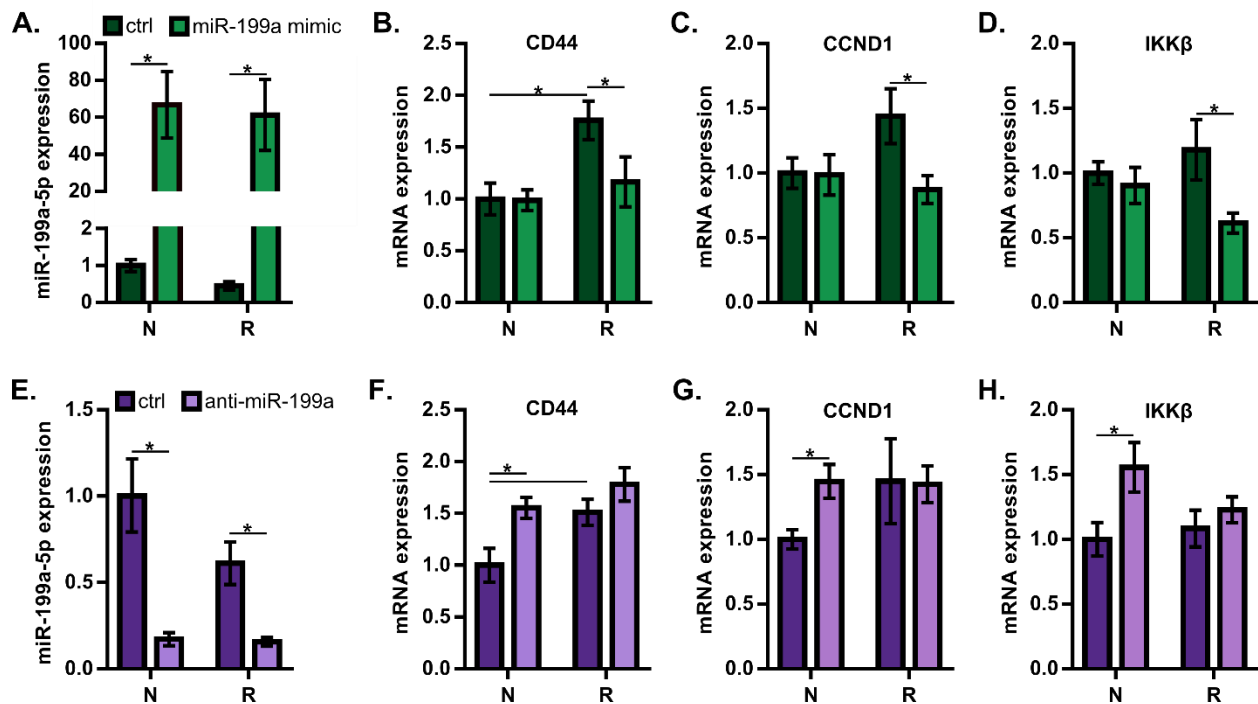


Figure 6.2. MicroRNA-199a negatively regulates the expression of CD44, CCND1, and IKKβ in endothelial cells exposed to biomimetic shear stress waveforms in-vitro.

A) Bar graph of relative miR-199a expression 6-hours after simulated FAL in HUVECs transfected with miR-199a or non-targeting control (ctrl) mimics and subjected to non-reversed (N) or reversed (R) flow waveforms as outlined in Figure 6.1B (n=4). *p<0.05, Student's *t*-test. **B-D)** Bar graphs of relative CD44, CCND1, and IKKβ mRNA expression in each condition (n=4). *p<0.05, two-way ANOVA followed by a Holm-Sidak test for multiple comparisons. **E)** Bar graph of relative miR-199a expression 6-hours after simulated FAL in HUVECs transfected with anti-miR-199a or non-targeting control (ctrl) locked nucleic acid oligonucleotides (n=4). *p<0.05, Student's *t*-test. **F-H)** Bar graphs of relative CD44, CCND1, and IKKβ mRNA expression in each condition (n=4). *p<0.05, two-way ANOVA followed by a Holm-Sidak test for multiple comparisons. Data are mean ± SEM.

Transfection with miR-199a mimics increased relative miR-199a expression >60-fold (Figure 6.2A) and anti-miR-199a reduced miR-199a expression by ~80% (Figure 6.2E) compared to their respective non-targeting controls in HUVECs exposed to our biomimetic waveforms. Six-hours after simulated FAL, CD44 expression was significantly upregulated

between non-reversed and reversed flow waveforms in HUVECs under non-targeting control-treated conditions (**Figure 6.2B, F**). However, transfection with miR-199a mimic significantly decreased the relative expression of CD44, CCND1, and IKK β in HUVECs exposed to reversed flow conditions (**Figure 6.2B-D**). Inhibition of miR-199a led to an upregulation in CD44, CCND1, and IKK β expression in HUVECs exposed to a non-reversed waveform, while there was no significant effect under reversed flow conditions (**Figure 6.2F-H**).

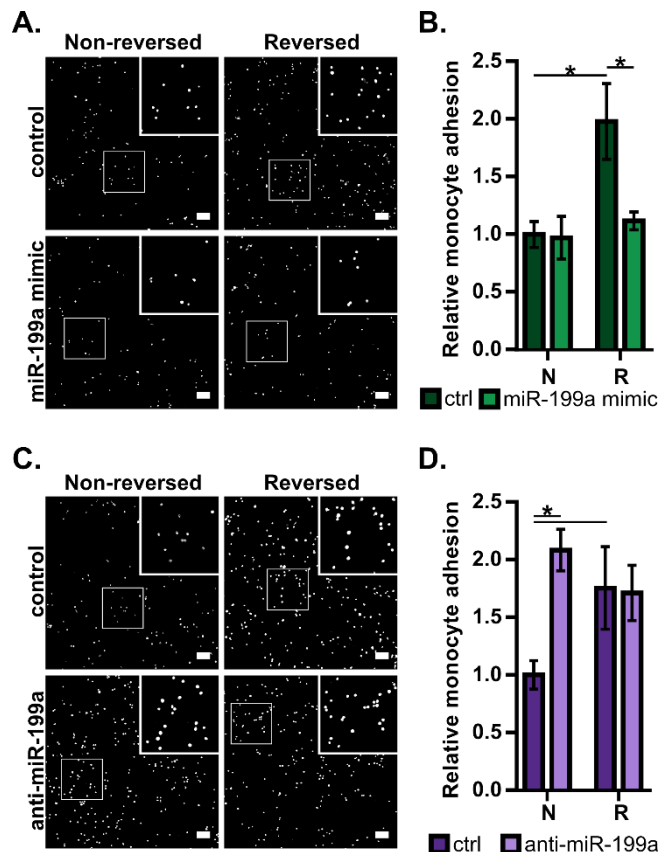


Figure 6.3. Monocyte adhesion to HUVECs exposed to shear stress waveforms biomimetic of arteriogenic collaterals is modulated by miR-199a.

A) Representative confocal microscopy images of fluorescently labeled THP-1 monocytes adhered to HUVECs transfected with miR-199a or non-targeting control (ctrl) mimic then subjected to non-reversed (N) or reversed (R) flow waveforms outlined in Figure 6.1B, 6-hours post-simulated FAL (Scale bar = 100 μ m). Insets are the magnified 300 μ m x 300 μ m regions outlined by white boxes. **B)** Bar graph quantifying relative number of adhered monocytes in each condition (n=4). *p<0.05, two-way ANOVA followed by a Holm-Sidak multiple comparisons test. **C)** Representative images of fluorescently labeled THP-1 monocytes adhered to flow exposed HUVECs transfected with anti-miR-199a or non-targeting control (ctrl) locked nucleic acid oligonucleotides, 6-hours after simulated FAL (Scale bar = 100 μ m). **D)** Bar graph quantifying relative number of adhered monocytes in each condition (n=4). *p<0.05, two-way ANOVA followed by a Holm-Sidak multiple comparisons test. Data are mean \pm SEM.

Monocyte adhesion to activated endothelium is a required step in the arteriogenesis cascade^{52,56,58,60,62,246}. We sought to determine whether altered miR-199a expression modulates this critical process. In control-treated conditions, HUVECs exposed to the reversed flow waveform experienced increased monocyte adhesion compared to those exposed to the non-reversed waveform (**Figure 6.3**), consistent with previous results²³⁷. Overexpression of miR-199a attenuated this enhanced functional response, leading to a 44% decrease in monocyte adhesion

in reversed flow conditions (**Figure 6.3A-B**). In non-reversed flow conditions, miR-199a overexpression did not further reduce monocyte adhesion. Conversely, inhibition of miR-199a led to enhanced pro-arteriogenic function in-vitro as seen by a 90% increase in monocyte adhesion to non-reversed flow-exposed HUVECs, while there was no further increase with reversed flow (**Figure 6.3C-D**).

6.5.3 Overexpression of miR-199a limits foot reperfusion following FAL while miR-199a inhibition elicits complete perfusion recovery in Balb/c mice.

To test the hypothesis that miR-199a regulates perfusion recovery and/or arteriogenesis in-vivo, we performed FALs on Balb/c mice and modulated miR-199a expression via intramuscular injection of miR-199a mimic, anti-miR-199a locked nucleic acid oligonucleotides, or respective non-targeting control, directly into the gracilis muscle immediately following FAL. Local intramuscular injection of miR-199a mimic led to a ~5-fold increase in relative miR-199a expression (**Figure 6.4A**), while anti-miR-199a decreased miR-199a expression ~2.6-fold in the gracilis muscle 7 days post-FAL (**Figure 6.4B**). Perfusion measurements of the plantar surface of the foot indicated moderate ischemia immediately post-FAL, followed by an incomplete perfusion recovery in the control-treated mice of both overexpression (0.92 ± 0.02 , day 21 post-FAL) and inhibition (0.88 ± 0.02 , day 21 post-FAL) studies (**Figure 6.4C-F**). When miR-199a was overexpressed, the reperfusion response was further dampened as early as 4 days post-FAL and only reached 80% reperfusion 21 days post-FAL (**Figure 6.4C, E**). However, anti-miR-199a treated mice fully recovered foot perfusion by day 21 post-FAL (**Figure 6.4D, F**).

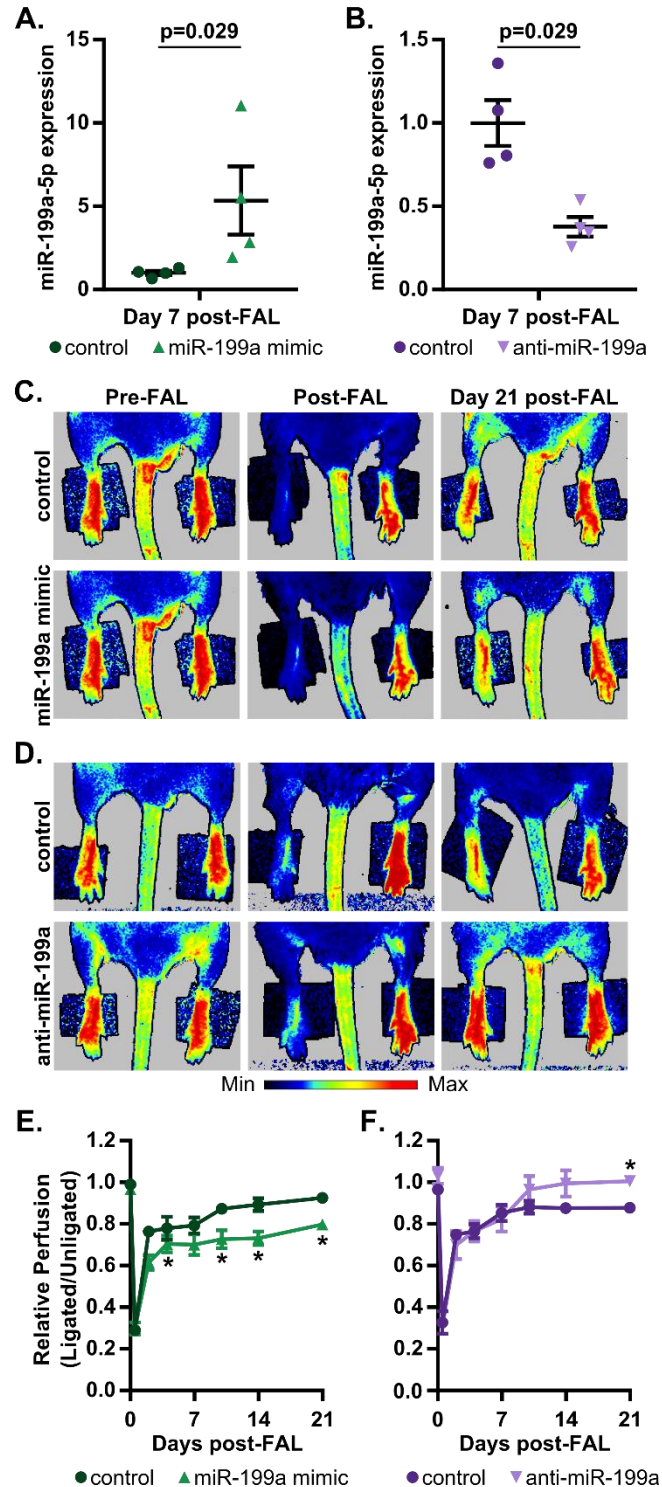


Figure 6.4. Overexpression of miR-199a limits foot reperfusion following FAL while miR-199a inhibition leads to complete perfusion recovery in Balb/c mice.

A-B) Relative miR-199a-5p expression in the gracilis muscle 7 days post-FAL in Balb/c mice. Mice were treated with a single i.m. injection of 7.5nmol miR-199a mimic, anti-miR-199a, or respective non-targeting control oligonucleotides immediately post-FAL (n=4). Mann-Whitney U test. **C-F)** Post-FAL foot perfusion recovery as assessed by laser Doppler perfusion imaging (n=6). * $p < 0.05$ vs. control, two-way ANOVA with repeated measures followed by Holm-Sidak test for multiple comparisons. Data are mean \pm SEM.

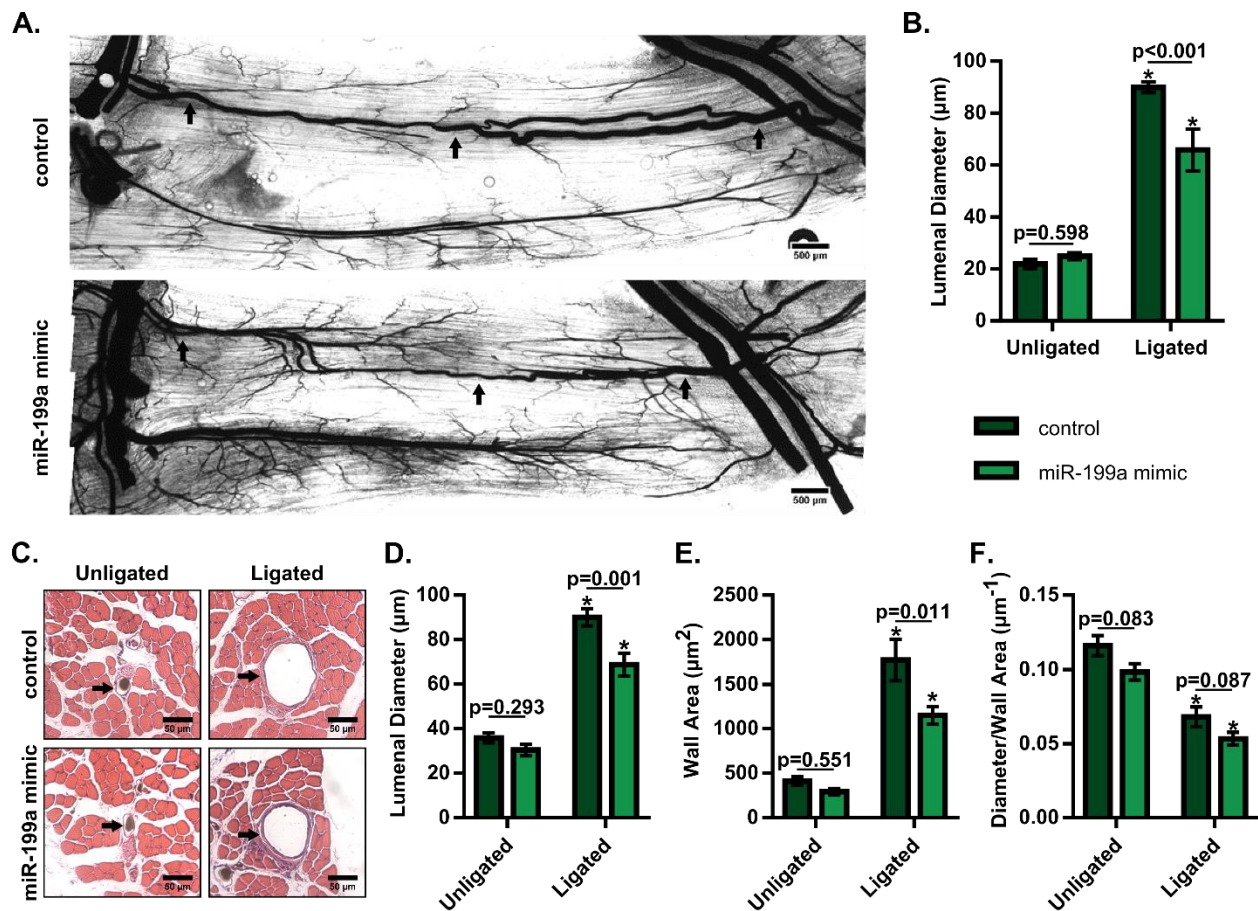


Figure 6.5. Overexpression of miR-199a inhibits arteriogenesis in Balb/c mice.

A) Representative whole mount vascular cast images of gracilis collateral arteries 21 days post-FAL in non-targeting control (top) or miR-199a mimic (bottom) treated Balb/c mice. **B)** Bar graph of mean luminal diameter along collateral artery length for ligated and unligated limbs of miR-199a mimic and control treated mice (n=5-6 for mimic and control groups respectively). *p<0.001 vs. unligated, two-way ANOVA followed by Holm-Sidak test for multiple comparisons. **C)** Representative H&E stained cross-sections of collateral arteries from ligated and unligated limbs. **D-F)** Bar graphs of luminal diameter, wall area, and diameter per wall area from H&E stained cross-sections (n=5-6 for mimic and control groups respectively). *p<0.001 vs. unligated, two-way ANOVA followed by Holm-Sidak test for multiple comparisons. Arrows indicate the primary collateral artery in (A) and (C). Data are mean ± SEM.

6.5.4 Overexpression of miR-199a inhibits arteriogenesis in Balb/c mice.

We next examined whether overexpression of miR-199a expression affects arteriogenesis by measuring the luminal diameter of gracilis collateral arteries 21 days post-FAL (Figure 6.5A,

Figure 6.6A). While both control and miR-199a mimic treated mice experienced significant ($p<0.0001$) arteriogenesis in their ligated limbs compared to sham-operated controls, treatment with a miR-199a mimic significantly ($p=0.0008$) reduced collateral artery growth by $>25\%$ (**Figure 6.5B**). Moreover, this reduction in arteriogenesis occurred at both the muscular (non-reversed) and saphenous (reversed) collateral artery regions (**Supplemental Figure 6.1**). Cross-sectional analysis of these collateral arteries was used to confirm whole-mount diameter measurements and to determine collateral wall area (**Figure 6.5C**). Mice treated with miR-199a mimic experienced a lesser degree of enhancement in luminal diameter (**Figure 6.5D**) and wall area (**Figure 6.5E**) than controls, while there was no significant difference ($p=0.087$) in the diameter to wall area ratio, 21 days after FAL.

6.5.5 Inhibition of miR-199a amplifies arteriogenesis in Balb/c mice following FAL

In contrast, when we administered a single intramuscular injection of an anti-miR-199a locked-nucleic acid oligonucleotide to mice immediately after FAL, arteriogenesis was significantly amplified (**Figure 6.6A**). Inhibition of miR-199a generated a 36% increase in collateral luminal diameter 21 days post-FAL ($p<0.0001$) (**Figure 6.6B**). Again, cross-sectional analysis was used to confirm whole-mount diameter measurements and to determine wall area (**Figure 6.6C**). Following FAL, intramuscular anti-miR-199a treatment produced increased collateral artery luminal diameter (**Figure 6.6D**) and wall area (**Figure 6.6E**) compared to control-treated Balb/c mice, while there was no significant difference in the diameter to wall area ratio (**Figure 6.6F**). The enhancement in luminal diameter and wall area in response to miR-199a inhibition was evident along the collateral at both the muscular (non-reversed) and saphenous (reversed) regions (**Supplemental Figure 6.2**).

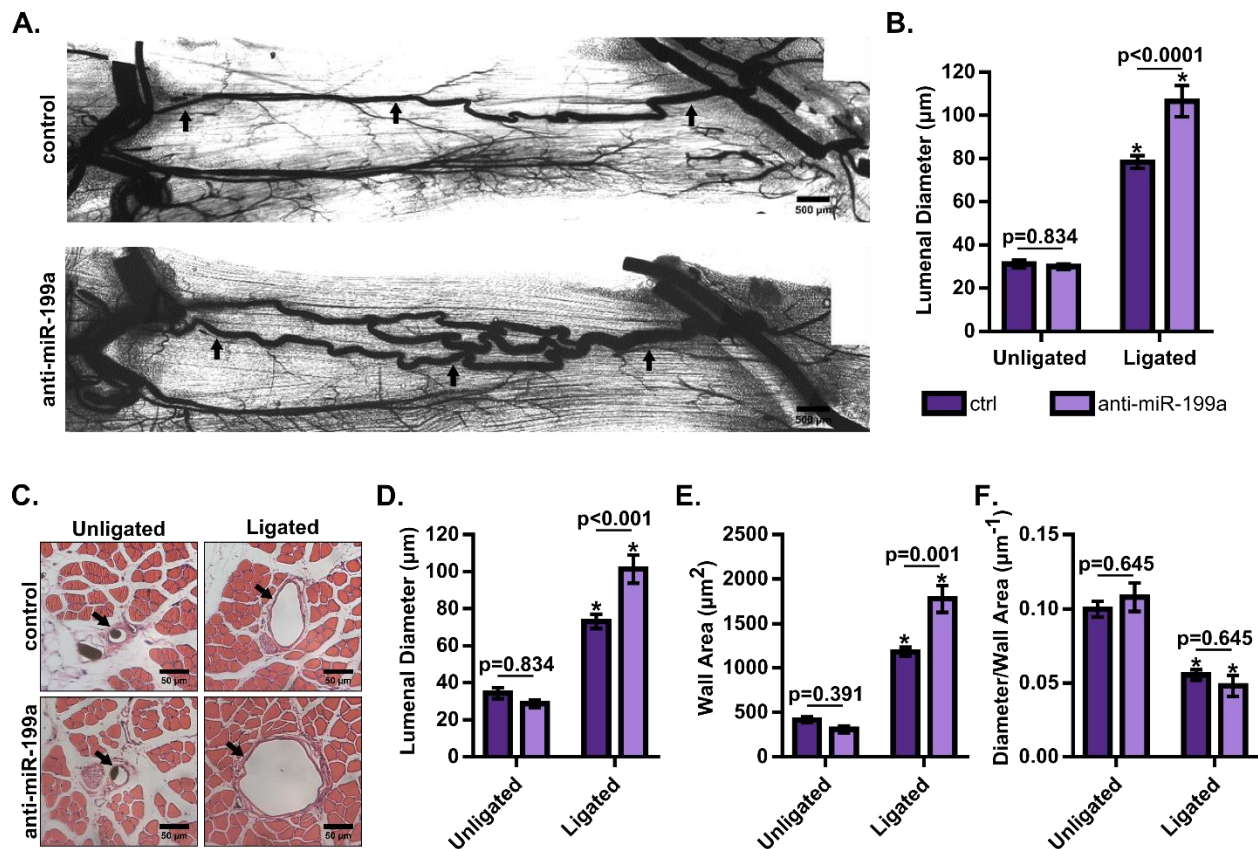


Figure 6.6. Inhibition of miR-199a amplifies arteriogenesis in Balb/c mice following FAL. **A)** Representative whole mount vascular cast images of gracilis collateral arteries 21 days post-FAL in non-targeting control (top) or anti-miR-199a (bottom) treated Balb/c mice. **B)** Bar graph of mean luminal diameter along collateral artery length for ligated and unligated limbs of anti-miR-199a and control treated mice (n=6). *p<0.001 vs. unligated, two-way ANOVA followed by Holm-Sidak test for multiple comparisons. **C)** Representative H&E stained cross-sections of collateral arteries from ligated and unligated limbs. **D-F)** Bar graphs of luminal diameter, wall area, and diameter per wall area from H&E stained cross-sections (n=6). *p<0.001 vs. unligated, two-way ANOVA followed by Holm-Sidak test for multiple comparisons. Arrows indicate the primary collateral artery in (A) and (C). Data are mean ± SEM.

6.5.6 Pericollateral macrophage recruitment is modulated by miR-199a.

We next sought to determine whether modulating miR-199a expression altered macrophage recruitment, a necessary component of collateral artery growth^{52,56,58,60,62,246,68}, in-vivo. We determined that miR-199a overexpression caused to a 36% decrease in pericollateral Mac3⁺ macrophages 7 days post-FAL in Balb/c mice, whereas miR-199a inhibition caused a 43% increase in pericollateral macrophage recruitment ([Figure 6.7](#)). This trend was also observed when the muscular (non-reversed) and saphenous (reversed) collateral artery regions were assessed individually ([Supplemental Figure 6.3](#)).

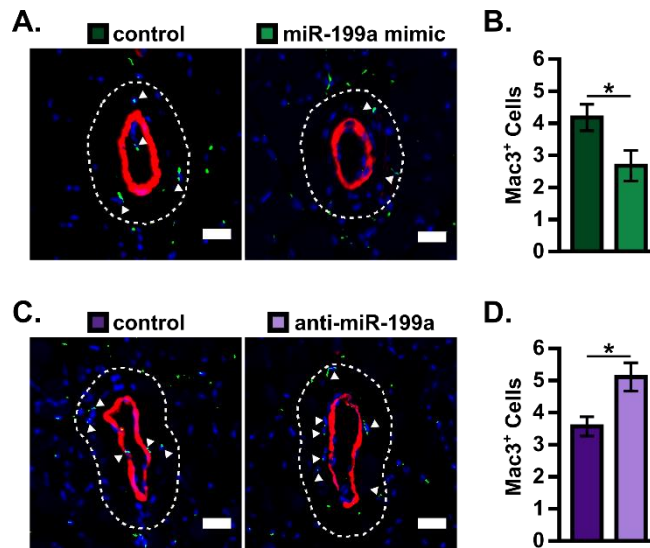


Figure 6.7. Pericollateral macrophage recruitment is modulated by miR-199a.

A) Representative cross-sections of gracilis collateral artery regions immunolabeled for macrophage marker, Mac3 (green), smooth muscle alpha actin (SMαA, red), and nuclei (DRAQ5, blue) in Balb/c mice treated with miR-199a mimic or non-targeting control mimic 7 days post-FAL. Dotted line indicates the pericollateral region (25μm from vessel wall) used for quantification. Arrowheads indicate Mac3⁺ cells (Scale bar=25μm). **B)** Bar graph of pericollateral Mac3⁺ cells (n=4-5 for miR-199a mimic and control, respectively). *p<0.05, Student's t-test. **C)** Immunolabeled gracilis collateral artery regions, as in (A), in Balb/c mice treated with anti-miR-199a or non-targeting control oligonucleotide 7 days post-FAL. **D)** Bar graph of pericollateral Mac3⁺ cells (n=3). *p<0.05, Student's t-test. Data are mean ± SEM.

6.5.7 MicroRNA-199a inhibition improves gastrocnemius muscle composition in FAL-operated Balb/c mice.

Finally, we examined the effect of altered miR-199a expression on the composition of ischemic muscle tissue downstream of the femoral artery occlusion. Gastrocnemius muscle tissue was categorized as viable (mature and regenerating fibers) or non-viable (necrotic and fibro-adipose tissue) by histological analysis 21 days after FAL ([Figure 6.8A-B](#)). Though muscle composition was not significantly altered in miR-199a mimic treated mice ([Supplemental Figure 6.4](#)), inhibition of miR-199a resulted in a greater than 34% reduction in the percentage of non-viable tissue in the gastrocnemius muscle ([Figure 6.8C](#)).

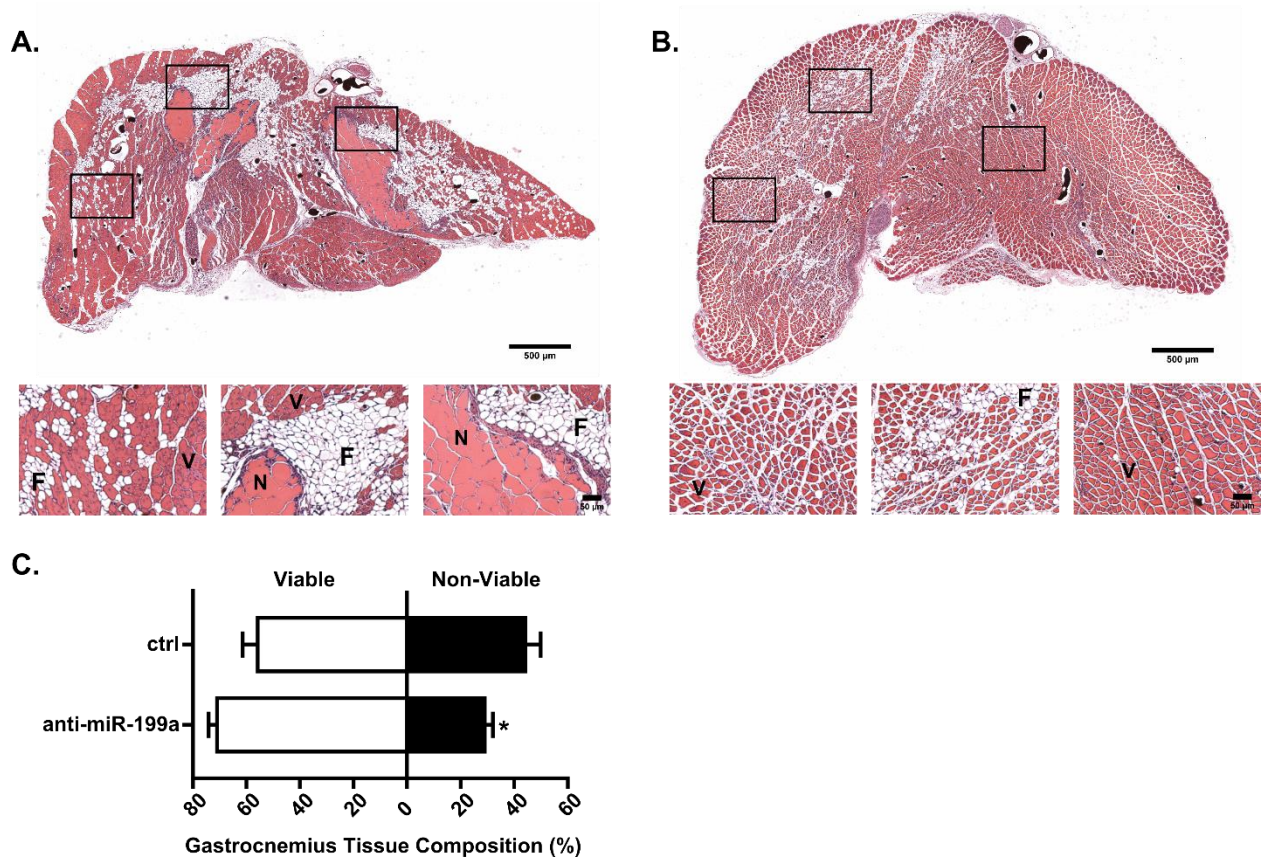


Figure 6.8. MicroRNA-199a inhibition improves gastrocnemius muscle composition in FAL-operated Balb/c mice.

A-B) Representative images of H&E staining of gastrocnemius muscle for ligated limb of Balb/c mice treated with non-targeting control (ctrl) (A) or anti-miR-199a (B) locked nucleic acid oligonucleotide immediately after FAL (Scale bar=500µm, inset scale bar=50µm). V=viable muscle, N=necrotic tissue, and F=fibro-adipose tissue. **C)** Bar graph of the percentage of gastrocnemius muscle that is viable (white) or non-viable (black) at day 21 post-FAL in each group (n=5). *p<0.05 vs. control, Student's t-test. Data are mean ± SEM.

6.6 Discussion

The primary goal of this study was to determine whether mechanosensitive miRNAs regulate endogenous collateral artery growth and perfusion recovery following femoral arterial occlusion. First, we identified candidate regulators of arteriogenesis by comparing differential miRNA expression in ECs exposed to shear stress waveforms corresponding to moderate and amplified arteriogenesis responses in-vivo. Among these candidate miRNAs, miR-199a was significantly downregulated by the amplified arteriogenesis (reversed flow) waveform and shown to regulate

pro-arteriogenic gene (CD44, IKK β , and CCND1) expression and monocyte adhesion to shear stress-exposed endothelium. In-vivo, overexpression of miR-199a limited foot perfusion, arteriogenesis, and monocyte recruitment in the mouse FAL model. In contrast, inhibition of miR-199a elicited complete foot perfusion recovery, substantially enhanced collateral arteriogenesis via increased pericollateral macrophage recruitment, and considerably improved gastrocnemius muscle tissue composition. We have therefore identified miR-199a as a novel mechanosensitive miRNA that regulates perfusion recovery and arteriogenesis. MicroRNA-199a may represent a new target for the therapeutic stimulation of arteriogenesis and the treatment of peripheral arterial disease.

6.6.1 Identification of microRNA-199a as a novel mechanosensitive regulator of pro-arteriogenic gene expression

Our strategy of interrogating differential mechano-signaling in ECs exposed to a biomimetic “amplified arteriogenesis” waveform represents a unique approach for identifying miRNA regulators of vascular growth and perfusion recovery in response to arterial occlusion(s). This strategy was enabled by our group’s previous development of a transillumination laser speckle flowmetry method customized for measuring blood velocities in the collateral arteries of the mouse gracilis adductor muscle¹⁷⁶. Using this method, we were able to determine segment-to-segment hemodynamic changes induced by FAL¹⁷⁶, correlate these to variations in arteriogenesis²³⁷, and directly apply these flow waveforms to ECs in-vitro. The utility of this approach is supported by our present results, as well as by our approach’s identification of miR-100 as another candidate miRNA (**Figure 6.1 C**). Inhibition of miR-100 has been shown previously to enhance perfusion recovery following FAL¹⁶¹. When considered in light of our findings, we postulate that the enhancement of shear stress-mediated collateral arteriogenesis may be a probable component of perfusion recovery with anti-miR-100 treatment.

We also identified miR-34a and miR-146a as potential mechanosensitive regulators of arteriogenesis that could be targeted for therapeutic arteriogenesis (**Figure 6.1**). However, based on their known downstream targets and functions, we postulate that these miRNAs could be subject to the so-called “Janus phenomenon”, wherein pro-arteriogenic therapies also tend to promote atherosclerosis²⁶². To this end, miR-146a^{-/-}Ldlr^{-/-} mice on a high-cholesterol diet display an increased number of atherosclerotic plaques²⁷⁰. Moreover, while miR-34a is significantly down-regulated in the peripheral blood of a subpopulation of PAD patients¹⁴⁰, it has been found to be significantly up-regulated in human atherosclerotic plaques²⁷¹.

To date, miR-199a has been mostly studied for its roles in cardiac hypertrophy^{272,273}, smooth muscle proliferation²⁷⁴, angiogenesis^{275–280}, and as a tumor suppressor in a variety of cancers^{269,276,278,281–285}. However, miR-199a also regulates several genes important for arteriogenesis via direct seed sequence binding to target mRNAs. To this end, it has been shown that miR-199a negatively regulates NFκB, which is necessary for arteriogenesis²⁵⁶, by directly targeting IKKβ²⁶⁹. Another verified miR-199a target known to be necessary for arteriogenesis is CD44^{266,267}. CD44 is a glycoprotein involved in leukocyte adhesion, cell growth, survival, and differentiation by regulating the activity of several pro-arteriogenic growth factors, including FGF and HGF²⁸⁶. Additionally, miR-199a indirectly moderates cyclin D1 (CCDN1) expression²⁶⁸, a key regulator of cell cycle and proliferation²⁸⁷. Here, we found that miR-199a alters both IKKβ and CD44 expression in ECs exposed to our biomimetic shear stress waveforms, suggesting potential pathways by which altered miR-199a is able to regulate arteriogenesis. Indeed, in-vitro, CD44 was significantly altered between reversed and non-reversed conditions in control-treated ECs, suggesting possible endogenous regulation by miR-199a. Furthermore, through both loss- and gain-of-function studies, we found miR-199a to regulate EC proliferation and monocyte adhesion, both key aspects of arteriogenesis. Altogether, this made miR-199a a compelling candidate miRNA to study in the context of arteriogenesis in-vivo.

Our experimental approaches also allowed us to examine whether miR-199a regulated functions depend on hemodynamic context. In-vitro, anti-miR-199a interventions primarily affected ECs exposed to the non-reversed flow waveform, while miR-199a mimic interventions primarily affected ECs exposed to the reversed flow waveform. This response pattern appears to be dependent on the relative miR-199a expression in ECs rather than the hemodynamic context, per se ([Supplemental Figure 6.5](#)). Moreover, modulation of miR-199a expression in-vivo led to similar relative changes in collateral growth responses and macrophage recruitment in both muscular (non-reversed) and saphenous (reversed) collateral regions ([Supplemental Figure 6.1](#) - [Supplemental Figure 6.3](#)).

6.6.2 Previous studies implicating a role of miRNA-regulated arteriogenesis

Despite a number of previous reports indicating miRNA regulation of perfusion recovery in hindlimb ischemia models^{143,150,151,154,155,159,161,162,164}, only a few of these microRNAs (e.g. miR-155, miR-17~92a, miR-487b) have been suggested to have a role in arteriogenesis per se. Inhibition of miR-155 attenuates blood flow recovery and leukocyte recruitment, despite promoting angiogenesis in the ischemic tissue of FAL-treated mice, thereby indirectly implying a role for miR-155 in arteriogenesis. However, collateral diameters were not explicitly reported¹⁶². In another study, endothelial-specific deletion of the miR-17~92 cluster increased foot perfusion 14 days following FAL as well as arteriole density in FAL-operated limbs. However, arteriole diameters were not significantly greater in these mice, indicating increased perfusion was due to an increase in arteriole density, rather than endogenous collateral artery growth¹⁵¹. Finally, miR-329, miR-487b, miR-494, and miR-495 inhibition all led to a 25-40% increase in blood flow recovery following FAL, though only miR-487b inhibition increased vessel diameters from PBS-treated controls¹⁵⁵. While this study further corroborates microRNA-mediated regulation of arteriogenesis, it is difficult to directly compare our results with this study due to differences in

oligonucleotide dosing, the extent of ischemia in FAL models, and methods for assessing arteriogenesis¹⁵⁵.

6.6.3 MicroRNA-199a as a regulator of arteriogenesis leading to enhanced perfusion recovery

In testing our hypothesis that miR-199a negatively regulates perfusion recovery and arteriogenesis in-vivo, we chose to perform our FAL model in Balb/c mice to enable for the necessary dynamic range for both loss and gain-of function studies, as these mice exhibit a more blunted arteriogenic response compared to C57BL/6^{165,168}. Following FAL, control treated mice exhibited incomplete perfusion recovery as expected, though they did recover 80-90% perfusion in ligated limbs compared to the ~50-60% perfusion recovery seen in previous studies¹⁶⁵. This greater than expected recovery was likely due to the more mild nature of our ligation scheme; nonetheless, we were still able to observe significant changes in foot perfusion with modulation of miR-199a expression, similar to those seen by previous miRNA studies^{161,164,288}.

Corresponding to the observed changes in foot perfusion, we found that miR-199a negatively regulates arteriogenesis. Our results indicating miR-199a modulates monocyte/macrophage recruitment are consistent with the known necessary role for leukocyte recruitment in arteriogenesis^{56,60,62,289} and suggest that this is the mechanism through which miR-199a regulates arteriogenesis following FAL. Critical in determining the reperfusion response, alterations to endogenous collateral growth can lead to substantial changes in collateral conductance. To this end, miR-199a overexpression attenuated collateral artery growth ~25% (~2.4-fold decrease in conductance) and miR-199a inhibition enhanced arteriogenesis by 36% (>3.4-fold conductance increase). Of particular importance for potential clinical translation, collateral arteries in anti-miR-199a treated mice were morphologically normal as there was no difference in the luminal diameter to wall area ratio when miR-199a expression was altered.

In addition to arteriogenesis, perfusion recovery following FAL can also be dependent upon angiogenesis²⁹ and/or tissue clearance and skeletal muscle regeneration³⁰. Here, we did not observe any significant differences in gastrocnemius capillary density in anti-miR-199a treated mice at day 21 post-FAL (**Supplemental Figure 6.6**). However, we did find that a single bolus of anti-miR-199a oligonucleotide was sufficient to improve gastrocnemius muscle tissue composition in FAL-operated mice (**Figure 6.8**), though there was no significant change in muscle composition with miR-199a overexpression (**Supplemental Figure 6.4**). While it is probable that this improvement in muscle composition is a consequence of enhanced downstream tissue perfusion due to amplified arteriogenesis with miR-199a inhibition, miR-199a may also play a direct role in tissue clearance and regeneration. Indeed, miR-199a has been implicated in tissue fibrosis²⁹⁰, myoblast proliferation and differentiation²⁶⁸, and adipocyte differentiation²⁹¹, all of which are consistent with the hypothesis that miR-199a can directly regulate skeletal muscle proliferation and/or differentiation in a hypoxic environment.

6.6.4 Clinical perspective

Based on both our results and previous studies, we postulate that miRNA-199a inhibition represents a potentially promising treatment for arterial occlusive diseases. MicroRNA-199a is up-regulated in patients with coronary artery disease (CAD) versus matched controls²⁹². Additionally, the expression of CD44, which is directly regulated by miR-199a, correlates to the degree of vascular remodeling in CAD patients. Specifically, low levels of CD44 expression in peripheral blood monocytes correlate to poor collateralization²⁶⁶. Furthermore, our results indicate that the inhibition of miR-199a improves limb perfusion by enhancing arteriogenesis and reverses the fibro-adipose composition of ischemic muscle, which is often found in PAD patients^{293–296}.

6.7 Acknowledgements

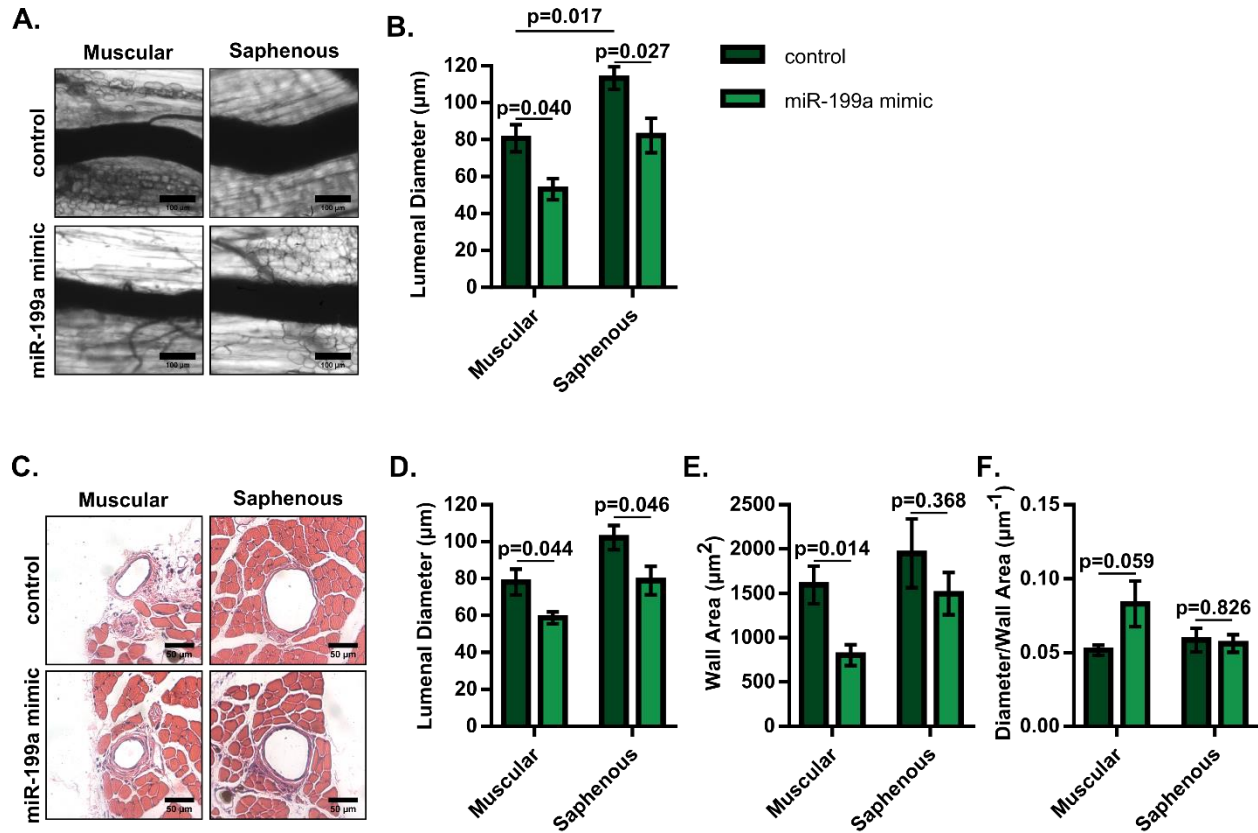
The authors would like to thank the University of Virginia Research Histology Core (under the direction of Sheri VanHoose) for histological tissue processing and the DNA Sciences Core

(under the direction of Yongde Bao), which is supported by the University Of Virginia School Of Medicine, for running TaqMan miRNA qRT-PCR plates.

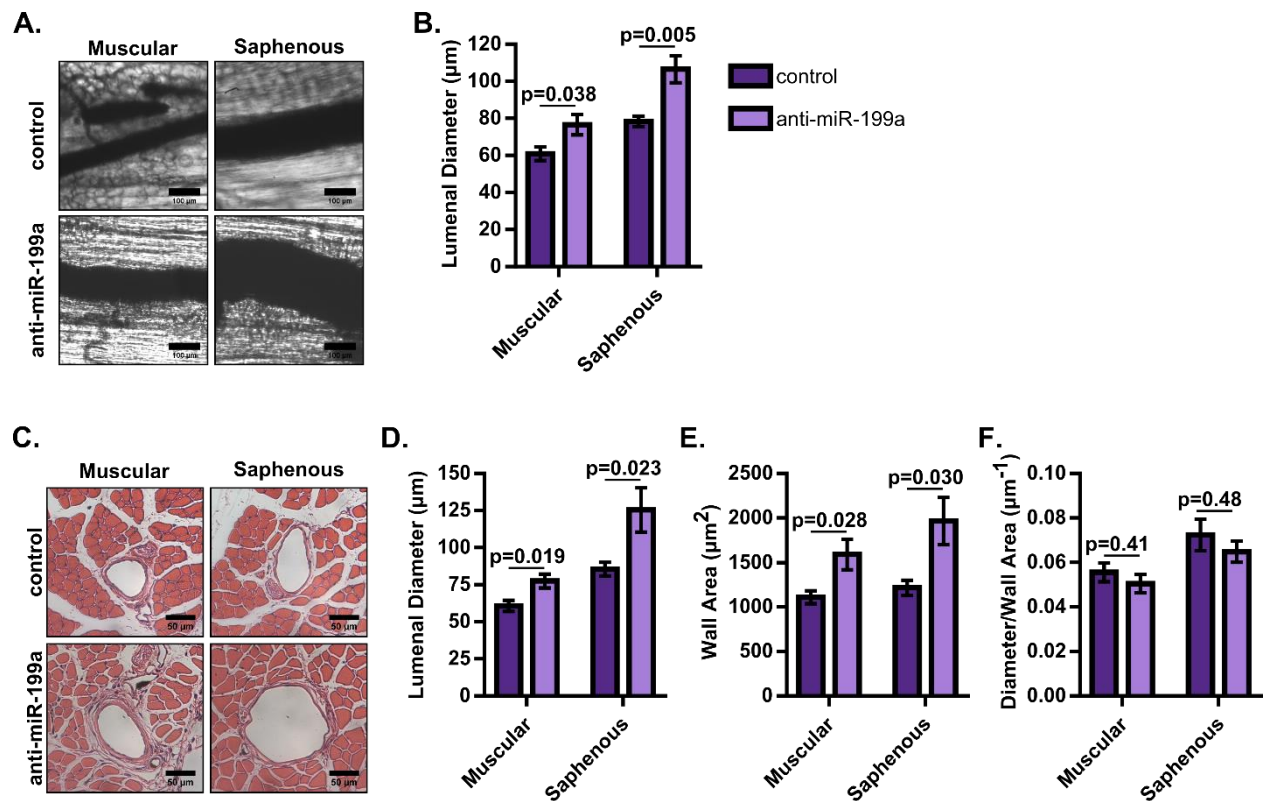
6.8 Sources of Funding

Supported by NIH R03 EB017927 and R01 EB020147. JLH was also supported by National Science Foundation Graduate Research Fellowship Program Grant No. NSF DGE-1315231.

6.9 Supplemental Figures

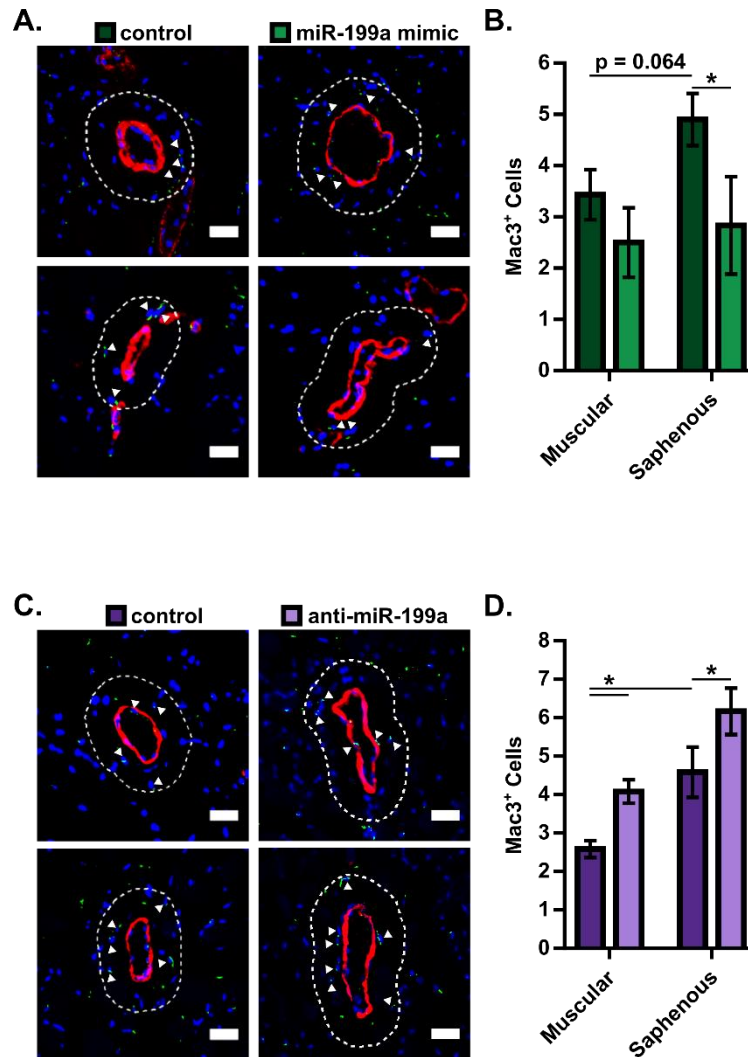


Supplemental Figure 6.1. Regional analysis of Balb/c mice treated with miR-199a mimic after FAL. **A)** Representative whole mount vascular cast images of collateral artery regions in non-targeting control or miR-199a mimic treated Balb/c mice 21 days post-FAL (Scale bar = 100µm). **B)** Bar graph of luminal diameter for each group. *p<0.001 vs. unligated, two-way ANOVA followed by Holm-Sidak test for multiple comparisons. **C)** Representative H&E stained cross-sections of collateral arteries regions (n=5-6 for mimic and control groups respectively). **D-F)** Bar graphs of luminal diameter, wall area, and diameter per wall area ratio from H&E stained cross-sections (n=5-6 for mimic and control groups respectively); Student's t-test. Data are mean ± SEM.



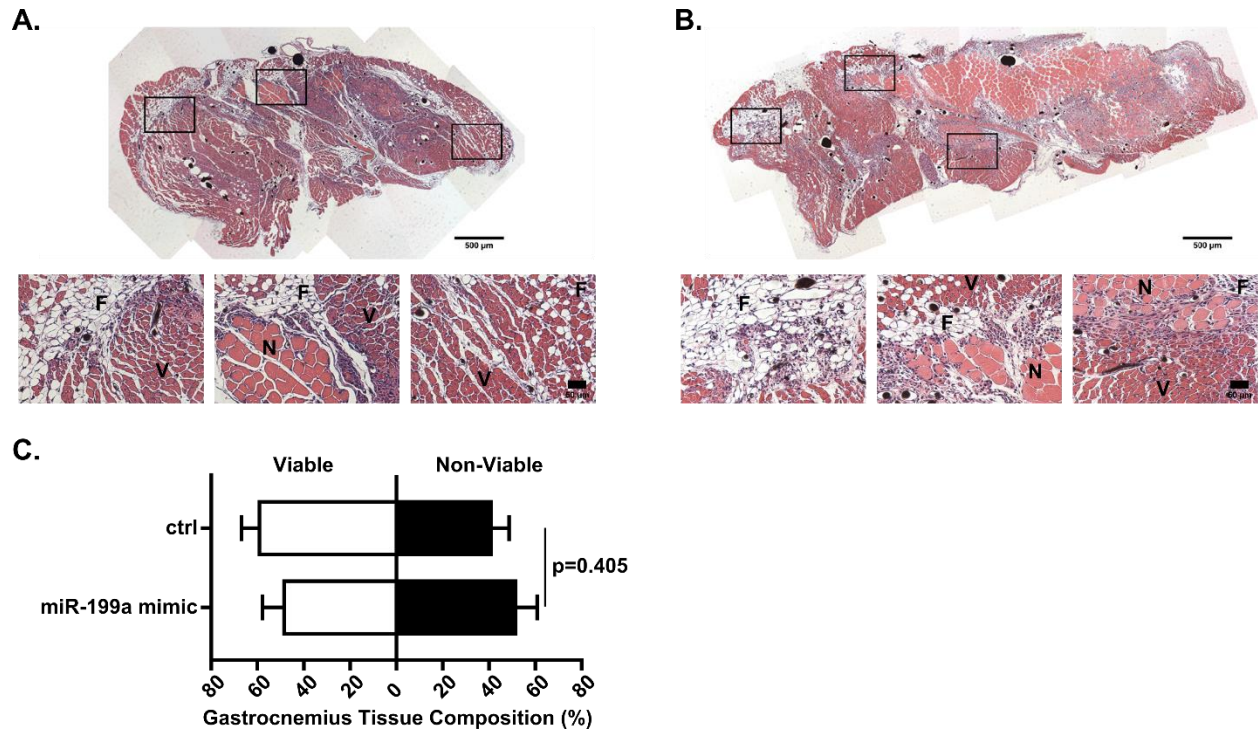
Supplemental Figure 6.2. Regional analysis of Balb/c mice treated with anti-miR-199a after FAL.

A) Representative whole mount vascular cast images of collateral artery regions in non-targeting control or anti-miR-199a treated Balb/c mice 21 days post-FAL (Scale bar=100μm). **B)** Bar graph of luminal diameter for each group (n=6). *p<0.001 vs. unligated, two-way ANOVA followed by Holm-Sidak test for multiple comparisons. **C)** Representative H&E stained cross-sections of collateral arteries regions (n=6). **D-F)** Bar graphs of luminal diameter, wall area, and diameter per wall area ratio from H&E stained cross-sections (n=6); Student's t-test. Data are mean ± SEM.



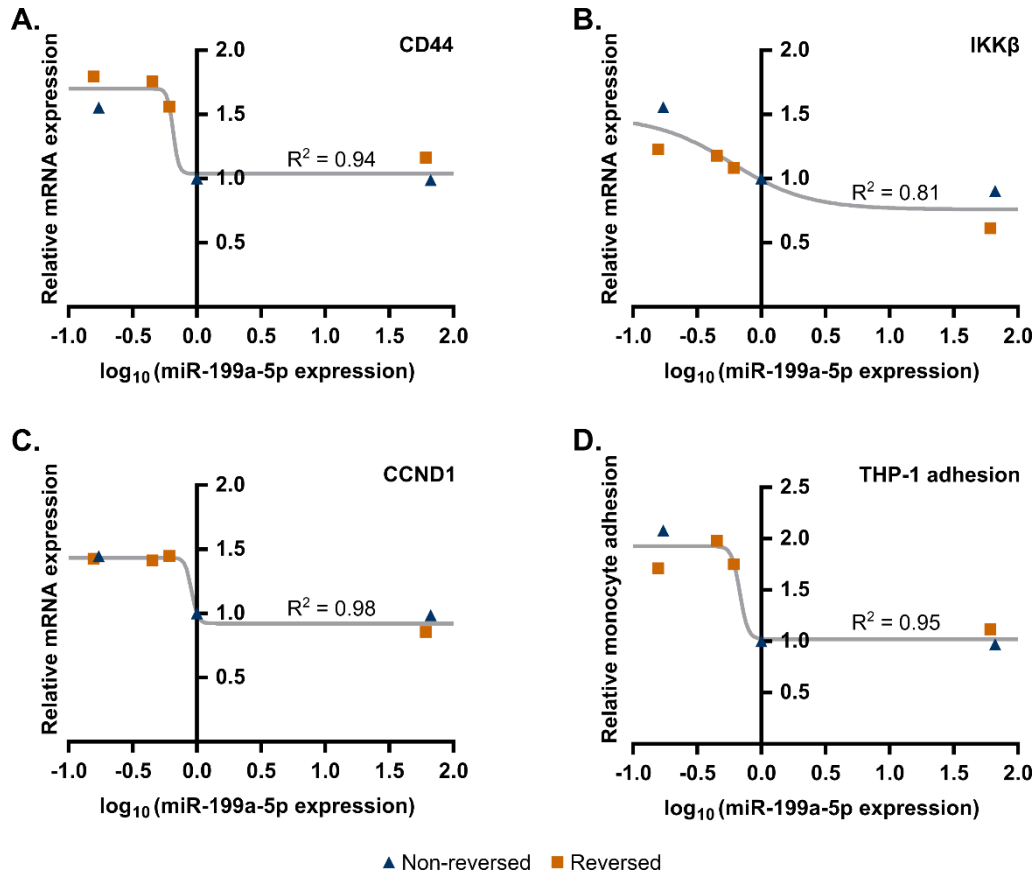
Supplemental Figure 6.3. Regional pericollateral macrophage recruitment is modulated by miR-199a.

A) Representative cross-sections of gracilis collateral artery regions 7 days post-FAL immunolabeled for macrophage marker, Mac3 (green), smooth muscle alpha actin (SMαA, red), and nuclei (DRAQ5, blue) in Balb/c mice treated with miR-199a mimic or non-targeting control mimic. Dotted line indicates the pericollateral region (25μm from vessel wall) used for quantification. Arrowheads indicate Mac3⁺ cells (Scale bar=25μm). **B)** Bar graph of pericollateral Mac3⁺ cells (n=4-5 for miR-199a mimic and control, respectively). *p<0.05, two-way ANOVA followed by a Holm-Sidak test for multiple comparisons. **C)** Immunolabeled gracilis collateral artery regions, as in (A), in Balb/c mice treated with anti-miR-199a or non-targeting control oligonucleotide. **D)** Bar graph of pericollateral Mac3⁺ cells (n=3). *p<0.05, two-way ANOVA followed by a Holm-Sidak test for multiple comparisons. Data are mean ± SEM.



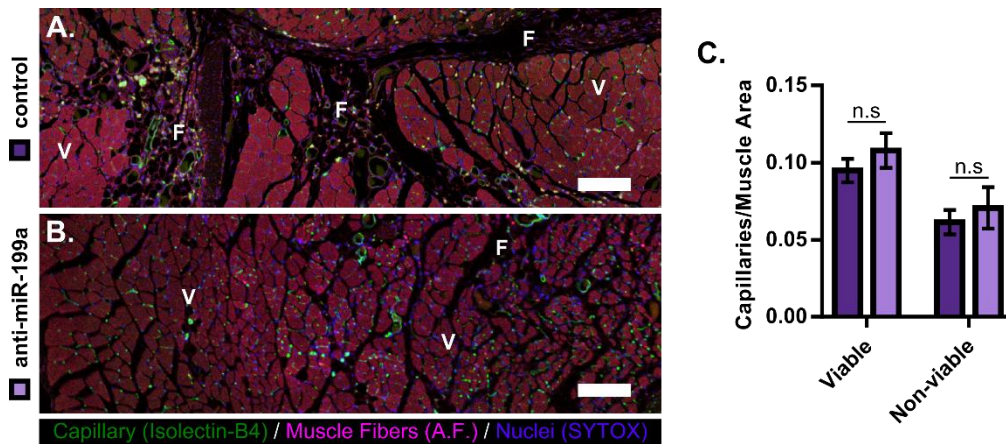
Supplemental Figure 6.4. Gastrocnemius muscle composition is not further impaired with miR-199a overexpression following FAL

A-B) Representative images of H&E staining of gastrocnemius muscle for ligated limb of Balb/c mice treated with non-targeting control (ctrl) (A) or miR-199a mimic (B) (Scale bar=500μm, inset scale bar=50μm). V=viable muscle, N=necrotic tissue, and F=fibro-adipose tissue. **C)** Bar graph of the percentage of gastrocnemius muscle that is viable (white) or non-viable (black) at day 21 post-FAL in each group (n=6-5 for ctrl and miR-199a mimic, respectively). Student's t-test. Data are mean ± SEM.



Supplemental Figure 6.5. Sigmoidal response of CD44, IKK β , CCND1 mRNA expression and THP-1 monocyte adhesion to alterations in miR-199a expression in endothelial cells exposed to biomimetic shear stress waveforms in-vitro.

A-D) Scatter plots of mean relative CD44, IKK β , CCND1 mRNA expression and THP-1 monocyte adhesion plotted against \log_{10} miR-199a expression. Data points are from both miR-199a overexpression and inhibition studies in HUVECs subjected to non-reversed (blue) or reversed (orange) flow waveforms. Data was fitted to a logistic function (gray line) of the general form: $y(x) = \frac{a}{b + ce^{-d(f-x)}} + t$, where x is the \log_{10} (miR-199a expression).



Supplemental Figure 6.6. MicroRNA-199a inhibition does not affect capillary density in the gastrocnemius muscle of FAL-operated Balb/c mice.

A-B) Representative photomerged images of gastrocnemius muscle for ligated limb of Balb/c mice treated with non-targeting control (ctrl) (A) or anti-miR-199a (B) locked nucleic acid oligonucleotides immediately after FAL (Scale bar=500 μ m). Tissues are immunolabeled for capillaries (green, isolectin-B4), muscle fibers (red, autofluorescence [A.F]), and nuclei (blue, SYTOX). **C)** Capillary density was determined for both groups in viable tissue (mature and regenerating muscle, V) and non-viable tissue (necrotic and fibro-adipose [F]) (n=4-5, for ctrl and anti-miR-199a, respectively). n.s = not significant, Student's t-test. Data are mean \pm SEM.

6.10 Supplemental Tables

Supplemental Table 6.1. Differential microRNA gene expression in ECs exposed to arteriogenesis-biomimetic shear stress waveforms.

Symbol	Name	NvC FC	RvC FC	RvN FC	log ₁₀ (FDR)
MIR146A	microRNA 146a	0.99	0.52	0.52	2.00
MIR155	microRNA 155	1.23	0.77	0.63	0.76
MIR224	microRNA 224	1.07	0.73	0.68	0.87
MIR29A	microRNA 29a	1.13	0.78	0.69	0.37
MIR34A	microRNA 34a	0.99	0.72	0.73	0.00
MIR21	microRNA 21	1.05	0.77	0.73	0.59
MIR199A2	microRNA 199a-2	0.95	0.72	0.76	1.89
MIR32	microRNA 32	1.00	0.76	0.76	0.64
MIR425	microRNA 425	1.28	0.97	0.76	0.03
MIR100	microRNA 100	0.91	0.69	0.76	1.49
MIR223	microRNA 223	1.27	0.97	0.77	0.07
MIR216A	microRNA 216a	0.93	0.74	0.79	1.26
MIR199A1	microRNA 199a-1	1.12	0.89	0.79	0.45
MIR24-1	microRNA 24-1	1.14	0.90	0.80	0.19
MIR93	microRNA 93	1.05	0.84	0.80	1.19
MIR17HG	miR-17-92 cluster host gene	1.01	0.81	0.80	0.97
MIR29B2	microRNA 29b-2	1.07	0.86	0.81	0.35
MIR181B1	microRNA 181b-1	0.99	0.81	0.82	0.83
MIR126	microRNA 126	0.85	0.70	0.82	0.87
MIR495	microRNA 495	1.16	0.96	0.83	0.07
MIR23A	microRNA 23a	1.02	0.84	0.83	0.48
MIR600HG	MIR600 host gene	1.14	0.96	0.85	0.07
MIRLET7C	microRNA let-7c	0.96	0.82	0.85	0.51
MIR504	microRNA 504	1.20	1.03	0.86	0.04
MIR181B2	microRNA 181b-2	0.96	0.84	0.87	0.57
MIR129-2	microRNA 129-2	1.11	0.97	0.87	0.04
MIR195	microRNA 195	1.06	0.93	0.88	0.22
MIR92A2	microRNA 92a-2	1.12	0.99	0.88	0.03
MIR137	microRNA 137	1.18	1.04	0.88	0.07
MIR143	microRNA 143	1.05	0.92	0.88	0.35
MIR210	microRNA 210	1.07	0.95	0.89	0.18
MIR301A	microRNA 301a	1.09	0.96	0.89	0.06
MIR30C1	microRNA 30c-1	1.00	0.89	0.90	0.32
MIR217	microRNA 217	0.98	0.88	0.90	0.10
MIR302B	microRNA 302b	1.11	1.01	0.91	0.01
MIR503	microRNA 503	1.07	0.97	0.91	0.05
MIRLET7A3	microRNA let-7a-3	1.02	0.93	0.91	0.10
MIR520C	microRNA 520c	0.99	0.91	0.91	0.16
MIR29C	microRNA 29c	1.20	1.10	0.92	0.13
MIR125B2	microRNA 125b-2	1.08	0.99	0.92	0.01
MIR148B	microRNA 148b	1.05	0.97	0.92	0.03
MIR181C	microRNA 181c	1.10	1.01	0.92	0.01
MIR519A2	microRNA 519a-2	1.00	0.92	0.92	0.08
MIR516B1	microRNA 516b-1	1.06	0.98	0.92	0.02
MIRLET7A1	microRNA let-7a-1	1.01	0.93	0.93	0.13
MIR1-2	microRNA 1-2	1.06	0.98	0.93	0.02
MIR487A	microRNA 487a	1.12	1.04	0.93	0.06
MIR127	microRNA 127	0.96	0.90	0.93	0.54
MIR124-3	microRNA 124-3	1.03	0.95	0.93	0.06

MIR30C2	microRNA 30c-2	0.99	0.92	0.93	0.07
MIRLET7A2	microRNA let-7a-2	1.03	0.96	0.93	0.04
MIR181A1	microRNA 181a-1	0.99	0.92	0.93	0.23
MIR106B	microRNA 106b	0.98	0.91	0.94	0.41
MIR135A1	microRNA 135a-1	1.00	0.93	0.94	0.12
MIR184	microRNA 184	0.99	0.94	0.94	0.17
MIR30E	microRNA 30e	0.93	0.88	0.94	0.56
MIR423	microRNA 423	1.04	0.98	0.94	0.02
MIR153-1	microRNA 153-1	1.01	0.95	0.94	0.11
MIR222	microRNA 222	1.03	0.98	0.95	0.02
MIR124-2	microRNA 124-2	1.00	0.95	0.95	0.25
MIR24-2	microRNA 24-2	0.93	0.88	0.95	0.29
MIR188	microRNA 188	1.08	1.03	0.95	0.09
MIR26A1	microRNA 26a-1	0.94	0.90	0.96	0.26
MIR98	microRNA 98	1.05	1.00	0.96	0.00
MIR99B	microRNA 99b	0.96	0.93	0.96	0.21
MIR519A2	microRNA 519a-2	1.00	0.96	0.96	0.10
MIR153-2	microRNA 153-2	1.01	0.98	0.97	0.05
MIR200B	microRNA 200b	1.03	1.00	0.97	0.01
MIR141	microRNA 141	1.01	0.98	0.97	0.02
MIRLET7B	microRNA let-7b	1.00	0.97	0.97	0.06
MIR10A	microRNA 10a	0.81	0.78	0.97	0.51
MIR183	microRNA 183	0.98	0.95	0.97	0.11
MIR30B	microRNA 30b	1.06	1.03	0.97	0.03
MIRLET7BHG	MIRLET7B host gene	1.01	0.98	0.97	0.03
MIR138-1	microRNA 138-1	1.05	1.02	0.97	0.02
MIR516B2	microRNA 516b-2	0.97	0.94	0.97	0.07
MIR320C1	microRNA 320c-1	1.11	1.08	0.97	0.25
MIR122	microRNA 122	1.09	1.07	0.97	0.21
MIR191	microRNA 191	1.01	0.99	0.97	0.02
MIR192	microRNA 192	1.06	1.03	0.97	0.03
MIR185	microRNA 185	0.98	0.96	0.98	0.09
MIR323A	microRNA 323a	1.08	1.06	0.98	0.14
MIR133B	microRNA 133b	1.04	1.02	0.98	0.03
MIR140	microRNA 140	0.98	0.97	0.98	0.06
MIR410	microRNA 410	0.96	0.95	0.99	0.09
MIR107	microRNA 107	1.02	1.00	0.99	0.00
MIR31	microRNA 31	1.03	1.02	0.99	0.01
MIR9-1	microRNA 9-1	1.02	1.01	0.99	0.01
MIR105-1	microRNA 105-1	1.24	1.24	0.99	0.17
MIR330	microRNA 330	1.01	1.01	1.00	0.01
MIR214	microRNA 214	0.93	0.93	1.00	0.24
MIR33A	microRNA 33a	0.93	0.93	1.00	0.09
MIR7-3	microRNA 7-3	0.97	0.97	1.00	0.05
MIR187	microRNA 187	0.96	0.97	1.00	0.06
MIR10B	microRNA 10b	1.01	1.01	1.00	0.01
MIR124-1	microRNA 124-1	1.04	1.05	1.00	0.07
MIR494	microRNA 494	1.00	1.00	1.00	0.00
MIR27A	microRNA 27a	0.85	0.85	1.01	0.37
MIR16-2	microRNA 16-2	0.95	0.96	1.01	0.08
MIR296	microRNA 296	1.00	1.01	1.01	0.01
MIR339	microRNA 339	1.03	1.04	1.01	0.06
MIR331	microRNA 331	1.03	1.04	1.01	0.05
MIR205	microRNA 205	0.99	1.00	1.01	0.00

MIR26A2	microRNA 26a-2	1.04	1.06	1.01	0.06
MIR150	microRNA 150	0.99	1.01	1.01	0.01
MIR200C	microRNA 200c	0.99	1.01	1.01	0.01
MIR509-1	microRNA 509-1	1.02	1.03	1.01	0.06
MIR26B	microRNA 26b	0.94	0.96	1.01	0.13
MIR106A	microRNA 106a	0.99	1.01	1.02	0.01
MIR31HG	MIR31 host gene	0.99	1.01	1.02	0.01
MIR139	microRNA 139	1.02	1.04	1.02	0.09
MIR129-1	microRNA 129-1	0.97	0.99	1.02	0.01
MIR99A	microRNA 99a	0.93	0.95	1.02	0.10
MIR197	microRNA 197	0.93	0.95	1.02	0.09
MIR125B1	microRNA 125b-1	0.97	0.99	1.02	0.01
MIR206	microRNA 206	1.04	1.06	1.02	0.24
MIR101-2	microRNA 101-2	1.03	1.05	1.02	0.15
MIR302A	microRNA 302a	0.94	0.97	1.02	0.08
MIR128-2	microRNA 128-2	0.97	0.99	1.03	0.00
MIR152	microRNA 152	0.98	1.01	1.03	0.01
MIR1247	microRNA 1247	0.95	0.98	1.03	0.05
MIR135A2	microRNA 135a-2	0.96	0.98	1.03	0.02
MIR130B	microRNA 130b	1.00	1.03	1.03	0.05
MIR103A1	microRNA 103a-1	0.87	0.90	1.04	0.70
MIR412	microRNA 412	1.01	1.05	1.04	0.09
MIR455	microRNA 455	0.95	0.98	1.04	0.03
MIR196A2	microRNA 196a-2	0.98	1.01	1.04	0.02
MIR202	microRNA 202	1.00	1.04	1.04	0.06
MIRLET7E	microRNA let-7e	0.89	0.93	1.04	0.08
MIR134	microRNA 134	1.00	1.04	1.04	0.07
MIR194-2	microRNA 194-2	0.98	1.02	1.04	0.03
MIR130A	microRNA 130a	0.98	1.02	1.04	0.02
MIR136	microRNA 136	1.03	1.08	1.04	0.12
MIR492	microRNA 492	1.03	1.08	1.05	0.15
MIR142	microRNA 142	0.96	1.01	1.05	0.01
MIR22HG	MIR22 host gene	1.07	1.12	1.05	0.58
MIR128-1	microRNA 128-1	0.98	1.02	1.05	0.06
MIR451A	microRNA 451a	0.98	1.03	1.05	0.06
MIR95	microRNA 95	0.97	1.02	1.05	0.03
MIR9-3	microRNA 9-3	0.91	0.96	1.05	0.07
MIR182	microRNA 182	0.92	0.96	1.05	0.06
MIR1-1	microRNA 1-1	0.98	1.03	1.06	0.06
MIR375	microRNA 375	0.96	1.01	1.06	0.01
MIR132	microRNA 132	0.92	0.97	1.06	0.03
MIR199B	microRNA 199b	0.87	0.93	1.06	0.11
MIR7-3HG	MIR7-3 host gene	0.89	0.95	1.06	0.12
MIR218-1	microRNA 218-1	0.85	0.91	1.07	0.16
MIR96	microRNA 96	0.98	1.05	1.07	0.08
MIR9-2	microRNA 9-2	1.00	1.07	1.07	0.31
MIR125A	microRNA 125a	0.90	0.97	1.07	0.04
MIR212	microRNA 212	0.90	0.97	1.07	0.06
MIR23B	microRNA 23b	0.85	0.91	1.07	0.16
MIRLET7I	microRNA let-7i	1.03	1.11	1.08	0.39
MIR137HG	MIR137 host gene	1.00	1.08	1.08	0.20
MIR28	microRNA 28	1.01	1.09	1.08	0.14
MIRLET7G	microRNA let-7g	0.91	0.98	1.08	0.01
MIR34C	microRNA 34c	0.86	0.93	1.08	0.24

MIR25	microRNA 25	0.85	0.91	1.08	0.26
MIR204	microRNA 204	0.96	1.03	1.08	0.04
MIR215	microRNA 215	0.94	1.02	1.08	0.03
MIR138-2	microRNA 138-2	0.93	1.01	1.08	0.01
MIR193A	microRNA 193a	0.96	1.04	1.08	0.07
MIR181A2	microRNA 181a-2	0.86	0.93	1.09	0.08
MIRLET7F1	microRNA let-7f-1	1.07	1.16	1.09	0.30
MIR218-2	microRNA 218-2	0.88	0.95	1.09	0.07
MIR196A1	microRNA 196a-1	0.93	1.01	1.09	0.01
MIR208A	microRNA 208a	0.97	1.06	1.09	0.11
MIRLET7F2	microRNA let-7f-2	1.00	1.08	1.09	0.09
MIR203	microRNA 203	0.94	1.03	1.09	0.06
MIR34A	microRNA 34a	0.92	1.00	1.09	1.50
MIR200A	microRNA 200a	0.98	1.08	1.10	0.14
MIR27B	microRNA 27b	0.94	1.03	1.10	0.02
MIR377	microRNA 377	0.98	1.07	1.10	0.20
MIR15A	microRNA 15a	0.80	0.87	1.10	0.16
MIR30D	microRNA 30d	0.95	1.04	1.10	0.08
MIR34B	microRNA 34b	0.94	1.03	1.10	0.04
MIR105-2	microRNA 105-2	1.12	1.23	1.10	0.69
MIR29B1	microRNA 29b-1	0.91	1.00	1.10	0.00
MIR429	microRNA 429	1.01	1.11	1.11	0.50
MIR145	microRNA 145	1.07	1.18	1.11	0.70
MIR299	microRNA 299	0.91	1.00	1.11	0.00
MIRLET7D	microRNA let-7d	0.94	1.04	1.11	0.07
MIR101-1	microRNA 101-1	0.89	0.99	1.12	0.01
MIR219-1	microRNA 219-1	0.96	1.07	1.12	0.11
MIR148A	microRNA 148a	0.92	1.03	1.12	0.05
MIR219-2	microRNA 219-2	0.97	1.10	1.13	0.58
MIR485	microRNA 485	0.99	1.12	1.13	0.55
MIR190A	microRNA 190a	0.90	1.02	1.14	0.04
MIR133A1	microRNA 133a-1	0.97	1.11	1.14	0.38
MIR149	microRNA 149	0.89	1.02	1.14	0.02
MIR320A	microRNA 320a	0.92	1.06	1.15	0.14
MIR376C	microRNA 376c	0.92	1.05	1.15	0.16
MIR144	microRNA 144	0.91	1.05	1.16	0.10
MIR30A	microRNA 30a	0.91	1.06	1.16	0.07
MIR16-1	microRNA 16-1	0.82	0.96	1.17	0.13
MIR365A	microRNA 365a	0.78	0.91	1.18	0.24
MIR186	microRNA 186	0.94	1.11	1.18	0.24
MIR15B	microRNA 15b	0.77	0.91	1.18	0.25
MIR326	microRNA 326	0.85	1.01	1.19	0.01
MIR194-1	microRNA 194-1	0.92	1.10	1.20	0.20
MIR221	microRNA 221	0.95	1.14	1.21	0.22
MIR103A2	microRNA 103a-2	0.87	1.05	1.21	0.06
MIR211	microRNA 211	0.77	0.94	1.23	0.09
MIR154	microRNA 154	0.97	1.24	1.27	0.28
MIR382	microRNA 382	0.95	1.22	1.28	0.87
MIR147A	microRNA 147a	0.71	0.94	1.33	0.14
MIR622	microRNA 622	0.90	1.21	1.36	0.36
MIR19B2	microRNA 19b-2	0.72	1.02	1.42	0.03
MIR7-2	microRNA 7-2	0.61	1.04	1.71	0.10

*FC = fold change. FDR = false discovery rate of RvC dataset. from Heuslein and Meisner et al.

7 Discussion and future directions

7.1 Summary

In this thesis, we have described several significant contributions toward improving our understanding of each stage (i.e. initiation, growth, and maturation) of arteriogenesis.

In [Chapter 4](#), we discovered that collateral artery segments in the mouse hindlimb exhibit either “moderate” or “amplified” arteriogenesis, depending on the initiating hemodynamics to which they are exposed (i.e. non-reversed or reversed flow waveforms, respectively) following femoral arterial ligation (FAL). We determined that this reversed flow-mediated amplification of collateral artery growth to be dependent on ICAM-1 mediated macrophage recruitment. Moreover, enabled by our lab’s ability to quantitatively measure the relative hemodynamics in these collateral segments in-vivo and apply them to ECs in-vitro, we were able to utilize genome-wide analyses to, for the first time, comprehensively map EC mechanosensitive signaling to sustained, differential arteriogenesis responses.

In [Chapter 5](#), we used this unique case of differential collateral growth as a model system to uncover molecular regulators of arteriogenic capacity and collateral artery maturation. We determined that ECs exposed to a non-reversed flow waveform exhibit increased DNMT1 expression and DNA hypermethylation. Moreover, we determined that DNMT1-dependent EC DNA hypermethylation regulates arteriogenic capacity via adjustments to shear stress set-point in-vivo, identifying a role for DNA methylation in arteriogenesis for the first time.

Finally, in [Chapter 6](#), we interrogated our genome-wide analysis of EC mechanosensitive signaling mapped to differential arteriogenesis responses to identify potentially novel microRNA regulators of arteriogenesis. Using this unique approach, we identified microRNA-199a as a potent mechanosensitive regulator of perfusion recovery and arteriogenesis after arterial occlusion.

Overall, these studies, stemming from an initial observation of differential collateral artery growth in-vivo, demonstrate the importance of EC signaling and epigenetics in regulating shear stress-mediated arteriogenesis. These results may also have significant implications for therapeutically stimulating arteriogenesis in patients with arterial occlusive diseases.

7.2 Thoughts and future studies: DNMT1, DNA methylation, and regulation to the shear stress set-point

In [Chapter 5](#), though the pharmacological DNMT1-inhibitor, 5AZA, enabled us to determine a role for DNMT1-dependent DNA methylation in regulating arteriogenic capacity via shear stress set-point alteration, it likely affected more than endothelial DNA methylation. Future studies could seek to determine the significance of cell-specific loss of DNMT1 expression on the regulation of arteriogenic capacity. To do this, we could generate EC- and/or SMC-specific inducible DNMT1 KO mice by breeding floxed DNMT1 knockout mice ($\text{DNMT1}^{2lox/lox}$)²⁹⁷ with tamoxifen-inducible, EC-specific, Cre-recombinase mice (VECad-Cre-ER^{T2})²⁹⁸ or tamoxifen-inducible, SMC-specific, Cre-recombinase mice (Myh11-Cre-ER^{T2})²⁹⁹ mice. As an additional or alternative approach, future work could also develop a platform for local delivery of and transfection of ECs and/or SMCs with shDNMT1 plasmids. Techniques for gene-specific editing of DNA methylation are beginning to be reported^{300–302}. As these gene-editing techniques, such as the CRISPR-Cas9 system, continue to develop, we could investigate the contribution of gene-specific DNA methylation to arteriogenic capacity and shear stress set-point.

Future studies could also seek to determine if DNMT1-dependent DNA methylation regulates shear stress set-point in other vascular networks. Selective ligations of mesenteric arteries can induce different levels of shear stress in collateral vessels that correspond to differential growth⁴⁶. The nearly two-dimensional nature of these mesenteric windows would enable for us to simultaneously measure collateral diameter and relative hemodynamic changes. Additionally, we could potentially use the dorsal skinfold window chamber¹⁶⁷ or ear artery

ligation^{303,304} models followed by non-invasive imaging (e.g. LSF, photoacoustic microscopy) to enable for longitudinal study of the same vascular network over-time. Each of these experimental models would enable us to simultaneously determine DNMT1-dependent alterations in collateral artery growth, sensitivity, and shear stress set-point.

As several early studies investigated the shear stress set-point hypothesis in the carotid artery, it would be interesting to also determine the role of DNMT1-dependent DNA methylation in these arteries. Interestingly, shear stress set-point was shown to be augmented in the common carotid artery experiencing the greatest relative flow increases in a canine arteriovenous-shunt model⁴⁷. This is similar to the phenotype we observed in non-reversed collateral segments following FAL, indicating that DNA hypermethylation may also be regulating the set-point in the carotid. Moreover, despite an initial increase in flow, several studies have shown that aged animals exhibit impaired diameter enlargement of the carotid, thereby leading to an elevated shear set-point^{83,94}. Young, healthy animals, however, exhibit significant diameter enlargement and are able to restore shear stress to the original set-point^{83,94}. The phenotype seen in aged animals is again similar to the constrained collateral artery growth and shear stress set-point augmentation due to DNA hypermethylation that we observed in [Chapter 5](#). Given that age alters DNA methylation¹²³, we would hypothesize that the carotid arteries of age animals undergo DNA hypermethylation, which in turn, constrains remodeling capacity by augmenting shear stress set-point.

7.3 Thoughts and future directions: miR-199a and mechanosensitive miRNA as regulators of arteriogenesis and as therapeutic targets

There are a number of potential future studies stemming from our work on mechanosensitive miRNAs in [Chapter 6](#). Though we showed miR-199a regulates the expression of several direct binding targets (e.g. IKK β , and CD44) previously validated in other studies^{269,281}, we did not explicitly determine miR-199a to directly bind to these targets in our system. We could therefore

perform luciferase reporter assays to test if these mRNAs are indeed direct seed-sequence binding targets. Future studies could also seek to further establish the clinical relevance of miR-199a. To this end, we can determine if miR-199a-5p expression and/or target(s) are differentially expressed in muscle biopsies of PAD patients and if expression is correlated to disease outcomes. Additionally, it may be worthwhile to determine if anti-miR-199a improves functional outcome (i.e. perfusion, vascular growth, muscle composition, exercise capacity) in more pre-clinical models of PAD. While the FAL model used here is an excellent tool for studying endogenous arteriogenesis, it is not a model of PAD per se. Pre-clinical models could incorporate more severe ischemia, mouse strains with co-morbidities typically associated with PAD (i.e. hyperlipidemia and diabetes), and delayed treatment of anti-miRs to better account for the chronic nature of PAD. Moreover, though a single, direct intramuscular injection of anti-miR-199a showed some therapeutic promise, there is still significant non-localized delivery. This highlights a critical need to develop a more optimized, targeted delivery method. To this end, our lab has successfully used an ultrasound-microbubble system for the targeted delivery of gene-carrying nanoparticles to the skeletal muscle³⁰⁵. We could utilize a similar approach for the delivery of nanoparticles carrying miR-targeted plasmids or by electrostatic conjugation of anti-miRs to microbubbles.

7.4 Thoughts and future studies: arteriogenesis, angiogenesis, and beyond

7.4.1 Promise for pro-arteriogenic and pro-angiogenic combination therapy

Therapeutic arteriogenesis is promising for restoring blood flow to the distal tissue because of its efficiency. Only a few collaterals are needed to protect against ischemia³⁰⁶ and small changes in diameter lead to large changes in conductance³⁰⁷. However, the stimulation of angiogenesis is also important as capillary density is reduced in PAD patients^{4,25,28}. Exercise, which has been shown to improve arteriole²⁶ and capillary density²⁵, improves peak treadmill walking time to a greater extent than stent revascularization in PAD patients with claudication, further highlighting

the need to restore the underlying microvasculature to improve patient outcome (CLEVER study)³⁰⁸.

It is likely necessary to stimulate both arteriogenic and angiogenic adaptive responses to arterial occlusion(s)^{29,39,309}. Our recent results using a computational arteriolar network model to estimate perfusion in PAD patients after exercise and/or percutaneous interventions emphasize the importance of designing therapeutics to restore normal microvascular structure and function in combination with restoration of upstream perfusion pressure (via revascularization or arteriogenesis)²⁶. These computational results are supported by the recent results of the ERASE study which demonstrate that, at 12-months post-treatment, a combined treatment of endovascular revascularization followed by supervised exercise improved maximal walking distance, pain-free walking distance, and patient-reported quality of life compared to supervised exercise only³¹⁰. Though it would be beneficial to have one clinical trial directly comparing PAD patients receiving revascularization, supervised exercise, or a combination therapy, together, these clinical trials support the hypothesis that while microvascular expansion and revascularization individually provide a similar, modest clinical benefit, a combination therapy would be an “optimal” treatment.

7.4.2 Need to consider muscle composition and metabolism

Tissue clearance, composition, and metabolism are critical, but often over-looked, responses to an upstream arterial occlusion³⁰. PAD patients exhibit a number of abnormalities and impairments in the muscles of their lower limbs including fatty tissues^{18,293}, smaller calf muscles^{18,293}, increased apoptosis²⁹⁵, abnormal fiber distribution^{293,311,312}, denervation²⁹³, and inflammation²⁰. Moreover, the Lsq-1 locus was shown to be responsible for the strain-dependent, differential skeletal muscle responses to ischemia in a pre-clinical, murine hindlimb ischemia model³¹³.

These abnormalities indicate that targeting muscle fiber composition and metabolism, likely in concert with stimulation of arteriogenesis and angiogenesis, may be a therapeutically beneficial

approach. To this end, miR-199a inhibition was sufficient to improve gastrocnemius muscle tissue composition in FAL-operated mice and has been implicated in tissue fibrosis²⁹⁰, myoblast proliferation and differentiation²⁶⁸, and adipocyte differentiation²⁹¹. It may therefore be interesting to determine if miR-199a regulates proliferation, regeneration, and/or differentiation of ischemic skeletal muscle.

Additionally, recent studies in humans have highlighted that the reduction in blood flow alone does not fully account for the exercise limitations of PAD patients²⁰. To this point, there appears to be an uncoupling of calf muscle perfusion and muscle metabolism in PAD patients³¹⁴. Acylcarnitine, a metabolite that reflects the metabolic state/capacity of the muscle, has been found to be elevated in PAD patients and to be associated with reduced peak treadmill exercise performance^{315,316}. Furthermore, PAD patients exhibit abnormal mitochondria function³¹⁷ and reduced activity of complex III of the mitochondrial electron transport chain³¹⁸, leading to significant oxidative stress³¹⁷. Collectively, this emphasizes that treatments for PAD are faced with two fundamental transport problems: (1) getting enough oxygenated blood to the ischemic muscle and (2) ensuring that oxygen is functionally available for proper mitochondrial usage. To design effective therapeutics, we need to determine how these issues are inter-related – i.e. if we can increase the vascular supply (via stenting, arteriogenesis, angiogenesis, etc), do we mitigate mitochondrial dysfunction and increase O₂ bioavailability? Alternatively, if we can repair the mitochondria, do we prevent capillary and arteriolar rarefaction and maintain an intact vascular supply? Which is a more effective strategy?

A potentially interesting idea would be to determine if oxygen delivery, independent of the vasculature, could provide therapeutic benefit. For example, delivery of oxygen-generating biomaterials^{319–321} may be able to provide sufficient oxygen to areas with an insufficient vascular supply due to microvascular defects. This approach could help to test the hypothesis whether an oxygen supply is sufficient for restoring mitochondrial and skeletal muscle function. Additionally, it could be used in concert with other therapies, such as exercise, whereby a short-lived “dose” of

supplemental oxygen to ischemic limbs (via oxygen-generating biomaterials) enhances a patient's exercise capacity, which in turn, restores microvascular and metabolic function.

7.5 Thoughts and future directions: applications to other disease models

Our results identifying mechanosensitive epigenetic regulators of arteriogenesis may also have broader implications outside of PAD. Adequate collateral development and growth is also critical for patient outcomes in CAD³²² and ischemic stroke³²³. Additionally, arteriogenesis is the predominant vascular adaptation in the surgical “flap delay” strategy for autologous transplantation for reconstructive plastic surgery³²⁴. Future studies could determine if inhibition of miR-199a or DNMT1 enhances arteriogenesis and functional outcomes in pre-clinical models of these clinical scenarios. In contrast, other future studies could seek to inhibit arteriogenesis (e.g. via ICAM-1 inhibition, miR-199a overexpression) to elicit therapeutic benefit. To this end, recombinant parathyroid hormone (rPTH) therapy promotes scarless healing of critical bone defects via inhibition of arteriogenesis and mast cell recruitment. However, given that rPTH therapy is contraindicated for cancer patients, which constitutes a large percentage of patients with critical bone defects, alternate strategies for limiting mast cell recruitment and arteriogenesis are needed³²⁵. Moreover, though largely unstudied, there is some evidence of luminal expansion of feeder arterioles during tumor growth^{326,327}. Additionally, both the inherent heterogeneity of the tumor vasculature and surgical excision treatments may alter flow pathways such that “tumor collaterals” develop. Targeting collateral artery growth may therefore be a novel anti-cancer therapeutic strategy.

8 References

1. Norgren L, Hiatt WR, Dormandy JA, Nehler MR, Harris KA, Fowkes FGR. Inter-society consensus for the management of peripheral arterial disease (TASC II). *Eur J Vasc Endovasc Surg.* 2007;33:S1–S75.
2. Norgren L, Hiatt WR, Dormandy JA, Hirsch AT, Jaff MR, Diehm C, Baumgartner I, Belch JJF. The next 10 years in the management of peripheral artery disease: Perspectives from the “PAD 2009” conference. *Eur J Vasc Endovasc Surg.* 2010;40:375–380.
3. Fowkes FGR, Rudan D, Rudan I, Aboyans V, Denenberg JO, McDermott MM, Norman PE, Sampson UKA, Williams LJ, Mensah GA, Criqui MH. Comparison of global estimates of prevalence and risk factors for peripheral artery disease in 2000 and 2010: a systematic review and analysis. *Lancet.* 2013;382:1329–40.
4. Annex BH. Therapeutic angiogenesis for critical limb ischaemia. *Nat Rev Cardiol.* 2013;10:387–96.
5. Hiatt WR, Hoag S, Hamman RF. Effect of diagnostic criteria on the prevalence of peripheral arterial disease : The San Luis Valley diabetes study. *Circulation.* 1995;91:1472–1479.
6. Selvin E, Erlinger TP. Prevalence of and risk factors for peripheral arterial disease in the United States: Results from the National Health and Nutrition Examination Survey, 1999-2000. *Circulation.* 2004;110:738–743.
7. Belch JJF, Topol EJ, Agnelli G, Bertrand M, Califf RM, Clement DL, Creager M a, Easton JD, Gavin JR, Greenland P, Hankey G, Hanrath P, Hirsch AT, Meyer J, Smith SC, Sullivan F, Weber MA. Critical issues in peripheral arterial disease detection and management: a call to action. *Arch Intern Med.* 2003;163:884–92.
8. Gandhi S, Weinberg I, Margey R, Jaff MR. Comprehensive medical management of peripheral arterial disease. *Prog Cardiovasc Dis.* 2011;54:2–13.
9. Criqui MH, Fronek A, Barrett-Connor E, Goodman D. The prevalence of peripheral arterial disease in defined population. *Circulation.* 1985;71:510–515.
10. Beckman JA, Creager MA, Libby P. Diabetes and atherosclerosis: epidemiology, pathophysiology, and management. *JAMA.* 2002;287:2570–2581.
11. Lau JF, Weinberg MD, Olin JW. Peripheral artery disease. Part 1: clinical evaluation and noninvasive diagnosis. *Nat Rev Cardiol.* 2011;8:405–18.
12. Hirsch AT, Criqui MH, Treat-Jacobson D, Regensteiner JG, Creager M a, Olin JW, Krook SH, Hunninghake DB, Comerota AJ, Walsh ME, McDermott MM, Hiatt WR. Peripheral arterial disease detection, awareness, and treatment in primary care. *JAMA.* 2001;286:1317–24.
13. McDermott MM, Liu K, Criqui MH, Ruth K, Goff D, Saad MF, Wu C, Homma S, Sharrett AR. Ankle-brachial index and subclinical cardiac and carotid disease: The multi-ethnic study of atherosclerosis. *Am J Epidemiol.* 2005;162:33–41.
14. Jude E, Chalmers N, Oyibo S, Boulton A. Peripheral arterial disease in diabetic and nondiabetic patients. *Diabetes Care.* 2001;24:1433–1437.
15. Kullo IJ, Leeper NJ. The genetic basis of peripheral arterial disease: current knowledge, challenges, and future directions. *Circ Res.* 2015;116:1551–60.

16. Ankle Brachial Index Collaboration. Ankle brachial index combined with Framingham Risk Score to predict cardiovascular events and mortality: a meta-analysis. *JAMA*. 2008;300:197–208.
17. Lau JF, Weinberg MD, Olin JW. Peripheral artery disease. Part 1: clinical evaluation and noninvasive diagnosis. *Nat Rev Cardiol*. 2011;8:405–18.
18. McDermott MM, Guralnik JM, Ferrucci L, Tian L, Liu K, Liao Y, Green D, Sufit R, Hoff F, Nishida T, Sharma L, Pearce WH, Schneider JR, Criqui MH. Asymptomatic peripheral arterial disease is associated with more adverse lower extremity characteristics than intermittent claudication. *Circulation*. 2008;117:2484–2491.
19. Criqui MH, Langer R, Fronek A, Feigelson H, Klauber M, McCann TJ, Browner D. Mortality over a period of 10 years in patients with peripheral arterial disease. *N Engl J Med*. 1992;326:381–386.
20. Hiatt WR, Armstrong EJ, Larson CJ, Brass EP. Pathogenesis of the limb manifestations and exercise limitations in peripheral artery disease. *Circ Res*. 2015;116:1527–1539.
21. Tabas I, García-Cardena G, Owens GK. Recent insights into the cellular biology of atherosclerosis. *J Cell Biol*. 2015;209:13–22.
22. Lusis AJ. Atherosclerosis. *Nature*. 2000;407:233–241.
23. Liao JK, Bettmann M a, Sandor T, Tucker JI, Coleman SM, Creager MA. Differential impairment of vasodilator responsiveness of peripheral resistance and conduit vessels in humans with atherosclerosis. *Circ Res*. 1991;68:1027–34.
24. Schellong SM, Boger RH, Burchert W, Bode-Boger SM, Galland A, Frolich JC, Hundeshagen H, Alexander K. Dose-related effect of intravenous L-arginine on muscular blood flow of the calf in patients with peripheral vascular disease: a H215O positron emission tomography study. *Clin Sci (Lond)*. 1997;93:159–165.
25. Robbins JL, Jones WS, Duscha BD, Allen JD, Kraus WE, Regensteiner JG, Hiatt WR, Annex BH. Relationship between leg muscle capillary density and peak hyperemic blood flow with endurance capacity in peripheral artery disease. *J Appl Physiol*. 2011;111:81–86.
26. Heuslein JL, Li X, Murrell KP, Annex BH, Peirce SM, Price RJ. Computational network model prediction of hemodynamic alterations due to arteriolar rarefaction and estimation of skeletal muscle perfusion in peripheral arterial disease. *Microcirculation*. 2015;22:360–369.
27. Berceli SA, Hevelone ND, Lipsitz SR, Bandyk DF, Clowes AW, Moneta GL, Conte MS. Surgical and endovascular revision of infrainguinal vein bypass grafts: analysis of midterm outcomes from the PREVENT III trial. *J Vasc Surg*. 2007;46:1173–1179.
28. Duscha BD, Robbins JL, Jones WS, Kraus WE, Lye RJ, Sanders JM, Allen JD, Regensteiner JG, Hiatt WR, Annex BH. Angiogenesis in skeletal muscle precede improvements in peak oxygen uptake in peripheral artery disease patients. *Arterioscler Thromb Vasc Biol*. 2011;31:2742–8.
29. Meisner JK, Song J, Annex BH, Price RJ. Myoglobin overexpression inhibits reperfusion in the ischemic mouse hindlimb through impaired angiogenesis but not arteriogenesis. *Am J Pathol*. 2013;183:1–10.
30. Meisner JK, Annex BH, Price RJ. Despite normal arteriogenic and angiogenic responses, hind limb perfusion recovery and necrotic and fibroadipose tissue clearance are impaired

- in matrix metalloproteinase 9-deficient mice. *J Vasc Surg*. 2014;61:1583–1594.
31. Seiler C, Pohl T, Wustmann K, Hutter D, Nicolet P a, Windecker S, Eberli FR, Meier B. Promotion of collateral growth by granulocyte-macrophage colony-stimulating factor in patients with coronary artery disease: a randomized, double-blind, placebo-controlled study. *Circulation*. 2001;104:2012–7.
 32. van Royen N, Schirmer SH, Atasever B, Behrens CYH, Ubbink D, Buschmann EE, Voskuil M, Bot P, Hoefer I, Schlingemann RO, Biemond BJ, Tijssen JG, Bode C, Schaper W, Oskam J, Legemate DA, Piek JJ, Buschmann I. START Trial: a pilot study on STimulation of ARTeriogenesis using subcutaneous application of granulocyte-macrophage colony-stimulating factor as a new treatment for peripheral vascular disease. *Circulation*. 2005;112:1040–6.
 33. Zbinden S, Zbinden R, Meier P, Windecker S, Seiler C. Safety and efficacy of subcutaneous-only granulocyte-macrophage colony-stimulating factor for collateral growth promotion in patients with coronary artery disease. *J Am Coll Cardiol*. 2005;46:1636–42.
 34. Ripa RS, Jørgensen E, Wang Y, Thune JJ, Nilsson JC, Søndergaard L, Johnsen HE, Køber L, Grande P, Kastrup J. Stem cell mobilization induced by subcutaneous granulocyte-colony stimulating factor to improve cardiac regeneration after acute ST-elevation myocardial infarction: result of the double-blind, randomized, placebo-controlled stem cells in myocardial infarct. *Circulation*. 2006;113:1983–92.
 35. Subramaniam V, Waller EK, Murrow JR, Manatunga A, Lonial S, Kasirajan K, Sutcliffe D, Harris W, Taylor WR, Alexander RW, Quyyumi AA. Bone marrow mobilization with granulocyte macrophage colony-stimulating factor improves endothelial dysfunction and exercise capacity in patients with peripheral arterial disease. *Am Hear J*. 2009;158:53–60.
 36. Ziegler MA, Distasi MR, Bills RG, Miller SJ, Alloosh M, Murphy MP, Akingba AG, Sturek M, Dalsing MC, Unthank JL. Marvels, mysteries, and misconceptions of vascular compensation to peripheral artery occlusion. *Microcirculation*. 2010;17:3–20.
 37. Schaper W. Collateral circulation: past and present. *Basic Res Cardiol*. 2009;104:5–21.
 38. Liebeskind DS. Collateral circulation. *Stroke*. 2003;34:2279–2284.
 39. Meisner JK, Price RJ. Spatial and temporal coordination of bone marrow-derived cell activity during arteriogenesis: regulation of the endogenous response and therapeutic implications. *Microcirculation*. 2010;17:583–599.
 40. Scholz D, Schaper W. Preconditioning of arteriogenesis. *Cardiovasc Res*. 2005;65:513–23.
 41. Langille BL, O'Donnell F. Reductions in arterial diameter produced by chronic decreases in blood flow are endothelium-dependent. *Science (80-)*. 1986;231:405–407.
 42. Moraes F, Paye J, Mac Gabhann F, Zhuang ZW, Zhang J, Lanahan AA, Simons M. Endothelial cell-dependent regulation of arteriogenesis. *Circ Res*. 2013;113:1076–86.
 43. Davies PF. Flow-mediated endothelial mechanotransduction. *Physiol Rev*. 1995;75:519–560.
 44. Garcia-Cardena G, Comander J, Anderson KR, Blackman BR, Gimbrone MA. Biomechanical activation of vascular endothelium as a determinant of its functional phenotype. *Proc Natl Acad Sci U S A*. 2001;98:4478–85.

45. Topper JN, Gimbrone MA. Blood flow and vascular gene expression: fluid shear stress as a modulator of endothelial phenotype. *Mol Med Today*. 1999;5:40–6.
46. Tuttle JL, Nachreiner RD, Bhuller AS, Condict KW, Connors BA, Herring BP, Dalsing MC, Unthank JL. Shear level influences resistance artery remodeling : wall dimensions , cell density, and eNOS expression. *Am J Physiol Hear Circ Physiol*. 2001;H1380–H1389.
47. Kamiya A, Togawa T. Adaptive regulation of wall shear stress to flow change in the canine carotid artery. *Am J Physiol Hear Circ Physiol*. 1980;239:H14–H21.
48. Zarins CK, Zatina MA, Giddens DP, Ku DN, Glagov S. Shear stress regulation of artery lumen diameter in experimental atherogenesis. *J Vasc Surg*. 1987;5:413–420.
49. Eitenmüller I, Volger O, Kluge A, Troidl K, Barancik M, Cai W-J, Heil M, Pipp F, Fischer S, Horrevoets AJG, Schmitz-Rixen T, Schaper W. The range of adaptation by collateral vessels after femoral artery occlusion. *Circ Res*. 2006;99:656–62.
50. Tzima E, Irani-Tehrani M, Kiosses WB, Dejana E, Schultz DA, Engelhardt B, Cao G, DeLisser H, Schwartz MA. A mechanosensory complex that mediates the endothelial cell response to fluid shear stress. *Nature*. 2005;437:426–31.
51. Chen Z, Rubin J, Tzima E. Role of PECAM-1 in arteriogenesis and specification of preexisting collaterals. *Circ Res*. 2010;107:1355–63.
52. Scholz D, Ito W, Fleming I, Deindl E, Sauer A, Wiesnet M, Busse R, Schaper J, Schaper W. Ultrastructure and molecular histology of rabbit hind-limb collateral artery growth (arteriogenesis). *Virchows Arch*. 2000;436:257–70.
53. Lee CW, Stabile E, Kinnaird T, Shou M, Devaney JM, Epstein SE, Burnett MS. Temporal patterns of gene expression after acute hindlimb ischemia in mice: Insights into the genomic program for collateral vessel development. *J Am Coll Cardiol*. 2004;43:474–482.
54. Pipp F, Boehm S, Cai W-J, Adili F, Ziegler B, Karanovic G, Ritter R, Balzer J, Scheler C, Schaper W, Schmitz-Rixen T. Elevated fluid shear stress enhances postocclusive collateral artery growth and gene expression in the pig hind limb. *Arterioscler Thromb Vasc Biol*. 2004;24:1664–8.
55. Nagel T, Resnick N, Atkinson WJ, Dewey CF, Gimbrone MA. Shear stress selectively upregulates intercellular adhesion molecule-1 expression in cultured human vascular endothelial cells. *J Clin Invest*. 1994;94:885–891.
56. Hoefer IE, van Royen N, Rectenwald JE, Deindl E, Hua J, Jost M, Grundmann S, Voskuil M, Ozaki CK, Piek JJ, Buschmann IR. Arteriogenesis proceeds via ICAM-1/Mac-1-mediated mechanisms. *Circ Res*. 2004;94:1179–85.
57. Shireman P. The Chemokine System in Arteriogenesis and Hind Limb Ischemia. *J Vasc Surg*. 2007;45:A48–A56.
58. Buschmann IR, Hoefer IE, van Royen N, Katzer E, Braun-Dulleaus R, Heil M, Kostin S, Bode C, Schaper W. GM-CSF: a strong arteriogenic factor acting by amplification of monocyte function. *Atherosclerosis*. 2001;159:343–56.
59. Vries MHM, Wagenaar A, Post MJ. CXCL1 promotes arteriogenesis through enhanced monocyte recruitment into the peri-collateral space. *Angiogenesis*. 2015;18:163–71.
60. Bergmann CE, Hoefer IE, Meder B, Roth H, Royen N Van, Breit SM, Jost MM, Aharinejad S, Hartmann S, Buschmann IR. Arteriogenesis depends on circulating monocytes and macrophage accumulation and is severely depressed in op / op mice. *J Leukoc Biol*. 2006;80:59–65.

61. Pipp F, Heil M, Issbrücker K, Ziegelhoeffer T, Martin S, van den Heuvel J, Weich H, Fernandez B, Golomb G, Carmeliet P, Schaper W, Clauss M. VEGFR-1-selective VEGF homologue PlGF is arteriogenic: evidence for a monocyte-mediated mechanism. *Circ Res*. 2003;92:378–85.
62. Arras M, Ito WD, Scholz D, Winkler B, Schaper J, Schaper W. Monocyte activation in angiogenesis and collateral growth in the rabbit hindlimb. *J Clin Invest*. 1998;101:40–50.
63. Heil M, Ziegelhoeffer T, Pipp F, Kostin S, Martin S, Clauss M, Schaper W. Blood monocyte concentration is critical for enhancement of collateral artery growth. *Am J Physiol Heart Circ Physiol*. 2002;283:H2411–9.
64. Francke A, Weinert S, Strasser RH, Braun-Dullaeus RC, Herold J. Transplantation of bone marrow derived monocytes: a novel approach for augmentation of arteriogenesis in a murine model of femoral artery ligation. *Am J Transl Res*. 2013;5:155–69.
65. Troidl C, Jung G, Troidl K, Hoffmann J, Mollmann H, Nef H, Schaper W, Hamm CW, Schmitz-Rixen T. The temporal and spatial distribution of macrophage subpopulations during arteriogenesis. *Curr Vasc Pharmacol*. 2013;11:5–12.
66. Awojodu AO, Ogle ME, Sefcik LS, Bowers DT, Martin K, Brayman KL, Lynch KR, Peirce-Cottler SM, Botchwey E. Sphingosine 1-phosphate receptor 3 regulates recruitment of anti-inflammatory monocytes to microvessels during implant arteriogenesis. *Proc Natl Acad Sci U S A*. 2013;110:13785–90.
67. Heil M, Ziegelhoeffer T, Wagner S, Fernández B, Helisch A, Martin S, Tribulova S, Kuziel W a, Bachmann G, Schaper W. Collateral artery growth (arteriogenesis) after experimental arterial occlusion is impaired in mice lacking CC-chemokine receptor-2. *Circ Res*. 2004;94:671–7.
68. Bruce AC, Kelly-Goss MR, Heuslein JL, Meisner JK, Price RJ, Peirce SM. Monocytes are recruited from venules during arteriogenesis in the murine spinotrapezius ligation model. *Arterioscler Thromb Vasc Biol*. 2014;34:2012–22.
69. Schirmer SH, Bot PT, Fledderus JO, Van Der Laan AM, Volger OL, Laufs U, Böhm M, De Vries CJM, Horrevoets AJG, Piek JJ, Hoefer IE, Van Royen N. Blocking interferon β stimulates vascular smooth muscle cell proliferation and arteriogenesis. *J Biol Chem*. 2010;285:34677–34685.
70. Hoefer IE, Royen N Van, Rectenwald JE, Bray EJ, Abouhamze Z, Moldawer LL, Voskuil M, Piek JJ, Buschmann IR, Ozaki CK. Direct evidence for tumor necrosis factor- α signaling in arteriogenesis. *Circulation*. 2002;105:1639–1641.
71. van Royen N, Hoefer I, Buschmann I, Heil M, Kostin S, Deindl E, Vogel S, Korff T, Augustin H, Bode C, Piek JJ, Schaper W. Exogenous application of transforming growth factor β 1 stimulates arteriogenesis in the peripheral circulation. *FASEB J*. 2002;16:432–4.
72. Deindl E, Hoefer IE, Fernandez B, Barancik M, Heil M, Strniskova M, Schaper W. Involvement of the fibroblast growth factor system in adaptive and chemokine-induced arteriogenesis. *Circ Res*. 2003;92:561–568.
73. Heil M, Schaper W. Influence of mechanical, cellular, and molecular factors on collateral artery growth (arteriogenesis). *Circ Res*. 2004;95:449–58.
74. Ziegelhoeffer T, Fernandez B, Kostin S, Heil M, Voswinckel R, Helisch A, Schaper W. Bone marrow-derived cells do not incorporate into the adult growing vasculature. *Circ Res*. 2004;94:230–238.

75. Kinnaird T, Burnett ES, Shou M, Lee CW, Barr S, Fuchs S, Epstein SE. Local delivery of marrow-derived stromal cells augments collateral perfusion through paracrine mechanisms. *Circulation*. 2004;109:1543–1549.
76. Cai W, Vosschulte R, Afsah-Hedjri a, Koltai S, Kocsis E, Scholz D, Kostin S, Schaper W, Schaper J. Altered balance between extracellular proteolysis and antiproteolysis is associated with adaptive coronary arteriogenesis. *J Mol Cell Cardiol*. 2000;32:997–1011.
77. Cai W-J, Kocsis E, Wu X, Rodrigues M, Luo X, Schaper W, Schaper J. Remodeling of the vascular tunica media is essential for development of collateral vessels in the canine heart. *Mol Cell Biochem*. 2004;264:201–210.
78. Hacking WJ, Vanbavel E, Spaan JA. Shear stress is not sufficient to control growth of vascular networks : a model study. *Am J Physiol Hear Circ Physiol*. 1996;270:H364–H375.
79. Longland CJ. The collateral circulation of the limb. *Ann R Coll Surg Engl*. 1953;13:161–176.
80. Heil M, Schaper W. Pathophysiology of collateral development. *Coron Artery Dis*. 2004;15:373–8.
81. Unthank JL, Fath SW, Burkhart HM, Miller SC, Dalsing MC. Wall remodeling during luminal expansion of mesenteric arterial collaterals in the rat. *Circ Res*. 1996;79:1015–1023.
82. Langille BL, Bendeck MP, Keeley FW. Adaptations of carotid arteries of young and mature rabbits to reduced carotid blood flow. *Am J Physiol*. 1989;256:H931–H939.
83. Brownlee RD, Langille BL. Arterial adaptations to altered blood flow. *Can J Physiol Pharmacol*. 1991;69:978–983.
84. Rodbard S. Vascular Caliber. *Cardiology*. 1975;60:4–49.
85. Kassab GS, Fung Y-CB. The pattern of coronary arteriolar bifurcations and the uniform shear hypothesis. *Ann Biomed Eng*. 1995;23:13–20.
86. Murray CD. The physiological principle of minimum work: I. The vascular system and the cost of blood volume. *Proc Natl Acad Sci U S A*. 1926;12:207–214.
87. Zamir M. Shear forces and blood vessel radii in the cardiovascular system. *J Gen Physiol*. 1977;69:449–61.
88. Cheng C, Helderma n F, Tempel D, Segers D, Hierck B, Poelmann R, Tol A Van, Duncker DJ, Robbers-visser D, Ursem NTC, Haperen R Van, Wentzel JJ, Gijzen F, Steen AFW Van Der, Crom R De, Krams R. Large variations in absolute wall shear stress levels within one species and between species. *Atherosclerosis*. 2007;195:225–235.
89. Reneman RS, Arts T, Hoeks APG. Wall shear stress--an important determinant of endothelial cell function and structure--in the arterial system in vivo. *J Vasc Res*. 2006;43:251–69.
90. Mayrovitz HN, Roy J. Microvascular blood flow : evidence indicating a cubic dependence on arteriolar diameter. *Am J Physiol Hear Circ Physiol*. 1983;H1031–H1038.
91. Kamiya A, Bukhari R, Togawa T. Adaptive regulation of wall shear stress optimizing vascular tree function. *Bull Math Biol*. 1984;46:127–137.
92. LaBarbera M. Principles of design of fluid transport systems in zoology. *Science (80-)*. 1990;249:992–1000.

93. Kassab GS, Gregersen H, Nielsen SL, Lu X, Tanko LB, Falk E. Remodelling of the left anterior descending artery in a porcine model of supraaortic stenosis. *J Hypertens*. 2002;20:2429–37.
94. Miyashiro JK, Poppa V, Berk BC. Flow-induced vascular remodeling in the rat carotid artery diminishes with age. *Circ Res*. 1997;81:311–319.
95. Baeyens N, Nicoli S, Coon BG, Ross TD, Dries K Van Den, Han J, Lauridsen HM, Mejean CO, Eichmann A, Thomas J-L, Humphrey JD, Schwartz MA. Vascular remodeling is governed by a VEGFR3-dependent fluid shear stress set point. *Elife*. 2015;
96. Baccarelli A, Rienstra M, Benjamin EJ. Cardiovascular epigenetics: basic concepts and results from animal and human studies. *Circ Cardiovasc Genet*. 2010;3:567–73.
97. Ordovas JM, Smith CE. Epigenetics and cardiovascular disease. *Nat Rev Cardiol*. 2010;7:510–519.
98. Matouk CC, Marsden PA. Epigenetic regulation of vascular endothelial gene expression. *Circ Res*. 2008;102:873–87.
99. Chen L-J, Wei S-Y, Chiu J-J. Mechanical regulation of epigenetics in vascular biology and pathobiology. *J Cell Mol Med*. 2013;17:437–448.
100. Dunn J, Thabet S, Jo H. Flow-dependent epigenetic DNA methylation in endothelial gene expression and atherosclerosis. *Arterioscler Thromb Vasc Biol*. 2015;1–9.
101. Jiang Y-Z, Manduchi E, Jimenez JM, Davies PF. Endothelial epigenetics in biomechanical stress: disturbed flow-mediated epigenomic plasticity in vivo and in vitro. *Arterioscler Thromb Vasc Biol*. 2015;35:1317–1326.
102. Goldberg AD, Allis CD, Bernstein E. Epigenetics: A landscape takes shape. *Cell*. 2007;128:635–638.
103. Yan MS, Marsden PA. Epigenetics in the vascular endothelium. *Arterioscler Thromb Vasc Biol*. 2015;25:ATVBAHA.115.305043.
104. Bestor TH. The DNA methyltransferases of mammals. *Hum Mol Genet*. 2000;9:2395–2402.
105. Handy DE, Castro R, Loscalzo J. Epigenetic modifications: basic mechanisms and role in cardiovascular disease. *Circulation*. 2011;123:2145–56.
106. Ito S, Shen L, Dai Q, Wu SC, Collins LB, Swenberg JA, He C, Zhang Y. Tet proteins can convert 5-methylcytosine to 5-formylcytosine and 5-carboxylcytosine. *Science (80-)*. 2011;333:1300–3.
107. Hill PWS, Amouroux R, Hajkova P. DNA demethylation, Tet proteins and 5-hydroxymethylcytosine in epigenetic reprogramming: An emerging complex story. *Genomics*. 2014;104:324–333.
108. Miranda TB, Jones PA. DNA methylation: The nuts and bolts of repression. *J. Cell. Physiol*. 2007;213:384–390.
109. Jones PA. Functions of DNA methylation: islands, start sites, gene bodies and beyond. *Nat Rev Genet*. 2012;13:484–92.
110. Song F, Smith JF, Kimura MT, Morrow AD, Matsuyama T, Nagase H, Held WA. Association of tissue-specific differentially methylated regions (TDMs) with differential gene expression. *Proc Natl Acad Sci U S A*. 2005;102:3336.

111. Grunau C, Hindermann W, Rosenthal A. Large-scale methylation analysis of human genomic DNA reveals tissue-specific differences between the methylation profiles of genes and pseudogenes. *Hum Mol Genet.* 2000;9:2651–2663.
112. Weber M, Davies JJ, Wittig D, Oakeley EJ, Haase M, Lam WL, Schübeler D. Chromosome-wide and promoter-specific analyses identify sites of differential DNA methylation in normal and transformed human cells. *Nat Genet.* 2005;37:853–862.
113. Kamakaka RT, Biggins S. Histone variants: Deviants? *Genes Dev.* 2005;19:295–310.
114. Bernstein BE, Meissner A, Lander ES. The mammalian epigenome. *Cell.* 2007;128:669–81.
115. Uchida S, Dimmeler S. Long noncoding RNAs in cardiovascular diseases. *Circ Res.* 2015;116:737–50.
116. Mercer TR, Mattick JS. Structure and function of long noncoding RNAs in epigenetic regulation. *Nat Struct Mol Biol.* 2013;20:300–7.
117. Bartel DP. MicroRNAs: genomics, biogenesis, mechanism, and function. *Cell.* 2004;116:281–297.
118. Ha M, Kim VN. Regulation of microRNA biogenesis. *Nat Rev Mol Cell Biol.* 2014;15:509–524.
119. Jonas S, Izaurralde E. Towards a molecular understanding of microRNA-mediated gene silencing. *Nat Rev Genet.* 2015;16:421–433.
120. Lewis BP, Shih IH, Jones-Rhoades MW, Bartel DP, Burge CB. Prediction of mammalian microRNA targets. *Cell.* 2003;115:787–798.
121. Khaleghi M, Isseh IN, Bailey KR, Kullo IJ. Family history as a risk factor for peripheral arterial disease. *Am J Cardiol.* 2014;114:928–932.
122. Wahlgren CM, Magnusson PKE. Genetic influences on peripheral arterial disease in a twin population. *Arterioscler Thromb Vasc Biol.* 2011;31:678–682.
123. Pal S, Tyler JK. Epigenetics and aging. *Sci Adv.* 2016;2:e1600584.
124. Breitling LP. Current genetics and epigenetics of smoking/tobacco-related cardiovascular disease. *Arterioscler Thromb Vasc Biol.* 2013;33:1468–72.
125. Schones DE, Leung A, Natarajan R. Chromatin modifications associated with diabetes and obesity. *Arterioscler Thromb Vasc Biol.* 2015;35:1557–1561.
126. Joehanes R, Just AC, Marioni RE, Pilling LC, Reynolds LM, Mandaviya PR, Guan W, Xu T, Elks CE, Aslibekyan S, Moreno-Macias H, Smith JA, Brody JA, Dhingra R, Yousefi P, Pankow JS, Kunze S, Shah SH, McRae AF, Lohman K, Sha J, Absher DM, Ferrucci L, Zhao W, Demerath EW, Bressler J, Grove ML, Huan T, Liu C, Mendelson MM, Yao C, Kiel DP, Peters A, Wang-Sattler R, Visscher PM, Wray NR, Starr JM, Ding J, Rodriguez CJ, Wareham NJ, Irvin MR, Zhi D, Barrdahl M, Vineis P, Ambatipudi S, Uitterlinden AG, Hofman A, Schwartz J, Colicino E, Hou L, Vokonas PS, Hernandez DG, Singleton AB, Bandinelli S, Turner ST, Ware EB, Smith AK, Klengel T, Binder EB, Psaty BM, Taylor KD, Gharib SA, Swenson BR, Liang L, DeMeo DL, O'Connor GT, Herceg Z, Ressler KJ, Conneely KN, Sotoodehnia N, Kardina SLR, Melzer D, Baccarelli AA, van Meurs JBJ, Romieu I, Arnett DK, Ong KK, Liu Y, Waldenberger M, Deary IJ, Fornage M, Levy D, London SJ. Epigenetic signatures of cigarette smoking. *Circ Cardiovasc Genet.* 2016;9:436–447.

127. Wan ES, Qiu W, Baccarelli A, Carey VJ, Bacherman H, Rennard SI, Agusti A, Anderson W, Lomas DA, Demeo DL. Cigarette smoking behaviors and time since quitting are associated with differential DNA methylation across the human genome. *Hum Mol Genet*. 2012;21:3073–82.
128. Breitling LP, Yang R, Korn B, Burwinkel B, Brenner H. Tobacco-smoking-related differential DNA methylation: 27K discovery and replication. *Am J Hum Genet*. 2011;88:450–457.
129. Ling C, Groop L. Epigenetics: a molecular link between environmental factors and type 2 diabetes. *Diabetes*. 2009;58:2718–25.
130. Sharma P, Kumar J, Garg G, Kumar A, Patowary A, Karthikeyan G, Ramakrishnan L, Brahmachari V, Sengupta S. Detection of altered global DNA methylation in coronary artery disease patients. *DNA Cell Biol*. 2008;27:357–365.
131. Mandaviya PR, Stolk L, Heil SG. Homocysteine and DNA methylation: A review of animal and human literature. *Mol Genet Metab*. 2014;113:243–252.
132. Khandanpour N, Loke YK, Meyer FJ, Jennings B, Armon MP. Homocysteine and peripheral arterial disease: systematic review and meta-analysis. *Eur J Vasc Endovasc Surg*. 2009;38:316–322.
133. Brunelli S, Fusco A, Iosa M, Ricciardi E, Trallesi M. Functional outcome after lower limb amputation: Is hyperhomocysteinemia a predictive factor?: An observational study. *Medicine (Baltimore)*. 2015;94:e2167.
134. Heneghan HM, Sultan S. Homocysteine, the cholesterol of the 21st century. Impact of hyperhomocysteinemia on patency and amputation-free survival after intervention for critical limb ischemia. *J Endovasc Ther*. 2008;15:399–407.
135. Yan T-T, Li Q, Zhang X-H, Wu W-K, Sun J, Li L, Zhang Q, Tan H-M. Homocysteine impaired endothelial function through compromised vascular endothelial growth factor/Akt/endothelial nitric oxide synthase signaling. *Clin Exp Pharmacol Physiol*. 2010;37:1071–7.
136. Jiang X, Yang F, Tan H, Liao D, Bryan RM, Randhawa JK, Rumbaut RE, Durante W, Schafer AI, Yang X, Wang H. Hyperhomocysteinemia impairs endothelial function and eNOS activity via PKC activation. *Arter Thromb Vasc Biol*. 2005;25:2515–21.
137. Bosch-Marcé M, Pola R, Wecker AB, Silver M, Weber A, Luedemann C, Curry C, Murayama T, Kearny M, Yoon Y, Malinow MR, Asahara T, Isner JM, Losordo DW. Hyperhomocyst(e)inemia impairs angiogenesis in a murine model of limb ischemia. *Vasc Med*. 2005;10:15–22.
138. Veeranki S, Givvimani S, Pushpakumar S, Tyagi SC. Hyperhomocysteinemia attenuates angiogenesis through reduction of HIF-1 α and PGC-1 α levels in muscle fibers during hindlimb ischemia. *Am J Physiol Heart Circ Physiol*. 2014;306:H1116–27.
139. Duan J, Murohara T, Ikeda H, Sasaki K -i., Shintani S, Akita T, Shimada T, Imaizumi T. Hyperhomocysteinemia impairs angiogenesis in response to hindlimb ischemia. *Arterioscler Thromb Vasc Biol*. 2000;20:2579–2585.
140. Stather PW, Sylvius N, Wild JB, Choke E, Sayers RD, Bown MJ. Differential microRNA expression profiles in peripheral arterial disease. *Circ Cardiovasc Genet*. 2013;6:490–497.
141. Zampetaki A, Kiechl S, Drozdov I, Willeit P, Mayr U, Prokopi M, Mayr A, Weger S,

- Oberhollenzer F, Bonora E, Shah A, Willeit J, Mayr M. Plasma microRNA profiling reveals loss of endothelial miR-126 and other microRNAs in type 2 diabetes. *Circ Res*. 2010;107:810–7.
142. Spinetti G, Fortunato O, Caporali A, Shantikumar S, Marchetti M, Meloni M, Descamps B, Floris I, Sangalli E, Vono R, Faglia E, Specchia C, Pintus G, Madeddu P, Emanuelli C. MicroRNA-15a and microRNA-16 impair human circulating proangiogenic cell functions and are increased in the proangiogenic cells and serum of patients with critical limb ischemia. *Circ Res*. 2013;112:335–46.
 143. Caporali A, Meloni M, Völlenkle C, Bonci D, Sala-Newby GB, Addis R, Spinetti G, Losa S, Masson R, Baker AH, Agami R, Le Sage C, Condorelli G, Madeddu P, Martelli F, Emanuelli C. Deregulation of microRNA-503 contributes to diabetes mellitus-induced impairment of endothelial function and reparative angiogenesis after limb ischemia. *Circulation*. 2011;123:282–291.
 144. Bastiaansen AJNM, Ewing MM, De Boer HC, Van Der Pouw Kraan TC, De Vries MR, Peters EAB, Welten SMJ, Arens R, Moore SM, Faber JE, Jukema JW, Hamming JF, Nossent AY, Quax PHA. Lysine acetyltransferase PCAF is a key regulator of arteriogenesis. *Arterioscler Thromb Vasc Biol*. 2013;33:1902–1910.
 145. Krishna SM, Trollope AF, Golledge J. The relevance of epigenetics to occlusive cerebral and peripheral arterial disease. *Clin Sci*. 2015;128:537–558.
 146. Kaluza D, Kroll J, Gesierich S, Manavski Y, Boeckel J-N, Doebele C, Zelent A, Rössig L, Zeiher AM, Augustin HG, Urbich C, Dimmeler S. Histone deacetylase 9 promotes angiogenesis by targeting the antiangiogenic microRNA-17-92 cluster in endothelial cells. *Arterioscler Thromb Vasc Biol*. 2013;33:533–43.
 147. Fatemi M, Wade P a. MBD family proteins: reading the epigenetic code. *J Cell Sci*. 2006;119:3033–3037.
 148. Volkmann I, Kumarswamy R, Pfaff N, Fiedler J, Dangwal S, Holzmann A, Batkai S, Geffers R, Lothar A, Hein L, Thum T. MicroRNA-mediated epigenetic silencing of sirtuin1 contributes to impaired angiogenic responses. *Circ Res*. 2013;113:997–1003.
 149. Rao X, Zhong J, Zhang S, Zhang Y, Yu Q, Yang P, Wang MH, Fulton DJ, Shi H, Dong Z, Wang D, Wang CY. Loss of methyl-CpG-binding domain protein 2 enhances endothelial angiogenesis and protects mice against hind-limb ischemic injury. *Circulation*. 2011;123:2964–2974.
 150. Bonauer A, Carmona G, Iwasaki M, Mione M, Koyanagi M, Fischer A, Burchfield J, Fox H, Doebele C, Ohtani K, Chavakis E, Potente M, Tjwa M, Urbich C, Zeiher AM, Dimmeler S. MicroRNA-92a controls angiogenesis and functional recovery of ischemic tissues in mice. *Science (80-)*. 2009;324:1710–1713.
 151. Landskroner-Eiger S, Qiu C, Perrotta P, Siragusa M, Lee MY, Ulrich V, Luciano AK, Zhuang ZW, Corti F, Simons M, Montgomery RL, Wu D, Yu J, Sessa WC. Endothelial miR-17~92 cluster negatively regulates arteriogenesis via miRNA-19 repression of WNT signaling. *Proc Natl Acad Sci U S A*. 2015;112:12812–12817.
 152. Shi L, Fisslthaler B, Zippel N, Frömel T, Hu J, Elgheznawy A, Heide H, Popp R, Fleming I. MicroRNA-223 antagonizes angiogenesis by targeting β 1 integrin and preventing growth factor signaling in endothelial cells. *Circ Res*. 2013;113:1320–30.
 153. Yin KJ, Deng Z, Hamblin M, Xiang Y, Huang H, Zhang J, Jiang X, Wang Y, Chen YE. Peroxisome proliferator-activated receptor delta regulation of miR-15a in ischemia-

- induced cerebral vascular endothelial injury. *J Neurosci*. 2010;30:6398–6408.
154. Yin KJ, Olsen K, Hamblin M, Zhang J, Schwendeman SP, Chen YE. Vascular endothelial cell-specific microRNA-15a inhibits angiogenesis in hindlimb ischemia. *J Biol Chem*. 2012;287:27055–27064.
 155. Welten SM, Bastiaansen AJ, de Jong R, de Vries MR, Peters EH, Boonstra M, Sheikh SP, La Monica N, Kandimalla ER, Quax PH, Nossent AY. Inhibition of 14q32 microRNAs miR-329, miR-487b, miR-494 and miR-495 increases neovascularization and blood flow recovery after ischemia. *Circ Res*. 2014;115:696–708.
 156. van Solingen C, Seghers L, Bijkerk R, Duijs JMGJ, Roeten MK, van Oeveren-Rietdijk AM, Baelde HJ, Monge M, Vos JB, de Boer HC, Quax PHA, Rabelink TJ, van Zonneveld AJ. Antagomir-mediated silencing of endothelial cell specific microRNA-126 impairs ischemia-induced angiogenesis. *J Cell Mol Med*. 2009;13:1577–85.
 157. Wang S, Aurora AB, Johnson B a., Qi X, McAnally J, Hill J a., Richardson J a., Bassel-Duby R, Olson EN. The endothelial-specific microRNA miR-126 governs vascular integrity and angiogenesis. *Dev Cell*. 2008;15:261–271.
 158. Fish JE, Santoro MM, Morton SU, Yu S, Yeh R-F, Wythe JD, Ivey KN, Bruneau BG, Stainier DYR, Srivastava D. miR-126 regulates angiogenic signaling and vascular integrity. *Dev Cell*. 2008;15:272–284.
 159. Cao WJ, Rosenblat JD, Roth NC, Kuliszewski M a., Matkar PN, Rudenko D, Liao C, Lee PJH, Leong-Poi H. Therapeutic angiogenesis by ultrasound-mediated microRNA-126-3p delivery. *Arterioscler Thromb Vasc Biol*. 2015;35:2401–2411.
 160. Semo J, Sharir R, Afek A, Avivi C, Barshack I, Maysel-Auslender S, Krelin Y, Kain D, Entin-Meer M, Keren G, George J. The 106b~25 microRNA cluster is essential for neovascularization after hindlimb ischaemia in mice. *Eur Heart J*. 2014;35:3212–3223.
 161. Grundmann S, Hans FP, Kinniry S, Heinke J, Helbing T, Bluhm F, Sluijter JPG, Hoefer I, Pasterkamp G, Bode C, Moser M. MicroRNA-100 regulates neovascularization by suppression of mammalian target of rapamycin in endothelial and vascular smooth muscle cells. *Circulation*. 2011;123:999–1009.
 162. Pankratz F, Bemtgen X, Zeiser R, Leonhardt F, Kreuzaler S, Hilgendorf I, Smolka C, Helbing T, Hoefer I, Esser JS, Kustermann M, Moser M, Bode C, Grundmann S. MicroRNA-155 exerts cell-specific antiangiogenic but proarteriogenic effects during adaptive neovascularization. *Circulation*. 2015;131:1575–1589.
 163. Lei Z, van Mil A, Brandt MM, Grundmann S, Hoefer I, Smits M, El Azzouzi H, Fukao T, Cheng C, Doevendans PA, Sluijter JPG. MicroRNA-132/212 family enhances arteriogenesis after hindlimb ischaemia through modulation of the Ras-MAPK pathway. *J Cell Mol Med*. 2015;20:1–12.
 164. Hazarika S, Farber CR, Dokun AO, Pitsillides AN, Wang T, Lye RJ, Annex BH. MicroRNA-93 controls perfusion recovery following hind-limb ischemia by modulating expression of multiple genes in the cell cycle pathway. *Circulation*. 2013;127:1818–1828.
 165. Helisch A, Wagner S, Khan N, Drinane M, Wolfram S, Heil M, Ziegelhoeffer T, Brandt U, Pearlman JD, Swartz HM, Schaper W. Impact of mouse strain differences in innate hindlimb collateral vasculature. *Arterioscler Thromb Vasc Biol*. 2006;26:520–6.
 166. Mac Gabhann F, Peirce SM. Collateral capillary arterIALIZATION following arteriolar ligation in murine skeletal muscle. *Microcirculation*. 2010;17:333–47.

167. Meisner JK, Sumer S, Murrell KP, Higgins TJ, Price RJ. Laser speckle flowmetry method for measuring spatial and temporal hemodynamic alterations throughout large microvascular networks. *Microcirculation*. 2012;19:619–31.
168. Scholz D, Ziegelhoeffer T, Helisch A, Wagner S, Friedrich C, Podzuweit T, Schaper W. Contribution of arteriogenesis and angiogenesis to postocclusive hindlimb perfusion in mice. *J Mol Cell Cardiol*. 2002;34:775–87.
169. Li Q, Hu B, Hu G, Chen C, Niu X, Liu J, Zhou S, Zhang C, Wang Y, Deng Z-F. tRNA-derived small non-coding RNAs in response to ischemia inhibit angiogenesis. *Sci Rep*. 2016;6:20850.
170. Voellenkle C, Garcia-Manteiga JM, Pedrotti S, Perfetti A, De Toma I, Da Silva D, Maimone B, Greco S, Fasanaro P, Creo P, Zaccagnini G, Gaetano C, Martelli F. Implication of Long noncoding RNAs in the endothelial cell response to hypoxia revealed by RNA-sequencing. *Sci Rep*. 2016;6:24141.
171. Michalik KM, You X, Manavski Y, Doddaballapur A, Zörnig M, Braun T, John D, Ponomareva Y, Chen W, Uchida S, Boon RA, Dimmeler S. Long noncoding RNA MALAT1 regulates endothelial cell function and vessel growth. *Circ Res*. 2014;114:1389–97.
172. van Royen N, Piek JJ, Schaper W, Fulton WF. A critical review of clinical arteriogenesis research. *J Am Coll Cardiol*. 2009;55:17–25.
173. Simons M, Annex BH, Laham RJ, Kleiman N, Henry T, Dauerman H, Udelson JE, Gervino E V., Pike MP, Whitehouse M., Moon T, Chronos NA. Pharmacological treatment of coronary artery disease with recombinant fibroblast growth factor-2: double-blind, randomized, controlled clinical trial. *Circulation*. 2002;105:788–793.
174. Kusumanto YH, van Weel V, Mulder NH, Smit AJ, van den Dungen JJAM, Hooymans JMM, Sluiter WJ, Tio RA, Quax PHA, Gans ROB, Dullaart RPF, Hospers GAP. Treatment with intramuscular vascular endothelial growth factor gene compared with placebo for patients with diabetes mellitus and critical limb ischemia: a double-blind randomized trial. *Hum Gene Ther*. 2006;17:683–91.
175. Schierling W, Troidl K, Mueller C, Troidl C, Wustrack H, Bachmann G, Kasprzak PM, Schaper W, Schmitz-Rixen T. Increased intravascular flow rate triggers cerebral arteriogenesis. *J Cereb blood flow Metab*. 2009;29:726–37.
176. Meisner JK, Niu J, Sumer S, Price RJ. Trans-illuminated laser speckle imaging of collateral artery blood flow in ischemic mouse hindlimb. *J Biomed Opt*. 2013;18:96011.
177. Chappell JC, Song J, Burke CW, Klibanov AL, Price RJ. Targeted delivery of nanoparticles bearing fibroblast growth factor-2 by ultrasonic microbubble destruction for therapeutic arteriogenesis. *Small*. 2008;4:1769–1777.
178. Nickerson MM, Burke CW, Meisner JK, Shuptrine CW, Song J, Price RJ. Capillary arterialization requires the bone-marrow-derived cell (BMC)-specific expression of chemokine (C-C motif) receptor-2, but BMCs do not transdifferentiate into microvascular smooth muscle. *Angiogenesis*. 2009;12:355–63.
179. Distasi MR, Case J, Ziegler MA, Dinanuer MC, Yoder MC, Haneline LS, Dalsing MC, Miller SJ, Labarrere CA, Murphy MP, Ingram DA, Unthank JL. Suppressed hindlimb perfusion in *Rac2*^{-/-} and *Nox2*^{-/-} mice does not result from impaired collateral growth. *Am J Physiol Hear Circ Physiol*. 2009;296:H877-86.
180. Dai X, Faber JE. Endothelial nitric oxide synthase deficiency causes collateral vessel

- rarefaction and impairs activation of a cell cycle gene network during arteriogenesis. *Circ Res*. 2010;106:1870–81.
181. Schindelin J, Arganda-Carreras I, Frise E, Kaynig V, Longair M, Pietzsch T, Preibisch S, Rueden C, Saalfeld S, Schmid B, Tinevez J-Y, White DJ, Hartenstein V, Eliceiri K, Tomancak P, Cardona A. Fiji: an open-source platform for biological-image analysis. *Nat Methods*. 2012;9:676–82.
 182. McCue S, Dajnowiec D, Xu F, Zhang M, Jackson MR, Langille BL. Shear stress regulates forward and reverse planar cell polarity of vascular endothelium in vivo and in vitro. *Circ Res*. 2006;98:939–46.
 183. Tzima E, Kiosses WB, del Pozo M a, Schwartz MA. Localized cdc42 activation, detected using a novel assay, mediates microtubule organizing center positioning in endothelial cells in response to fluid shear stress. *J Biol Chem*. 2003;278:31020–3.
 184. Rogers KA, McKee NH, Kalnins VI. Preferential orientation of centrioles toward the heart in endothelial cells of major blood vessels is reestablished after reversal of a segment. *Proc Natl Acad Sci U S A*. 1985;82:3272–6.
 185. Allan VJ, Thompson HM, McNiven MA. Motoring around the Golgi. *Nat Cell Biol*. 2002;4:E236–42.
 186. Coan DE, Wechezak AR, Viggers RF, Sauvage LR. Effect of shear stress upon localization of the Golgi apparatus and microtubule organizing center in isolated cultured endothelial cells. *J Cell Sci*. 1993;104:1145–53.
 187. Blackman BR, García-Cardeña G, Gimbrone MA. A new in vitro model to evaluate differential responses of endothelial cells to simulated arterial shear stress waveforms. *J Biomech Eng*. 2002;124:397.
 188. Irizarry RA, Bolstad BM, Collin F, Cope LM, Hobbs B, Speed TP. Summaries of Affymetrix GeneChip probe level data. *Nucleic Acids Res*. 2003;31:e15.
 189. Eden E, Navon R, Steinfeld I, Lipson D, Yakhini Z. GOrilla: a tool for discovery and visualization of enriched GO terms in ranked gene lists. *BMC Bioinformatics*. 2009;10:48.
 190. Chiu J-J, Chien S. Effects of disturbed flow on vascular endothelium: pathophysiological basis and clinical perspectives. *Physiol Rev*. 2011;91:327–87.
 191. Zhang J, Friedman MH. Adaptive response of vascular endothelial cells to an acute increase in shear stress magnitude. *Am J Physiol Hear Circ Physiol*. 2012;302:H983–991.
 192. Mack PJ, Zhang Y, Chung S, Vickerman V, Kamm RD, García-Cardeña G. Biomechanical regulation of endothelium-dependent events critical for adaptive remodeling. *J Biol Chem*. 2009;284:8412–20.
 193. Morigi BM, Zoja C, Figliuzzi M, Foppolo M, Micheletti G, Bontempelli M, Saronni M, Remuzzi G, Remuzzi A. Fluid shear stress modulates surface expression of adhesion molecules by endothelial cells. *Blood*. 1995;85:1696–1703.
 194. Malek AM, Jiang L, Lee I, Sessa WC, Izumo S, Alper SL. Induction of nitric oxide synthase mRNA by shear stress requires intracellular calcium and G-protein signals and is modulated by PI 3 kinase. *Biochem Biophys Res Commun*. 1999;254:231–42.
 195. Davis ME, Grumbach IM, Fukai T, Cutchins A, Harrison DG. Shear stress regulates endothelial nitric-oxide synthase promoter activity through nuclear factor kappaB binding. *J Biol Chem*. 2004;279:163–8.

196. Boo YC, Sorescu G, Boyd N, Shiojima I, Walsh K, Du J, Jo H. Shear stress stimulates phosphorylation of endothelial nitric-oxide synthase at Ser1179 by Akt-independent mechanisms: role of protein kinase A. *J Biol Chem*. 2002;277:3388–96.
197. Dekker RJ, Boon RA, Rondaij MG, Kragt A, Volger OL, Elderkamp YW, Meijers JCM, Voorberg J, Pannekoek H, Horrevoets AJG. KLF2 provokes a gene expression pattern that establishes functional quiescent differentiation of the endothelium. *Blood*. 2006;107:4354–63.
198. Dekker RJ, van Thienen J V, Rohlena J, de Jager SC, Elderkamp YW, Seppen J, de Vries CJM, Biessen EAL, van Berkel TJC, Pannekoek H, Horrevoets AJG. Endothelial KLF2 links local arterial shear stress levels to the expression of vascular tone-regulating genes. *Am J Pathol*. 2005;167:609–18.
199. Fledderus JO, van Thienen J V, Boon RA, Dekker RJ, Rohlena J, Volger OL, Bijmens A-PJJ, Daemen MJAP, Kuiper J, van Berkel TJC, Pannekoek H, Horrevoets AJG. Prolonged shear stress and KLF2 suppress constitutive proinflammatory transcription through inhibition of ATF2. *Blood*. 2007;109:4249–57.
200. Boon RA, Leyen TA, Fontijn RD, Fledderus JO, Baggen JMC, Volger OL, van Nieuw Amerongen GP, Horrevoets AJG. KLF2-induced actin shear fibers control both alignment to flow and JNK signaling in vascular endothelium. *Blood*. 2010;115:2533–42.
201. Parmar KM, Nambudiri V, Dai G, Larman HB, Gimbrone MA, García-Cardena G. Statins exert endothelial atheroprotective effects via the KLF2 transcription factor. *J Biol Chem*. 2005;280:26714–9.
202. van Keulen JK, Timmers L, van Kuijk LP, Retnam L, Hoefer IE, Pasterkamp G, Lim SK, de Kleijn DP V. The Nuclear Factor-kappa B p50 subunit is involved in flow-induced outward arterial remodeling. *Atherosclerosis*. 2009;202:424–30.
203. Castier Y, Ramkhalawon B, Riou S, Tedgui A, Lehoux S. Role of NF-kappaB in flow-induced vascular remodeling. *Antioxid Redox Signal*. 2009;11:1641–9.
204. Tirziu D, Jaba IM, Yu P, Larrivée B, Coon BG, Cristofaro B, Zhuang ZW, Lanahan AA, Schwartz MA, Eichmann A, Simons M. Endothelial nuclear factor-kB-dependent regulation of arteriogenesis and branching. *Circulation*. 2012;126:2589–600.
205. Toyota E, Warltier DC, Brock T, Ritman E, Kolz C, O'Malley P, Rocic P, Focardi M, Chilian WM. Vascular endothelial growth factor is required for coronary collateral growth in the rat. *Circulation*. 2005;112:2108–13.
206. Babiak A, Schumm A-M, Wangler C, Loukas M, Wu J, Dombrowski S, Matuschek C, Kotzerke J, Dehio C, Waltenberger J. Coordinated activation of VEGFR-1 and VEGFR-2 is a potent arteriogenic stimulus leading to enhancement of regional perfusion. *Cardiovasc Res*. 2004;61:789–95.
207. Hayashi S, Morishita R, Nakamura S, Yamamoto K, Moriguchi A, Nagano T, Taiji M, Noguchi H, Matsumoto K, Nakamura T, Higaki J, Ogihara T. Potential role of hepatocyte growth factor, a novel angiogenic growth factor, in peripheral arterial disease: downregulation of HGF in response to hypoxia in vascular cells. *Circulation*. 1999;100:II301–308.
208. Taniyama Y, Morishita R, Aoki M, Nakagami H, Yamamoto K, Yamazaki K, Matsumoto K, Nakamura T, Kaneda Y, Ogihara T. Therapeutic angiogenesis induced by human hepatocyte growth factor gene in rat and rabbit hindlimb ischemia models: preclinical study for treatment of peripheral arterial disease. *Gene Ther*. 2001;8:181–9.

209. Masaki I, Yonemitsu Y, Yamashita A, Sata S, Tanii M, Komori K, Nakagawa K, Hou X, Nagai Y, Hasegawa M, Sugimachi K, Sueishi K. Angiogenic gene therapy for experimental critical limb ischemia: acceleration of limb loss by overexpression of vascular endothelial growth factor 165 but not of fibroblast growth factor-2. *Circ Res*. 2002;90:966–73.
210. Fujii T, Yonemitsu Y, Onimaru M, Tanii M, Nakano T, Egashira K, Takehara T, Inoue M, Hasegawa M, Kuwano H, Sueishi K. Nonendothelial mesenchymal cell-derived MCP-1 is required for FGF-2-mediated therapeutic neovascularization: critical role of the inflammatory/arteriogenic pathway. *Arterioscler Thromb Vasc Biol*. 2006;26:2483–9.
211. Ren B, Deng Y, Mukhopadhyay A, Lanahan AA, Zhuang ZW, Moodie KL, Mulligan-Kehoe MJ, Byzova T V, Peterson RT, Simons M. ERK1/2-Akt1 crosstalk regulates arteriogenesis in mice and zebrafish. *J Clin Invest*. 2010;120:1217–28.
212. Sarateanu CS, Retuerto MA, Beckmann JT, McGregor L, Carbray J, Patejunas G, Nayak L, Milbrandt J, Rosengart TK. An Egr-1 master switch for arteriogenesis: studies in Egr-1 homozygous negative and wild-type animals. *J Thorac Cardiovasc Surg*. 2006;131:138–45.
213. Kinnaird T, Stabile E, Zbinden S, Burnett MS, Epstein SE. Cardiovascular risk factors impair native collateral development and may impair efficacy of therapeutic interventions. *Cardiovasc Res*. 2008;78:257–64.
214. Senthilkumar A, Smith RD, Khitha J, Arora N, Veerareddy S, Langston W, Chidlow JH, Barlow SC, Teng X, Patel RP, Lefer DJ, Kevil CG. Sildenafil promotes ischemia-induced angiogenesis through a PKG-dependent pathway. *Arterioscler Thromb Vasc Biol*. 2007;27:1947–54.
215. Bir SC, Xiong Y, Kevil CG, Luo J. Emerging role of PKA/eNOS pathway in therapeutic angiogenesis for ischaemic tissue diseases. *Cardiovasc Res*. 2012;95:7–18.
216. Venkatesh PK, Pattillo CB, Branch B, Hood J, Thoma S, Illum S, Pardue S, Teng X, Patel RP, Kevil CG. Dipyridamole enhances ischaemia-induced arteriogenesis through an endocrine nitrite/nitric oxide-dependent pathway. *Cardiovasc Res*. 2010;85:661–70.
217. Sweet DT, Chen Z, Givens CS, Owens AP, Rojas M, Tzima E. Endothelial Shc regulates arteriogenesis through dual control of arterial specification and inflammation via the Notch and NF- κ B pathways. *Circ Res*. 2013;113:32–39.
218. Lan Q, Mercurius KO, Davies PF. Stimulation of transcription factors NF κ B and AP1 in ECs subjected to shear stress. *Biochem Biophys Res Commun*. 1994;201:950–956.
219. Gruionu G, Hoying JB, Pries AR, Secomb TW. Structural remodeling of mouse gracilis artery after chronic alteration in blood supply. *Am J Physiol Hear Circ Physiol*. 2005;288:2047–2054.
220. Gruionu G, Hoying JB, Pries AR, Secomb TW. Structural remodeling of the mouse gracilis artery: coordinated changes in diameter and medial area maintain circumferential stress. *Microcirculation*. 2012;19:610–618.
221. Johnson C, Sung H-J, Lessner SM, Fini ME, Galis ZS. Matrix metalloproteinase-9 is required for adequate angiogenic revascularization of ischemic tissues: potential role in capillary branching. *Circ Res*. 2004;94:262–8.
222. Deindl E, Buschmann I, Hoefer IE, Podzuweit T, Boengler K, Vogel S, van Royen N, Fernandez B, Schaper W. Role of ischemia and of hypoxia-inducible genes in arteriogenesis after femoral artery occlusion in the rabbit. *Circ Res*. 2001;89:779–786.

223. Ito WD, Arras M, Scholz D, Winkler B, Htun P, Schaper W. Angiogenesis but not collateral growth is associated with ischemia after femoral artery occlusion. *Am J Physiol Hear Circ Physiol*. 1997;273:H1255–H1265.
224. Adamson RH, Sarai RK, Altangerel A, Clark JF, Weinbaum S, Curry F-RE. Microvascular permeability to water is independent of shear stress, but dependent on flow direction. *Am J Physiol Hear Circ Physiol*. 2013;304:H1077–1084.
225. Melchior B, Frangos JA. Shear-induced endothelial cell-cell junction inclination. *Am J Physiol Cell Physiol*. 2010;299:C621–9.
226. Passerini AG, Milsted A, Rittgers SE. Shear stress magnitude and directionality modulate growth factor gene expression in preconditioned vascular endothelial cells. *J Vasc Surg*. 2003;37:182–90.
227. Wang C, Baker BM, Chen CS, Schwartz MA. Endothelial cell sensing of flow direction. *Arter Thromb Vasc Biol*. 2013;33:2130–2136.
228. Tzima E. Role of small GTPases in endothelial cytoskeletal dynamics and the shear stress response. *Circ Res*. 2006;98:176–85.
229. Tzima E, Del Pozo MA, Kiosses WB, Mohamed SA, Li S, Chien S, Schwartz MA. Activation of Rac1 by shear stress in endothelial cells mediates both cytoskeletal reorganization and effects on gene expression. *EMBO J*. 2002;21:6791–800.
230. Imberti B, Morigi M, Zoja C, Angioletti S, Abbate M, Remuzzi a, Remuzzi G. Shear stress-induced cytoskeleton rearrangement mediates NF-kappaB-dependent endothelial expression of ICAM-1. *Microvasc Res*. 2000;60:182–8.
231. Troidl K, Rüdinger I, Cai W-J, Mücke Y, Grosseckettler L, Piotrowska I, Apfelbeck H, Schierling W, Volger OL, Horrevoets AJ, Grote K, Schmitz-Rixen T, Schaper W, Troidl C. Actin-binding rho activating protein (Abra) is essential for fluid shear stress-induced arteriogenesis. *Arterioscler Thromb Vasc Biol*. 2009;29:2093–101.
232. Yu J, deMuinck ED, Zhuang Z, Drinane M, Kauser K, Rubanyi GM, Qian HS, Murata T, Escalante B, Sessa WC. Endothelial nitric oxide synthase is critical for ischemic remodeling, mural cell recruitment, and blood flow reserve. *Proc Natl Acad Sci U S A*. 2005;102:10999–1004.
233. Park B, Hoffman A, Yang Y, Yan J, Tie G, Bagshahi H, Nowicki PT, Messina LM. eNOS affects both early and late collateral arterial adaptation and blood flow recovery after induction of hindlimb ischemia in mice. *J Vasc Surg*. 2010;51:1–17.
234. Lloyd PG, Yang HT, Terjung RL. Arteriogenesis and angiogenesis in rat ischemic hindlimb: role of nitric oxide. *Am J Physiol Hear Circ Physiol*. 2001;281:H2528–38.
235. Mees B, Wagner S, Ninci E, Tribulova S, Martin S, van Haperen R, Kostin S, Heil M, de Crom R, Schaper W. Endothelial nitric oxide synthase activity is essential for vasodilation during blood flow recovery but not for arteriogenesis. *Arterioscler Thromb Vasc Biol*. 2007;27:1926–33.
236. Kassab GS. Scaling laws of vascular trees : of form and function. *Am J Physiol Hear Circ Physiol*. 2005;290:894–903.
237. Heuslein JL, Meisner JK, Li X, Song J, Vincentelli H, Leiphart RJ, Ames EG, Blackman BR, Price RJ. Mechanisms of amplified arteriogenesis in collateral artery segments exposed to reversed flow direction. *Arterioscler Thromb Vasc Biol*. 2015;35:2354–2365.
238. Jiang Y-Z, Jiménez JM, Ou K, McCormick ME, Zhang L-D, Davies PF. Hemodynamic

- disturbed flow induces differential DNA methylation of endothelial Kruppel-Like Factor 4 promoter in vitro and in vivo. *Circ Res*. 2014;115:32–43.
239. Dunn J, Qiu H, Kim S, Jjingo D, Hoffman R, Kim CW, Jang I, Son DJ, Kim D, Pan C, Fan Y, Jordan IK, Jo H. Flow-dependent epigenetic DNA methylation regulates endothelial gene expression and atherosclerosis. *J Clin Invest*. 2014;124:3187–3199.
 240. Zhou J, Li Y-S, Chien S. Epigenetic mechanism in regulation of endothelial function by disturbed flow: Induction of DNA hypermethylation by DNMT1. *Cell Mol Bioeng*. 2014;7:218–224.
 241. Jiang Y-Z, Manduchi E, Stoeckert CJ, Davies PF. Arterial endothelial methylome: differential DNA methylation in athero-susceptible disturbed flow regions in vivo. *BMC Genomics*. 2015;16:506.
 242. Heuslein JL, Murrell KP, Leiphart RJ, Llewellyn RA, Meisner JK, Price RJ. Vascular growth responses to chronic arterial occlusion are unaffected by myeloid specific focal adhesion kinase (FAK) deletion. *Sci Rep*. 2016;6:27029.
 243. Newman MR, Blyth BJ, Hussey DJ, Jardine D, Sykes PJ, Ormsby RJ. Sensitive quantitative analysis of murine LINE1 DNA methylation using high resolution melt analysis. *Epigenetics*. 2012;7:92–105.
 244. Tse MY, Ashbury JE, Zwingerman N, King WD, Taylor SA, Pang SC. A refined, rapid and reproducible high resolution melt (HRM)-based method suitable for quantification of global LINE-1 repetitive element methylation. *BMC Res Notes*. 2011;4:565.
 245. Subramanian A, Tamayo P, Mootha VK, Mukherjee S, Ebert BL. Gene set enrichment analysis : A knowledge-based approach for interpreting genome-wide. *Proc Natl Acad Sci U S A*. 2005;102:15545–15550.
 246. Hoefer IE, Grundmann S, van Royen N, Voskuil M, Schirmer SH, Ulusans S, Bode C, Buschmann IR, Piek JJ. Leukocyte subpopulations and arteriogenesis: specific role of monocytes, lymphocytes and granulocytes. *Atherosclerosis*. 2005;181:285–93.
 247. Ghoshal K, Datta J, Majumder S, Bai S, Kutay H, Motiwala T, Jacob ST. 5-Aza-deoxycytidine induces selective degradation of DNA methyltransferase 1 by a proteasomal pathway that requires the KEN box, bromo-adjacent homology domain, and nuclear localization signal. *Mol Cell Biol*. 2005;25:4727–4741.
 248. Illi B, Nanni S, Scopece A, Farsetti A, Biglioli P, Capogrossi MC, Gaetano C. Shear stress-mediated chromatin remodeling provides molecular basis for flow-dependent regulation of gene expression. *Circ Res*. 2003;93:155–61.
 249. Chen W, Bacanamwo M, Harrison DG. Activation of p300 histone acetyltransferase activity is an early endothelial response to laminar shear stress and is essential for stimulation of endothelial nitric-oxide synthase mRNA transcription. *J Biol Chem*. 2008;283:16293–16298.
 250. Lee D-Y, Lee C-I, Lin T-E, Lim SH, Zhou J, Tseng Y-C, Chien S, Chiu J-J. Role of histone deacetylases in transcription factor regulation and cell cycle modulation in endothelial cells in response to disturbed flow. *Proc Natl Acad Sci U S A*. 2012;109:1967–72.
 251. Chen L-J, Chuang L, Huang Y-H, Zhou J, Lim SH, Lee C-I, Lin W-W, Lin T-E, Wang W-L, Chen L, Chien S, Chiu J-J. MicroRNA mediation of endothelial inflammatory response to smooth muscle cells and its inhibition by atheroprotective shear stress. *Circ Res*. 2015;116:1157–1169.

252. Fang Y, Shi C, Manduchi E, Civelek M, Davies PF. MicroRNA-10a regulation of proinflammatory phenotype in athero-susceptible endothelium in vivo and in vitro. *Proc Natl Acad Sci U S A*. 2010;107:13450–13455.
253. Ni C-W, Qiu H, Jo H. MicroRNA-663 upregulated by oscillatory shear stress plays a role in inflammatory response of endothelial cells. *Am J Physiol Heart Circ Physiol*. 2011;300:H1762-9.
254. Qin X, Wang X, Wang Y, Tang Z, Cui Q, Xi J, Li Y-SJ, Chien S, Wang N. MicroRNA-19a mediates the suppressive effect of laminar flow on cyclin D1 expression in human umbilical vein endothelial cells. *Proc Natl Acad Sci U S A*. 2010;107:3240–3244.
255. Tao Y, Huang C, Huang Y, Hong L, Wang H, Zhou Z, Qiu Y. SIRT4 suppresses inflammatory responses in human hmbilical vein endothelial cells. *Cardiovasc Toxicol*. 2015;15:217–223.
256. Tirziu D, Jaba IM, Yu P, Larrivée B, Coon BG, Cristofaro B, Zhuang ZW, Lanahan AA, Schwartz MA, Eichmann A, Simons M. Endothelial nuclear factor-κB-dependent regulation of arteriogenesis and branching. *Circulation*. 2012;126:2589–600.
257. Gorski DH, Walsh K. The role of homeobox genes in vascular remodeling and angiogenesis. *Circ Res*. 2000;87:865–872.
258. Myers C, Charboneau A, Boudreau N. Homeobox B3 promotes capillary morphogenesis and angiogenesis. *J Cell Biol*. 2000;148:343–351.
259. Hastings NE, Feaver RE, Lee MY, Wamhoff BR, Blackman BR. Human IL-8 regulates smooth muscle cell VCAM-1 expression in response to endothelial cells exposed to atheroprone flow. *Arterioscler Thromb Vasc Biol*. 2009;29:725–31.
260. Chiu JJ, Wung BS, Shyy JYJ, Hsieh HJ, Wang DL. Reactive oxygen species are involved in shear stress-induced intercellular adhesion molecule-1 expression in endothelial cells. *Arterioscler Thromb Vasc Biol*. 1997;17:3570–3577.
261. Herold J, Pipp F, Fernandez B, Xing Z, Heil M, Tillmanns H, Braun-Dullaues RC. Transplantation of monocytes: a novel strategy for in vivo augmentation of collateral vessel growth. *Hum Gene Ther*. 2004;15:1–12.
262. Epstein SE, Stabile E, Kinnaird T, Lee CW, Clavijo L, Burnett MS. Janus phenomenon: the interrelated tradeoffs inherent in therapies designed to enhance collateral formation and those designed to inhibit atherogenesis. *Circulation*. 2004;109:2826–31.
263. Neth P, Nazari-Jahantigh M, Schober A, Weber C. MicroRNAs in flow-dependent vascular remodelling. *Cardiovasc Res*. 2013;
264. Urbich C, Kuehbachner A, Dimmeler S. Role of microRNAs in vascular diseases, inflammation, and angiogenesis. *Cardiovasc Res*. 2008;79:581–8.
265. van Rooij E. The art of microRNA research. *Circ Res*. 2011;108:219–34.
266. van Royen N. CD44 regulates arteriogenesis in mice and is differentially expressed in patients with poor and good collateralization. *Circulation*. 2004;109:1647–1652.
267. Bot PT, Grundmann S, van Royen N, Joosten SPJ, Schirmer SH, de Kleijn DP V, Pals ST, Pasterkamp G, Piek JJ, Hoefer IE. Distinct CD44 splice variants differentially affect collateral artery growth. *Curr Vasc Pharmacol*. 2013;11:13–20.
268. Alexander MS, Kawahara G, Motohashi N, Casar JC, Eisenberg I, Myers J a, Gasperini MJ, Estrella EA, Kho AT, Mitsunashi S, Shapiro F, Kang PB, Kunkel LM. MicroRNA-199a

- is induced in dystrophic muscle and affects WNT signaling, cell proliferation, and myogenic differentiation. *Cell Death Differ.* 2013;20:1194–208.
269. Chen R, Alvero AB, Silasi D a, Kelly MG, Fest S, Visintin I, Leiser A, Schwartz PE, Rutherford T, Mor G. Regulation of IKKbeta by miR-199a affects NF-kappaB activity in ovarian cancer cells. *Oncogene.* 2008;27:4712–23.
 270. Cheng HS, Siu A, Cybulsky MI, Fish JE. Abstract 640: Role of microRNA-146a in vascular inflammation and atherosclerosis. *Arterioscler Thromb Vasc Biol.* 2014;34:A640.
 271. Raitoharju E, Lyytikäinen L-P, Levula M, Oksala N, Mennander A, Tarkka M, Klopp N, Illig T, Kähönen M, Karhunen PJ, Laaksonen R, Lehtimäki T. miR-21, miR-210, miR-34a, and miR-146a/b are up-regulated in human atherosclerotic plaques in the Tampere Vascular Study. *Atherosclerosis.* 2011;219:211–7.
 272. Song XW, Li Q, Lin LI, Wang XC, Li DF, Wang GK, Ren ANJ, Wang YR, Qin YW, Yuan WJ, Jing Q. MicroRNAs are dynamically regulated in hypertrophic hearts, and miR-199a is essential for the maintenance of cell size in cardiomyocytes. *J Cell Physiol.* 2010;225:437–443.
 273. Li Z, Song Y, Liu L, Hou N, An X, Zhan D, Li Y, Zhou L, Li P, Yu L, Xia J, Zhang Y, Wang J, Yang X. miR-199a impairs autophagy and induces cardiac hypertrophy through mTOR activation. *Cell Death Differ.* 2015;63895937:1–9.
 274. Gheinani AH, Burkhard FC, Rehrauer H, Fournier CA, Monastyrskaya K. MicroRNA MiR-199a-5p regulates smooth muscle cell proliferation and morphology by targeting WNT2 signaling pathway. *J Biol Chem.* 2015;290:7067–7086.
 275. Chan YC, Roy S, Huang Y, Khanna S, Sen CK. The microRNA miR-199a-5p down-regulation switches on wound angiogenesis by derepressing the v-ets erythroblastosis virus E26 oncogene homolog 1-matrix metalloproteinase-1 pathway. *J Biol Chem.* 2012;287:41032–43.
 276. Ding G, Huang G, Liu HD, Liang HX, Ni YF, Ding ZH, Ni GY, Hua HW. MiR-199a suppresses the hypoxia-induced proliferation of non-small cell lung cancer cells through targeting HIF1alpha. *Mol Cell Biochem.* 2013;384:173–180.
 277. He J, Jing Y, Li W, Qian X, Xu Q, Li FS, Liu LZ, Jiang BH, Jiang Y. Roles and mechanism of miR-199a and miR-125b in tumor angiogenesis. *PLoS One.* 2013;8:e56647.
 278. Raimondi L, Amodio N, Teresa M, Martino D, Altomare E, Leotta M, Caracciolo D, Gullà A, Neri A, Aquila PD, Alessandro R, Giordano A, Tassone P. Targeting of multiple myeloma-related angiogenesis by miR- 199a-5p mimics : in vitro and in vivo anti-tumor activity. *Oncotarget.* 2014;5:3039–3054.
 279. Dai L, Lou W, Zhu J, Zhou X, Di W. MiR-199a inhibits the angiogenic potential of endometrial stromal cells under hypoxia by targeting HIF-1α / VEGF pathway. *Int J Clin Exp Pathol.* 2015;8:4735–4744.
 280. Liu G-T, Huang Y-L, Tzeng H-E, Tsai C-H, Wang S-W, Tang C-H. CCL5 promotes vascular endothelial growth factor expression and induces angiogenesis by down-regulating miR-199a in human chondrosarcoma cells. *Cancer Lett.* 2015;357:476–487.
 281. Cheng W, Liu T, Wan X, Gao Y, Wang H. MicroRNA-199a targets CD44 to suppress the tumorigenicity and multidrug resistance of ovarian cancer-initiating cells. *FEBS J.* 2012;279:2047–59.
 282. Song J, Gao L, Yang G, Tang S, Xie H, Wang Y, Wang J, Zhang Y, Jin J, Gou Y, Yang Z,

- Chen Z, Wu K, Liu J, Fan D. MiR-199a regulates cell proliferation and survival by targeting FZD7. *PLoS One*. 2014;9:e110074.
283. Zhang L, Lou J, Lu M, Gao C, Zhao S, Li B. Suppression of miR-199a maturation by HuR is crucial for hypoxia-induced glycolytic switch in hepatocellular carcinoma. *EMBO J*. 2015;34:2671–2685.
 284. Gui R, Huang R, Zhang J-H, Wen X-H, Nie X-M. MicroRNA-199a-5p inhibits VEGF-induced tumorigenesis through targeting oxidoreductase domain-containing protein 1 in human HepG2 cells. *Oncol Rep*. 2016;35:2216–2222.
 285. Yang X, Lei S, Long J, Liu X, Wu Q. MicroRNA-199a-5p inhibits tumor proliferation in melanoma by mediating HIF-1a. *Mol Med Rep*. 2016;13:5241–5247.
 286. Ponta H, Sherman L, Herrlich PA. CD44: from adhesion molecules to signalling regulators. *Nat Rev Mol Cell Biol*. 2003;4:33–45.
 287. Stacey DW. Cyclin D1 serves as a cell cycle regulatory switch in actively proliferating cells. *Curr Opin Cell Biol*. 2003;15:158–163.
 288. Van Solingen C, Seghers L, Bijkerk R, Duijs JMGJ, Roeten MK, Van Oeveren-Rietdijk AM, Baelde HJ, Monge M, Vos JB, De Boer HC, Quax PHA, Rabelink TJ, Van Zonneveld AJ. Antagomir-mediated silencing of endothelial cell specific microRNA-126 impairs ischemia-induced angiogenesis. *J Cell Mol Med*. 2009;13:1577–1585.
 289. Heil M, Ziegelhoeffer T, Pipp F, Kostin S, Martin S, Clauss M, Schaper W. Blood monocyte concentration is critical for enhancement of collateral artery growth. *Am J Physiol Heart Circ Physiol*. 2002;283:H2411-9.
 290. Lino Cardenas CL, Henaoui IS, Courcot E, Roderburg C, Cauffiez C, Aubert S, Copin MC, Wallaert B, Glowacki F, Dewaeles E, Milosevic J, Maurizio J, Tedrow J, Marcet B, Lo-Guidice JM, Kaminski N, Barbry P, Luedde T, Perrais M, Mari B, Pottier N. miR-199a-5p is upregulated during fibrogenic response to tissue injury and mediates TGFbeta-induced lung fibroblast activation by targeting caveolin-1. *PLoS Genet*. 2013;9:e1003291.
 291. Oskowitz AZ, Lu J, Penforis P, Ylostalo J, McBride J, Flemington EK, Prockop DJ, Pochampally R. Human multipotent stromal cells from bone marrow and microRNA: regulation of differentiation and leukemia inhibitory factor expression. *Proc Natl Acad Sci U S A*. 2008;105:18372–7.
 292. D'Alessandra Y, Carena MC, Spazzafumo L, Martinelli F, Bassetti B, Devanna P, Rubino M, Marenzi G, Colombo GI, Achilli F, Maggiolini S, Capogrossi MC, Pompilio G. Diagnostic potential of plasmatic microRNA signatures in stable and unstable angina. *PLoS One*. 2013;8:e80345.
 293. Regensteiner JG, Wolfel EE, Brass EP, Carry MR, Ringel SP, Hargarten ME, Stamm ER, Hiatt WR. Chronic changes in skeletal muscle histology and function in peripheral arterial disease. *Circulation*. 1993;87:413–421.
 294. Hedberg B, Angquist K-A, Henriksson-Larsen K, Sjöström M. Fibre Loss and distribution in skeletal muscle from patients with severe peripheral arterial insufficiency. *Eur J Vasc Surg*. 1989;3:315–322.
 295. Mitchell RG, Duscha BD, Robbins JL, Redfern SI, Chung J, Bensimhon DR, Kraus WE, Hiatt WR, Regensteiner JG, Annex BH. Increased levels of apoptosis in gastrocnemius skeletal muscle in patients with peripheral arterial disease. *Vasc Med*. 2007;12:285–290.
 296. Koutakis P, Myers SA, Cluff K, Ha DM, Haynatzki G, McComb RD, Uchida K, Miserlis D,

- Papoutsis E, Johanning JM, Casale GP, Pipinos II. Abnormal myofiber morphology and limb dysfunction in claudication. *J Surg Res*. 2015;196:172–179.
297. Fan G, Beard C, Chen RZ, Csankovszki G, Sun Y, Siniaia M, Biniszkiwicz D, Bates B, Lee PP, Kuhn R, Trumpp a, Poon C, Wilson CB, Jaenisch R. DNA hypomethylation perturbs the function and survival of CNS neurons in postnatal animals. *J Neurosci*. 2001;21:788–797.
 298. Monvoisin A, Alva J a., Hofmann JJ, Zovein AC, Lane TF, Iruela-Arispe ML. VE-cadherin-CreERT2 transgenic mouse: A model for inducible recombination in the endothelium. *Dev Dyn*. 2006;235:3413–3422.
 299. Shankman LS, Gomez D, Cherepanova O a, Salmon M, Alencar GF, Haskins RM, Swiatlowska P, Newman A a C, Greene ES, Straub AC, Isakson B, Randolph GJ, Owens GK. KLF4-dependent phenotypic modulation of smooth muscle cells has a key role in atherosclerotic plaque pathogenesis. *Nat Med*. 2015;21:628–37.
 300. Xu X, Tao Y, Gao X, Zhang L, Li X, Zou W, Ruan K, Wang F, Xu G-L, Hu R. A CRISPR-based approach for targeted DNA demethylation. *Cell Discov*. 2016;2:16009.
 301. Maeder ML, Angstman JF, Richardson ME, Linder SJ, Cascio VM, Tsai SQ, Ho QH, Sander JD, Reyon D, Bernstein BE, Costello JF, Wilkinson MF, Joung JK. Targeted DNA demethylation and activation of endogenous genes using programmable TALE-TET1 fusion proteins. *Nat Biotechnol*. 2013;31:1137–1142.
 302. Vojta A, Dobrinić P, Tadić V, Bočkor L, Korać P, Julg B, Klasić M, Zoldoš V. Repurposing the CRISPR-Cas9 system for targeted DNA methylation. *Nucleic Acids Res*. 2016;44:5615–28.
 303. Demicheva E, Hecker M, Korff T. Stretch-induced activation of the transcription factor activator protein-1 controls monocyte chemoattractant protein-1 expression during arteriogenesis. *Circ Res*. 2008;103:477–84.
 304. Billaud M, Ross JA, Greyson MA, Bruce AC, Seaman SA, Heberlein KR, Han J, Best AK, Peirce SM, Isakson BE. A new method for in vivo visualization of vessel remodeling using a near-infrared dye. *Microcirculation*. 2011;18:163–71.
 305. Burke CW, Soo J, Kim AJ, Hsiang YJ, Klibanov AL, Hanes J, Price RJ. Markedly enhanced skeletal muscle transfection achieved by the ultrasound-targeted delivery of non-viral gene nanocarriers with microbubbles. *J Control Release*. 2012;162:414–421.
 306. Mac Gabhann F, Peirce SM. Collateral capillary arterialization following arteriolar ligation in murine skeletal muscle. *Microcirculation*. 2010;17:333–47.
 307. Scholz D. Contribution of arteriogenesis and angiogenesis to postocclusive hindlimb perfusion in mice. *J Mol Cell Cardiol*. 2002;34:775–787.
 308. Murphy TP, Cutlip DE, Regensteiner JG, Mohler ER, Cohen DJ, Reynolds MR, Massaro JM, Lewis B a, Cerezo J, Oldenburg NC, Thum CC, Goldberg S, Jaff MR, Steffes MW, Comerota AJ, Ehrman J, Treat-Jacobson D, Walsh ME, Collins T, Badenhop DT, Bronas U, Hirsch AT. Supervised exercise versus primary stenting for claudication resulting from aortoiliac peripheral artery disease: six-month outcomes from the claudication: exercise versus endoluminal revascularization (CLEVER) study. *Circulation*. 2012;125:130–9.
 309. van Royen N, Piek JJ, Buschmann I, Hoefer I, Voskuil M, Schaper W. Stimulation of arteriogenesis; a new concept for the treatment of arterial occlusive disease. *Cardiovasc Res*. 2001;49:543–53.

310. Fakhry F, Spronk S, van der Laan L, Wever JJ, Teijink JAW, Hoffmann WH, Smits TM, van Brussel JP, Stultiens GNM, Derom A, den Hoed PT, Ho GH, van Dijk LC, Verhofstad N, Orsini M, van Petersen A, Woltman K, Hulst I, van Sambeek MRHM, Rizopoulos D, Rouwet E V., Hunink MGM. Endovascular revascularization and supervised exercise for peripheral artery disease and intermittent claudication. *Jama*. 2015;314:1936.
311. Teravainen H, Makitie J. Striated muscle ultrastructure in intermittent claudication. *Arch Pathol Lab Med*. 1977;101:230–35.
312. Makitie J, Teravainen H. Histochemical changes in striated muscle in patients with intermittent claudication. *Arch Pathol Lab Med*. 1977;101:658–63.
313. McClung JM, McCord TJ, Keum S, Johnson S, Annex BH, Marchuk DA, Kontos CD. Skeletal muscle-specific genetic determinants contribute to the differential strain-dependent effects of hindlimb ischemia in mice. *Am J Pathol*. 2012;180:2156–69.
314. Anderson JD, Epstein FH, Meyer CH, Hagspiel KD, Wang H, Berr SS, Harthun NL, Weltman A, Dimaria JM, West AM, Kramer CM. Multifactorial determinants of functional capacity in peripheral arterial disease: uncoupling of calf muscle perfusion and metabolism. *J Am Coll Cardiol*. 2009;54:628–635.
315. Hiatt WR, Nawaz D, Brass EP. Carnitine metabolism during exercise in patients with peripheral vascular disease. *J Appl Physiol*. 1987;62:2383–7.
316. Hiatt WR, Wolfel EE, Regensteiner JG, Brass EP. Skeletal muscle carnitine metabolism in patients with unilateral peripheral arterial disease. *J Appl Physiol*. 1992;73:346–353.
317. Pipinos II, Judge AR, Zhu Z, Selsby JT, Swanson SA, Johanning JM, Baxter BT, Lynch TG, Dodd SL. Mitochondrial defects and oxidative damage in patients with peripheral arterial disease. *Free Radic Biol Med*. 2006;41:262–269.
318. Brass EP, Hiatt WR, Gardner AW, Hoppel CL. Decreased NADH dehydrogenase and ubiquinol-cytochrome c oxidoreductase in peripheral arterial disease. *Am J Physiol Hear Circ Physiol*. 2001;280:H603-9.
319. Pedraza E, Coronel MM, Fraker C a., Ricordi C, Stabler CL. Preventing hypoxia-induced cell death in beta cells and islets via hydrolytically activated, oxygen-generating biomaterials. *Proc Natl Acad Sci U S A*. 2012;109:4245–4250.
320. Harrison BS, Eberli D, Lee SJ, Atala A, Yoo JJ. Oxygen producing biomaterials for tissue regeneration. *Biomaterials*. 2007;28:4628–4634.
321. Ward CL, Corona BT, Yoo JJ, Harrison BS, Christ GJ. Oxygen generating biomaterials preserve skeletal muscle homeostasis under hypoxic and ischemic conditions. *PLoS One*. 2013;8:e72485.
322. van Royen N, Piek JJ, Schaper W, Fulton WF. A critical review of clinical arteriogenesis research. *J Am Coll Cardiol*. 2009;55:17–25.
323. Nishijima Y, Akamatsu Y, Weinstein PR, Liu J. Collaterals: implications in cerebral ischemic diseases and therapeutic interventions. *Brain Res*. 2015;1–12.
324. Seaman SA, Cao Y, Campbell CA, Peirce SM. Macrophage recruitment and polarization during collateral vessel remodeling in murine adipose tissue. *Microcirculation*. 2016;23:75–87.
325. Antebi B, Zhang L, Sheyn D, Pelled G, Zhang X, Gazit Z, Schwarz E, Gazit D. Controlling arteriogenesis and mast cells are central to bioengineering solutions for critical bone defect repair using allografts. *Bioengineering*. 2016;3:6.

326. Yu JL, Rak JW. Host microenvironment in breast cancer development: inflammatory and immune cells in tumour angiogenesis and arteriogenesis. *Breast Cancer Res.* 2003;5:83–88.
327. Muto J, Shirabe K, Yoshizumi T, Ikegami T, Aishima S, Ishigami K, Yonemitsu Y, Ikeda T, Soejima Y, Maehara Y. The apelin-APJ system induces tumor arteriogenesis in hepatocellular carcinoma. *Anticancer Res.* 2014;34:5313–5320.